Combining Carbon Nanoparticle Coatings with Textured Surfaces for Enhanced Solid Lubrication

Dissertation

zur Erlangung des Grades
des Doktors der Ingenieurswissenschaften
der Naturwissenschaftlich-Technischen Fakultät
der Universität des Saarlandes

vorgelegt von

Timothy MacLucas

Saarbrücken

März 2024

Tag des Kolloquiums:	09.09.2024
Dekan:	Prof. Dr.-Ing. Michael Vielhaber
Berichterstatter:	Prof. Dr.-Ing. Frank Mücklich Prof. Dr.-Ing. Dirk Bähre
Akad. Mittelbau:	Dr.-Ing. Florian Schäfer
Vorsitz:	Prof. Dr. Roland Bennewitz

„Es steckt oft mehr Geist und Scharfsinn in einem Irrtum als in einer Entdeckung."

(Joseph Jouberg)

Table of contents

Acknowledgements

First and foremost, I would like to emphasize that the completion of a doctoral thesis is not an individual achievement but a collective effort and this thesis in particular is based on the ideas and work efforts of numerous individuals.

I would like to express my most heartfelt gratitude towards Prof. Dr.-Ing. Frank Mücklich for his confidence and for giving me the opportunity to write my thesis at the Chair of Functional Materials at Saarland University. I am thankful for his support and consider myself lucky to have had the possibility to develop scientifically in a great academic environment.

I would also like to thank Prof. Dr. Guido Kickelbick for his engagement as my scientific advisor.

I am also grateful to Dr. Philipp Grützmacher and Prof. Dr.-Ing. Carsten Gachot who were at first colleagues here in Saarbrücken and later moved to TU Wien. Both were close colleagues and collaborateurs within the framework of a DFG project related to this thesis and have developed into valued friends over the years.

I would like to extend my thanks to several other academic colleagues for their fruitful collaboration on several research topics related to this work including Prof. Dr. Michael Moseler and Dr. Andreas Klemenz from IWM Fraunhofer in Freiburg as well as Prof. Dr. Volker Presser from INM in Saarbrücken.

Naturally, many thanks to my FuWe colleagues and fellow “Kicker” enthusiasts who have been great over the years and a lot of fun to banter with. This includes Dr. Leander Reinert, Christian Schäfer, Daniel Müller, Tobias Fox, Bruno Alderete, Rouven Zimmer, Dr. Idriss El Azhari, Nadja Schorr, Dr. Flavio Soldera, Silas Schütz, and Dr. Pranav Nayak. I will miss our day-to-day lunch and work together.

In addition, I would like to express my sincere appreciation to Dr. Flavio Soldera and the EUSMAT team for accepting me into the AMASE master’s program in 2014. This opportunity paved the way for my progress in Materials Science and ultimately enabled the completion of this dissertation.

I am immensely grateful to my colleague and friend, Dr. Sebastian “Seba” Suarez, who was instrumental in convincing me to write a doctoral thesis in the first place. Beyond that, I thank him for the many fruitful and always instructive discussions, his mentoring, guidance, support, and motivation. He always readily shared his knowledge and his insights and taught me the value of diligence, and academic excellence.

Furthermore, I would like to acknowledge Manel Ripoll Rodrigues for conducting the friction tests in vacuum and at elevated temperatures at the Austrian Excellence Centre of Tribology (AC2T research GmbH) and funding by the Austrian COMET-Programme (Project K2 InTribology2, no. 906860).

Special thanks once again to Dr. Pranav Nayak and Dr. Sebastian Suarez for proofreading and their constructive feedback which has substantially elevated the quality of this thesis.

Finally, I would like to mention my beloved family, Inge, Neil and Dennis without whom this thesis would not have been possible. Thank you for believing in me and for your unwavering support.

Abstract

Combining carbon nanoparticle coatings with textured metallic surfaces forms an effective solid lubrication system. As the adhesion of nanocarbons on metallic surfaces is poor, the sustained lubricity of this system is based on storing the nanocarbons in the topographical minima of the texture from where the particles are continuously supplied directly to the contact. This dissertation investigates various aspects of this lubrication system, including the primary lubrication and degradation mechanisms of the particles in the contact, and their lubricity under extreme operating environments. Furthermore, the structural depth of the surface texture is optimized to improve the lubricity of carbon nanoparticle coatings. The obtained results strongly and consistently indicate that rolling is not the primary lubrication mechanism of carbon nanotubes. Instead, a multi-step lubrication mechanism based on progressing particle amorphization and the saturation of superficial dangling bonds is proposed. Among all the tested carbon nanoparticles, carbon nanotubes exhibit superior lubricity in ambient conditions. In contrast to the other particles, patch formation on the textures is observed with the carbon nanotubes which likely contributes to their enhanced tribological properties. The carbon nanotubes also demonstrate superior lubricity compared to the other examined lubricant coatings (including conventional solid lubricants) under high loads and otherwise ambient conditions.

Zusammenfassung

Die Kombination von Kohlenstoff-Nanopartikel-Beschichtungen mit strukturierten Metalloberflächen bildet ein effektives Festschmiersystem. Aufgrund der schwachen, nicht-kovalenten Haftung von Nanokohlenstoffen auf metallischen Oberflächen, beruht die Schmierfähigkeit dieses Systems auf der Speicherung der Nanokohlenstoffe in den topografischen Minima der Struktur. Im Rahmen dieser Dissertation werden verschiedene Aspekte dieses Schmiersystems untersucht, z.B. die primären Schmier- und Degradationsmechanismen, und ihre Schmierfähigkeit unter extremen Betriebsbedingungen. Des Weiteren wird die Tiefe der Oberflächenstruktur optimiert, um die Schmierfähigkeit der Kohlenstoff-Nanopartikel-Beschichtungen zu verbessern. Die Ergebnisse deuten darauf hin, dass Rollen nicht der primäre Schmiermechanismus der Carbon Nanotubes ist. Stattdessen wird ein mehrstufiger Schmiermechanismus vorgeschlagen, der auf fortschreitender Amorphisierung der Partikel sowie der Sättigung oberflächlicher, gebrochener Kohlenstoff-Bindungen beruht. Unter Umgebungsbedingungen weisen Carbon Nanotubes die beste Schmierfähigkeit aller getesteten Kohlenstoff-Nanopartikel auf, diese ist aller Wahrscheinlichkeit nach zumindest in Teilen auf die Bildung von Carbon Nanotube-Patches auf den Oberflächenstrukturen zurückzuführen. Die Carbon Nanotubes weisen auch im Vergleich zu den anderen untersuchten Schmierstoffbeschichtungen bei hohen Lasten und unter atmosphärischen Bedingungen eine überlegene Schmierfähigkeit auf.

Abbreviations and symbols

Abbreviation	Definition
ADF	Amplitude density function
CLSM	Confocal laser scanning microscopy
CNH	Carbon nanohorn
CNP	Carbon nanoparticles
CO	Carbon onion
COF	Coefficient of friction
(MW)CNT	(Multiwall) Carbon nanotubes
CVD	Chemical vapor deposition
DLC	Diamond-like carbon
DLIP	Direct laser interference patterning
DLW	Direct laser writing
EJ	Exajoules
EPD	Electrophoretic deposition
h-BN	Hexagonal boron nitride
HD	High depth
ID	Intermediate depth
LD	Low depth
Mg-Nit	Magnesium nitrate hexahydrate
Mt	Million tons
NASA	National Aeronautics and Space Administration
PTFE	Polytetrafluorethylene
PVD	Physical vapor deposition
TEA	Triethylamine
TEM	Transmission electron microscopy
TMD	Transition-metal dichalcogenide
USP	Ultrashort pulses

Symbol	Definition
F_R, F_N	Frictional force, normal force
μ	Coefficient of friction
R_q	Root mean square roughness
R_a	Arithmetic average roughness
l	Sampling length
y(x)	Arithmetic mean of the absolute ordinate within the sampling length
R_{sk}	Skewness
R_{ku}	Kurtosis
E’	Reduced Youngs’ modulus
R’	Reduced contact radius
v	Poisson ratio
E	Youngs’s modulus
Λ	Periodicity
τ_P	Pulse duration
δ_{opt}	Optical penetration depth
τ_{ep}	Electron-phonon interaction time
C_e	Electronic heat capacity
G	Electron-phonon coupling constant
τ_{mech}	Minimal time needed to initiate expansion of the heated lattice
τ_{heat}	Lattice heating time
t_{th}	Characteristic time of heat dissipation
δ_{eff}	Effective penetration depth
D_{EQ}	Thermal diffusion coefficient during electron-lattice equilibrium

1. Introduction

Tribology is the science and engineering of interacting surfaces in relative motion. It deals with the study and application of friction, wear, and lubrication. Whenever movement occurs, be it in the bearing of a mechanical system or a joint in a biological system, tribological processes take place. The primary objective of tribology is to develop a better understanding of the mechanisms of surface interactions, improve the efficiency and durability of mechanical systems and reduce energy consumption and environmental impacts.

Most people are unaware to the ubiquity of tribology in everyday life. For instance, wearing slippers at home gives us better grip on the floor, enabling quicker and more efficient navigation. Breaking pads pressed against the rim of the bicycle wheel allow us to decelerate and stop. Even the mouthfeel of food is heavily influenced by tribological phenomena. Tribology also plays a major role in high-tech as it represents a crucial aspect in modern micro electronical systems, integrated circuits, electrical vehicles, and aerospace. The consequences of a major tribological failure became apparent in 2013 at NASA's Kepler telescope when the flywheel shaft system failed due to friction-induced problems [1]. This led to the loss of critical control and stabilization functions and resulted in the discontinuation of the original mission after only 4 years of service.

Friction is always associated with wear and, thus, material as well as energy loss which represents an immense economic factor, particularly in a highly industrialized society. Based on data from 2014, calculations by Holmberg and Erdemir have shown, that 23 % of the annual energy consumption globally, which corresponds to 119 exajoules (EJ), originates from tribological contacts. 87 % of that is used to overcome friction while the remaining 13 % goes into remanufacturing wear parts and spare equipment due to wear and wear-related failures [2]. However, considering that the replacement of worn parts not only results in energy cost but also leads to other problems such as maintenance cost and production losses, the total cost of wear is significantly higher. Holmberg and Erdemir estimate that the total economic damage worldwide originating from tribological contacts in all societal sectors is up to 2.5 trillion euros annually of which 73 % is due to friction and due to 27 % wear [3]. When relating the used energy directly to emissions, friction and wear would account for 8,120 million tons (Mt) of emitted CO_2 per year. In the transportation sector, friction losses are most significant as it accounts for

roughly 30 % of the total energy use, compared to 20 % in the energy industry and manufacturing whereas in the residential sector, it is only 10 % [3].

As humankind starts to transition away from fossil fuels to a more sustainable economy, the associated technologies such as renewable energies dominate the public debate, however, the significant impact tribology has on resource conservation is widely disregarded. Holmberg and Erdemir have determined that implementing advanced tribological technologies in different mechanical systems such as passenger cars, trucks and buses, equipment in the mining industry and paper machines would save substantial amounts of friction and wear [2].

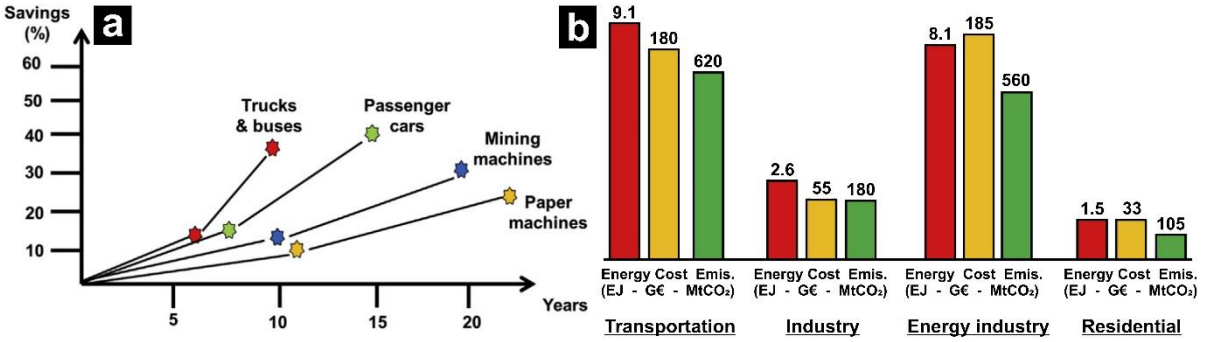

Figure 1. (a) Calculated potential friction and wear savings over current state of the art by the introduction of advanced tribology solutions in four case studies and their time scale of implement [2]. The savings and timescale of implementation are based on the present transportation and industry infrastructure and do not consider future trends (e.g., the introduction of electric vehicles). (b) Potential annual savings in energy, cost, and CO_2 emissions globally (linearized) in different sectors during the initial 8 years of advanced tribology implementation [2].

The calculations displayed in **Fig. 1a** indicate considerable differences in the duration required for implementation. Truck and bus manufacturers are able to adopt new technologies faster as there are fewer owners with large fleets hence the implementation time is considered relatively short. In the paper and mining industry, however, the machines have extensive lifetimes and return on invest is prioritized over immediate adoption. **Fig. 1b** shows the absolute potential savings in the most relevant sectors during the initial 8 years after implementation which amounts to 21 EJ, 453 billion euros and 1,460 Mt of CO_2 annually and worldwide. The transportation and energy industry hold the greatest potential for savings, however, immediate savings in these sectors would not be as significant due to longer implementation times.

One approach to mitigate friction and wear is by introducing a texture to either one or both surfaces in a contact [4,5] as the true contact area is reduced [6]. The impact of surface texturing,

e.g. in the form of patterns with respect to tribological optimization can be observed in nature, specifically in marine life. Paleontologists assume, that the bodies of animals such as sharks evolved into streamlined shapes with specifically structured skin to minimize flow resistance during locomotion (**Fig. 2a** and **b**). This adaptation is crucial for their survival as the majority of shark species rely on speed and maneuverability to hunt. The ability to minimize flow resistance is so significant [7–9] that it inspired German companies Lufthansa Technik and BASF to develop a polymer foil, that mimics shark skin [10]. The foil is designed for attachment on specific parts of the aircraft fuselage to reduce aerodynamic drag and, thus, fuel emissions. According to the two companies, this technology enables annual fuel savings of up to 1.1 %, which in the case of a Boeing 777 corresponds to 4,800 tons of kerosene or 15,200 tons of carbon dioxide [10]. The described efficiency gain has led Lufthansa Cargo and Swiss to introduce this technology in their fleet from 2022 onwards [11].

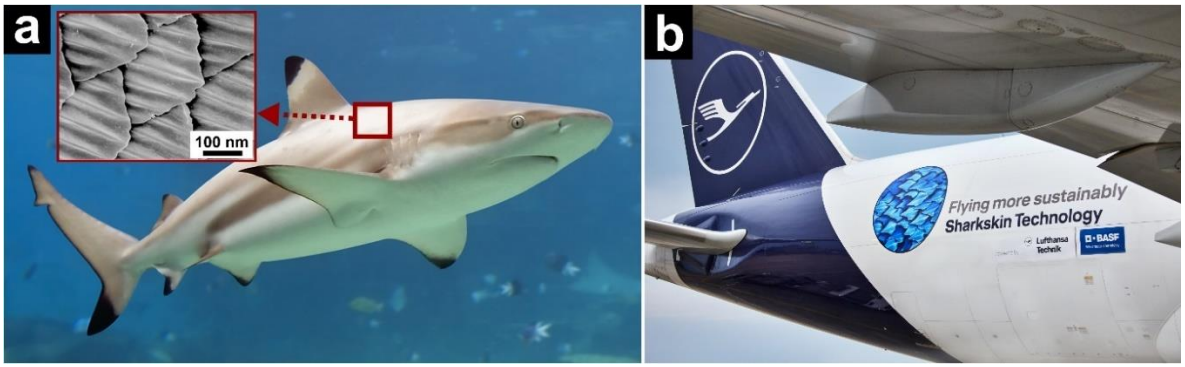

Figure 2. (a) Blacktip shark (*Carcharhinus limbatus* [1], inlet: scanning electron micrograph of the placoid scales of the shark from the dorsal body wall anterior to the dorsal fin [12]). (b) Fuselage of a Lufthansa Cargo aircraft equipped with the polymer foil [13].

The shark skin foil represents a fine example of how biological structures influence and improve the design of technical components to increase performance and efficiency. The most effective approach to mitigating friction and wear, however, is lubrication. Liquid lubricants (typically oil-based) are the most widely used form of lubrication today as they combine high lubricity with simple applicability and accessibility while being cost-effective, which makes them well-suited for a wide range of applications. However, oil cannot be used in extreme environments as it solidifies in the cold or starts to evaporate at the latest between 300 °C and 350 °C and in vacuum. Operating under high load represents another challenging scenario

[1] Shutterstock

where lubricants are exposed to elevated temperatures. Firstly, this causes the viscosity of oil-based lubricants to break down and results in decreasing film strengths. This is often followed by a transition to a more unfavorable lubrication regime and in extreme cases, the contact starves entirely. Secondly, oil tends to oxidize when exposed to heat. As a result, acidic compounds are formed that corrode the surface, causing enhanced wear [14,15]. Naturally, oil is also hazardous to the environment if not handled and disposed correctly. Conventional solid lubricants such as graphite, diamond-like carbon (DLC), transition metal dichalcogenides (TMD: e.g., molybdenum disulfide and tungsten disulfide) are more suitable for these conditions and generally more eco-friendly, however, their individual lubricity also depends strongly on the operational conditions and is, thus, limited.

Carbon nanoparticles such as carbon nanotubes (CNT), carbon onions (CO) and carbon nanohorns (CNH) combine a variety of properties that make them suitable for high performance solid lubrication. Due to sp^2 hybridization, these nanocarbons are highly conductive with strong mechanical properties. This is paired with a cylindrical (CNT) or spherical (CO, CNH) morphology, which means they are less susceptible to oxidation as they have little to no edge area and can theoretically roll. Therefore, the lubricity of CNT, CO and CNH might be significantly less dependent on its operating environment compared to that of conventional solid lubricants.

As shown by Reinert et al. [16], the friction-reducing effect of a surface texture is brief as it is worn off rapidly by the counter body. CNTs, on the other hand, do not form a covalent bond with the substrate hence CNT coatings are pushed out of the contact when exposed to frictional stress. When both approaches are combined, however, the topographical minima of the texture function as lubricant reservoirs that store the particles and prevent their removal. Moreover, the particles are continuously passed from the reservoirs to the contact. This way, the weaknesses of the individual approaches are negated, and an effective solid lubrication system is formed.

The objective of this dissertation is to study and optimize crucial aspects and properties of this solid lubrication system. This includes the coating process, design optimization of the surface texture, the elucidation of the fundamental lubrication mechanism of CNTs, the lubricity in extreme environments and the long-term lubricity of this solid lubrication system.

2. State of the art

2.1. Dry tribology and contact mechanics

Tribology is the scientific and engineering field that focuses on the study and understanding of friction, wear, and lubrication of interacting surfaces in relative motion. The word "tribology" is derived from the Greek words *tribos* ("rubbing") and the suffix *-logy* ("science" or "knowledge of") and, thus, translates to "the science of rubbing" [17,18]. Tribology encompasses various aspects such as the design of lubricants, surfaces, and coatings as well as the analysis of the causes and effects of friction and wear in mechanical systems. It is highly interdisciplinary with relevance in various fields such as mechanical engineering, biology, chemistry, material science and medicine. Advances in tribology reduce energy and resource consumption which leads to significant cost and emission savings and increased efficiency. Moreover, they enhance the quality of medical products such as artificial joints and thus directly benefit people's health.

Humans became familiar with the concept of friction during the Stone Age when they discovered that fire could be created by rubbing together pieces of wood or striking pyrite [19]. The earliest documented application of tribological principles dates back to the ancient civilizations of Egypt and China [20,21]. The continuous placement of rolling wood sticks underneath heavy objects enabled the ancient Egyptians to transport massive stone blocks used for the construction of the Pyramids over long distances and on slopes [20]. Further, there is evidence, that they used water for its lubricity along with vegetable oils and animal fats [20]. Leonardo da Vinci is considered the first tribologist as he formulated two fundamental laws of friction in 1493, however, his notes remained unpublished. Over 200 years later, afore-mentioned laws were rediscovered by the French physicist Guillaume Amontons and published in 1699 [22].

2.1.1. Amontons' laws

The discoveries of Da Vinci and Coulomb became known as Amontons' laws (also referred to as the fundamental laws of friction) and they are particularly useful for understanding and predicting the behavior of friction. They are as follows:

- The friction force F_R is directly proportional to the applied normal force F_N pressing two surfaces together (Amontons 1st law) [23].

$$F_R = \mu \cdot F_N \quad (1)$$

  with μ denoting the coefficient of friction (COF).
- The friction force is independent of the apparent contact area (Amontons 2nd law) [23].
- The friction force is independent of the sliding velocity (Coulomb's law) [24].

These laws provided the foundation for engineering designs involving mechanisms and machines and were further expanded on by Bowden and Tabor.

2.1.2. Technical surfaces and contact between solids

The two physicists Frank Philip Bowden and David Tabor are regarded as the pioneers of modern tribology for providing a physical explanation for the laws of friction [25]. Firstly, they recognized that technical surfaces are rough on an atomic scale (**Fig. 3a**). This translates to the microscopic scale, where technical surfaces consist primarily of asperities and grooves. In tribological contacts, only the asperities of the surfaces touch and the real contact area of rough surfaces is small, particularly in comparison to the apparent contact area (**Fig. 3b**) [26]. Consequently, friction and wear at the onset of sliding are governed by intense stresses at the asperity contacts and extreme concentrations of frictional energy, even at modest nominal loads. Bowden and Tabor measured the conductivity between two contacting metal surfaces and observed that the conductivity was proportional to the normal load [27]. By applying greater loads, more asperities came into contact and the average area of asperity contact (real contact area) grew due to plastic deformation, which lead to an increase in conductivity. Thus, Bowden and Tabor concluded that the real contact area must be proportional to the applied load.

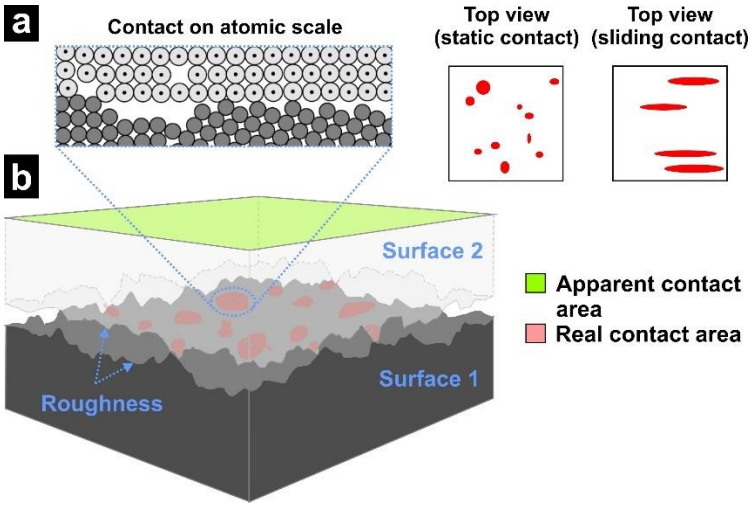

Figure 3. Schematic illustration of the interface between two contacting technical surfaces. (a) Contact on an atomic scale and (b) comparison between apparent and real contact area with top views of static and sliding contact (partially adapted from [28]).

The specific topographies of the contacting surfaces have a significant impact on the tribological behavior. Topography and surface roughness are closely related aspects that describe the physical characteristics of a surface. Topography refers to the three-dimensional feature arrangement on a surface (including height variations and contours) that shapes the roughness, while roughness parameters quantitatively describe the topographical variations present on the surface. There is a wide variety of parameters which can be used to determine the roughness, each offering specific insights into the surface texture. The most commonly used parameters to quantify roughness are:

- Root mean square roughness (R_q):

$$R_q = \sqrt{\frac{1}{l}\int_0^l |y^2(x)|\,dx} \tag{2}$$

- Arithmetic average roughness (R_a):

$$R_a = \frac{1}{l}\int_0^l |y(x)|\,dx \tag{3}$$

with l as the sampling length and y(x) as the arithmetic mean of the absolute ordinate within the sampling length. However, surfaces with different topographies can exhibit similar roughness parameters. A more comprehensive description of the surface topography requires information on the probability distribution of surface heights and the spatial distribution of asperities and grooves across the surface [29]. Based on a given surface profile (**Fig. 4a**), integrating the corresponding amplitude density function (ADF, **Fig. 4b**) yields the Abbott-

Firestone curve (**Fig. 4c**) [28,29]. Different parameters that provide useful information on the surface topography can be derived from the ADF and the Abbott-Firestone curve, i.e., the *skewness* (R_{sk}, measure of the surface profiles' asymmetry in the amplitude density function) and the *kurtosis* (R_{ku}, measure of the sharpness of the peak of the distribution curve). These two parameters allow for an assessment on the load bearing capacity, which has significant implications for initial friction and wear, as well as lubrication strategies.

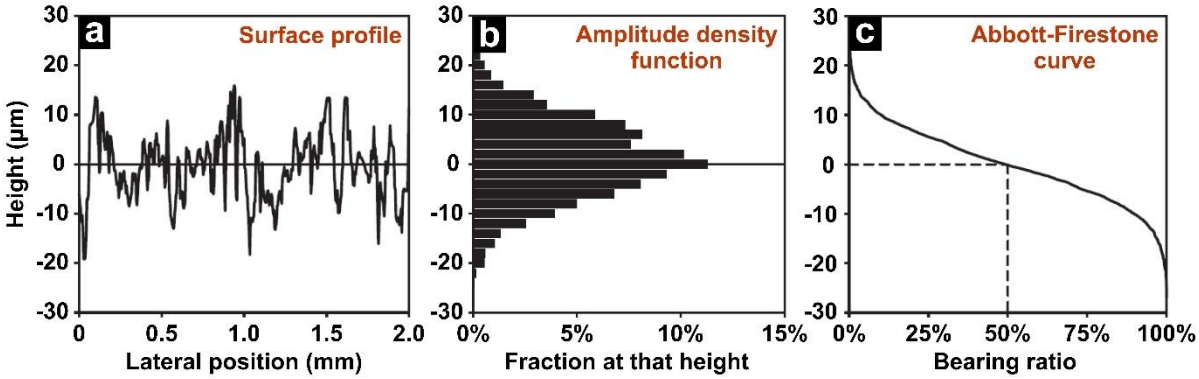

Figure 4. (a) Exemplary surface profile with (b) the corresponding amplitude density function and (c) the derived Abbott-Firestone curve (adapted from [29]).

When two surfaces come into contact and there is relative motion or an attempt at relative motion between them, friction arises. Friction is a fundamental force that opposes relative motion or the tendency of motion between two contacting surfaces and is caused by the interaction between the atoms and/or molecules of the involved surfaces. Friction is always associated with energy dissipation where kinetic energy is converted into heat, sound energy, deformation (elastic and plastic), and the breaking of atomic bonds which can lead to the generation of wear particles and thus abrasion-related material removal. On an atomic level, phonon dissipation (a phonon is a quantized vibrational mode in a crystalline lattice) is well-established and among the most significant friction models as it has been verified in numerous studies [30–35]. During phonon dissipation, interatomic bonds in the surface of the interface materials are distorted by mechanical stress, resulting in the generation of atomic lattice vibrations. Rising vibrational energy leads to an increase in temperature, which is why phonon excitation is associated with heat generation. This phenomenon is described by the Prandtl-Tomlinson model and the Frenkel-Kontorova-Tomlinson model, the core idea of which is the transformation of spring deformation energy into vibration energy [1]. Furthermore, frictional heat between sliding surfaces is also generated by electron dissipation, which describes the

lattice scattering of excited electrons [36,37]. Friction-induced electron dissipation is based on the Coulomb drag effect occurring between two closely juxtaposed surfaces. The Coulomb forces between the charges lead to a momentum and energy transfer between the layers, resulting in the observed drag effect [1]. Both phonon and electron dissipation are still being researched, however, they generally occur in concert and interdependently, which complicates their isolated investigation [1]. In addition to that, there are four non-contact frictional energy dissipation mechanisms: Van der Waals friction, electrostatic friction, phononic friction (phonon dissipation occurs both in contact and contactless), and adsorbate drag friction. The above mechanisms have all been experimentally verified [38–42], however, especially the mechanisms related to quantum mechanics such as phonon dissipation are not well understood and require further research.

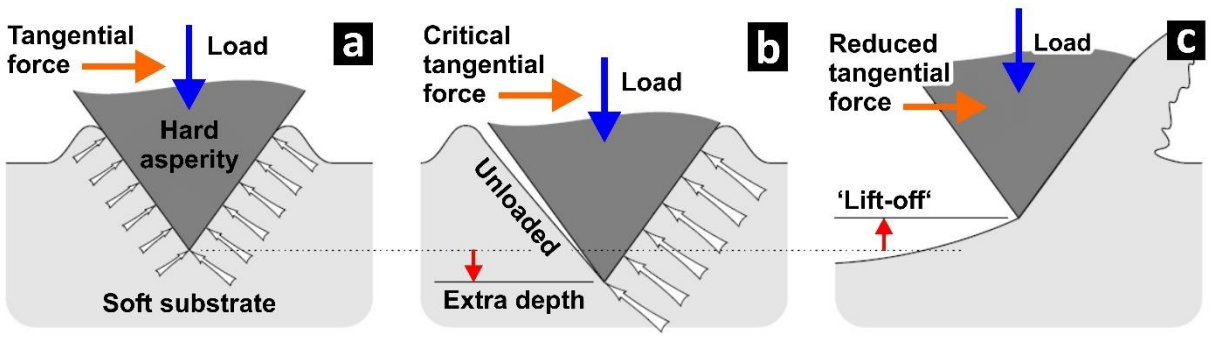

Figure 5. Schematic illustration depicting the transition process from stationary to sliding contact of a hard asperity on a soft substrate. (a) Stationary contact with a small tangential force unable to overcome the static friction. (b) Threshold stage where the tangential force reaches a critical level and the asperity sinks deeper into the substrate material. (c) Sliding contact is initiated by the *lift-off* effect and an immediate reduction of the tangential force (adapted from [28]).

There are two types of friction, static and kinetic friction. Static friction represents the force that hinders the initiation of movement between two contacting objects. The magnitude of this static frictional force adjusts itself to correspond with the magnitude of the externally applied force, but only up to a certain limit. When the applied force fails to overcome the resisting static friction, the object in question will not move. Kinetic friction (also known as dynamic friction) describes the force that hinders or opposes relative motion between two contacting objects which are in motion and is typically lower than static friction. Kinetic friction remains relatively stable for a specific material pairing, assuming that external conditions like temperature and roughness remain consistent. Maintaining the motion of an object requires less effort than

setting it in motion, due to the concept of inertia and the natural tendency of objects to maintain their state of motion (Newton's first law). From examining hard asperities on soft substrates, Challen et al. have derived a qualitative description of the transition from stationary contact to sliding [43]. As illustrated in **Fig. 5**, three distinct stages were observed:

(1) Stationary contact (static friction, **Fig. 5a**): The tangential force is minor and thus insufficient to fully shift the load to the leading side of the asperity.

(2) Threshold (**Fig. 5b**): The tangential force reaches a critical level at which the asperity is pressed against the leading side, causing it to dig in further into the substrate.

(3) Sliding contact (kinetic friction, **Fig. 5c**): The asperity *lifts off* as movement is initiated. Simultaneously, the tangential force decreases.

The occurrence of fluctuations between static and kinetic friction is a common tribological phenomenon and referred to as *stick-slip*. During stick-slip, sliding is jerky meaning the sliding velocity of an object consistently fluctuates between nearly immobile and extremely rapid motion. In tribological applications, mitigating stick-slip is comparably significant to reducing the overall COF due to the detrimental impact of the induced vibrations.

2.1.3. Fundamental wear mechanisms

Wear is the progressive loss of material from a solid surface due to mechanical interactions and has been the subject of scientific interest due to its enormous economic importance for decades. Replacing worn components requires the manufacturing of spare parts as well as their transportation and fitting. In addition, there may be production losses due to standstill. This process is therefore immensely costly and energy-intensive, causing further CO_2 emissions. Understanding the wear mechanisms is thus crucial for optimizing the performance, efficiency, and service life of any mechanical systems. There are various fundamental wear mechanisms, which usually occur simultaneously:

- **Adhesive wear:** When two solid surfaces are in contact, adhesion occurs due to intermolecular forces between the surface atoms and/or molecules that join the contact points (micro-welding). During sliding, the contacting asperity junctions plastically deform and are subsequently sheared off. When the joint asperities are broken, one of two cases occurs:

(1) Adhesion strength at the junction is below softer metals' shear strength. In that case, breaking occurs at the metal-metal interface without material transfer.

(2) Adhesion strength at the junction is greater than the softer metals' shear strength. In that case, breaking occurs within the softer metal and part of the softer material is transferred to the harder metal (as shown in **Fig. 6a**). This phenomenon is known as adhesive wear.

Metals are especially susceptible therefore adhesive wear is of great practical significance. The most substantial adhesive wear arises between identical metals, i.e., iron-iron contacts [28]. Outside of tribological stress, adhesion is effectively prevented by the presence of oxide layers and/or contaminant layers of organic matter, oxygen, or water, among others. Factors influencing adhesive wear include roughness, contact pressure, temperature, and material properties.

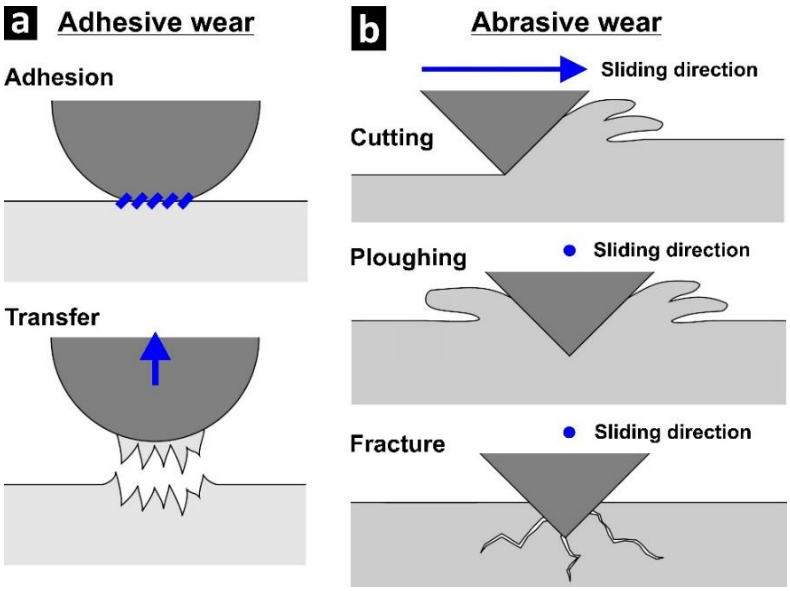

Figure 6. (a) Schematic illustration of adhesion-related material transfer. (b) Schematic illustration of three most prominent abrasive wear mechanisms: cutting, ploughing, and fracture (adapted from [28]).

- **Abrasive wear:** Material loss caused by hard particles passing over a surface is known as abrasive wear and it occurs whenever a solid object is loaded against particles of a material that have equal or greater hardness [28]. Abrasive wear is influenced by the hardness of the materials involved as well as particle concentration, shape, and size. Within the realm of abrasion, there exist multiple variants that generally act in conjunction (**Fig. 6b**) [28]:

(a) Cutting: This is a common abrasive wear mechanism where hard particles or asperities on one surface mechanically incise or sever the softer material of an opposing surface, causing material removal through a process resembling miniature cutting or chiseling at the microscale.

(b) Ploughing: During this abrasive wear process, hard particles, or asperities on one surface embed into the surface of a softer material, displacing material and creating grooves due to applied load and relative motion, akin to ploughing through at the microscale.

(c) Fracture: Fracture wear (also known as subsurface fatigue) occurs within the material's bulk or subsurface region due to localized stresses induced by abrasive particles and leads to the initiation of and propagation of cracks. Over time, these cracks grow and merge, eventually causing the material to fracture. This type of wear is commonly observed in in components subjected to repetitive loading such as springs or gears.

- **Fatigue wear:** Fatigue wear describes the accumulation of superficial microcracks and their propagation leading to spalling and pitting. It results from repeated cyclic loading, causing progressive surface damage and eventual material failure. Fatigue often occurs in rolling or sliding contacts, such as gears and bearings. Key factors influencing fatigue wear include stress amplitude, frequency, and the presence of surface defects. In contrast to fracture, fatigue specifically refers to localized surface damage.
- **Tribology-related oxidation:** This type of wear results from the synergistic action of chemical oxidation and mechanical wear. Sliding or rolling contacts induce material deformation, exposing fresh surfaces susceptible to oxidation which leads to surface degradation and wear. In this context, the term *corrosion* is frequently used in the literature. To specify the terminology, corrosion is a broad term encompassing any wear mechanism influenced by chemical or corrosive processes, while oxidative wear specifically refers to wear induced by atmospheric oxygen [28]. It is characteristic for both wear types to feature high wear rates which are often accompanied by a reduced friction coefficient [28].

There are additional, more specific types of wear in the literature, which often represent variants of the main mechanisms, i.e., erosive wear, which is associated with abrasion, or fretting, which is based on adhesion, however, these will not be discussed in further detail [28]. In summary, wear is a complex process during which multiple wear mechanisms are active simultaneously with one typically being dominant.

2.1.4. Friction curves and running-in

A friction curve is obtained through tribological experiments and crucial for the understanding of the frictional behavior of materials, lubricants and tribosystems in general. It provides valuable information about the COF development and thus surface interactions, lubrication effectiveness and enables the prediction of wear damage. As shown in **Fig. 7**, a friction curve can be divided into different regimes [44]:

- **Run-in:** Refers to the initial period of contact between two surfaces in relative motion. During this regime, the topographies, surface structures and material properties of the surfaces change and adjust. The running-in is a highly complex process due to contributions of various mechanisms that eventually find a balance, resulting in a stabilization of the friction behavior.
- **Steady-state:** The condition of a given tribological system in which the average friction coefficient, wear rate, and other specified parameters have reached and maintained a relatively constant level [44]. Steady-state behavior occurs both in lubricated and unlubricated conditions. In dry sliding, localized contact pressures decrease over time due to a reduction in roughness. This is often due to the formation of a more stable and wear-resistant surface layer.
- **Transition:** A transition from one lubrication regime to another represents a significant change in the frictional behavior between two sliding surfaces. It occurs when the tribological conditions change (i.e., from lubricated to dry and vice versa), leading to different mechanisms governing the interaction between the surfaces. Transitions are essential to understand in tribology as they substantially impact the performance and wear characteristics of mechanical systems.

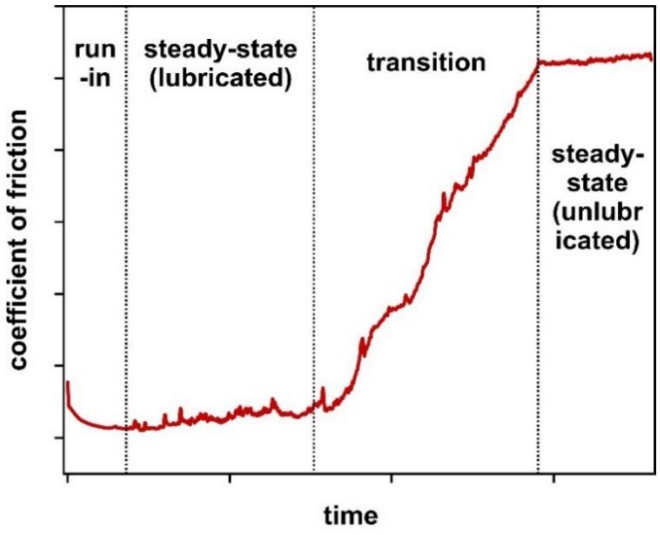

Figure 7. Exemplary friction curve displaying the different lubrication regimes: running-in, transition and steady-state (lubricated and unlubricated).

Running-in is an especially critical stage in the life cycle of any mechanical system as it can affect the reliability, performance, and durability of the involved components considerably. After discussing the general wear mechanisms in chapter 2.1.4., the more specific mechanisms associated with running-in are presented below:

- **Asperity truncation:** During running-in, highly concentrated contact stresses at the tips of the highest interacting surface asperities (microscopic roughness) lead to their rapid truncation where protruding asperities are more likely to wear off first. In the process, surface roughness is gradually reduced, and a state of surface conformity between the sliding surfaces is established. This results in improved load distribution and reduced friction and wear in the long run.
- **Wear debris formation:** Surfaces sliding against each other during running-in generate wear particles which often act abrasively and thus contribute to further wear. However, as running-in progresses, the quantity of wear particles typically diminishes.
- **Microstructural changes:** Specifically in metals, friction-related stresses cause a multitude of microstructural alterations during running-in, a prominent example would be stress-induced phase transformations [45,46]. The creation and rearrangement of dislocations and other defects due to plastic deformation often leads to a strengthening of the material properties (work hardening). A surface that yields plastically at the beginning eventually reaches an *elastic shakedown* limit. This means that the near-surface layers no longer deform plastically due to reaching a work-hardening condition

which is sufficient to support the contact pressure in an elastic manner [44]. This typically occurs during an advanced stage of running-in and the wear rate of the contacting materials typically decreases and stabilizes. Grain size is also influenced. It was shown that coarse near surface microstructures of Ni undergo grain refinement during tribological load whereas finer microstructures are coarsened [47]. This results in comparable grain sizes over time, irrespective of the original microstructure.

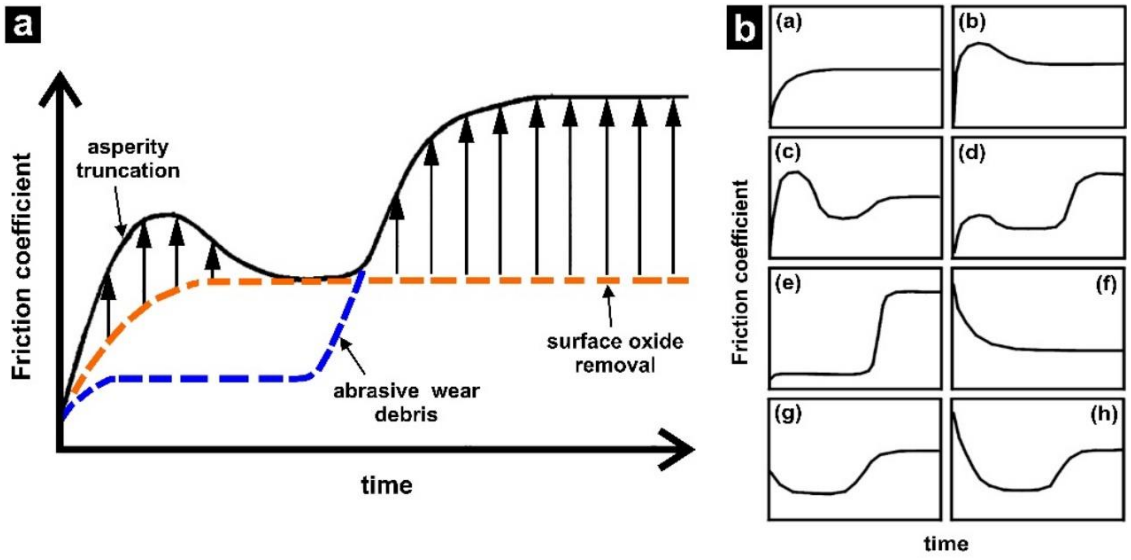

Figure 8. (a) Possible contributions of different mechanisms for a type (d) run-in. A combination of asperity truncation and surface oxide removal causes the first peak whereas the second peak is primarily due to the contribution of abrasive wear debris along with continued surface oxide removal (adapted from [48]). (b) Overview of the various curve shapes observable during running-in according to Blau [49].

- **Material transfer:** In a sliding contact, adhesion can lead to the transfer of a thin material film from one surface onto the other. This film may act as a protective layer, reducing subsequent wear and improving the tribological performance of the system.
- **Thermal effects:** Friction between sliding surfaces causes localized heating of the asperities which can induce a multitude of other processes. As the thermal expansion coefficients of different materials may vary, they expand at different rates, causing plastic deformation and surface irregularities to be smoothened. In certain materials, localized heating can induce phase transformations in the near-surface layers of the material [46]. These transformations alter the microstructure, lead to changes in surface topography, and even surface hardening [50]. The generated heat can further lead to

localized softening of the material surfaces. Softened material deforms more easily which contributes to the reduction of asperities and thus surface smoothing.

It is important to emphasize the complexity of running-in due to the overlapping contributions of most of the above-mentioned mechanisms. This is illustrated in **Fig. 8a** using the example of a type (d) run-in.

To improve our understanding of this phenomenon, Peter Blau conducted a survey on the available tribology literature in the early 1980s and identified eight different shapes of run-in curves, which are presented in **Fig. 8b** [48]. The displayed shapes cannot be uniquely related to a singular process or unique combination of processes. In fact, analogous curve shapes may emerge from dissimilar interfacial processes and must therefore be analyzed in the context of the given tribosystem [49]. The most common and significant run-in curve types and their possible causes are discussed in greater detail below. Types (b)-(d) are related and thus grouped into a curve family. All variants in that family share a similar initial peak that is associated with the wear of the asperities of the original surface due to high local contact pressures. In the case of type (b), the COF remains constant after surface conformity is achieved. This variant is common in either dry or boundary lubricated metallic contacts [44,48]. Compared to type (b), a type (c) run-in features a slight friction increase after the initial peak which Blau attributes to subsequent debris formation or material transfer [44]. This behavior is frequently encountered in the case of dry oxidized metallic surfaces and in combinations involving ferrous or ferrous-nonferrous materials [44]. The final variant of the curve family, type (d), exhibits an even greater friction increase compared to type (c) that is linked to a more tenacious and protective initial oxide layer [44]. Type (f) is characteristic for clean, pure metals and associated with crystallographic reorientation occurring within the near-surface layers, leading to a reduction in their shear strength and a decrease in friction. A type (g) curve shape can be observed in graphite-graphite contacts or metal sliding on graphite [44]. The running-in process involves the creation of a thin, lubricating film, explaining the initial COF decrease [44]. The following rise in friction could be caused by the generation of debris or material transfer.

In summary, running-in curves provide valuable data for researchers working on novel or improved lubrication systems. Understanding the running-in behavior helps to design improved surface interactions which leads to reduced wear and friction-related energy losses and enhances the reliability of mechanical systems.

2.1.5. Hertzian contact model

The Hertzian contact theory is a mathematical model used to describe the deformation and stress distribution in elastic bodies during contact and was developed by Heinrich Hertz in the 19th century. The Hertzian model postulates the interaction between two elastic bodies, typically represented as perfectly smooth and homogeneous spheres, which are in contact with each other. The model is based on the theory of elasticity, which describes the behavior of solid materials under the action of external forces. According to this theory, when a force is applied to an elastic body, it deforms elastically, meaning it undergoes temporary deformation and returns to its original shape once the force is removed. Deformation of the bodies is described by the equations of elasticity, specifically the equations for the deformation of spheres under the action of a concentrated force. These equations consider the elastic properties of the materials, such as their Youngs' modulus and Poisson ratio (measure of lateral contraction). As shown in **Fig. 9**, the contact area is also circular hence the mathematical description for sphere-sphere contact is also valid for sphere-plane contact.

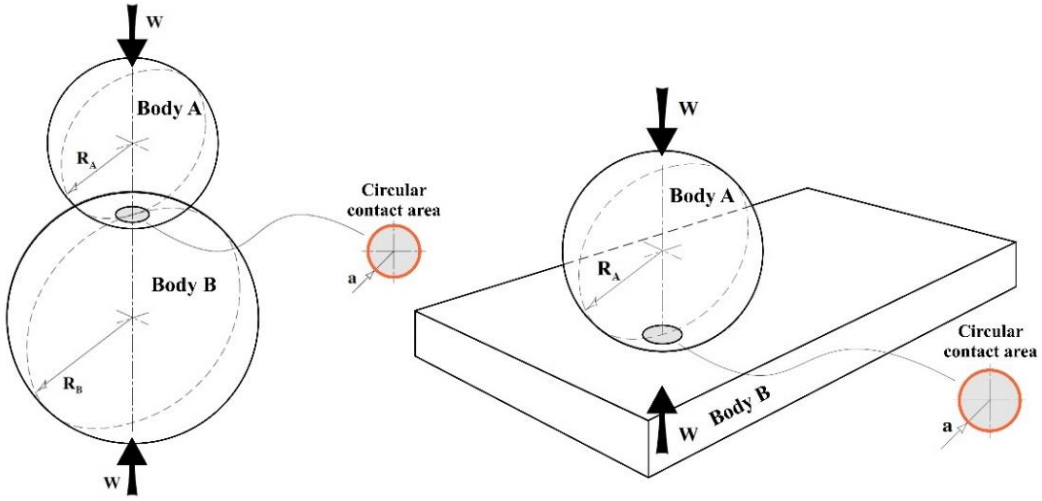

Figure 9. Contact between two spheres and a sphere and plane both with identical contact areas (marked in orange) (adapted from [51]).

The model calculates the contact area between the bodies, known as the Hertzian contact area, and determines the distribution of stresses within this area. Understanding how stresses are distributed helps in predicting failure modes, material behavior under different loads, and designing structures able to withstand the applied forces without experiencing excessive deformation or failure. In terms of stress, non-conformal contacts such as sphere-sphere and

sphere-plane represent the most extreme form of contact as the pressure is concentrated on the smallest area. To determine the maximum Hertzian contact pressure (in the literature often referred to as Hertzian pressure) between two bodies A and B, the reduced Youngs' modulus E' and the reduced contact radius R' must be calculated first [52]:

$$\frac{1}{E\prime} = \left[\frac{1-v_A^2}{E_A} + \frac{1-v_B^2}{E_B}\right] \tag{4}$$

where v_A and v_B are the Poisson ratios and E_A and E_B the Young's moduli of the contacting bodies. The reduced contact radius between two spheres A and B is defined as follows:

$$\frac{1}{R\prime} = \frac{1}{R_A} + \frac{1}{R_B} \tag{5}$$

once E' and R' are known, the radius of the contact area a can be determined:

$$a = \left(\frac{3F_N R\prime}{4E\prime}\right)^{1/3} \tag{6}$$

where F_N represents the normal load. The maximum contact pressure is defined as:

$$p_{max} = \frac{3F_N}{2\pi a^2} = \frac{1}{\pi}\left[6F_N\left(\frac{E\prime}{R\prime}\right)^2\right]^{1/3} \tag{7}$$

The stresses are highest at the center of the contact area and decrease as the distance from the center increases. These parameters are crucial for designing and evaluating the performance of various mechanical systems, such as bearings and other structural elements. In summary, the Hertzian contact model is based on the following assumptions:

- The contacting materials are homogeneous, and the strains are small hence the contact is fully elastic without plastic deformation.
- The area of contact is substantially smaller compared to the dimensions of the contacting solids.
- The contacting bodies are not in motion. This means the contact stress is caused exclusively by the normal load, thus no tangential forces act between the solids (no friction).
- Surface roughness is negligible.

As evidenced by the listed assumptions, the Hertzian contact model is a highly simplified representation of the complex behavior of real surfaces. However, it is often utilized to define (elastic) limits and provides a useful approximation for many engineering applications involving elastic bodies in machinery and biomedicine.

Since its inception, the Hertzian model has served as a foundation for more advanced contact mechanics theories and models. More sophisticated models such as the one by Greenwood and Williamson incorporate additional factors, such as roughness and elasto-plastic behavior. This

makes it more suitable for real-world applications where surface roughness and plasticity are significant factors influencing contact mechanics. However, much like the Hertzian model, the Greenwood-Williamson model is also based on oversimplified assumptions. In addition to that, the Hertzian contact model is prevalent in the literature, thus, for comparison purpose and its simplicity, it remains the most widely used contact model.

2.2. Surface patterning

The patterning of surfaces can mitigate friction and wear in dry and lubricated contacts [53–55]. In dry conditions, the improvement is based on two factors:

(1) Introducing surface patterns leads to a reduction of the real contact area. This effect, however, tends to be temporary as the patterns gradually wear off and the contact area increases again along with the COF [13,25].

(2) If the topographical are sufficiently large, they as reservoirs that capture and entrap wear debris that would otherwise enhance ploughing in the contact and, thus, further accelerate friction and wear [56].

In lubricated contacts, the reservoirs additionally store lubricants which are gradually released into the contact area, thereby considerably extending the lubrication [57–59]. Patterns can be introduced to a surface by various techniques, e.g. laser-based processes (direct laser writing; short: DLW, direct laser interference patterning; short: DLIP), mechanical techniques (coining, stamping) and chemical processes (etching, nanolithography).

2.2.1. Principles of laser processing

Laser-based techniques offer several advantages as they are highly precise, flexible, extremely fast, versatile, and compared to the other techniques do not require harmful chemicals or vacuum. Laser-based techniques are also non-contact, thus eliminating the need for expensive coining moulds that wear out over time and have to be replaced. Although highly precise, DLW is a relatively slow technique limited to creating small patterns at a time. In contrast, DLIP is capable of processing large areas within short periods and the dimensions of the structures can be in the sub-micron range which is not achievable with DLW [60,61].

During DLIP, a short-pulsed laser beam is split into 2 or more partial beams which are then parallelized with a prism and brought to interference directly on the surface of the processed material as shown in **Fig. 10a**. Constructive and destructive interference results in the formation of an intensity pattern (**Fig. 10b**) which can be controlled by adjusting angle, polarization, and intensity of the laser beams. Using different beam configurations, a variety of interference patterns can be created. These intensity distributions are then transferred to the material surface to produce respective surface patterns.

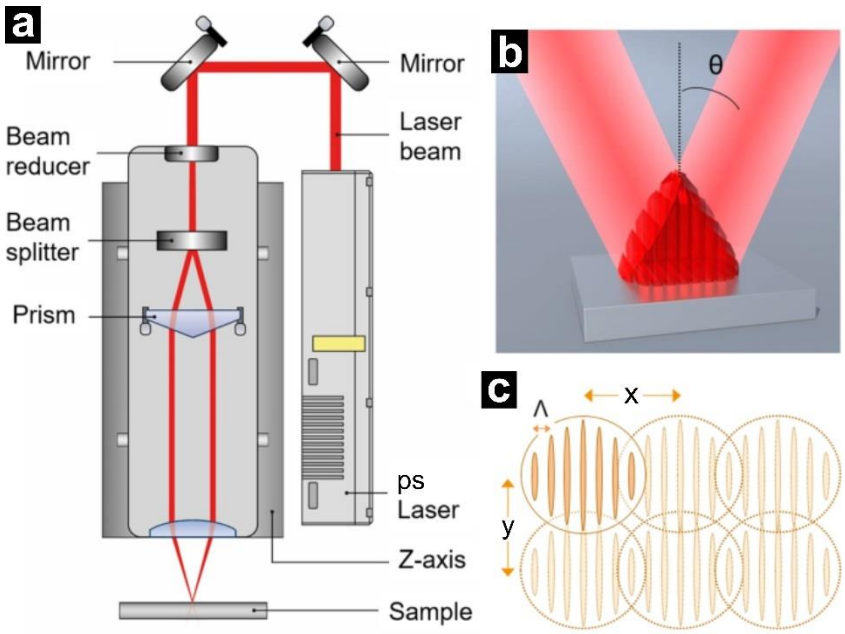

Figure 10. Schematic illustration of (a) laser set up with beam guidance, (b) a resulting intensity pattern between two interfering (continuous) laser beams and (c) overlapping laser spots for scanning large areas [62].

Interference patterns can be used to create a variety of periodical surface patterns. While 2-beam interference creates line and cross patterns (by rotating the sample by 90°), 3- or 4-beam interference leads to dimple patterns. To pattern large areas, the laser spot is scanned over the surface with an adjustable degree of overlap in x and y direction (**Fig. 10c**). The distance between individual features is referred to as periodicity Λ.

DLIP is applicable to a wide range of materials including polymers [63,64], semiconductors [65,66] and ceramics [67]. However, its feasibility and effectiveness on a specific material depends on various factors which is why DLIP is predominantly used on metals due to their high absorption and thermal conductivity.

2.2.2. Laser pulse-metal interaction

During the physical interaction between laser pulse and metal surface, the electromagnetic field of the photon interacts with a superficial electron. The electron absorbs the photon's energy causing the electron to elevate to a higher energy state or even to be ejected from the surface (photoelectric effect). The amount of energy absorbed by the material is related to the laser intensity and pulse duration, as well as material properties such as thermal conductivity, reflectivity, and absorption. Laser pulses used for DLIP are distinguished between short and ultrashort pulses (USP), with the transition threshold being 10 ps (10^{-12} s) [68,69].

Short laser pulses are typically in the micro- and nanosecond regime where the interaction between light and matter is dominated by thermal effects, more specifically, localized temperature increases at the intensity maxima lead to superficial melting of the substrate. The presence of a temperature gradient in the molten material induces a variation in surface tension, resulting in Marangoni convection causing a material flow from regions of higher temperature to regions of lower temperature where the intensity is at its minimum [70]. After that, the material re-solidifies and the resulting topographies are shaped by material throw-ups [16,71].

In the USP regime where pulse durations are in the pico- and femtosecond range, the ablated surface material is not just melted and re-solidified but removed [72]. In principle, two main ablation types are distinguished: spallation and phase explosion. To understand the circumstances under which they occur, sequence and duration of each of the consecutive physical excitation mechanisms during and after the light-metal interaction need to be considered. When metal surfaces are exposed to USP, the energy is absorbed and deposited in the electron system which is characterized by the pulse duration τ_P and the optical penetration depth δ_{opt} [73]. The energy absorption profoundly disrupts the electron-lattice equilibrium and electron-electron relaxation causes the absorbed energy to be converted into thermal energy. Subsequently, the thermal energy is transferred within the electron system and to the lattice by electron-phonon coupling which takes 1-10 ps, depending on the material [73,74]. The electron-phonon interaction time $\tau_{ep} = C_e/G$, where C_e stands for the electronic heat capacity and G is the electron-phonon coupling constant, describes the time required to transfer the energy from the thermalized electrons to the lattice [73]. The subsequent transfer of thermal energy within the lattice from the heated zone to the surrounding area is characterized by the mechanical expansion time τ_{mech} (minimal time needed to initiate expansion of the heated lattice) [75,76]. Another significant factor is the lattice heating time τ_{heat} which equals either τ_{ep} or τ_P, whichever

is longer [73]. When τ_{heat} of the irradiated zone is shorter than τ_{mech}, lattice heating can be regarded as isochoric (volume of the irradiated zone remains constant) as a result of which enormous thermoelastic pressures are generated [73]. This condition is referred to as "stress confinement" in the literature and is expressed by the notation max $\{\tau_P, \tau_{ep}\} \approx \tau_{heat} \leq \tau_{mech}$ [73,75,76]. This means that for pulses longer than τ_{ep}, the heating time τ_{heat} of the material is given by the pulse duration τ_P. If simultaneously τ_P is below the characteristic time of heat dissipation via heat conduction $t_{th} = \delta_{eff}^2/D_{EQ}$ (with δ_{eff} denoting the effective penetration depth and D_{EQ} the thermal diffusion coefficient during electron-lattice equilibrium), the thermoelastic stress remains confined in the irradiated volume, consequently, the surface temperature peaks [73,76]. This is followed by the aforementioned pressure build-up causing thermal expansion of the surface, thus, stress-confinement near the surface is no longer fully but partially fulfilled and this results in a mechanically driven separation (spallation) of molten material in concert with a thermally dominated phase explosion [72,73,77]. The current research suggests that spallation remains absent when the stress confinement condition is not fulfilled [72,77]. The higher the degree of stress confinement, the more the ablation character is dominated by photomechanical spallation whereas no confinement favors photothermal phase explosion. In the case of partial stress confinement, the ablation character is represented by a mixture of both [77]. It should be emphasized that during every ablation process, the two regimes occur simultaneously with one being more dominant than the other.

The second requirement for spallation to occur besides stress confinement, is a well-defined minimum fluence (energy delivered per area), referred to as ablation threshold in the literature [78,79]. During spallation, the rapid expansion of the overheated material generates a high-power shock wave that propagates into the bulk of the metal and is reflected from its rear side as a backward rarefaction wave. If the resulting tensile stress exceeds the tensile strength of the liquid metal, it fractures, and cavities are formed beneath the surface resulting in a foam-like material. Expanding subsurface vapor cavities lead to spallation which is followed by the expulsion of a liquid layer. When the fluence surpasses the spallation threshold, photomechanical disruption of the melt zone can lead to the expulsion of entire layers along with sizeable droplets [72]. As the fluence increases further, the photothermal phase explosion character of the ablation process becomes gradually more dominant over spallation [75,80]. During phase explosion, the magnitude of the accumulated energy causes the lattice bonds to break and the material to evaporate [81].

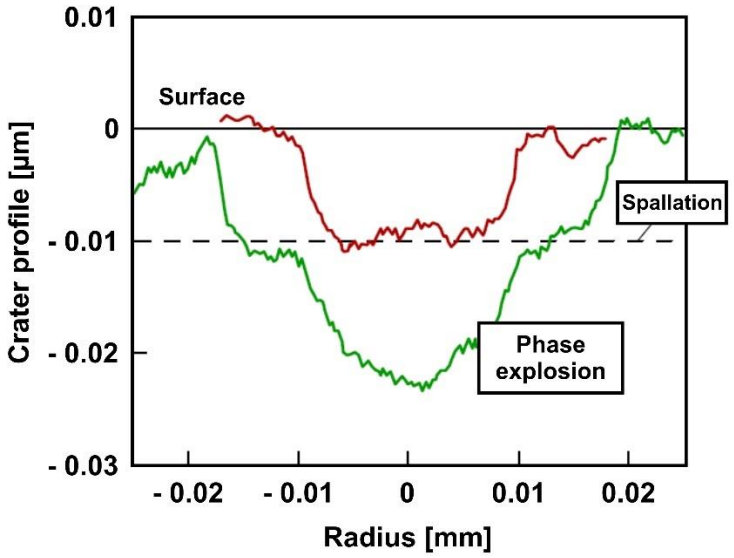

Figure 11. 2D crater profiles on an iron surface after single-pulse femtosecond ablation with the peak fluence above the spallation (brown profile) and the phase explosion threshold (green profile) (adapted by Ionin et al.[82] from [83]).

However, the interaction between laser pulse and matter is so short that only a fraction of the material can undergo a sustained evaporation whereas the remaining material transitions to a state of overheated liquid instead [71]. This transition involves extreme temperatures and results in the formation of a high-pressure amalgamation of liquid droplets and vapor which is then forcibly ejected from the processing area. The transition from the spallation to the phase explosion regime is characterized by a significantly increased concentration of vaporized atoms. This shift reflects the contrasting physical mechanisms governing material ejection in these two regimes. During phase explosion, the expulsion of an overheated melt layer is predominantly driven by explosive vapor expansion, rather than the relaxation of the confined elastothermic stresses [72]. This distinction is also expressed by the resulting craters on stainless steel as shown in **Fig. 11**, where phase explosion ablation after femtosecond single pulses causes deeper craters with a differently structured cross-section [82]. In addition to a relatively plane outer crater created by spallation, the phase explosion crater exhibits a second inner crater. This also demonstrates that the melt ejection during phase explosion removes significantly more material than spallative ablation [84].

2.2.3. Surface topographies

Due to the multiplex interaction mechanisms of short and ultrashort pulses with metallic surfaces including surface melting & re-solidification, spallation and phase explosion, the material response varies considerably and as a result, differing topographies are formed (**Fig. 12**).

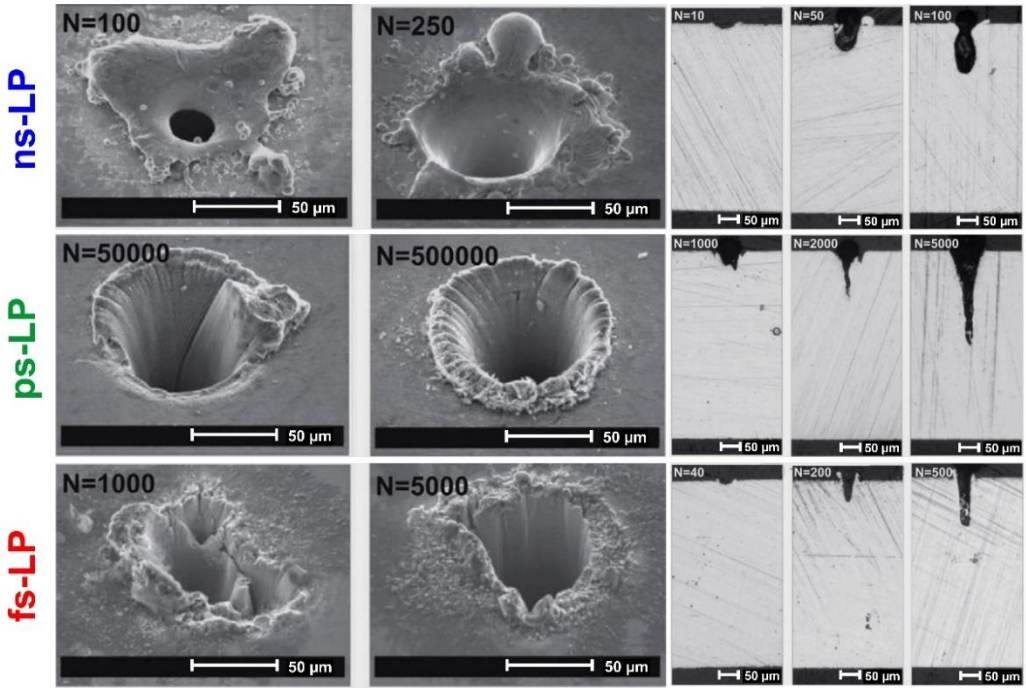

Figure 12. Scanning electron micrographs of resulting craters on stainless steel surfaces after irradiation with different numbers (N) of nano- (ns-LP), pico- (ps-LP) and femtosecond (fs-LP) laser pulses with the according cross sections (adapted from [71]).

Ultrashort pulses tend to create more defined topographies exhibiting sharper edges with minor or no throw-ups and achieve higher aspect ratios (ratio between depth and width of a surface structure) compared to their short-pulse equivalent [71,85,86]. However, USP processing can lead to protruding deposits at the edges due to material re-deposition after vaporization and is enhanced with increasing shot numbers, as shown by the femtosecond cross-sections in **Fig. 12**. Schäfer et al. demonstrated that such deposits should be avoided when the laser patterns are intended as lubricant reservoirs since they block lubricant supply to the contact [59]. In addition, heat conduction is negligible with ultrashort laser pulses so the energy transfer to the adjacent lattice is minimal and the thermal impact on the surrounding areas greatly reduced [69,86]. The

ability to create periodic patterns with different topographical nuances enables DLIP to optimize patterns to a specific application.

2.3. Solid lubrication

2.3.1. Conventional solid lubricants

Liquid or oil-based lubricants continue to dominate in mechanical applications due to their excellent lubricity, versatility (i.e., viscosity adjustment to specific conditions), efficient heat dissipation, and ease of application. However, liquid lubricants suffer from viscosity changes at high temperatures and tend to leak or evaporate, limiting their utility in high-temperature or vacuum environments. In addition, high loads can cause oil films to thin out or rupture entirely, consequently, surface separation can no longer be maintained, resulting in increased friction and wear. Moreover, the ecological consequences are catastrophic if oil-based products leak into the environment.

Solid lubricants have garnered increasing attention in recent years due to their ability to overcome the limitations of conventional liquid lubricants in extreme operating environments. For those reasons, solid lubricant particles are often used as additives to enhance the properties of commercial oil-based lubricants [87]. Prominent representatives of this materials class include transition-metal dichalcogenides (TMDs) such as molybdenum disulfide (MoS_2) and tungsten disulfide (WS_2), carbon-based materials like graphite and diamond-like carbon (DLC), polytetrafluorethylene (PTFE), hexagonal boron nitride (h-BN), and soft metals (i.e., gold, tin, and silver). Conventional solid lubricants are generally used in environments, where oil is completely ineffective, however, their lubricity is restricted to specific operating conditions. For example, graphite requires humid, oxygen-rich atmospheres to lubricate effectively [88–90] . TMDs lubricate exclusively in dry inert gas or ultrahigh vacuum below 300 °C (MoS_2), respectively, 400 °C (WS_2) [91,92]. Soft metals are primarily applied in rolling rather than sliding contacts and lubricate most effectively in vacuum or high temperatures [93]. PTFE represents a special case as its low friction behavior is linked to unacceptably high wear rates and limited to moderate temperatures (< 300 °C) [93–95].

2.3.2. Carbon nanoparticles as solid lubricants

In sp^2 hybridized carbon nanoparticles, each carbon atom forms three equivalent σ bonds with its neighboring atoms, resulting in in honeycomb-like arrangement of hexagons for the carbon atoms. The remaining, non-hybridized p_z orbital is perpendicular to the graphene plane and forms a delocalized π bond system. This material class includes particles with promising lubrication properties, in particular multiwalled CNT [57,59,96] but also CO and CNH as demonstrated by Hirata et al. [97] and MacLucas et al. [98], respectively. **Tab. 1** provides an overview of the morphology and the dimensions of the different carbon nanoparticle types.

Table 1. Overview of the structure, morphology, and TEM images of CNT, CO and CNH particles including their diameter range. The various colorings signify different layers. The white bars in the TEM images represent 200 nm.

CNT (multiwall)	**CO**	**CNH**
cylindrical structure	spherical structure	

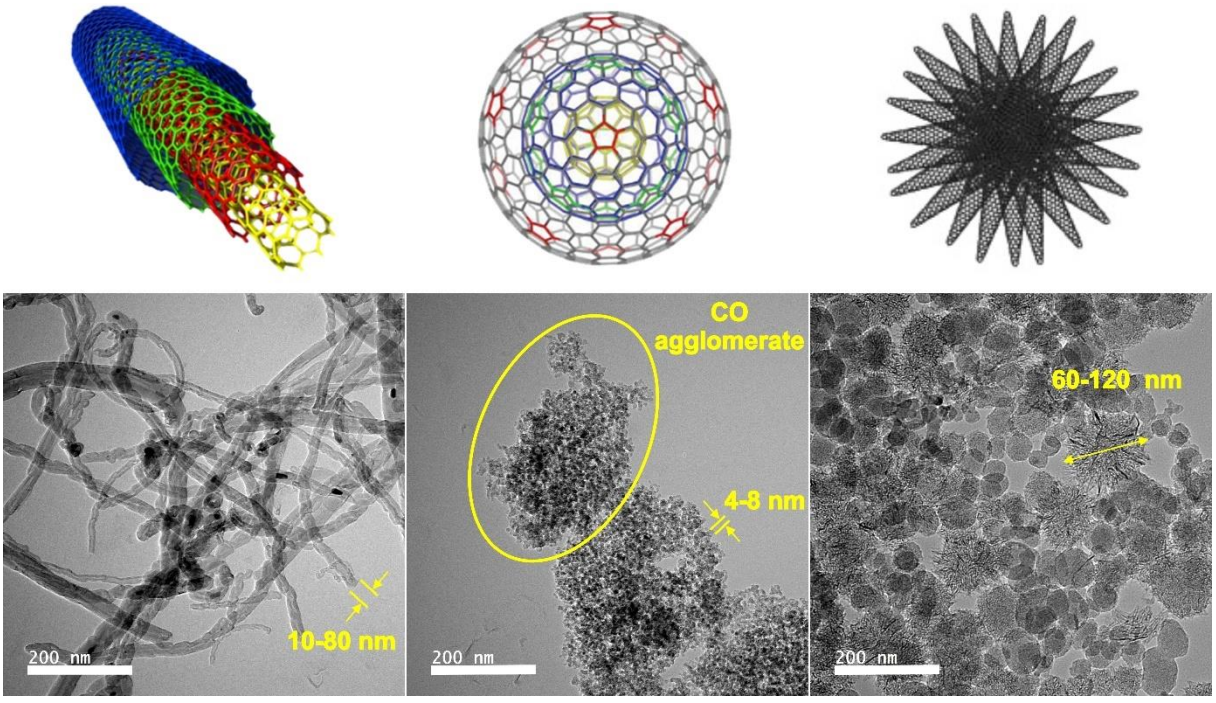

Due to their spherical or cylindrical morphology, which are either largely or completely closed, carbon nanoparticles have significantly less edge area and, thus, fewer (highly reactive) dangling bonds compared to conventional solid lubricants like graphite and TMDs which typically exhibit a layered sheet structure (**Fig. 13**). This means closed structures are less

reactive and, more specifically, less susceptible to oxidation. Therefore, CNT, CO, and CNH should have an advantage concerning lubrication at higher temperatures over their layered counterparts.

Owing to the sigma bond, carbon nanoparticles exhibit high tensile strength and Young's moduli [99,100]. At the same time, CNTs in particular are also flexible due to their cylindrical structure combined with a high aspect ratio, which results in their agglomerates being compressible [57]. In addition to that, the delocalized π-electrons ensure high thermal conductivity hence, compared to conventional solid lubricants, generated heat is likely to dissipate more effectively thus delaying tribo-oxidation [101]. Both are interesting properties for solid lubricants that are expected to perform at high loads.

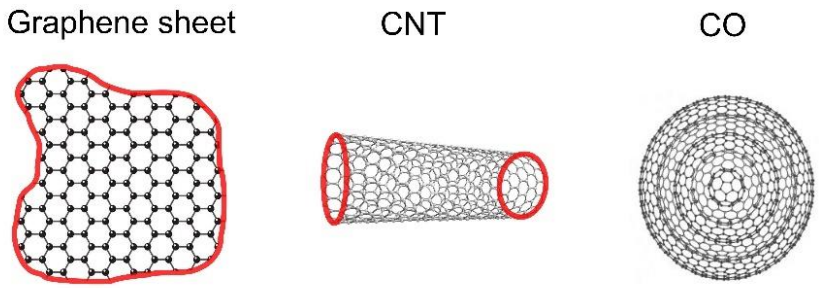

Figure 13. Illustration of the edge area of a graphene sheet (single layer of graphite), a singlewall CNT and a CO (no edge area for CNH either).

The lubrication mechanism of carbon nanoparticles like CNT, CO and CNH remains unknown, however, considering their closed cylindrical or spherical morphology in combination with high mechanical stability, the question arises whether their lubricity is based on a rolling or gliding mechanism or a combination thereof. Hirata et al. conducted ball-on-disc testing of COs (synthesized from diamond clusters) on a silicon wafer at room temperature and measured extremely low friction coefficients both in air at 55 % relative humidity and in vacuum. During further experiments conducted by Hirata and coworkers in a similar setup as described previously, carbon onions were subjected to friction testing at elevated temperatures of up to 300 °C either in ambient conditions or vacuum against an AISI 440C stainless steel ball [102]. The COs maintained lubricity in both environments with a COF around 0.20 in air and roughly 0.03 in vacuum. The extremely low COF measured at room temperature combined with the fact that most conventional solid lubricants perform effectively either in humidity or vacuum, not in both, is indicative of a mechanism based on rolling.

Based on their structure, the lubricity of carbon nanoparticles has the potential to be considerably less dependent on their operating environment than that of conventional solid lubricants. In the case of COs, this is supported by tribological testing results at elevated temperature tests. However, to determine, whether carbon nanoparticle coatings perform superior to conventional solid lubricants, they must be compared directly in further tribological tests under identical conditions.

2.4. Carbon nanoparticle coatings on patterned metallic surfaces

Generally, the lubricity of conventional solid lubricants is restricted to specific operating conditions (**Tab. 2**). For instance, graphite lubrication is humidity-dependent [90], TMDs require dry inert environments or ultrahigh vacuum to achieve effective lubricity, whereas PTFE cannot provide low friction and low wear concurrently due to irregular and patchy transfer films. Because of poor conductivity and heat dissipation, PTFE is further limited to low-speed sliding applications and moderate temperatures (melting point: 327 °C) [93].

Table 2. Overview of the macroscale tribological properties of widely used solid lubricants. The lubricity of various solid lubricant materials in either dry or humid operating environments is framed in green [103].

Solid lubricant coating	Deposition methods	Coating thickness (μm)	Typical friction coefficient
Graphite	Evaporation, pyrolysis	0.2–5	Dry: 0.5–0.6; Humid: 0.1–0.2
Diamond like carbon (near frictionless carbon)	Sputtering (rf and dc), ion-beam, PECVD	1–3	Dry: 0.001–0.05; Humid: 0.2–0.3
Tetrahedral amorphous carbon	Ion beam, cathodic arc, pulsed laser	0.01–1	Dry: 0.7; Humid: 0.1
Ultrananocrystalline diamond	MPCVD, HFCVD	0.5–1.5	Dry: 0.05–0.13; Humid: 0.007–0.1
MoS_2 and WS_2	Sputtering (rf and dc), thermal evaporation CVD, ALD	0.2–2	Dry: 0.02–0.06; Humid: 0.15–0.25 initial and increasing
Graphene/graphene oxide	CVD, chemical and mechanical exfoliation	0.001–0.002	Dry: 0.15–0.2; Humid: 0.15–0.2

Although DLC (doped) also lubricates in humid air, its lubricity is substantially enhanced in dry and inert air or nitrogen atmospheres and/or high vacuum. However, DLC coatings are deposited using elaborate processes like physical vapor deposition (PVD), sputtering and/or chemical vapor deposition (CVD) that require reactors with high or partial vacuums. As described in the previous chapter, CNPs represent interesting solid lubricants, however, since they do not form covalent bonds with the substrate, adhesion to the underlying substrate is weak. Consequently, lubricating carbon nanoparticle coatings are rapidly removed from plain metal surfaces due to a lack of covalent surface bonding, resulting in the removal of the CNPs from the wear track when subjected to sliding [57,104]. Introducing a texture to tribologically stressed surfaces decreases friction only temporarily as it gradually wears off. However, when CNP coatings are combined with textured metal surfaces, the disadvantages of these two individual approaches can be compensated and their strengths retained [57]. This was shown by Reinert et al. who evaluated the influence of the roughness of a stainless-steel substrate on the lubricity of CNT and CO coatings [105]. While CNT coatings were able to maintain lubricity over 500 cycles regardless of the surface roughness, the lubricity of the COs was strongly dependent on the surface roughness and improved with decreasing roughness. In a different study conducted by Reinert and co-workers, well-defined, and line-patterned steel surfaces (DLIP-processed) were coated with CNTs and formed a solid lubrication system that enables effective and reproducible solid lubrication over extensive periods of time [57].

Once the surface structures' topographical minima are filled with particles and experience frictional load, they serve as reservoirs that impede lubricant removal and from where the particles are continuously supplied directly to the contact. Reinert et al. formulated a detailed mechanism consisting of multiple steps which is listed below (**Fig. 14a**) [57]:

(1) Upon contact with the coating, CNTs experience partial adhesion to the alumina ball. This induces a displacement of the CNTs towards the grooves.
(2) Concurrently, pressure is exerted on the peaks of the laser texture across the coating, resulting in plastic deformation and detachment of metallic material.
(3) Owing to adhesion, superficial CNTs are drawn towards the contact region, preventing direct contact between the alumina ball and the steel substrate and provide lubrication. The laser structure inhibits complete CNT transfer by retaining the majority of the particles within the reservoir.
(4) Alongside the CNT storage capacity of the reservoirs, metallic or oxidic wear particles may also be retained, consequently mitigating abrasive wear.

(5) As depicted in the FIB cross-section in **Fig. 14b** (the last stroke proceeded from left to right), the compressed CNT bodies in the grooves tilt during their contact with the passing counter body, resulting in a subtle elevation on one side. This suggests, that the protruding CNTs will be retracted into the direct contact zone once the sliding direction is reversed. This phenomenon arises from the aforementioned adhesion between the alumina ball and the CNT body during sliding.

(6) Another factor contributing to the elevation is the elastic rebound of the compressed CNT volume following the stroke.

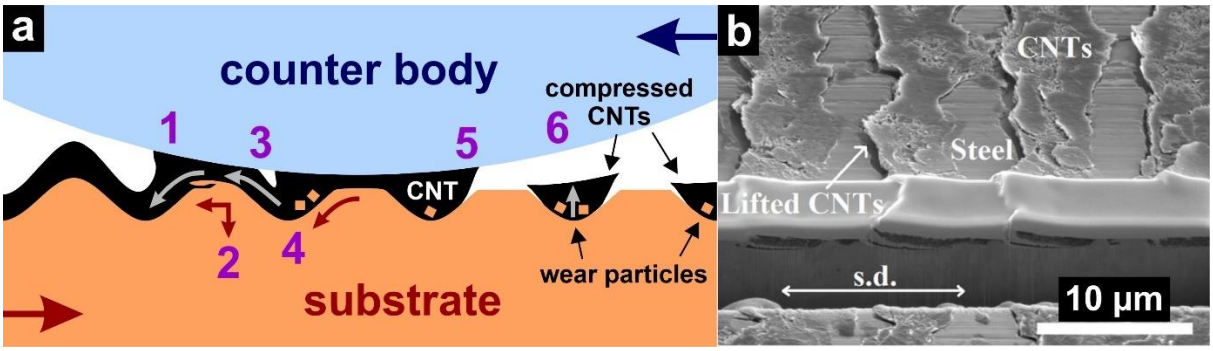

Figure 14. (a) Schematically illustrated cross-section of a solid lubrication system combining a line patterned surface with a CNT coating. Reinert et al. described the phenomena occurring in this system as follows: (1): CNT adhere to the counter body; (2): Deformation and detachment of substrate peaks; (3): CNTs get into the contact where they provide lubrication; (4): Wear particles are absorbed and stored in the CNT reservoirs; (5): Compressed CNT bodies tilt and stand up on one side due to the stroke; (6): Elastic rebound of the CNT body after the stroke. (b) FIB cross-section of CNT-coated wear track after sliding showing the lifted CNT bodies [57].

This reservoir mechanism represents the basis for a solid lubrication system capable of lubricating effectively over significant periods of time. Moreover, the reservoirs capture and store generated wear particles, thereby preventing them from entering the contact. Due to compression upon contact with the counter body and a subsequent shift, the upper part of the compressed CNT body protrudes the surface and, thus, re-establishes contact with the counter body.

As elucidated in chapter 2.3, based on structure and properties, it is conceivable, that the lubricity of carbon nanoparticles like CNT, CO and CNH is less dependent on its operating environment than conventional solid lubricant coatings and could therefore be used for a wider range of applications. From the state of the art, the following scientific questions arise:

I. Since the applicability of a carbon nanoparticle-based lubrication system is particularly reliant on the coating technique, how can the deposition rates be optimized without compromising the homogeneity of the coating? In addition, can the coating thickness development be investigated and simulated using existing models (e.g., Hamaker) to save characterization time in the future?
II. Is it possible to further optimize the effectiveness of such a solid lubrication system?
III. Do carbon nanoparticles degrade during sliding and if yes, what are the degradation mechanisms? Do the particles degrade differently?
IV. Which mechanisms underlie the lubricity of carbon nanoparticles? Do they roll and, thus, function as nano-scale bearings?
V. How is the long-term lubricity of different carbon nanoparticle coatings and do they differ from each other? Does the differing particle morphology influence the tribological performance?
VI. Compared to coatings made from conventional carbon nanoparticles, how do carbon nanoparticle coatings lubricate in extreme operating environments and is their lubricity less dependent on their operating environment?

3. Objectives

The scientific questions arising from the state of the art, particularly from chapter 2.4 translate into the following, specific objectives:

- **Objective 1** (derived from I): To research the thickness development of CNT coatings on austenitic stainless-steel substrates during EPD using different parameters. Depositions shall be conducted with pristine and oxidized CNTs, using two different additives over a range of voltages to investigate their respective impact. It is further to be determined whether the coating thickness development is linear and can, thus, be accurately approximated by the relatively simple Hamaker equation. This represents an important aspect regarding applicability and upscaling of the EPD process.

- **Objective 2** (derived from II): To optimize the design of the line pattern for minimal friction and wear on austenitic stainless-steel surfaces, the influence of the patterns' structural depth on the CNT- and CO-coated surface during sliding is investigated. To achieve that, steel surface patterns with three different structural depths are produced, subsequently coated with either CNT or CO and subjected to tribological testing.

- **Objective 3** (derived from III): The degree of degradation of CNT and COs after friction testing is to be investigated to gain novel insights regarding the lubrication and degradation mechanisms at play. Comparative friction testing shall be used to determine whether these particles degrade at a different speed or magnitude. A further objective is to examine whether there exists a correlation between lubricity and particle degradation.

- **Objective 4** (derived from IV): To understand the underlying lubrication mechanisms of CNT coatings between sliding surfaces, a combined approach of tribological experiments with subsequent wear track characterization and molecular dynamics simulation shall be adopted. If experiment and simulation can be correlated, the simulation can provide valuable insights into the atomistic mechanisms that occur.

- **Objective 5** (derived from IV and V): To examine the long-term lubricity of CNT-, CO- and CNH coatings on line-patterned steel surfaces against two of the most technically relevant counter body materials (bearing steel and alumina). During according friction tests, the influence of the counter body material as well as the particle morphology on the lubricity of the respective particle type shall be investigated.

- **Objective 6** (derived from VI): To research whether the lubricity of carbon nanoparticle coatings is less dependent on their operating environment compared to conventional solid lubricants. For that purpose, a set of benchmark tests on line-patterned stainless-steel substrates shall be conducted under extreme operating conditions including elevated temperatures, vacuum, and high loads. During those benchmark tests, the lubrication performance of carbon nanoparticle coatings is directly compared to that of conventional solid lubricant coatings.

4. Methodology

4.1. Tribometry

Tribometry is a specific branch of tribology that describes the measurement and quantification of friction and wear between two sliding surfaces and relies heavily on the use of tribometers which are the primary instruments utilized for measuring parameters related to friction and wear, most importantly the COF. This is achieved by subjecting both surfaces to controlled relative motion while applying a constant load and measuring the occurring tangential forces.

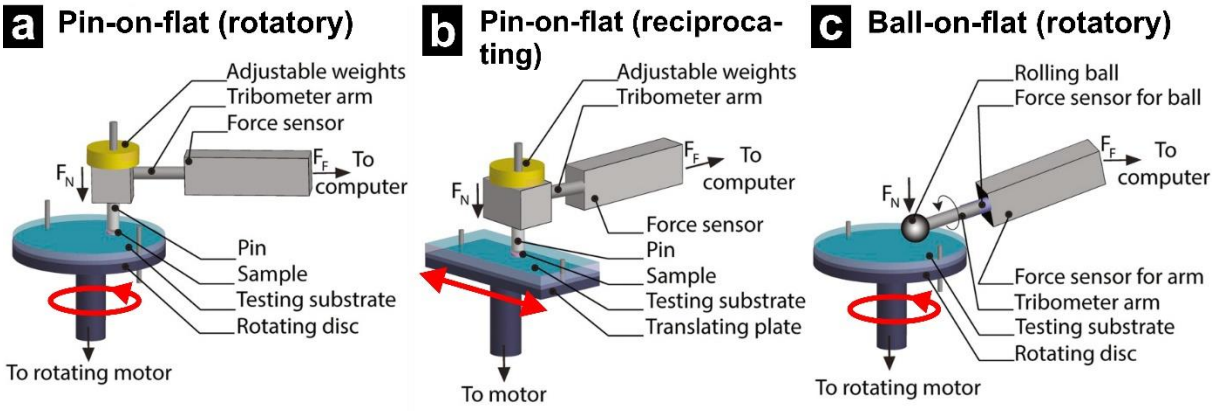

Figure 15. Schematic depiction of various tribometer configurations. (a) Rotatory pin-on-flat configuration, (b) linear reciprocating pin-on-flat configuration and (c) rotatory ball-on-flat configuration. In each configuration, the COF is computed by dividing the tangential friction force, ascertained from the force sensor, by the known load created by the adjustable weights or the motion of the tribometer arm [106].

As illustrated in **Fig. 15**, tribometers come in various designs and can operate in different configurations such as pin-on-flat or ball-on-flat. Pin-on-flat is conformal contact whereas ball-on-flat is non-conformal contact, which represents the configuration with the most extreme contact pressures. In addition, different sliding motions such as linear-reciprocating and rotatory are conducted during tribometry, linear-reciprocating and rotatory. Linear-

reciprocating substrates slide back-and-forth along a straight trajectory. In a tribometer, this is typically used to simulate real-world scenarios where surfaces experience oscillating motions in different types of machinery. Rotatory sliding, on the other hand, simulates scenarios where surfaces undergo rotational motions as in numerous mechanical systems. Due to the diverse range of inquiries in tribology, various tribometers have been engineered for specific application scenarios and measurement tasks. Custom built tribometers are equipped to measure under harsh conditions such as vacuum, extreme temperatures and humidities as well as elevated loads, and monitor the relevant parameters during friction testing. However, the interpretation and transferability of obtained tribometry data is scientifically demanding. Given that tribological parameters always reflect system characteristics, providing isolated values like friction coefficients without detailing the setup and the testing conditions does not hold any scientific value. Additionally, many tests are not standardized and do not undergo independent validation.

Tribometers provide essential perspectives on the behavior of materials under different friction and wear conditions hence they are used for research and development, for example, to design efficient braking systems, develop high-performance engine components, and study the wear of artificial joints. The contribution of tribometry to the advancement of the durability, reliability, and efficiency of mechanical systems is irreplaceable.

4.2. Electrophoretic deposition

4.2.1. Fundamentals

A reliable and well-established method to apply nanoparticles as a homogeneous coating is electrophoretic deposition (EPD). EPD was discovered in 1808 by Russian scientist Ruess, who observed the movement of clay particles in water induced by an electric field [107]. Its practical application was first patented in the USA in 1933 when the use of thoria particles for the deposition on a platinum plate cathode as an electron tube emitter was demonstrated [108].

EPD is a solution-based coating technique that consists of two steps: electrophoresis and deposition. Prior to deposition, the particles are dispersed in a suitable solvent and move towards an immersed electrode of opposite charge under the influence of an electric field (electrophoresis). Although the principle of electrophoresis is straightforward, the finer nuances

of the process are complex and influenced by a wide range of factors such as the applied voltage, solid content and solution viscosity, dielectric constant of the solvent, zeta potential and size of the coating particles as well as dispersion stability. Deposition represents the second step of EPD during which the particles accumulate and coagulate on the deposition electrode. The exact deposition mechanism remains unclear although several hypotheses have been proposed and described in the literature [109–112].

Assuming linear growth, Hamaker introduced an equation to model the deposition yield during EPD which was published in 1940 [113]:

$$w(t) = \int_0^t f \cdot \mu \cdot E \cdot A \cdot C_s \cdot dt \tag{8}$$

where w is the deposition yield, A the coated area, E the electric field strength, C_s the particle concentration, f an efficiency factor (also referred to as ”sticking parameter”, considers what fraction of particles reaching the deposition electrode actually contributes to the layer) and the electrophoretic mobility μ:

$$\mu = \frac{\varepsilon \cdot \varepsilon_0 \cdot \xi}{\eta} \tag{9}$$

with ε as the dielectric constant of the solvent, ε_0 as the dielectric constant of the vacuum, ξ as the zeta potential of the dispersed particles and η as the dynamic viscosity.

EPD requires both a conductive substrate with an appropriate counter electrode, and the particles to have a surface charge to interact with the electric field. The surface charge further stabilizes the dispersed particles in the solution by preventing immediate sedimentation and agglomeration. As a rough guideline, a solution can be considered stable with a zeta potential of ± 30 mV and beyond, whereas the sign of the potential determines the deposition direction (cathodic or anodic) [114]. Due to its versatility and modest requirements, EPD is applicable to a wide range of materials including $LiFePO_4$ (for Li-ion batteries) [115], biomaterials [116], graphene oxide [117], MoS_2 [118] and particularly carbon nanoparticles such as CNT [57,59,104,119–121], CO [120,121], CNH [98,120], and graphene [122,123].

4.2.2. Electrophoretic deposition of carbon nanoparticles

In the past, a multitude of different techniques have been utilized to produce carbon nanoparticle coatings. This includes spray coating [124], dip coating [125,126], drop casting [127,128], and spin coating [129,130]. However, EPD has emerged as the technique with superior coating homogeneity and reproducibility.

Due to the incorporation of oxygen-containing functional groups such as hydroxy or carboxy groups [131], carbon nanoparticles generally have a negative surface charge and as shown in **Fig. 16a**, deposit in random orientation on the positive electrode (anodic deposition).

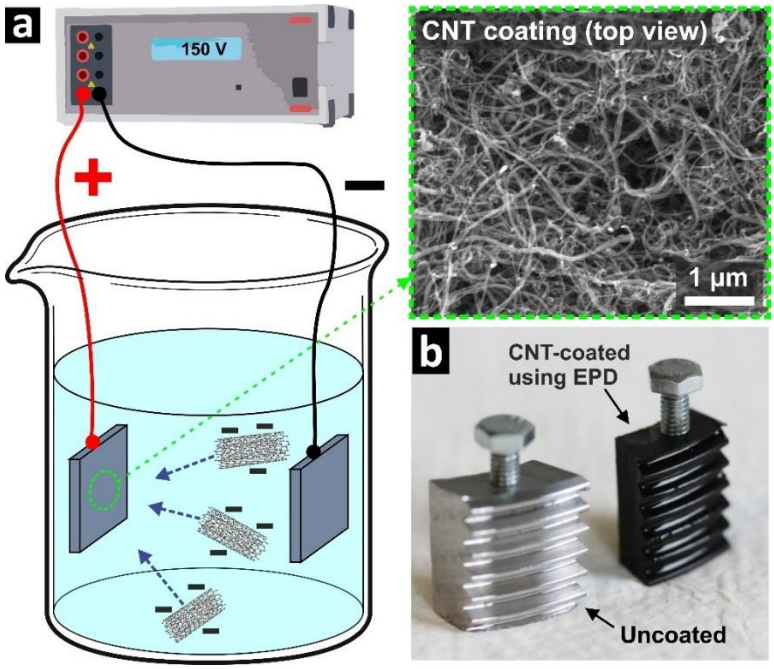

Figure 16. (a) Schematic illustration of an anodic CNT deposition at with a top view scanning electron micrograph of a CNT coating. (b) Uncoated and CNT-coated steel threads demonstrating the ability of EPD to homogeneously copy complex geometries.

A considerable range of solvents have been used for dispersing and depositing carbon nanoparticles. Among the most commonly used are isopropanol (IPA) and ethanol as nanocarbons have good electrophoretic mobility in them and the solution is sufficiently stable [104,120,132–134]. Additionally, both solvents are widely available and relatively safe from a health perspective. Besides organic solvents, aqueous solutions have also been used as solvents for depositing carbon nanoparticles [119,135,136]. Water is low cost and poses minimal environmental risks, however, hydrogen formation due to electrolysis represents a major safety

hazard. Further, bubble development particularly at higher deposition voltages prevents the formation of dense and uniform coatings [137].

The process of depositing carbon nanoparticles can be supported by using additives that act in different ways to improve dispersion and accelerate the deposition process. Triethylamine (TEA) is believed to enhance the negative surface charge by increasing the dissociation rate of the hydroxy- and carboxy groups and potentially adding the element of steric repulsion thus improving particle dispersion. Metal salts like $Mg(NO_3)_2$ represent another class of additives which have been effective at increasing CNT yield [104] and alter the wetting behavior of the resulting coatings [104,138]. In solution, $Mg(NO_3)_2$ dissolves into NO_3^- and bivalent Mg^{2+} ions. The latter is suspected to form non-covalent complexes with the monovalent negative surface groups hence the effective surface charge is overcompensated and thus reversed. As a result, deposition occurs on the cathode [104].

EPD allows the production of homogeneous carbon nanoparticle coatings even on complex substrate geometries (**Fig. 16b**). At the same time, it is simple and cost-effective. Furthermore, it is scalable and thus suitable for industrial use as it and enables precise process control through several parameters.

4.3. Confocal laser scanning microscopy

Confocal laser scanning microscopy (CLSM) is an advanced optical imaging technique utilized in materials and life sciences, as well as the semiconductor industry. It enables 3-dimensional, high-resolution visualization of samples by selectively focusing a laser beam onto a specific focal plane while excluding out-of-focus light through spatial filtering. The fundamental principle of CLSM revolves around the generation of a focused laser beam, typically in the visible or near-infrared spectrum, which is directed onto the specimen. This laser light interacts with the sample, causing fluorescence emission or reflection. A pinhole aperture, situated in front of the detector, is utilized to selectively capture emitted or reflected light originating exclusively from the focal plane of interest. By sequentially scanning the laser across the specimen and detecting the emitted or reflected light through the pinhole, a series of two-dimensional optical sections (or slices) are acquired. The resultant optical sections are computationally reconstructed to generate a three-dimensional representation of the specimen.

Compared to conventional light microscopy, CLSM utilizes a spatial pinhole which blocks out-of-focus light. As a consequence, CLSM provides superior optical sectioning which facilitates the reconstruction of complex three-dimensional structures. Furthermore, higher resolution images are achieved and the reduction of out-of-focus blur increases contrasts. Finally, CLSM generates digital images that can be easily processed, analyzed, and quantified using specialized software. This enables advanced post-processing techniques, such as deconvolution, stitching, and 3D rendering.

Within this work, CLSM was used to determine surface roughness parameters R_a and R_q as well as the structural depth of the DLIP-induced line-patterns (mean height R_c).

4.4. Raman spectroscopy

4.4.1. Fundamentals

Raman spectroscopy is an analytical technique used to investigate the vibrational modes of molecules and provides information about the molecular structure and chemical composition of a material. The underlying principle of Raman spectroscopy is based on the inelastic scattering of light. When a sample is radiated with monochromatic light, most of the incident photons undergo elastic scattering (Rayleigh scattering). However, a small fraction of the photons is scattered inelastically, resulting in an energy shift, known as the Raman effect. The Raman effect occurs when the incident photons interact with the vibrational modes of the molecules in the sample. These vibrational modes are specific to the molecular structure and can be thought of as the “fingerprints” of the molecules. When the incident photons interact with the molecules, they can transfer energy to or gain energy from the vibrational modes, resulting in a shift in their energy levels. The energy shift of the scattered photons can be measured using a spectrometer, which separates the scattered light into its different wavelengths. However, for a molecule to be Raman active, the vibrational mode must cause a change in the polarizability of the molecule. This means that the molecule must have some asymmetric characteristics, for example, stretching and bonding motions often result in changes in polarizability.

The Raman spectrum is obtained by plotting the intensity of the scattered light as a function of its energy shift. The spectrum typically consists of a series of peaks corresponding to the different vibrational modes of the molecules in the sample.

4.4.2. Carbon characterization

In the case of carbon, Raman spectroscopy is particularly useful for characterizing the different carbon materials. Carbon it its different forms and allotropes (diamond, graphite, CNT, etc.) exhibit distinct Raman spectra due to their unique structural arrangements. Diamond for example, has a highly ordered crystal structure, and its Raman spectrum exhibits a sharp peak known as the diamond band. Graphite on the other hand, has a layered structure, and its Raman spectrum shows two prominent peaks known as the G and the D band. CNTs, which are cylindrical, also display characteristic bands in their Raman spectra. The position, intensity, and shape of the Raman bands provide valuable information about the carbon material being analyzed. The position of the bands corresponds to the vibrational frequencies of the molecular bonds, which can be used to identify specific functional groups of structural features. The intensity of the bands is related to the abundance of the different carbon species present in the sample. The shape of the bands can also reveal details about the degree of disorder or crystallinity of the carbon material. Furthermore, Raman spectroscopy can be used to study other properties of carbon, such as strain, doping, and defects. Changes in these properties can be detected through shifts or modifications in the Raman spectra. This makes Raman spectroscopy a versatile tool for investigating the structural and chemical properties of carbon-based materials.

In summary, Raman spectroscopy is a powerful technique for characterizing carbon materials and allows scientists to identify different forms of carbon and study their structural properties.

5. Results and discussion

5.1. Included Publications

5.1.1. Outline

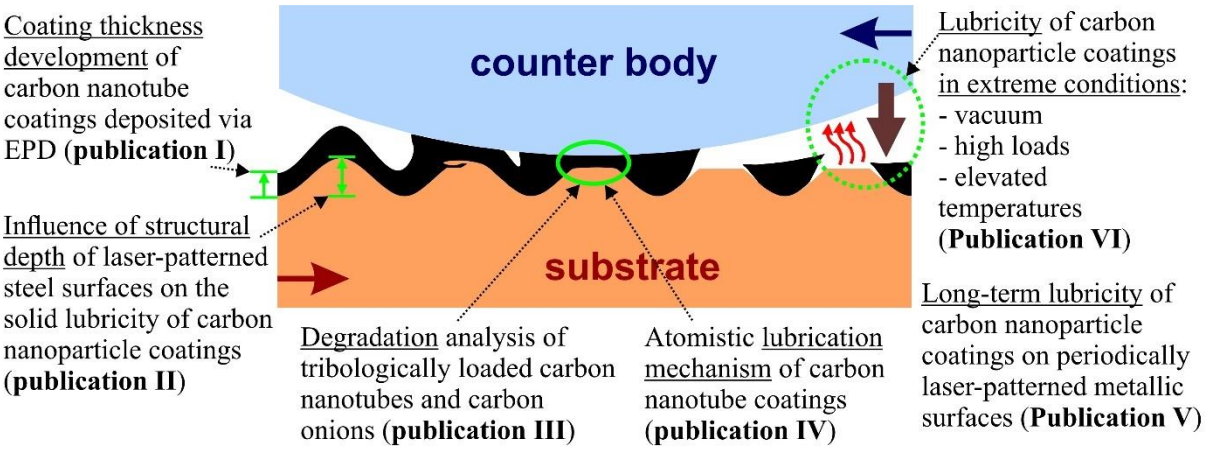

Figure 17. Graphical illustration of the outline, showing the different focus points of the publications included in this dissertation.

I

Parametric analysis of the coating thickness development of electrophoretically deposited carbon nanotube coatings

The objective of this publication was to investigate the temporal coating thickness development during the electrophoretic deposition of pristine and oxidized CNTs on stainless steel. The coating process was conducted in dependence of the deposition voltage and the additives (TEA and Mg-Nit) which are used to assist during coating. The development of the coating thickness was approximated using Hamaker's law, and its prediction accuracy was tested. The results indicate that elevated voltages lead to increased CNT deposition rates and solutions with Mg-Nit had higher deposition rates compared to TEA. Within the initial 5 min, the evolution of coating thickness could be characterized as approximately linear when using Mg-Nit and the initial 20 min when using TEA. Ultimately, Hamaker's law provided a good estimation for the coating thickness development of CNT coatings on stainless steel when TEA was utilized as an additive.

II

Influence of structural depth of laser-patterned steel surfaces on the solid lubricity of carbon nanoparticle coatings

Coatings of carbon nanoparticles on patterned surfaces create a solid lubrication system that utilizes the pattern's recessions as lubricant-retaining reservoirs. This study explored the influence of the recession's structural depth, coated with CNTs and COs, on their ability to reduce friction and wear. Employing DLIP, line patterns with varying structural depths were generated on stainless-steel platelets, followed by electrophoretic deposition to form homogeneous carbon nanoparticle coatings. Tribological experiments revealed that the shallower the structure, the lower the COF, with CNT coatings consistently achieving lower friction coefficients than the CO coatings. Furthermore, CNT-coated surfaces did not show any oxidation compared to minor oxidation on their CO-coated equivalents.

III

Degradation analysis of tribologically loaded carbon nanotubes and carbon onions

This study represents a follow-up that examined the tribological films that were formed in the wear tracks of the samples described in **publication II** with respect to structural degradation. The findings showed that CNT lubricity was linked to increased particle defectivity, more specifically, the more effective CNT lubricity, the greater the particle degradation. Although strong structural deterioration was observed for both particle types following the friction tests, the COs exhibited greater degradation compared to CNTs.

IV

Multiwall carbon nanotubes for solid lubrication of highly loaded contacts

In previous tribological experiments, CNTs showed strong degradation after friction testing at low loads despite their mechanical stability. In this work, experimental friction testing and subsequent wear track characterization was combined with Molecular Dynamics simulations to study the observed phenomenon and to gain novel insights into the friction mechanisms of carbon nanotubes on metallic surfaces. The simulations showed that the extent of particle degradation after sliding can be explained by an extreme concentration of the applied load at crossed contact points between individual CNTs. The described crossed contact was identified in the resulting tribofilm using high-resolution electron microscopy and confirmed the remarkable agreement between experiment and simulation which lead to the development of a multi-step lubrication mechanism.

V

Long-term lubricity of carbon nanoparticle coatings on periodically laser-patterned metallic surfaces

This paper examines the long-term lubricity of different carbon nanoparticle coatings such as CNH, CNT, and CO, on line-patterned stainless-steel substrates. Simultaneously, the influence of particle morphology (cylindrical vs. spherical) on the lubricity can be analyzed. Ball-on-disc tribometry is conducted with alumina and 100Cr6 as counter body materials. The friction tests reveal that CNTs maintain effective solid lubrication against both counter body materials. While COs and CNH sustain lubricity against 100Cr6, they exhibit diminished performance against alumina. In addition, the formation of CNT patches on the pattern is observed. These patches separate the sliding surfaces and represent a contributing factor to the CNTs superior lubricity compared to CO and CNH.

VI

Combining carbon nanoparticle coatings and laser surface texturing for enhanced lubricity under high loads

This article focused on the lubricity under high loads (20 N) of different solid lubricant coatings including various carbon nanoparticles such as CNT, CO, and CNH as well as conventional solid lubricants (MoS_2, WS_2, graphite). Line-patterned stainless-steel substrates were used as substrate whereby the patterning prevented lubricant depletion. Ball-on-disc friction testing was conducted against 100Cr6 and alumina counter bodies. The primary coating technique was electrophoretic deposition, air spraying was applied for WS_2). CNT exhibited superior lubricity and the longest wear life against both 100Cr6 and alumina. Material transfer was identified as a crucial aspect for effective and enduring lubrication.

I. Parametric analysis of the coating thickness development of electrophoretically deposited carbon nanotube coatings

Timothy MacLucas[a], Silas Schütz[a], Sebastian Suarez[a], Frank Müller[b] and Frank Mücklich[a]

[a] *Chair of Functional Materials, Campus D3 3, Saarland University, 66123, Saarbrücken, Germany*

[b] *Experimental Physics and Center for Biophysics, Campus E2 9, Saarland University, 66123 Saarbrücken, Germany*

Published in **"Carbon Trends"** (2023) (cite score: 2.6 [2019-2022])

Accessible online at: https://doi.org/10.1016/j.cartre.2023.100265

Own contribution: Conceptualization, data analysis, figures, tables, writing – original draft, discussion

Carbon Trends 11 (2023) 100265

Contents lists available at ScienceDirect

Carbon Trends

journal homepage: www.elsevier.com/locate/cartre

Parametric analysis of the coating thickness development of electrophoretically deposited carbon nanotube coatings

Timothy MacLucas[a,*], Silas Schütz[a], Sebastian Suarez[a], Frank Müller[b], Frank Mücklich[a]

[a] Chair of Functional Materials, Campus D3 3, Saarland University, 66123 Saarbrücken, Germany
[b] Experimental Physics and Center for Biophysics, Campus E2 9, Saarland University, 66123 Saarbrücken, Germany

ARTICLE INFO

Keywords:
Carbon nanotubes
Electrophoretic deposition
Carbon nanotube coating
Hamaker's law

ABSTRACT

In this study, the coating thickness evolution of pristine and oxidized carbon nanotubes (CNT) on stainless steel substrates is investigated. Potentiostatic electrophoretic deposition (EPD) is used as a coating technique with two different additives, triethylamine (TEA) and magnesium nitrate hexahydrate (Mg-Nit). Moreover, the depositions are conducted at different voltages (50, 100 and 150 V). Confocal laser scanning microscopy is used to determine the thickness of the CNT depositions after 1, 2, 5, 10, 20 and 30 min. Furthermore, the ability of Hamaker's law to accurately predict coating thickness development is investigated for the thickness evolution on stainless steel.

Independent of the additive, the results show that higher voltages lead to increased deposition rates. Comparing the two additives, Mg-Nit generally allows for a higher CNT deposition rate than TEA and forms thicker layers. Coating thickness development can be approximated as linear during the initial 5 min with Mg-Nit and during the initial 20 min with TEA. Finally, Hamaker's law allows for a fairly accurate approximation for the thickness development of CNT coatings with TEA on stainless steel.

1. Introduction

Electrophoretic deposition (EPD) is a technique that enables the deposition of charged particles from a colloidal suspension onto a conductive substrate to obtain homogeneous coatings. After being developed in 1808 by Reuss, EPD was applied for the first time in 1933 to coat platinum cathodes [1]. During EPD, particles dispersed in a suitable solvent move under the influence of an electric field (electrophoresis) towards an oppositely charged electrode immersed in the suspension and deposited on it over time. Primarily, EPD is known as a technique to deposit ceramic particles and has as such been successfully used for a wide range of mostly ceramic particles such as TiO_2 [2], CeO_2 [3], Al_2O_3 [4,5], yttria stabilized zirconia (YSZ) [6], hydroxyapatite [7,8] and bioglass [9] dispersed in various solvents. Considering practical aspects, EPD is a simple and cost-effective, yet efficient coating technique that requires modest equipment and has the ability to form homogeneous coatings even on geometrically complex substrates. At the same time, it is scalable and provides extensive process control by adjusting deposition time, voltage, electrode spacing and suspension composition.

Hamaker developed a linear equation in 1940 aiming to model the deposition process of EPD [10]. With different notations according to Cho et al. [11], Hamaker's equation can be written as follows:

$$w(t) = \int_0^t f \cdot \mu \cdot E \cdot A \cdot C_s \cdot dt \tag{1}$$

with w being the deposition yield in kg, $\mu = \frac{\varepsilon\varepsilon_0\xi}{\eta}$ the electrophoretic mobility in $\frac{m^2}{Vs}$ where ε is the dielectric constant of the solvent, ε_0 the dielectric constant of the vacuum in $\frac{As}{Vm}$, ξ the zeta potential in V and η the viscosity in $Pa \cdot s$, E the electric field strength in $\frac{V}{m}$, A the coated area in m^2, C_s the particle concentration in $\frac{kg}{m^3}$ and f an efficiency factor (also referred to as "sticking parameter"), depending on whether each particle reaching the anode will contribute to the layer. Assuming the simplification that all factors are time-independent, the integral transforms to a multiplication:

$$w(t) = f \cdot \mu \cdot E \cdot A \cdot C_s \cdot t \tag{2}$$

Ever since Thomas et al. deposited multiwall carbon nanotubes (CNTs) onto a metallic surface [12], EPD has started to generate wider interest for being applicable to sp^2-hybridized carbon nanoparticles, as it has proven to be an effective technique to form homogeneous carbon nanoparticle coatings. This applies particularly to CNT coatings for tribological applications [13–15], wettability tuning [14], in superca-

* Corresponding author.
E-mail address: timothy.maclucas@uni-saarland.de (T. MacLucas).

https://doi.org/10.1016/j.cartre.2023.100265
Received 31 March 2023; Received in revised form 2 May 2023; Accepted 2 May 2023
2667-0569/© 2023 The Authors. Published by Elsevier Ltd. This is an open access article under the CC BY license (http://creativecommons.org/licenses/by/4.0/)

pacitors [16] or vertically aligned CNTs on carbon fiber [17]. Moreover, EPD has proven to successfully deposit carbon onions [18,19], carbon nanohorns [20], but also graphene quantum dots [21] and other graphene-related materials [22].

In order to obtain coatings with EPD, the dispersed particles must have a surface charge in suspension. Carbon nanoparticles with sp^2 hybridization generally show a negative surface charge stemming from the deprotonation of oxygen-containing functional groups such as hydroxy or carboxy groups [23]. These groups are incorporated during synthesis, primarily at the caps but also on the side walls [24]. This is facilitated by their curved structure and the associated increased reactivity due to pyramidalization of the π-orbitals [25]. However, further oxidizing CNTs in a strongly acidic environment enhances the incorporation of functional groups and, thus, the negative surface charge which will influence the deposition kinetics. Functionalization may be advantageous as shown by Gojny and Schulte, where functionalizing CNTs lead to improved interfacial adhesion of CNTs in epoxy composites [26].

Deposition results during EPD can be improved by using additives, of which there is a wide variety, such as salts like nickel chloride [27] or quaternary ammonium salts [28] and nitrates, most prominently aluminium nitrate [29] and magnesium nitrate hexahydrate (Mg-Nit) [30,31]. The latter, along with triethylamine (TEA) [13,14], are amongst the most commonly used additives for CNT deposition. When using Mg-Nit, Mg^{2+} ions non-covalently attach to the negative surface groups causing the deposition to occur on the cathode. The use of TEA on the other hand leads to an anodic deposition [32].

In this work, the layer thickness evolution of CNT coatings on stainless steel substrates is studied during potentiostatic EPD with TEA and Mg-Nit as additives. Secondly, a linear approximation of CNT layer growth based on Hamaker's law was performed in order to precisely predict coating thickness, which can save a significant amount of characterization time and, therefore, increases applicability.

2. Materials and methods

2.1. Materials

Multiwall CNT acquired from Graphene Supermarket (Calverton, USA) were used in this study. According to the provider, the outer diameter varies between 30 and 85 nm, with a length of 10-15 µm and a carbon fraction above 94 %. Triethylamine (99.0 %, Chemsolute, Germany) and magnesium nitrate hexahydrate (Merck, Germany) were used as additives. As substrates, platelets (20×20×1 mm^3) of AISI 304 austenitic stainless steel (BRIO Kontrollspiegel GmbH, Germany) with mirror polished (S_q = 9 nm) surface were utilized.

2.2. Functionalization and dispersion preparation

Prior to the deposition, a batch of CNTs were functionalized with a HNO_3/H_2SO_4 mixture (v/v ratio 3:1). In a first step, the CNTs were dispersed in the acid mixture via ultrasonication (Bandelin, Sonorex Super RK 514 Bh, 35 kHz-860 W) for 10 min. Next, the CNTs were oxidized in the mixture for 72 h at 80°C under reflux. Subsequently, the CNTs were filtered and washed with deionized water until the pH of the permeated water reached 7. Finally, the functionalized CNTs were dried in an oven overnight at 100°C.

Each dispersion consists of 80 ml of isopropanol (IPA) and 8 mg (corresponds to a concentration of 0.1 mg/ml) of either pristine (p-CNTs) or oxidized CNTs (o-CNTs). In addition, either 10 ml of TEA or 2 mg of Mg-Nit were used as additives to support the deposition process. The four following suspensions were used:

- IPA + TEA + p-CNT
- IPA + TEA + o-CNT
- IPA + Mg-Nit + p-CNT
- IPA + Mg-Nit + o-CNT

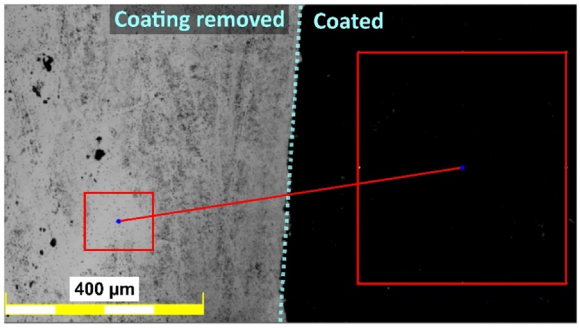

Fig. 1. Top view confocal laser scanning micrograph of a frontier between a CNT-coated part of the sample surface (right) and another part where the coating was removed (left). The coating thickness was determined by measuring the height difference between these two regions of interest using CLSM.

The CNTs were dispersed with an Ultra-Turrax (T25 digital, IKA, Germany) shear mixer for 5 min at 5000 rpm followed by 10 min of ultrasonication in the same device mentioned above.

2.3. Electrophoretic deposition

Two stainless steel platelets serving as electrodes were immersed in the dispersion and connected to a DC power supply (Consort EV3020, Carl Roth, Germany). Deposition was conducted in potentiostatic mode at three different voltages (50 V, 100 V and 150 V) for the following deposition times: 1, 2, 5, 10, 20 and 30 min. For each set of parameters one sample was coated.

2.4. Characterization

To assess the degree of functionalization, X-Ray Photoelectron Spectroscopy (XPS) was used to determine the oxygen content. XPS measurements were performed with an ESCA MkII spectrometer (Vacuum Generators) in normal emission mode using Al-Kα excitation ($\hbar\bullet\omega$ = 1486.6 eV) and a 150°-type hemispherical analyzer. Survey spectra were recorded with a pass energy of 50 eV, detail spectra (for analysis of elemental composition) were recorded with a pass energy of 20 eV. The calibration was made to the Au-4f $_{7/2}$ line at 83.80 eV.

Zeta potential measurements were performed with a Malvern Panalytical Zetasizer at a temperature of 20°C with a refractive index of 2.47 and an absorption of 0.99.

A Haake Rotational Rheometer (RheoStress 1, Thermo Fisher Scientific) was used to determine the viscosity of the EPD dispersions. Steady shear measurements were conducted at room temperature in constant-stress mode. The ratio of cup to bob radii was 1.0847 with a gap of 1.45 mm.

To determine the thickness of the CNT coatings, an Olympus LEXT OLS4100 confocal laser scanning microscope (CLSM) with a 50x objective (NA: 0.95) at a laser wavelength of 405 nm was used. As illustrated in Fig. 1, coating thickness was measured by comparing two regions of interest and forming the difference. To verify the CLSM data, coating thicknesses were also measured using scanning electron micrographs that were prepared using a Helios NanoLab 600 dual beam workstation (SEM/FIB, by Field Electron and Ion Company) at an acceleration voltage of 5 kV and a current of 1.4 nA.

3. Results and discussion

3.1. Dispersion, CNT and coating characterization

Fig. 2 shows the XPS survey spectra of p- and o-CNTs. The spectra display mainly the C1s and O1s peaks as well as the C-KVV and

Table 1
Overview of the characterization data. Carbon and oxygen content of p- and o-CNTs measured by XPS. Zeta potential of the CNTs in different dispersions with and without additives. Viscosity for the dispersions and for IPA.

	Pristine			Oxidized		
Carbon (at. %)	98.62			96.40		
Oxygen (at. %)	1.38			3.60		
Additive	-	TEA	Mg-Nit	-	TEA	Mg-Nit
Zeta potential (mV)	− 15.27 ± 1.50	− 10.99 ± 1.16	− 6.34 ± 0.98	− 29.63 ± 1.89	− 20.73 ± 1.31	+ 14.30 ± 0.86
Viscosity (mPa•s)	-	1.89 ± 0.08	2.37 ± 0.09	-	1.95 ± 0.08	2.24 ± 0.07

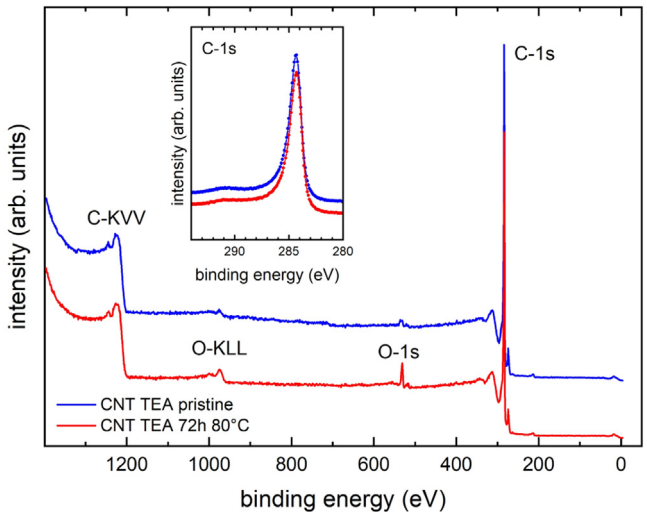

Fig. 2. XPS survey spectra of p- (blue) and o-CNTs (red). Inset: C1s detail spectra.

O-KKL Auger peaks with no traces of other elements. The C1s detail spectra (inset) of both samples display a narrow main contribution at 284.3 eV (as characteristic for sp^2 C bonds) and the small broad shake-up π satellite around 290.5 eV [33]. Between the main peak and the π satellite only small contributions from C-O, C-OH and/or C=O species contribute to a small shoulder of the main peak. The analysis of the C1s and O1s spectra (peak intensity above Shirley background [34] scaled with the photoemission cross sections by Yeh and Lindau [35]) provides atomic ratios of C:O = 98.62:1.38 and 96.40:3.60 for p- and o-CNTs, respectively (see Tab. 1) showing that the acid-functionalization leads to a considerable increase of the CNTs' oxygen content. The additional oxygen is incorporated to a large degree in the form of oxygen-containing functional surface groups such as carbonyl and hydroxy groups [23,36], but mainly carboxy groups [37].

To determine the CNTs' surface charge in solution, the zeta potential was measured while the particles are dispersed in different suspensions (results shown in Table 1). Comparing p- and o-CNTs reveals that the acid-functionalization causes the zeta potential in pure IPA to become more negative, roughly by a factor of 2.5. This outcome was to be expected due to the further incorporation of carbonyl, hydroxy or carboxy groups. Carboxy groups in particular are known to deprotonate in solution, and form carboxylate anions which dominate the interaction with the additives and provide the CNTs with negative surface charges [37].

Adding TEA to the deposition suspension seems to attenuate the CNTs negative zeta potential (regardless of oxidation state). We believe that, to a certain degree, TEA protonates to ammonium (NH_4^+) and subsequently non-covalently complexes some of the carboxylates on the surface of the CNTs, thereby mitigating the negative charge. The presence of Mg-Nit has the same yet more enhanced effect. In solution, Mg-Nit dissolves into Mg^{2+} and NO_3^-. The former also forms complexes with the surface groups. In the case of o-CNT, the zeta potential completely shifts to become positive.

The viscosities of the different dispersions were determined to model the coating thickness development according to Hamaker's equation. In general, low-viscosity suspensions are preferred as they pose less resistance to particle motion during EPD. The data presented in Table 1 indicate that CNT/Mg-Nit dispersions exhibit an increased dispersion viscosity compared to CNT/TEA dispersions. This can be explained by higher electrostatic forces from bivalent Mg^{+2} ions leading to stronger attracting forces between the CNTs which generally increases the viscosity. In addition to that, the viscosity of pure TEA is low (0.347 mPa•s [38]) resulting in an overall viscosity decrease of the CNT/TEA dispersion.

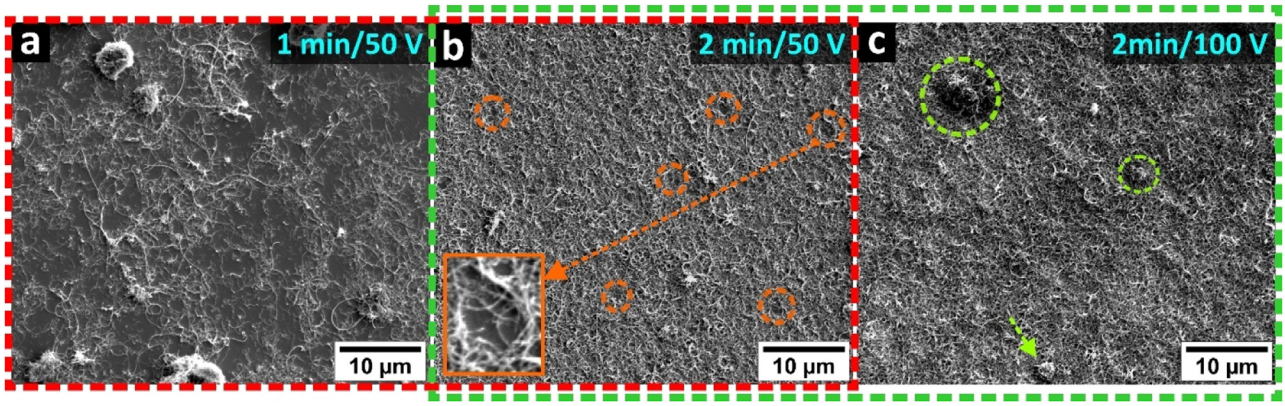

Fig. 3. Top view scanning electron micrographs showing the coating thickness development of o-CNTs deposited with TEA (a) after 1 min at 50 V, (b) 2 min at 50 V and (c) 2 min at 100 V.

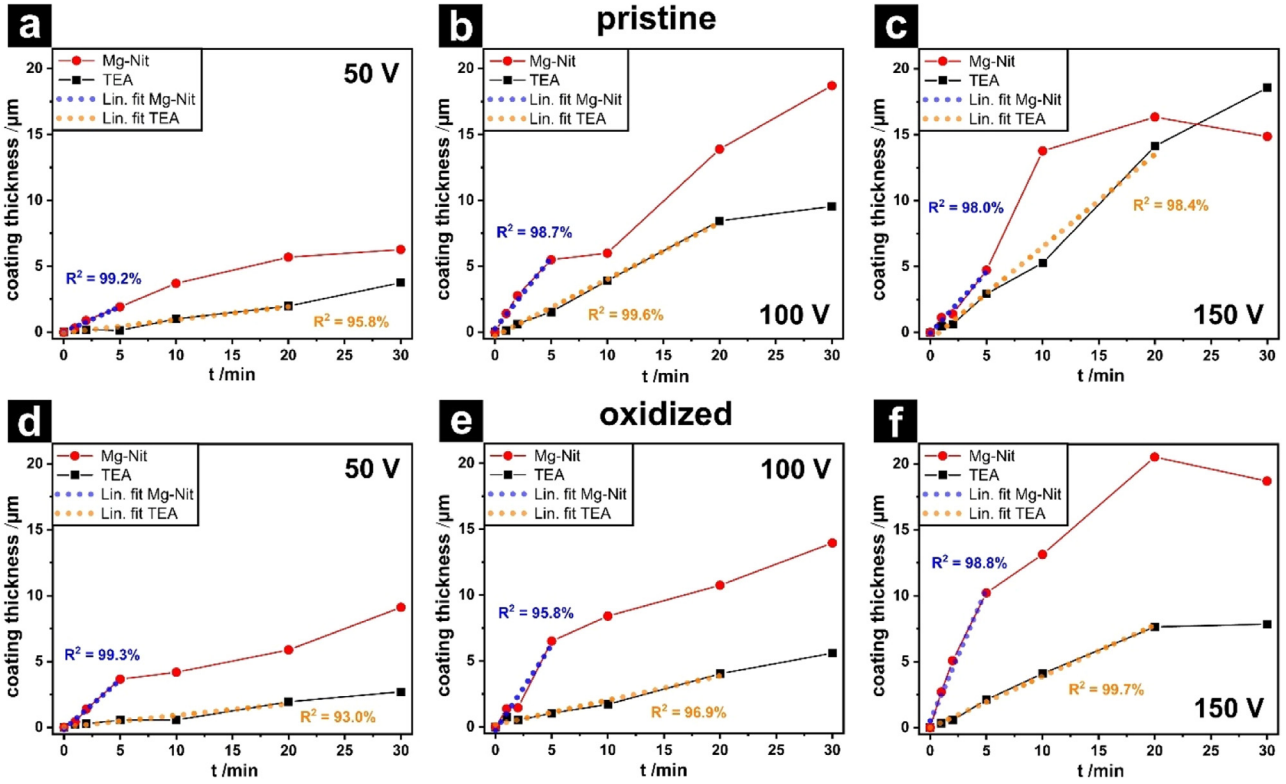

Fig. 4. Coating thickness development (measured using CLSM) in the presence of TEA and Mg-Nit for pristine (a-c) and oxidized (d-f) CNTs at 50, 100 and 150 V.

In Fig. 3, top view scanning electron micrographs at different stages of the thickness development of o-CNTs deposited with TEA are shown. The first deposition after 1 min at 50 V shows individual o-CNTs (randomly oriented) together with a few o-CNT agglomerates as well as the underlying substrate (Fig. 3a). When the deposition time is doubled (Fig. 3b), the coating covers the substrate almost completely, however, the underlying substrate is still recognizable in some locations (orange markings). Fig. 3c shows, that doubling the voltage over a deposition period of 2 min results in a coating that fully covers the surface and incorporates large agglomerates (green markings).

3.2. Development of CNT coating thickness

Fig. 4 shows the temporal coating thickness development of pristine (Fig. 4a-c) and oxidized (Fig. 4d-f) CNTs deposited with either TEA or Mg-Nit as an additive at 50 V, 100 V and 150 V measured by CLSM. The CNT coatings generally grow thicker as deposition time increases, regardless of the oxidation state or the additive. Moreover, higher voltages typically lead to higher deposition rates which is consistent with the literature [39,40]. Initially, the thickness development can be approximated as linear. In the presence of Mg-Nit, this applies during the first 5 min ($95.8\% < R^2 < 99.3\%$). Afterwards, the curve kinks downwards in most cases. This agrees well with the findings of Gardeshzadeh and Rasouli who investigated the deposition yield of multiwall CNTs dispersed in ethanol with Mg-Nit as an additive [40]. TEA exhibits similar behaviour, however, linear growth is maintained for roughly 20 min ($93.0\% < R^2 < 99.7\%$).

The difference in coating thickness between TEA and Mg-Nit tends to be more pronounced at higher voltages and longer deposition periods. However, p- and o-CNTs deposited in the presence of Mg-Nit at 150 V demonstrate that longer deposition periods and higher deposition rates do not necessarily result in thicker coatings. In those cases, the deposition rate starts to decline, and it appears as if a maximum is reached around 20 min (Fig. 4c and f). This maximum represents a saturation state where the CNT deposition shields and, thus, neutralizes the electrical field of the underlying electrode. This is in agreement with results obtained by Singh et al. for graphene oxide-polymer composite at 10 V [41].

Consequently, layer thickness decreases as both individual CNTs and CNT agglomerations detach from the deposition due to the lack of an attractive force. Decreasing CNT concentration in the suspension over the course of the deposition is another factor contributing to the slowdown of the deposition rate [40]. Saturation seems to occur in TEA also, as demonstrated by the o-CNTs' flattening deposition rate after 20 min at 150 V (Fig. 4f) or possibly exceeded it already. Achieving saturation below 150 V seems to require deposition periods beyond 30 min.

Within a study published in 2004, Wang and co-workers used EPD to coat copper substrate with ZnO nanoparticles [42]. The development of layer thickness was studied over time at deposition voltages of 20, 60 and 100 V. Initially, the ZnO layer grew almost linearly. After a certain period of time, the line starts to flatten and eventually plateau. Overall, these results correspond well with ours.

With just over 20 µm, o-CNTs with Mg-Nit at 150 V produce the thickest coatings. Several factors contribute to this. First, the highest voltage results in the strongest electrical field and hence the highest deposition rate prior to saturation. Secondly, functionalization increases the amount of superficial carboxyl groups and, thus, leads to an enhancement of the negative surface charge [23,43], as corroborated by the respective zeta potentials listed in Table 1. Moreover, Yi and Chen proved that Ca^{2+} forms bidentate rather than monodentate complexes with carboxyl groups on the surface of multiwalled CNTs [37]. Ca^{2+} binds more effectively to the carboxyl groups on highly

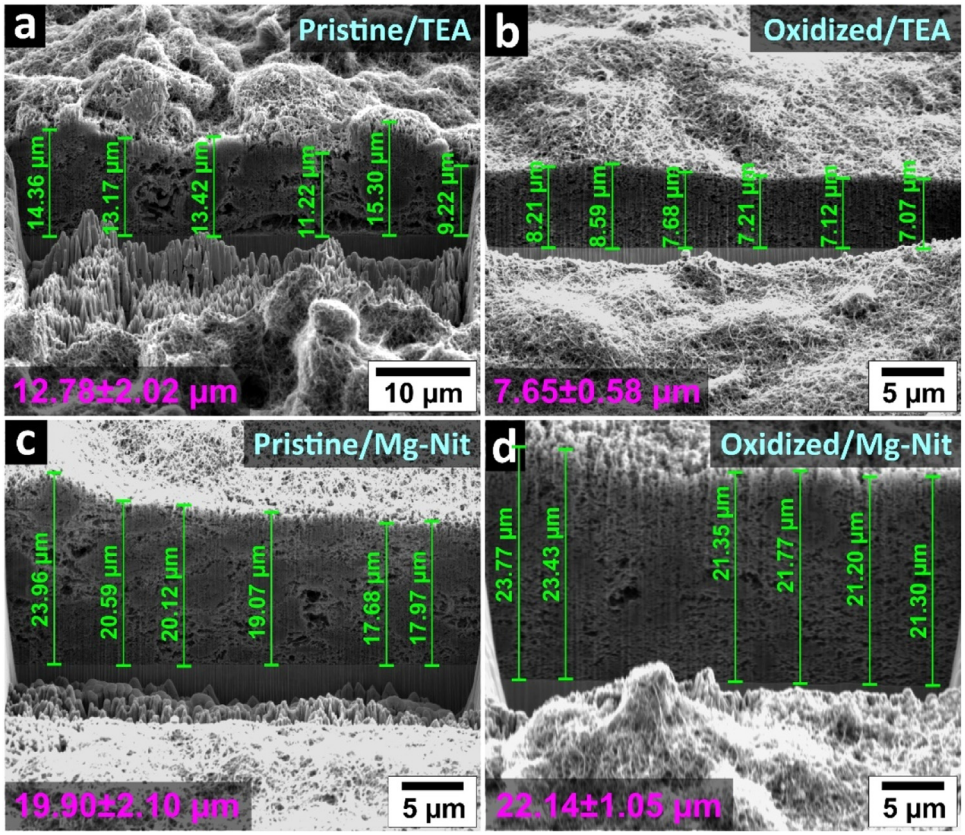

Fig. 5. FIB cross-sections of the CNT coatings (without protective coating) after a deposition time of 20 min at 150 V with (a) pristine CNTs with TEA, (b) oxidized CNTs with TEA, (c) pristine CNTs with Mg-Nit and (d) oxidized CNTs with Mg-Nit.

oxidized CNTs compared to lower oxidized CNTs because there is a greater probability that a larger proportion of carboxyl groups will be in sufficient proximity to form bidentate complexes on highly oxidized CNT surfaces. In isopropanol, Mg-Nit dissolves to nitrate and Mg^{2+}, which behaves similarly to Ca^{2+} (both bivalent). Once again, this is supported by the zeta potentials (Table 1) which shows that the addition of Mg-Nit leads to a positive charge on o-CNTs opposed to the p-CNTs.

Focused ion beam (FIB) was used to prepare cross-sections of the CNT coatings and their thickness was measured using SEM to validate the CLSM measurements. Contrary to the standard FIB procedure, protective Pt coatings were omitted due to the CNTs mechanical flexibility which otherwise resulted in the compression of the coatings. Fig. 5 shows electron micrographs with coating thicknesses of pristine and oxidized CNTs deposited with TEA and Mg-Nit after 20 min at 150 V, which are in good agreement with coating thicknesses measured by CLSM (additional FIB cross-sections after a deposition time of 10 min at 50 V are shown in S1 in the Supplementary Information). As previously mentioned, the increase in coating thickness can be approximated as linear during the initial 20 min of deposition using TEA and during the initial 5 min using Mg-Nit as an additive. Fig. 6 shows the linear regression lines fitted to the coating thicknesses deposited at 50 V, 100 V and 150 V obtained by CLSM. The corresponding Hamaker lines, which were calculated using experimentally determined parameters (Tables 1 and 2), are plotted alongside. To assess whether Hamaker is suitable for accurately predicting coating thickness evolution, we introduce a slope ratio $\beta = \frac{slope\ (linear\ fit)}{slope\ (Hamaker\ fit)}$ ($\beta = 1$ represents perfect conformity).

Independent of oxidation or deposition voltage, β_{TEA} is relatively close to 1, hence Hamaker's equation can be used for a rough approximation of the coating thickness when the CNT suspension contains TEA as an additive. This is not the case for Mg-Nit suspensions since $\beta_{Mg\text{-}Nit}$ deviates strongly from 1, meaning that the actual deposition rate is considerably higher than predicted by Hamaker's equation.

Table 2
Overview of the parameters used for Hamaker modelling.

A	$2.64 \cdot 10^{-4}$ m^2
E	3333.33 V·m^{-1} (50 V)
(assuming an electrode distance	6666.66 V·m^{-1} (100 V)
of 1.5 cm)	10000.00 V·m^{-1} (150 V)
C_S	0.10 kg·m^{-3}
ε (IPA)	20.18 [44]
ε_0	$8.85 \cdot 10^{-12}$ A·s·V^{-1}·m^{-1}

Analyzing each of the parameters considered by Hamaker, it is reasonable to state that the vast majority of them remain constant throughout the deposition. Particularly, considering that there are no significant changes in Zeta potential and viscosity, therefore, the electrophoretic mobility will remain constant. The same is true for the applied electric field (interelectrode distance is constant) and deposition area. Thus, the only two parameters in Hamaker's equation that indeed change with time are the efficiency factor f and the concentration. Considering that the concentration is expected to diminish with time, the only compensating parameter left is f. The increase in yield can thus be traced back to a high compactness of the CNTs deposited with Mg-Nit (as observable in Fig. 5c and d), likely associated to a stronger interaction of the bivalent ions with the applied electric field.

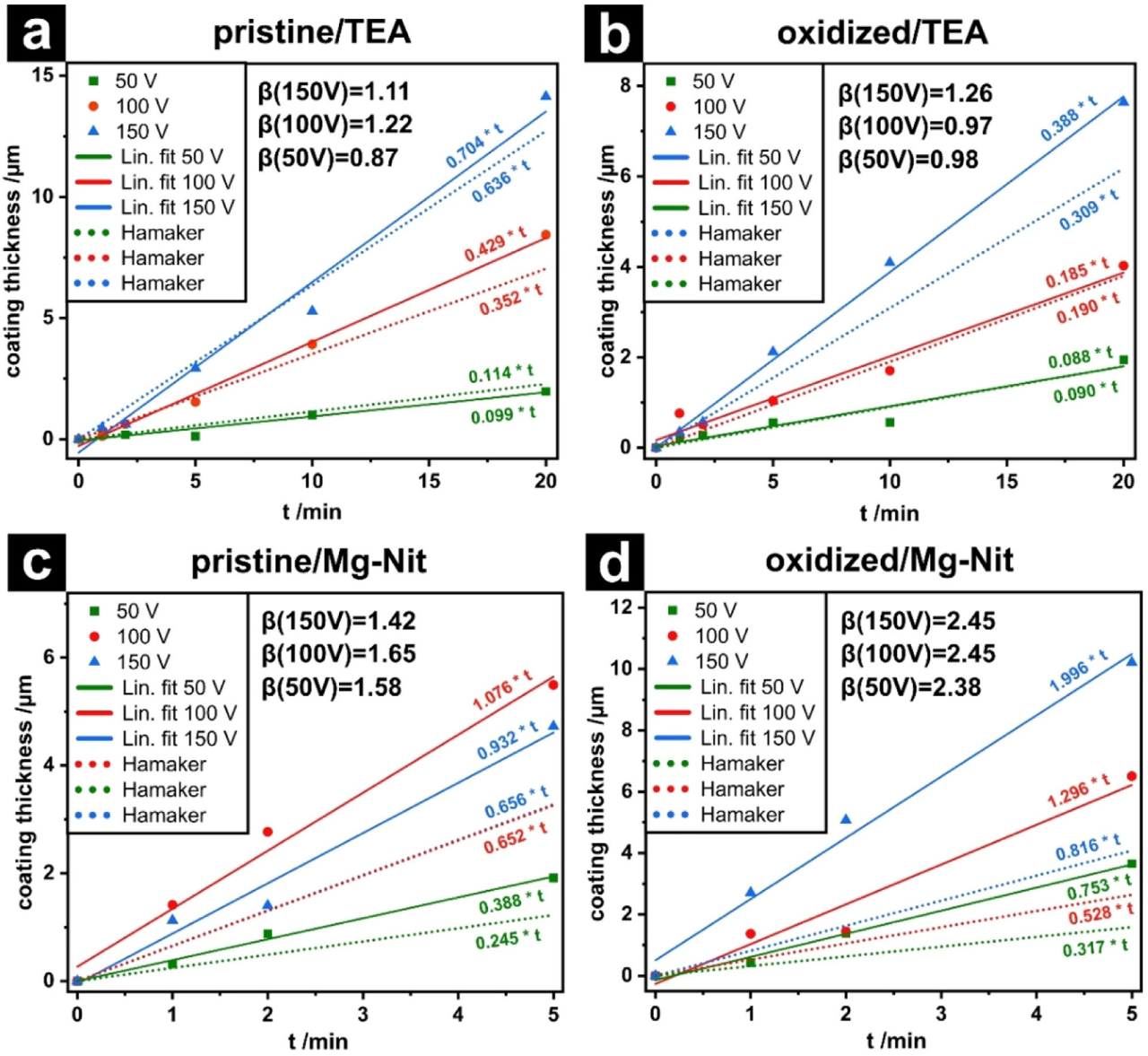

Fig. 6. Linear coating thickness development with TEA during the initial 20 min of deposition for (a) pristine and (b) oxidized CNT. Linear coating thickness development with Mg-Nit during the initial 5 min of deposition for (c) pristine and (d) oxidized CNT. The dotted lines represent the corresponding Hamaker lines.

4. Conclusion

Within this study, the temopral coating thickness development of pristine and oxidized CNTs on stainless steel substrates were investigated. EPD was used as a coating technique with dispersions containing two different additives over a range of voltages. The following are the key findings of this work:

- Regardless of additive or oxidation state, the coating thickness grows linearly during the initial phase of the deposition. The duration of that period depends on the additive.
- After deposition times of 20 min and more, coating growth indicates saturation. This becomes particularly evident at higher voltages.
- Regarding the additives, Mg-Nit typically exhibits higher deposition rates and, thus, forms thicker coatings than TEA over the same deposition period.
- Hamaker's equation can serve as a rough estimation for the thickness of CNT coatings deposited from dispersions containing TEA.

Declaration of Competing Interest

The authors declare that they have no known competing financial interests or personal relationships that could have appeared to influence the work reported in this paper.

Data availability

Data will be made available on request.

Acknowledgements

The activities within this work were financially supported by the State of Saarland from the European Regional Development Fund (Europäischer Fond für Regionale Entwicklung, EFRE) and Deutsche Forschungsgemeinschaft (DFG, German Research Foundation) within the project MU 959/47-1. Further, we acknowledge support by Saarland University within the 'Open Access Publication Funding' program.

Frank Müller acknowledges partial support from the German Research Foundation (DFG) via the Collaborative Research Center SFB 1027. Furthermore, the authors wish to thank Daniela Foetz, formerly part of the research group for structural and functional ceramics at Saarland University for granting the authors access to the viscosimeter as well as Rebekka Christmann, formerly part of the drug delivery department of the Helmholtz Institute for Pharmaceutical Research Saarland, for her assistance with the zeta potential measurements.

Supplementary materials

Supplementary material associated with this article can be found, in the online version, at doi:10.1016/j.cartre.2023.100265.

References

[1] E. Harsanyi, Method of coating radiant bodies, 1933.
[2] S. Yanagida, A. Nakajima, Y. Kameshima, N. Yoshida, T. Watanabe, K. Okada, Preparation of a crack-free rough titania coating on stainless steel mesh by electrophoretic deposition, Mater. Res. Bull. 40 (2005) 1335–1344.
[3] I. Zhitomirsky, A. Petric, Electrolytic and electrophoretic deposition of CeO2 films, Mater. Lett. 40 (1999) 263–268.
[4] B. Ferrari, R. Moreno, Electrophoretic deposition of aqueous alumina slips, J. Eur. Ceram. Soc. 17 (1997) 549–556.
[5] B. Ferrari, R. Moreno, The conductivity of aqueous Al2O3 slips for electrophoretic deposition, Mater. Lett. 28 (1996) 353–355.
[6] T. Ishihara, K. Sato, Y. Takita, Electrophoretic Deposition of Y2O3-Stabilized ZrO2 Electrolyte Films in Solid Oxide Fuel Cells, J. Am. Ceram. Soc. 79 (1996) 913–919.
[7] P. Ducheyne, S. Radin, M. Heughebaert, J.C. Heughebaert, Calcium phosphate ceramic coatings on porous titanium: effect of structure and composition on electrophoretic deposition, vacuum sintering and in vitro dissolution, Biomaterials 11 (1990) 244–254.
[8] T.M. Sridhar, U.K. Mudali, M. Subbaiyan, Preparation and characterisation of electrophoretically deposited hydroxyapatite coatings on type 316L stainless steel, Corros. Sci. 45 (2003) 237–252.
[9] A.R. Boccaccini, E.J. Minay, D. Krause, Bioglass® coatings on superelastic NiTi wires by electrophoretic deposition (EPD), Key Eng. Mater. Trans. Tech. Publ. (2006) 219–224.
[10] H.C. Hamaker, Formation of a deposit by electrophoresis, Trans. Faraday Soc. 35 (1940) 279–287.
[11] J. Cho, K. Konopka, K. Rozniatowski, E. García-Lecina, M.S.P. Shaffer, A.R. Boccaccini, Characterisation of carbon nanotube films deposited by electrophoretic deposition, Carbon 47 (2009) 58–67.
[12] B.J.C. Thomas, M.S.P. Shaffer, S. Freeman, M. Koopman, K.K. Chawla, A.R. Boccaccini, Electrophoretic Deposition of Carbon Nanotubes on Metallic Surfaces, Key Eng. Mater. 314 (2006) 141–146.
[13] L. Reinert, F. Lasserre, C. Gachot, P. Grützmacher, T. MacLucas, N. Souza, F. Mücklich, S. Suarez, Long-lasting solid lubrication by CNT-coated patterned surfaces, Sci. Rep. 7 (2017) 42873.
[14] T. Maclucas, S. Schütz, S. Suarez, F. Mücklich, Surface protection of austenitic steels by carbon nanotube coatings, Surf. Topogr. Metrol. Prop. 6 (2018) 14005.
[15] C. Schäfer, L. Reinert, T. MacLucas, P. Grützmacher, R. Merz, F. Mücklich, S. Suarez, Influence of Surface Design on the Solid Lubricity of Carbon Nanotubes-Coated Steel Surfaces, Tribol. Lett. 66 (2018) 89.
[16] C. Du, N. Pan, Supercapacitors using carbon nanotubes films by electrophoretic deposition, J. Power Sources. 160 (2006) 1487–1494.
[17] L. Li, W. Liu, F. Yang, W. Jiao, L. Hao, R. Wang, Interfacial reinforcement of hybrid composite by electrophoretic deposition for vertically aligned carbon nanotubes on carbon fiber, Compos. Sci. Technol. 187 (2020) 107946.
[18] C. Zhu, T. Liu, F. Qian, W. Chen, S. Chandrasekaran, B. Yao, Y. Song, E.B. Duoss, J.D. Kuntz, C.M. Spadaccini, M.A. Worsley, Y. Li, 3D printed functional nanomaterials for electrochemical energy storage, Nano Today 15 (2017) 107–120.
[19] P. Huang, D. Pech, R. Lin, J.K. McDonough, M. Brunet, P.L. Taberna, Y. Gogotsi, P. Simon, On-chip micro-supercapacitors for operation in a wide temperature range, Electrochem. Commun. 36 (2013) 53–56.
[20] T. MacLucas, S. Suarez, On the solid lubricity of electrophoretically deposited carbon nanohorn coatings, Lubricants 7 (2019) 62.
[21] T.D. Nguyen, O. Geuli, L.P. Yeo, S. Magdassi, D. Mandler, A.I.Y. Tok, Additive-free electrophoretic deposition of graphene quantum dots thin films, Chem. Eur. J. 25 (2019) 16573–16581.
[22] M. Diba, D.W.H. Fam, A.R. Boccaccini, M.S.P. Shaffer, Electrophoretic deposition of graphene-related materials: A review of the fundamentals, Prog. Mater. Sci. 82 (2016) 83–117.
[23] V. Datsyuk, M. Kalyva, K. Papagelis, J. Parthenios, D. Tasis, A. Siokou, I. Kallitsis, C. Galiotis, Chemical oxidation of multiwalled carbon nanotubes, Carbon 46 (2008) 833–840.
[24] S. Niyogi, M.A. Hamon, H. Hu, B. Zhao, P. Bhowmik, R. Sen, M.E. Itkis, R.C. Haddon, Chemistry of single-walled carbon nanotubes, Acc. Chem. Res. 35 (2002) 1105–1113.
[25] R.C. Haddon, Chemistry of the fullerenes: The manifestation of strain in a class of continuous aromatic molecules, Science 261 (1993) 1545–1550.
[26] F.H. Gojny, K. Schulte, Functionalisation effect on the thermo-mechanical behaviour of multi-wall carbon nanotube/epoxy-composites, Compos. Sci. Technol. 64 (2004) 2303–2308.
[27] D.A. Kurnosov, A.S. Baturin, A.S. Bugaev, K.N. Nikolski, R.G. Tchesov, E.P. Sheshin, Influence of the interelectrode distance in electrophoretic cold cathode fabrication on the emission uniformity, Appl. Surf. Sci. 215 (2003) 232–236.
[28] P.V. Kamat, K.G. Thomas, S. Barazzouk, G. Girishkumar, K. Vinodgopal, D. Meisel, Self-assembled linear bundles of single wall carbon nanotubes and their alignment and deposition as a film in a dc field, J. Am. Chem. Soc. 126 (2004) 10757–10762.
[29] G. Zhu, L. Pan, T. Lu, X. Liu, T. Lv, T. Xu, Z. Sun, Electrophoretic deposition of carbon nanotubes films as counter electrodes of dye-sensitized solar cells, Electrochim. Acta. 56 (2011) 10288–10291.
[30] K. Yu, Z. Zhu, Q. Li, W. Lu, Electronic properties and field emission of carbon nanotube films treated by hydrogen plasma, Appl. Phys. A Mater. Sci. Process. 77 (2003) 811–817.
[31] S. Santhanagopalan, F. Teng, D.D. Meng, High-Voltage Electrophoretic Deposition for Vertically Aligned Forests of One-Dimensional, Nanoparticles 27 (2011) 561–569.
[32] M.F. De Riccardis, D. Carbone, A. Rizzo, A novel method for preparing and characterizing alcoholic EPD suspensions, J. Colloid Interface Sci. 307 (2007) 109–115.
[33] X. Chen, X. Wang, D. Fang, A review on C1s XPS-spectra for some kinds of carbon materials, Fullerenes, Nanotub. Carbon Nanostruct. 28 (2020) 1048–1058.
[34] D.A. Shirley, High-resolution X-ray photoemission spectrum of the valence bands of gold, Phys. Rev. B. 5 (1972) 4709.
[35] J.J. Yeh, I. Lindau, Atomic subshell photoionization cross sections and asymmetry parameters: 1≤ Z≤ 103, At. Data Nucl. Data Tables 32 (1985) 1–155.
[36] I. Mazov, V.L. Kuznetsov, I.A. Simonova, A.I. Stadnichenko, A.V Ishchenko, A.I. Romanenko, E.N. Tkachev, O.B. Anikeeva, Oxidation behavior of multiwall carbon nanotubes with different diameters and morphology, Appl. Surf. Sci. 258 (2012) 6272–6280.
[37] P. Yi, K.L. Chen, Influence of Surface Oxidation on the Aggregation and Deposition Kinetics of Multiwalled Carbon Nanotubes in Monovalent and Divalent Electrolytes, Langmuir 27 (2011) 3588–3599.
[38] D.R. Lide, CRC Handbook of Chemistry and Physics, CRC Press, Boca Raton, 2010.
[39] I. Zhitomirsky, L. Gal-Or, Electrophoretic deposition of hydroxyapatite, J. Mater. Sci. Mater. Med. 8 (1997) 213–219.
[40] A.R. Gardeshzadeh, S. Rasouli, Kinetic investigation of carbon nanotube deposition by DC electrophoretic technique, (2011).
[41] B.P. Singh, B.K. Jena, S. Bhattacharjee, L. Besra, Development of oxidation and corrosion resistance hydrophobic graphene oxide-polymer composite coating on copper, Surf. Coatings Technol. 232 (2013) 475–481.
[42] Y.C. Wang, I.C. Leu, M.H. Hon, Kinetics of electrophoretic deposition for nanocrystalline zinc oxide coatings, J. Am. Ceram. Soc. 87 (2004) 84–88.
[43] K.A. Wepasnick, B.A. Smith, K.E. Schrote, H.K. Wilson, S.R. Diegelmann, D.H. Fairbrother, Surface and structural characterization of multi-walled carbon nanotubes following different oxidative treatments, Carbon 49 (2011) 24–36.
[44] M.T. Khimenko, V.V Litinskaya, G.P. Khomenko, Vliyanie kontsentratsii na polyarizuemost'molekuly izopropilovogo spirta v dimetilsul'fokside [Effect of concentration on the molecule polarizability of isopropyl alcohol in dimethyl sulphoxide], Zh. Fiz. Khim. 56 (1982) 867–870.

II. Influence of structural depth of laser-patterned steel surfaces on the solid lubricity of carbon nanoparticle coatings

Timothy MacLucas[1], Lukas Daut[1], Philipp Grützmacher[2], Maria Agustina Guitar[1], Volker Presser[3,4,5], Carsten Gachot[2,*], Sebastian Suarez[1], Frank Mücklich[1]

[1] *Chair of Functional Materials, Saarland University, Campus D3.3, Saarbrücken 66123, Germany*

[2] *Institute for Engineering Design and Product Development, TU Wien, Lehárgasse 6, 1060 Vienna, Austria*

[3] *INM – Leibniz Institute for New Materials, 66123 Saarbrücken, Germany*

[4] *Department of Materials Science & Engineering, Saarland University, Campus D3.3, 66123 Saarbrücken, Germany*

[5] *Saarene, Saarland Center for Energy Materials and Sustainability, Campus D4.2, 66123 Saarbrücken, Germany*

Published in **"Friction"** (2023) (IF: 6.8 [2022])

Accessible online at: https://doi.org/10.1007/s40544-022-0664-z

Own contribution: Sample preparation, tribometry, characterization, data analysis, figures, tables, discussion, writing – original

Friction **11**(7): 1276–1291 (2023)
https://doi.org/10.1007/s40544-022-0664-z
ISSN 2223-7690
CN 10-1237/TH

RESEARCH ARTICLE

Influence of structural depth of laser-patterned steel surfaces on the solid lubricity of carbon nanoparticle coatings

Timothy MACLUCAS[1,*], Lukas DAUT[1], Philipp GRÜTZMACHER[2], Maria Agustina GUITAR[1], Volker PRESSER[3,4,5], Carsten GACHOT[2,*], Sebastian SUAREZ[1], Frank MÜCKLICH[1]

[1] *Chair of Functional Materials, Saarland University, Saarbrücken 66123, Germany*

[2] *Institute for Engineering Design and Product Development, TU Wien, Wien 1060, Austria*

[3] *INM–Leibniz Institute for New Materials, Saarbrücken 66123, Germany*

[4] *Department of Materials Science & Engineering, Saarland University, Saarbrücken 66123, Germany*

[5] *Saarene-Saarland Center for Energy Materials and Sustainability, Saarbrücken 66123, Germany*

Received: 04 December 2021 / Revised: 07 March 2022 / Accepted: 13 June 2022

© The author(s) 2022.

Abstract: Carbon nanoparticle coatings on laser-patterned stainless-steel surfaces present a solid lubrication system where the pattern's recessions act as lubricant-retaining reservoirs. This study investigates the influence of the structural depth of line patterns coated with multi-walled carbon nanotubes (CNTs) and carbon onions (COs) on their respective potential to reduce friction and wear. Direct laser interference patterning (DLIP) with a pulse duration of 12 ps is used to create line patterns with three different structural depths at a periodicity of 3.5 μm on AISI 304 steel platelets. Subsequently, electrophoretic deposition (EPD) is applied to form homogeneous carbon nanoparticle coatings on the patterned platelets. Tribological ball-on-disc experiments are conducted on the as-described surfaces with an alumina counter body at a load of 100 mN. The results show that the shallower the coated structure, the lower its coefficient of friction (COF), regardless of the particle type. Thereby, with a minimum of just below 0.20, CNTs reach lower COF values than COs over most of the testing period. The resulting wear tracks are characterized by scanning electron microscopy, transmission electron microscopy, and energy-dispersive X-ray spectroscopy. During friction testing, the CNTs remain in contact, and the immediate proximity, whereas the CO coating is largely removed. Regardless of structural depth, no oxidation occurs on CNT-coated surfaces, whereas minor oxidation is detected on CO-coated wear tracks.

Keywords: solid lubricant coatings; carbon nanotubes; carbon onions; direct laser interference patterning (DLIP) surface structuring; electrophoretic deposition (EPD)

1 Introduction

Friction and wear reduction have been intensively studied for centuries because of their crucial importance in mechanical systems. An effective approach to mitigate friction between two surfaces moving relative to each other is introducing a well-defined surface pattern. It minimizes the real area of contact and possibly entraps abrasive wear particles, thus effectively keeping them out of contact [1–6]. Direct laser interference patterning (DLIP) might be the most versatile and productive among various techniques to create such topographies. During DLIP, multiple high-power laser pulses are brought to interference directly on the substrate's surface, which allows for the creation of periodic surface structures such as line-, cross-, and dimple patterns [7, 8].

Despite environmental concerns and limited applicability in harsh conditions for example, in space applications under vacuum, oil-based lubricants remain

* Corresponding authors: Timothy MACLUCAS, E-mail: timothy.maclucas@uni-saarland.de; Carsten GACHOT, E-mail: carsten.gachot@tuwien.ac.at

the most widely used form of lubrication with few alternatives. However, solid lubricants like graphitic materials and transition metal dichalcogenides have gained increasing attention in recent decades, particularly for extreme environments [9, 10]. Amongst the group of graphitic materials, multi-walled carbon nanotubes (CNTs) and carbon onions (COs), have proven their ability to provide effective solid lubrication either as reinforcement phase in composites [11–18] or as a coating [19–29]. Further studies have shown that CNTs and COs can achieve superlubricity under a specific set of conditions due to the formation of an incommensurate contact [30–33]. Their lubrication ability is attributed to a combination of their mechanical properties based on the sigma bonds formed between sp^2-hybridized carbon atoms and particle morphology [34–37]. While CNTs are cylindrical, COs are spherical, theoretically allowing the particles to rotate and therefore act as a nanoscale roller bearing. This can lead to extremely low coefficients of friction (COF). Hirata et al. [26] conducted ball-on-disc testing with COs spread on a silicon wafer and found a COF value well below 0.1 both in air and vacuum at a normal load of 0.95 N.

On austenitic stainless steel, purely DLIP-processed surfaces wear off rapidly when rubbed against a counter body of similar or higher hardness at sufficiently high loads. On the other hand, carbon nanoparticles are quickly removed from the contact area on a flat sample as they do not form a covalent bond with the chromium oxide layer [22–24]. As shown in a comprehensive review article by Rosenkranz et al. [38], a synergetic approach of textured surfaces combined with solid lubricant coatings like diamond-like carbon (DLC), polytetrafluorethylene (PTFE), and 2-dimensional (2D) layered materials can overcome each approach's limitations. A study conducted by Reinert et al. [23] demonstrated a combination of line-patterned steel surfaces and CNT coatings. Effective solid lubrication was provided over extended periods because the pattern's recessions act as reservoirs from where the lubricant is supplied to the contact area. Neither patterned/uncoated nor unpatterned/CNT-coated samples could provide long-lasting lubrication unless both approaches were combined, in which case a COF of 0.20 was reached and sustained over 10,000 cycles. A ball-on-disc tribometer was used with an alumina ball as a counter body at a load of 100 mN. Surfaces were DLIP-processed with pulses in the nanosecond range resulting in structural depths around 1 μm and subsequently coated with CNTs by electrophoretic deposition (EPD).

In recent years, EPD has been increasingly used to deposit various carbon nanoparticles due to its ability to form homogeneous coatings on geometrically complex substrates while being simple and cost-effective [20, 22–24, 39–41]. Consequently, EPD is a preferred method for manufacturing uniform particle films on steel surfaces.

In a closely related work, Schäfer et al. [22] studied the influence of the structural depth of laser-patterned stainless-steel surfaces, EPD-coated with CNTs. Direct laser writing (DLW) with ultrashort laser pulses in the femtosecond range created cross-patterns with structural depths of 1 and 3 μm. The lubrication performance was measured with a ball-on-disc micro tribometer, working in rotational mode at a normal load of 1 N. Despite having a larger lubricant storage volume, friction experiments with deeper patterns did not lead to an extended lifetime of the lubrication but behaved similarly to the uncoated patterns. This was attributed to the formation of material depositions along the structure's edges, impeding or even blocking the lubricant supply into the contact area.

The present study aims at improving our understanding of such lubrication systems. Stainless steel surfaces are laser-patterned to create line patterns with three different structural depths, thereby changing the slope's angle of the individual line structures. This variation is thought to have a pronounced impact on the laser pattern's ability to supply the contact with lubricious carbon nanoparticles. Surfaces in this work were processed with a pulse length of 12 ps (representing the transition regime between short and ultrashort laser pulses) and generally produced surfaces with slightly different topographies and surface chemistry compared to the nano- or femtosecond regime. Subsequently, EPD was used to coat the as-processed surfaces with CNT and CO films. Platelets

of commercially available AISI 304 austenitic stainless steel were used as substrate material due to the materials' technical relevance and comparability with previous works. The lubrication systems' tribological properties were determined, and the resulting wear tracks were analyzed to determine which structural depth in combination with which carbon nanoparticle coating reduces friction and wear most effectively and permanently.

2 Experimental

2.1 Materials

We used commercially available multiwall CNTs grown by chemical vapor deposition. The material showed an outer diameter of 30–85 nm, a length of 10–15 μm, and was purchased at Graphene Supermarket. COs derived from the annealing of detonation nanodiamonds (NaBond Technologies Co., purity > 98 %, individual particle diameter: 4–8 nm) were used. Annealing was conducted in a vacuum furnace (model: 1100-3580-W1, Thermal Technology Inc.) at a temperature of 1,750 °C for 3 h at a rate of 10 °C/min [42]. As a metal substrate, mirror polished AISI 304 austenitic stainless steel (Brio Kontrollspiegel GmbH) was used in the form of 20 mm × 20 mm platelets with a thickness of 1 mm. Before usage, steel platelets were cleaned thoroughly in acetone and isopropanol baths for 10 min each to remove contamination.

2.2 Pulsed direct laser interference patterning

Line-patterned surfaces were prepared using a Nd:YAG pulsed laser (Edgewave PX-series InnoSlab) integrated into a laser system RDX 500 nano by pulsar photonics. Two equally powerful sub-beams at a pulse duration of 12 ps were used to create line patterns with a periodicity of 3.5 μm. The laser operates with an elliptic laser spot (major axis: 80 μm, minor axis: 57 μm) at a wavelength of 532 nm and the samples were processed at 55% of its maximum power which corresponds to 0.5 W. The step width refers to the shift of the laser spot between each shot, hence a low step width corresponds to a high overlap and, thus, a high fluence. The following step widths were used for structuring: 1/5/10 μm, which translates into a respective fluence of 70/14/7 J/cm^2. Due to oxide formation during laser processing, particularly on surfaces structured at higher fluences, platelets were cleaned after laser processing by ultrasonication first in citric acid, followed by acetone, and finally, isopropanol for 15 min each.

2.3 Surface characterization

To measure the line-patterned steel surfaces' structural depth, the mean height R_C was determined over a sampling length of 259 μm with an Olympus LEXT OLS4100 confocal laser scanning microscope (CLSM) using a 50× objective (NA: 0.95). The equipment operates with a laser wavelength of 405 nm and a vertical and lateral resolution of 10 and 120 nm, respectively. For statistical representation, R_C was measured over 10 different sampling lengths at three different spots on the steel surface.

2.4 Solution preparation and electrophoretic deposition

EPD solutions consisted of 80 mL of isopropanol used as the solvent with 10 mL of triethylamine (TEA). TEA synthesized by ACROS organics with a purity of 99% was used as an additive to support particle deposition. The particle concentration in the solution was 0.1 mg/mL of solvent.

Subsequent particle dispersion was a two-step process. During the first step, the solution was homogenized in a shear mixer (Ultra-Turrax T25, IKA) at 7,000 rpm for 5 min (CO) and 10 min (CNT). Further dispersion was achieved by ultrasonication (Bandelin Sonorex RK514BH) for 10 min (CNT) and 45 min (CO). After the dispersion, two steel platelets were immersed in the solution. Substrate surfaces were arranged in parallel, separated by 1.3 cm, and connected to a DC voltage source. CNTs were deposited at a voltage of 150 V, while for COs, the voltage was set to 300 V. Both particles were processed for 15 min with the deposition occurring on the anode.

2.5 Tribological testing

The friction coefficients' temporal evolution was measured with a ball-on-disc nano-tribometer (CSM

Instruments) in linear-reciprocating mode transversal to the line-pattern. The stroke length was set to 0.6 mm and the velocity to 1 mm/s. A normal load of 100 mN was chosen, corresponding to a Hertzian contact pressure of 360 MPa. Alumina balls (grade 28, Anton Paar GmbH) measuring 6 mm in diameter, with a surface roughness of R_Q = 55.5 ± 12.8 nm were used as a counter body. 10,000 measurement cycles were conducted at room temperature and a constant relative humidity of 4%. This humidity level was explicitly chosen to exclude graphitic lubrication, which is enhanced by the presence of water vapor as it significantly facilitates interlamellar shearing of individual graphite or even graphene crystals [9]. For statistical representation, each sample was tested three times. The resulting raw data were slightly smoothed (Savitzky-Golay filter, 50 p) before being used to plot the COF development graphs.

2.6 Chemical and microstructural characterization

Micrographs of the coatings, cross-sections, and wear tracks were made with a Helios NanoLab 600 dual beam workstation (scanning electron microscope (SEM)/focussed ion beam (FIB)) by FEI. Subsequently, the wear tracks were characterized by energy-dispersive X-ray spectroscopy (EDS) with an EDAX detector. While EDS was performed at an acceleration voltage of 15 kV and a current of 11 nA, SEM micrographs were taken at 5 kV and 1.4 nA. Transmission electron microscopy (TEM) samples were extracted from the center of the wear track in the direction parallel to the sliding motion. The preparation was done using a focussed ion beam (FIB-Helios Nanolab 600-FEI Company) as detailed in [43]. A JEOL JEM 2010F was utilized for TEM at an acceleration voltage of 200 kV.

3 Results

3.1 Surface topography

To visualize the profiles of the patterns created by DLIP-processing, CLSM was used for coarse-scale 3D mapping. The maps shown in Fig. 1 span an area of approximately 170 µm × 170 µm and demonstrate pattern uniformity regardless of fluence and, thus, structural depth. In addition to that, FIB cross-sections were made and imaged by SEM. The FIB-cross sections depicted in Fig. 2 (CNT-coated) and Fig. 3 (CO-coated) show the topographies of the laser-patterned and coated samples processed at different structural depths. Pronounced curtaining is observable in the scanning electron micrographs of both coatings, particularly in the case of the COs and can be attributed to the high porosity of the coatings as it prevents the formation of a coherent protective platinum deposition. This porosity is a consequence of the formation of large and poorly interconnected agglomerates. Compared to CNTs, COs form smaller agglomerates as a result of which more homogeneous coatings are formed. CNTs are cylindrical with a high aspect ratio and a strong tendency to entangle. Convex flanks characterize both the shallow (Figs. 2, 3(a), and 3(d)) and the intermediate structures (Figs. 2, 3(b), and 3(e)), whereas the deeper structures (Figs. 2, 3(c), and 3(f)) exhibit a concave profile as well as higher burrs on each side of the line-like structure.

The three different structural depths were achieved by varying the laser spot's step width along the line-like structure. Laser processing at shorter step widths means more significant spot overlap and higher fluences, resulting in deeper structures with steeper flanks. This is confirmed by the results listed in Table 1.

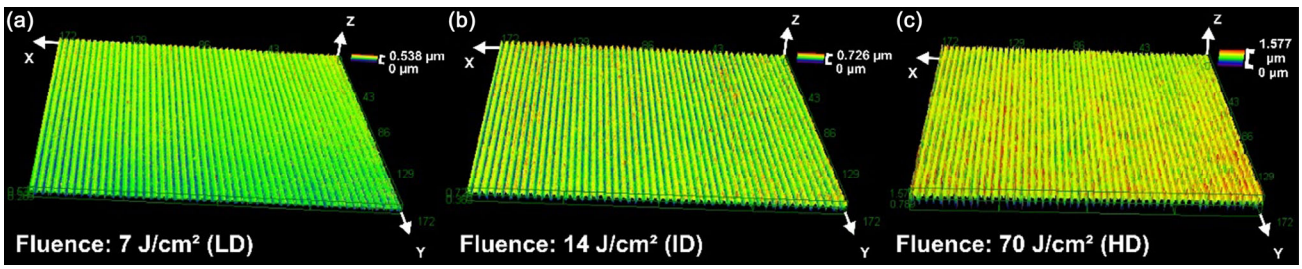

Fig. 1 Coarse-scale 3D maps of the patterned surfaces processed with fluences of (a) 7, (b) 14, and (c) 70 J/cm^2 resulting in different structural depths (low depth (LD), intermediate depth (ID), and high depth (HD), respectively). The maps were made using CLSM and display an area of approximately 170 µm × 170 µm (zoom: 1.1, *z*-factor: 9.1).

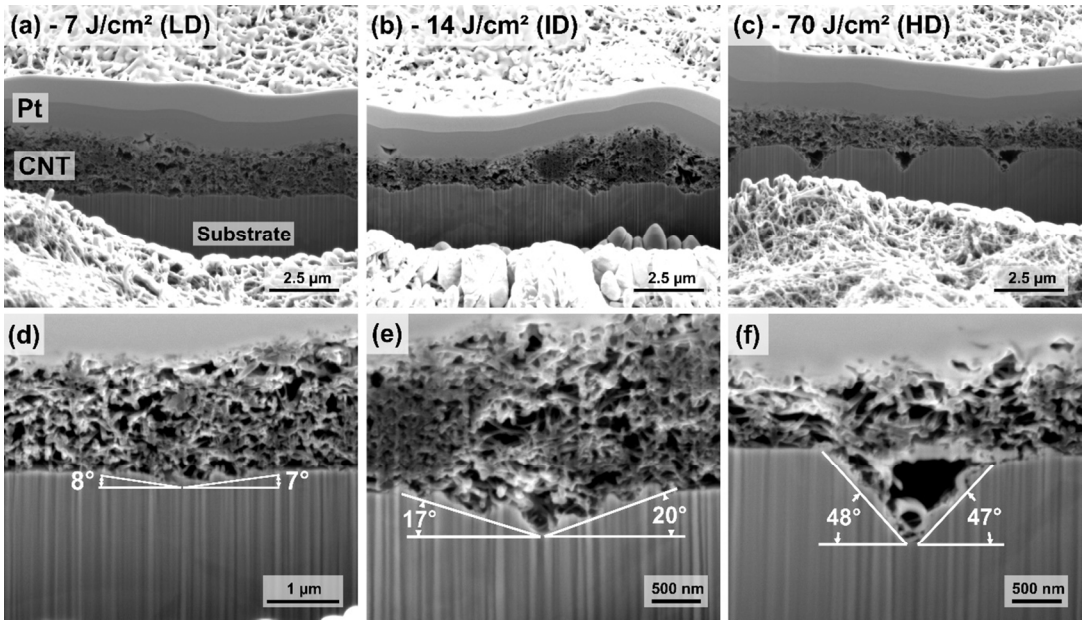

Fig. 2 FIB cross-sections of CNT-coated picosecond-laser processed steel surfaces at fluences of (a, d) 7, (b, e) 14, and (c, f) 70 J/cm^2 resulting in structural depths of 0.24, 0.36, and 0.77 µm, respectively.

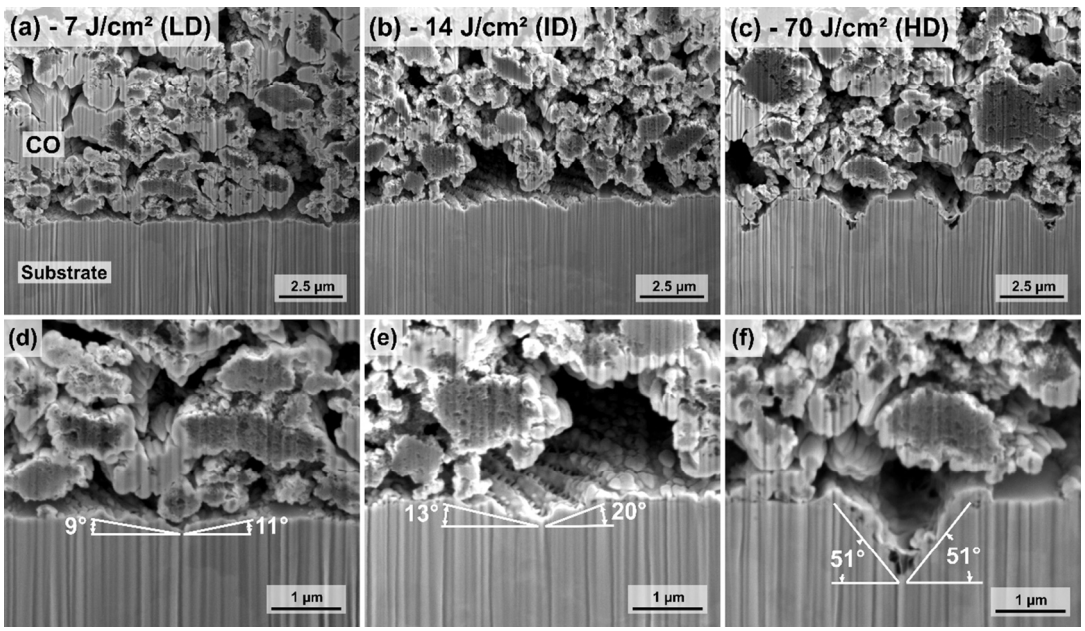

Fig. 3 FIB cross-sections of CO-coated picosecond-laser processed steel surfaces at fluences of (a, d) 7, (b, e) 14, and (c, f) 70 J/cm^2 resulting in structural depths of 0.20, 0.39, and 0.78 µm, respectively.

Table 1 Mean height R_C and slope angles of the line-patterned steel surfaces processed at different fluences.

Sample acronym	Fluence (J/cm^2)	Mean height R_C (µm)		Slope angles (°)	
		CNT-coated	OLC-coated	CNT-coated	OLC-coated
LD	7	0.237 ± 0.006	0.196 ± 0.002	9.7 ± 1.6	10.0 ± 3.0
ID	14	0.355 ± 0.003	0.389 ± 0.007	19.1 ± 3.4	16.3 ± 3.8
HD	70	0.770 ± 0.007	0.779 ± 0.020	47.0 ± 4.8	48.6 ± 2.9

The standard deviation of the structural depths is very low and lies between 0.8% and 2.6% for both CNT-coated and CO-coated surfaces. Therefore, the patterns can be described as highly homogeneous throughout all measured surfaces. Comparing the absolute depths of both substrates, patterned with the same fluence, shows that the shallow patterns are comparable. In contrast, the intermediate and deep patterns are close to identical, demonstrating the high reproducibility of the DLIP technique. For the smallest structural depth, produced with the longest step width, the substrate's initial state (e.g., roughness, absorptivity) will have a more significant effect on the result, thus slightly affecting the reproducibility.

Differing structural depths result in flanks with different slopes. Both features of the respective structures are listed in Table 1. The values obtained for CNT-coated and CO-coated structures do not deviate in any statistically significant way and are highly comparable.

3.2 Friction behavior

Figure 4 shows the temporal evolution of the COF. In both friction tests, Ref represents a non-patterned, mirror-polished stainless-steel substrate used as a reference. When rubbing against the aluminum oxide counter body, the COF of Ref rises sharply and reaches an early steady-state at 200–250 cycles after which, it oscillates between 0.7 and 0.8. According to Blau et al. [44], the tribological behavior is characteristic of dry metal-metal contact, where the metals' surfaces are either contaminated (e.g., hydrocarbons, adsorbed water) or covered by oxides. Furthermore, the obtained values lie within the range of what we have measured under identical conditions in previous works [20, 22–24].

The patterned and uncoated samples show similar tribological behavior as the reference, regardless of their respective structural depth. The COF of the LD and ID samples increase immediately and sharply, concurrent with the reference. In contrast, the increase in COF for the HD sample is slightly delayed. HD's asperities are significantly deeper; therefore, more material needs to be abraded until conformal contact is achieved. Thus, the real area of contact between surface and counter body remains reduced for more extended periods. The running-in behavior of LD and HD can be classified as type *a* according to Blau [44], while ID shows a clear type *b*. Both behaviors are typical for unlubricated metal contacts. The steady-state COF of all patterned surfaces without coating is comparable and oscillates around 0.7.

Coating the patterned surfaces with carbon nanoparticles results in an entirely different frictional behaviour. Generally, the samples combining both laser-patterning and CO coatings demonstrate a small COF peak at the very beginning of the test, which could be associated with a re-arrangement of the particles in the contact region until conformity is achieved. The initial peak is followed by a friction reduction down to COF values of 0.25–0.35. This represents a significant improvement compared to the reference or the merely laser-patterned samples, which can be ascribed to the lubricity of the COs

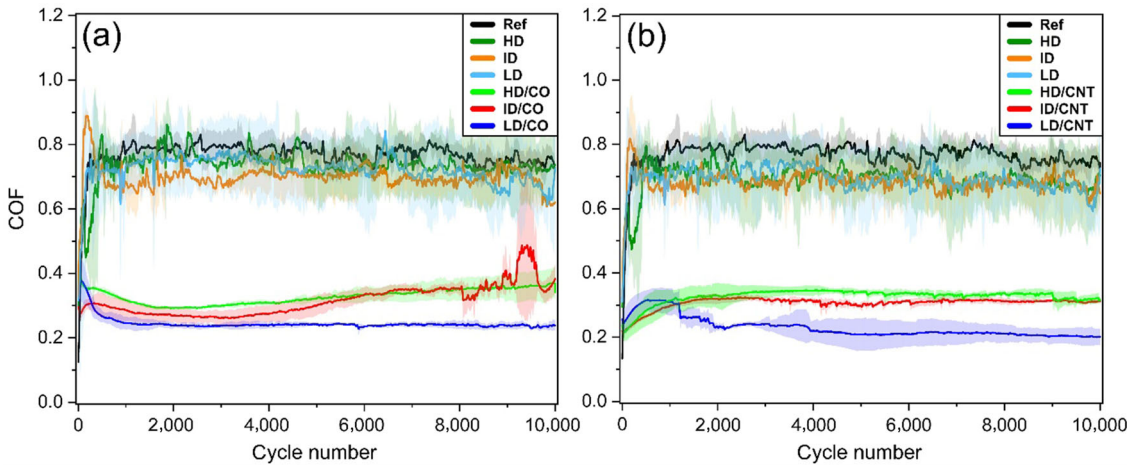

Fig. 4 Evolution of the COF of laser-patterned AISI 304 surfaces uncoated as well as coated with (a) COs or (b) CNTs.

combined with the function of the laser patterns as a reservoir. The laser pattern's structural depth greatly influences the initial COF peak value, the minimum COF, and the frictional performance towards the end of the test. The COF of HD/CO jumps to 0.40 during the first 20 cycles, followed by a steady decrease down to 0.30. After roughly 2,000 cycles, a turning point is reached, after which the COF increases steadily, reaching 0.37 after 10,000 cycles. ID/CO results in a lower peak value of 0.30 and a smaller minimum COF of 0.26. Like HD/CO, after reaching its minimum friction, the COF starts to increase again and attains a final value of just below 0.40. After 6,800 cycles, the oscillation of the COF grows stronger, resulting in a pronounced peak with a maximum COF of 0.50 after 9,400 cycles. Simultaneously, the standard deviation rises significantly.

The observed peak in the COF signal can be explained by the gradual degradation of the laser-pattern and the subsequent removal of the lubricious COs from the contact. As a result of local CO depletion, the contact area becomes inhomogeneous. This leads to a destabilization of the tribological behavior, which translates to a variable COF curve. The following return to a lower COF can be traced back to the replenishment of lubricant by tapping into a low-lying CO reservoir. For the first 5,500 cycles, ID/CO and HD/CO show near parallel COF development, with ID/CO maintaining a slightly lower COF. At the turning points, where the COF starts to increase, COs replenishment from the reservoirs begins to fade. The onset of oscillation in the case of ID/CO is a strong indicator for an at least partially unlubricated contact, leading to the degradation of the surface pattern and the formation of wear particles. The tribological performance of LD/CO differs notably from that of the deeper structures. After forming a significant peak during the first 80 cycles, the COF starts to decrease and reaches 0.24 at roughly 1,300 cycles. The COF remains constant for the following 8,700 cycles. A high reproducibility is inferred from the very low standard deviation.

Much like COs, combining laser patterns and CNT coatings leads to a significant friction reduction compared to the reference or the uncoated samples (Fig. 4(b)). ID/CNT and HD/CNT exhibit an almost identical COF development. Starting at around 0.22, their COF increases steadily to 0.31 and remains relatively constant after that. Both samples show low standard deviation during that period. For the most part, the COF of ID/CNT lies slightly below that of HD/CNT. The COF of LD/CNT rises during the initial 800 cycles. This increase is more substantial than ID/CNT or HD/CNT and could be explained by the weak-reservoir effect, meaning reservoirs are initially unable to retain the lubricant. After 1,300 cycles, there is a sudden drop from 0.30 to 0.26, followed by a gradual decrease reaching 0.20 at 4,000 cycles and remaining at that level for the final cycles. All CNT-coated/patterned surfaces can maintain a substantially lower COF than Ref and the uncoated samples over the entire test duration. Concerning the HD and ID samples, their corresponding COF developments indicate an increased lubrication lifetime of surfaces coated with CNT instead of CO, whose COF starts to increase after 2,000 and 3,000 cycles, respectively.

The shallowest CO-coated surfaces reach a COF of 0.24, whereas their CNT-coated equivalents achieve effective solid lubrication with a COF of 0.20. However, the detailed lubrication mechanisms of these particles are still being researched. In contrast to CO coatings, CNT coatings contain less coherent agglomerates alongside individual particles (Figs. 2 and 3). These particle types possess a higher range of motion and, thus, an increased ability to roll, which could explain a slightly lower COF.

An overall trend becomes apparent: the shallower the coated structure, the lower its COF, regardless of particle type. A possible explanation is related to the slopes' steepness (Figs. 2, 3(d)–3(f)) as shallow structures have a low angular slope that facilitates particle transport out of the structures and into the loaded contact area.

There is a good agreement between the COF values of the CNT-coated samples with those obtained by Schäfer et al. [22]; the latter work conducted micro tribometer tests on CNT-coated, cross-patterned stainless steel substrates with a depth of 1 and 3 μm fabricated by femtosecond laser pulses. Their results demonstrate that shallower patterned surfaces provide steady-state lubrication at a value of just under 0.20 for roughly 40,000 cycles. In contrast, the COF of the samples with higher structural depth starts to rise precipitously after a few thousand cycles and continues

until reaching that of the reference. However, all of our CNT-coated picosecond-patterned surfaces last over 10,000 cycles and more. While lubricating at maximum capacity, the coated surfaces with the deeper pattern (3 μm) showed slightly lower COF values than the shallower samples (1 μm) in contrast to our findings. Nonetheless, the samples were subject to a different type of tribological stress as Schäfer et al. measured in rotational mode with a higher load (1 N) [22].

Figures 2 and 3(f) show that before the tribological tests, the deep structures were not completely filled with particles during EPD as the shallower ones have. Nevertheless, the deeper patterns also demonstrated an effective COF reduction over significant periods during the tribological tests, albeit not as effective as the shallower patterns. Therefore, FIB cross-sections were prepared from inside the wear track of the HD samples after the initial 10 cycles of the friction test (Fig. 5). As seen, the particles get pressed into the structures from where they supply the contact with continuous lubrication as demonstrated by the results of the tribological tests. Due to their higher packing density, the CNTs can fill the structures more densely than the COs (Figs. 5(a) and 5(b)) which also explains the previously observed weak-reservoir effect. Large, coherent chunks of amorphous carbon and/or entangled CNTs are removed at once from the top of the reservoir bequeathing a superficial particle depletion which results in a temporary COF increase. Once the lower lubricant-filled regions of the reservoir get in contact, lubricant supply resumes and the COF increase is reversed. This effect is more likely to occur on shallow structures as their flat flanks facilitate lubricant removal and their filling ratio is higher compared to that of deep structures (Figs. 2 and 3) and, therefore, less compressible. In deep structures on the other hand, counter body pressure during tribological stress leads to a filling of existing voids and the particles are pressed further down the structure, preventing the above-mentioned removal mechanism. Additionally, the CNTs' known ability for mechanical restitution after compression in tribological contacts [23] combined with their large aspect ratio facilitates particle feed into the contact area, which could be why a weak-reservoir effect of similar magnitude is not observed for COs.

Furthermore, the CNT coatings in Fig. 5 remain largely intact after the initial cycles while the majority of the CO coating is removed. This can be explained by the particles' morphology. As the CNTs within the coating are highly entangled, they form a cohesive unit which is significantly more difficult to remove than an accumulation of large CO agglomerates.

3.3 Wear track and chemical analysis

3.3.1 HD pattern

To further understand the mechanisms responsible for the observed friction reduction, the occurred wear tracks were analyzed. SEM was used for identifying the primary wear mechanisms on representative wear tracks of each tested surface. At a higher resolution (Fig. 6(a)), the line pattern of the uncoated HD sample

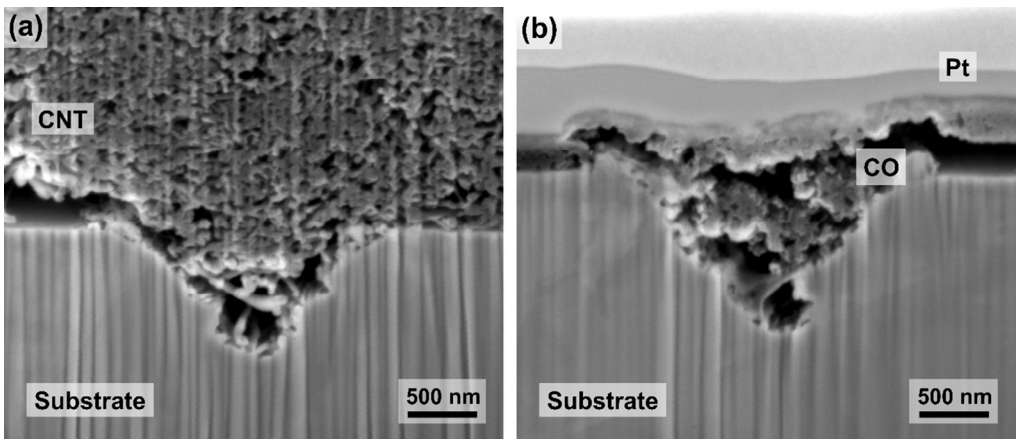

Fig. 5 SEM images showing cross-sections of (a) CNT-coated and (b) CO-coated picosecond-laser processed AISI 304 steel surfaces after 10 tribological cycles (HD sample).

has been completely worn off during the friction tests. Particularly in unlubricated tribological contacts, different wear mechanisms act simultaneously. In this case, sharp horizontal grooves are visible, stemming from both abrasive oxide particles formed during the tribo-test, and the asperities of the counter body. The most dominant wear mechanism, however, is adhesion which is caused by solid-state welding. Adhesion marks are visible in the wear tracks of all uncoated samples in the form of dark spots.

EDS was used to acquire elemental maps to get a better understanding of the tribo-chemical reactions during friction testing. The large bright green areas inside the wear track of the uncoated HD sample depicted in Fig. 6(b) indicate extensive oxidation and severe tribo-chemical wear, which conforms perfectly with the high COF value measured during tribological testing. It also shows that the material pile-up at the right edge of the wear track consists mainly of oxide particles.

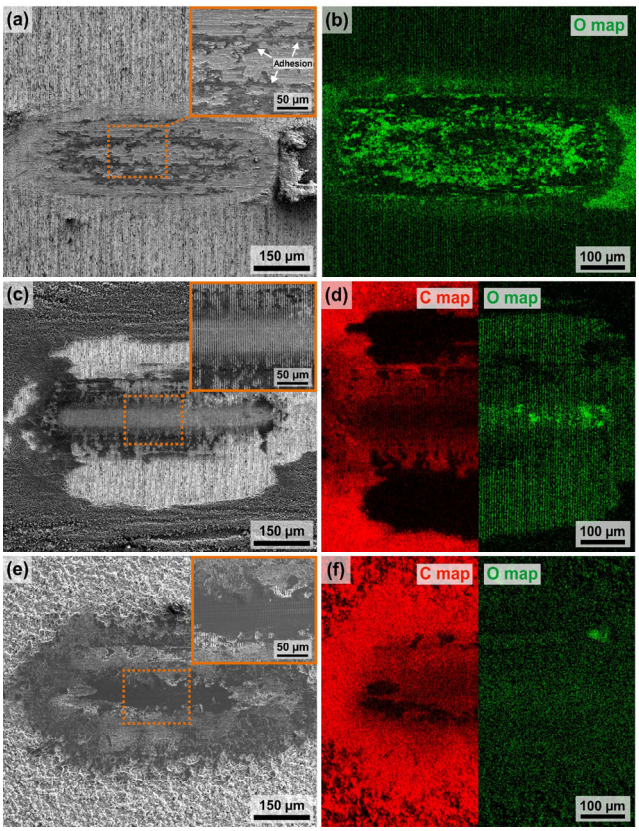

Fig. 6 SEM images of (a) uncoated, (c) CO-coated, and (e) CNT-coated wear tracks on the high depth patterns after friction testing with their corresponding EDS maps of carbon and oxygen (b, d, f).

Figure 6(c) provides an overview of the wear track on the CO-coated HD surface. In the magnified image, the line pattern in the center of the wear track is still clearly recognizable, despite showing a substantial degree of degradation. Particularly in areas on the left side of the wear track, where the pattern is better preserved, vertical dark lines are visible. Those lines represent carbon reservoirs in the remnants of the pattern's recessions. However, most of the coating in and around the wear track was removed during the friction test, confirmed by the carbon map shown in Fig. 6(d), as no carbon signals were detected outside of the wear track.

The remaining carbon reservoirs are also verified by vertical red lines inside the wear track. In the oxygen map (Fig. 6(d)), the wear track appears in a slightly brighter green compared to the surrounding substrate. Especially the right part contains areas of bright green, indicating mild oxidative wear. Simultaneously, the complete carbon map (Fig. 7) shows a near-complete absence of carbon in that particular area, leading to a higher mechanical impact on the substrate, resulting in faster oxidation. The measured COF of this sample, which is 0.37 after 10,000 cycles, correlates well with the observed wear behavior. The COF is well above the threshold of 0.20, which is considered effective lubrication according to Aouadi et al. [45], with no signs of wear. The measured COF is far below that of the patterned/uncoated sample, where severe wear and oxidation were observed (Fig. 6(b)).

Figure 6(e) shows the CNT-coated wear track of the HD sample after tribological testing, which, in

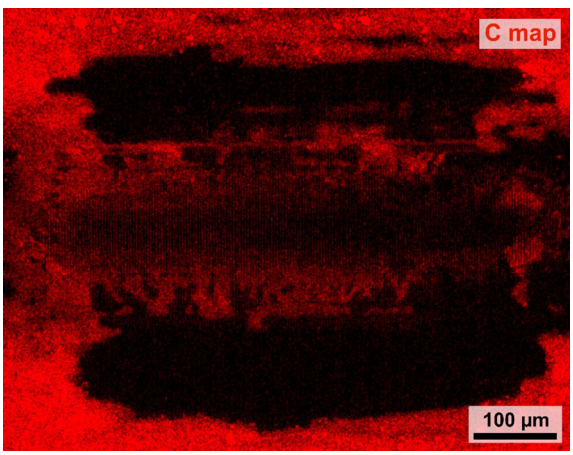

Fig. 7 Elemental carbon map of the CO-coated wear track on the HD surface after friction testing.

contrast to the CO-coated surface, is still largely covered by the coating. This can be attributed to a stronger cohesion of the CNT-coating resulting from the particles' entanglement. Those particles inside the wear track, which were in contact with the counter body, appear darker than the surrounding CNT-coating, most likely because of compression. Further magnification of the wear track shows that after 10,000 cycles, the line pattern underneath the coating remains fully intact. The carbon map (Fig. 6(f)) reveals that carbon has been detected throughout the wear track in the same locations as the compressed portions of carbon (Fig. 6(e)). At the same time, there is no strong oxygen signal inside the wear track (Fig. 6(f)); hence no significant oxidation has occurred.

3.3.2 *ID pattern*

Like the HD sample, the uncoated wear track of the ID sample depicted in Fig. 8(a) shows extensive wear due to which the line pattern was removed entirely.

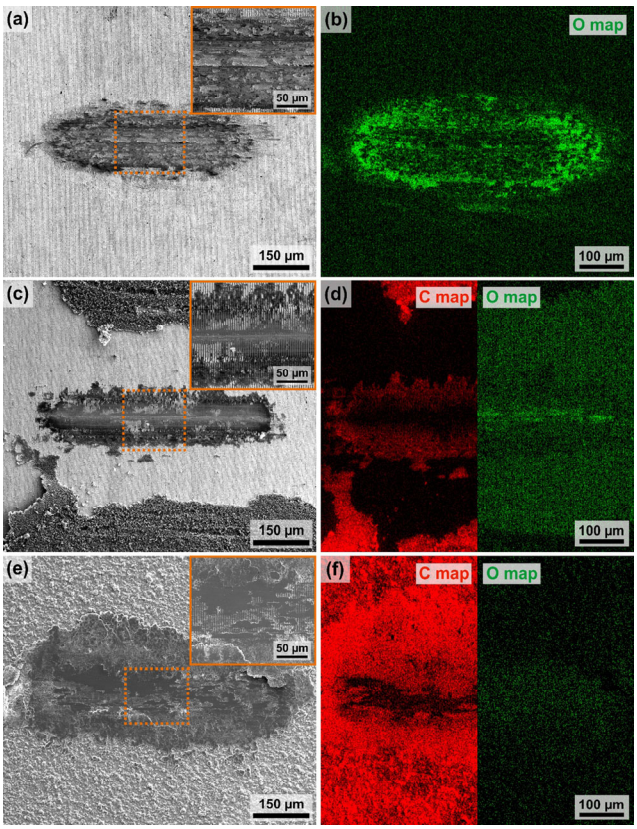

Fig. 8 SEM images of (a) uncoated, (c) CO-coated, and (e) CNT-coated wear tracks on the intermediate depth patterns after friction testing with their corresponding EDS maps of carbon and oxygen (b, d, f).

Particularly at higher resolution (Fig. 8(a)), adhesion is clearly identifiable as the dominant wear mechanism. As to be expected, the oxygen map (Fig. 8(b)) shows severe tribo-induced oxidation. However, in this case, there was no pile-up of oxide particles at the end of the wear track.

Figure 8(c) shows the wear track of the CO-coated and laser-patterned ID substrate, and as observed previously for the sample with the highest structural depth (Fig. 6(c)), most of the surrounding CO-coating was removed. Abrasive wear occurring in the center of the wear track, where the contact pressure was highest, induced a pronounced groove in sliding direction, stretching over the wear track's entire length. Apart from the groove, the line pattern in the contact area is still intact. The carbon map in Fig. 8(d) reveals a complete absence of carbon in the groove. Outside the groove, carbon is detected in the topographical minima of the pattern in the same locations as the dark areas in Fig. 8(c). The lack of lubricious carbon nanoparticles results in oxidation, as depicted in the oxygen map (Fig. 8(d)). Mild oxidation occurs along the groove, comparable to that of the HD pattern (Fig. 6(d)). The comparable wear behavior of the CO-coated samples with high and intermediate structural depth is in strong agreement with their final COF values, which are also close to identical.

Figure 8(e) shows the CNT-coated wear track of the ID sample. Despite the considerable sliding duration, large areas of the wear track remain CNT-covered, which is confirmed by the carbon map (Fig. 8(f)). Furthermore, a pristine laser pattern is recognizable underneath the coating in Fig. 8(e). At the same time, no oxidation has occurred according to the oxygen map (Fig. 8(f)).

3.3.3 *LD pattern*

Following the previous uncoated samples' wear behavior, the sample's wear track with the lowest structural depth shown in Fig. 9(a) is severely worn out, with abrasion and adhesion being the dominant wear mechanisms. Once again, the oxygen map in (Fig. 9(b)) confirms strong oxidation. Despite varying fluences and, therefore, different structural depths, all the uncoated wear tracks' wear and oxidation behavior is very similar, which stands in good agreement with their respective friction behavior.

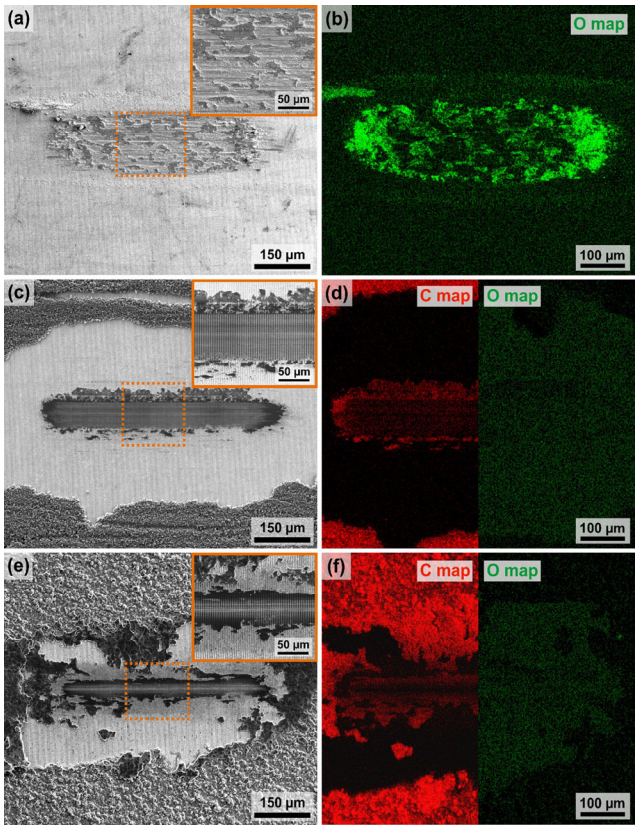

Fig. 9 SEM images of (a) uncoated, (c) CO-coated, and (e) CNT-coated wear tracks on the low depth patterns after friction testing, with their corresponding EDS maps of carbon and oxygen (b, d, f).

Figure 9(c) shows the CO-coated wear track of the surface, which was laser-processed at the lowest fluence, resulting in the lowest depth. In contrast to CNT, the removal of CO coatings directly surrounding the wear track seems to be characteristic and is attributed to a weak coating-substrate adhesion. As a result of large agglomerates' formation, COs are removed in large flakes upon contact with the counter body. Nevertheless, the dark vertical lines within the wear track depicted in Fig. 9(c), represent homogeneously filled structures in a near-pristine surface pattern. EDS mapping (Fig. 9(d)) confirms carbon in the structures, while no oxidation was detected (Fig. 9(d)). Overall, the average pattern on CO-coated surfaces with shallow structural depth is well sustained. In contrast to deeper patterns, no significant abrasion is observed. Fittingly, tribological testing performed on the shallowest CO-coated patterns shows the lowest COF.

As observed in the previous wear tracks of CNT-coated samples, the wear track on the shallowest surface pattern in Fig. 9(e) also shows large dark areas of compressed carbon nanoparticles around the wear track. The fact that parts of the surrounding CNT-coating are compressed implies direct contact with the counter body. This translates to an increased load distribution on the surface, thus reducing the load on the wear track. Moreover, the elastic restitution inherent to CNT particles exerts a counter pressure on the alumina ball, therefore, further relieving load from the wear track. Generally, the coating surrounding the CO-coated wear tracks is largely removed, which might contribute to the superior lubrication properties of CNT coatings compared to CO coatings.

The laser pattern on the LD surface depicted in Fig. 9(e) is mainly intact with particle filled structures. The elemental map in Fig. 9(f) confirms the carbon in said structures. This concludes that small amounts of CNT are sufficient to lubricate the contact and ensure a low COF effectively. No significant oxidation has occurred despite the diminished carbon content in the wear track's centerline (Fig. 9(f)). Also, no oxidation was detected for the ID and HD patterns, even though the COF was about 0.30, while the threshold of effective lubrication is 0.20. This can be explained by individual particles dragged from the reservoirs and/or extensive coating residuals on the wear tracks, thereby effectively preventing direct contact between the substrate surface and counter body and, thus, oxidation. After tribological testing, the wear tracks on the HD and ID structures are still largely covered by coherent patches of CNT-coating (Figs. 6 and 8(e)), with the corresponding patterns fully intact, suggesting a significantly longer lubrication lifetime. As previously mentioned, the CNT-coated LD patterns show the lowest COF values during friction testing despite completely lacking said patches, which cover the underlying pattern. The improved lubricity could be due to a direct supply of individual particles or small agglomerates from the reservoirs, which possess a relatively high degree of mobility and flexibility opposed to stationary coherent patches on top of the pattern. Irrespective of structural depth, all CNT-coated line patterns are well preserved after 10,000 testing cycles with little to no signs of degradation.

3.4 Microstructural characterization

We used TEM to investigate the impact of DLIP processing with laser pulses in the picosecond range on the underlying microstructure of AISI 304 stainless steel. Figures 10(a)–10(c) show cross-sections of the near-surface microstructure of the uncoated reference samples. Independent of structural depth, no significant differences can be observed between the original microstructure of the lower regions and the superficial microstructure. This illustrates that with the parameters used, the microstructure remains unaffected by picosecond DLIP processing at the displayed scale. However, microstructural changes may still occur on a smaller scale not visible in the existing TEM images.

Bieda et al. [46] simulated the thermal effect of picosecond DLIP on stainless steel (iron), among other metals, based on the two-temperature model. The resulting data reveal that thermal absorption depth (also referred to as thermal diffusion length) exceeded 250 nm at 425 ps. A reduced pulse duration to 35 ps significantly reduced thermal absorption depth to roughly 80 nm. A duration of 10 ps is the threshold to the ultrashort pulse regime below which the interaction is dominated by cold ablation. Based on Bieda's calculations, the thermal absorption depth further decreases to 45 nm at the pulse duration of 12 ps used in this study, as the ablative characteristics become increasingly non-thermal. Moreover, Artyukov et al. [47] conducted a study on electron/lattice

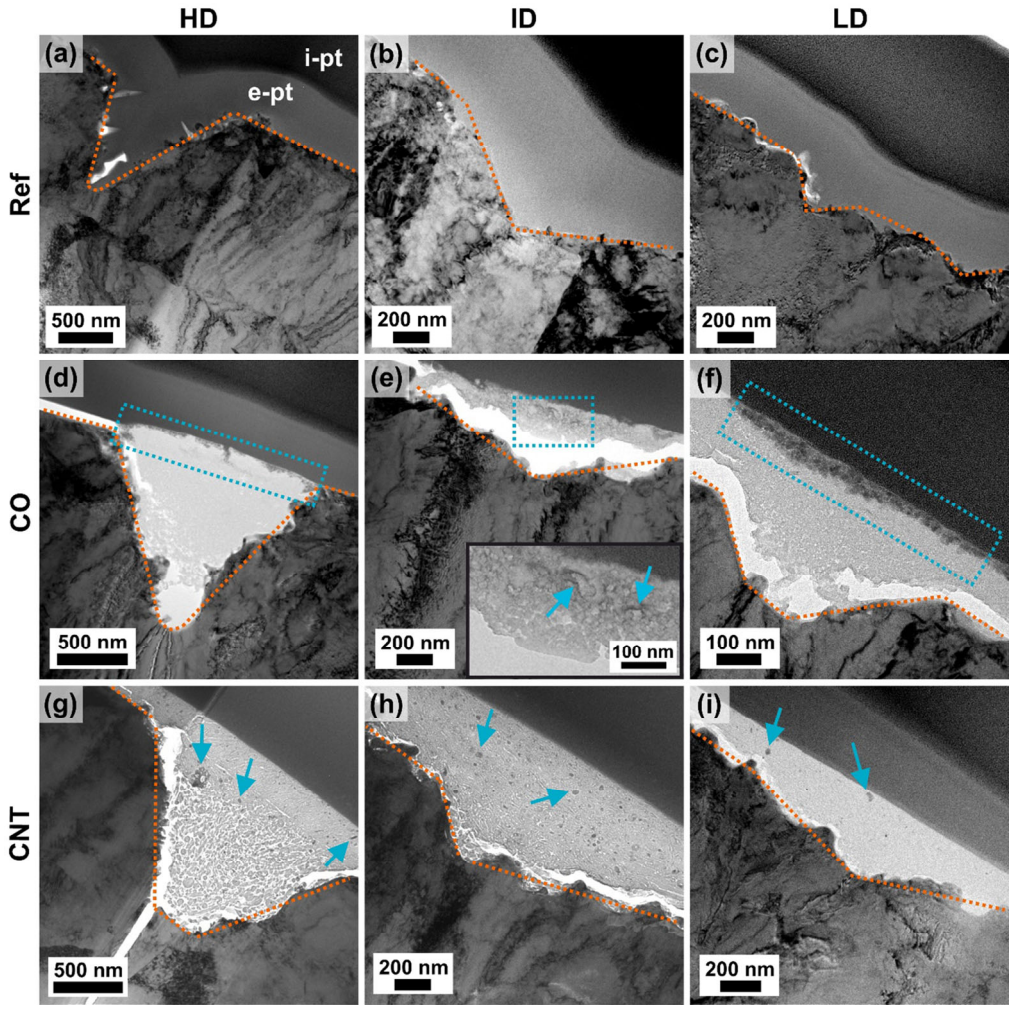

Fig. 10 Near-surface cross-sectional TEM images of (a–c) uncoated reference, (d–f) CO- and (g–i) CNT-coated structures with different structural depths. Both CO- and CNT-coated surfaces have been exposed to 10,000 cycles of tribological testing. The dotted orange lines draw the course of the surface. The blue arrows and blue dotted areas mark the areas where wear particles accumulate in the CO and CNT tribofilm, respectively.

relaxation phenomena of iron exposed to sub- and picosecond laser pulses (0.3–3.6 ps). Particularly at higher pulse durations, the obtained data suggest that ultrafast evaporative cooling is the dominant surface process following ablation, suggesting a low thermal impact on the underlying microstructure. Considering the results of both studies, it is viable to assume that thermally affected areas remain small and highly localized at the edges of the grooves. Thus, a large-scale alteration of the microstructure remains absent. REF was not exposed to friction testing and no microstructural changes can be observed

TEM was further used to examine whether the applied tribological load affects the underlying microstructure of the CO- (Figs. 10(d)–10(f)) and CNT-coated (Figs. 10(g)–10(i)) surfaces as well as to image the formed tribofilm. In both cases, microstructural damage such as deformation remains completely absent, regardless of structural depth and, thus, topography. As illustrated in Figs. 10(g), the CNTs at the bottom of the pattern's recession remain relatively pristine. However, continuous mechanical degradation of the CNTs close to the contact area induces the formation of a carbonaceous tribofilm that contains a significant share of at least partially amorphized CNTs, along with wear particles. Regarding the CO-coating, no structural changes can be observed at this scale. The coating types differ in the way they store resulting wear particles. As marked by the dotted blue lines in Figs. 10(d) and 10(f), wear particles seem to accumulate preferably directly at the tribofilm/Pt interface in CO-derived tribofilms. In CNT-derived tribofilms (Figs. 10(g)–10(i)) by contrast, wear particles are distributed randomly (marked by blue arrows).

Further, Fig. 11 suggests the formation of covalent bonds between CNTs and the substrate surface (marked by the orange circle), which mechanically anchor the particles to the surface, effectively keeping them in contact and, thus, increasing overall lubricity. The bond formation seems to occur at a local peak where the contact pressure is significantly increased by which a corresponding bonding reaction is made possible.

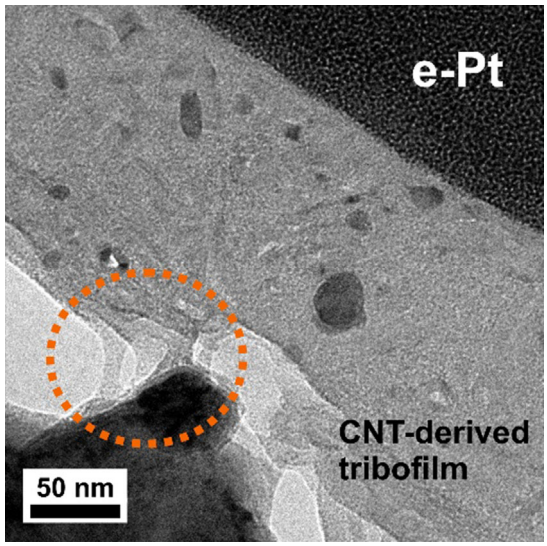

Fig. 11 Cross-sectional transmission electron micrograph of the CNT/substrate (LD) interface after friction testing.

4 Conclusions

We present a comprehensive study on the influence of the structural depth of line patterns on AISI 304 stainless steel coated with either carbon nanotubes (CNTs) or carbon onions (COs), on their solid lubricity.

Coating the surfaces with CNTs or COs always leads to a significant coefficient of friction (COF) reduction compared to their uncoated equivalent or the non-patterned reference, achieving a COF reduction factor between 2 and 4. During the studied contact scenario at low humidity and otherwise ambient conditions, CNTs exhibit superior lubricity compared to COs. Regarding the influence of the structural depth, a trend emerges from the results of the tribological experiments: the shallower the structure, the lower the COF of the respectively coated surface. Despite slightly different surface topographies and experimental conditions, the obtained results are in good agreement with those of a closely related work by Schäfer et al. [22]. The observed phenomenon could be attributed to the facilitation of particle supply from the reservoirs into the contact as slope steepness decreases. This allows for an adequate amount of lubricant in the contact areas leading to a lower COF. There is a distinction between the influence of structural depth and the steepness of the flanks. However, in this work, the structural depth of the pattern and flank steepness are inherently connected due to the material removal mechanism caused by laser pulses in the picosecond range. Wear track analysis after tribological testing has shown that the line patterns in CNT-coated wear tracks were largely preserved without

any surface oxidation being detected. In contrast, the intermediate and deep CO-coated structures exhibit significant wear along with mild surface oxidation as shown by energy-dispersive X-ray spectroscopy (EDS) mapping, which is fittingly reflected by their COF development. A possible explanation for the superior friction and wear-reducing properties of CNTs is the high aspect ratio, which enables the particles to be dragged directly into the contact region more easily. In addition, cross-sectional transmission electron microscopy (TEM) characterization has shown the underlying microstructure of the AISI 304 substrate to remain unaltered by both picosecond direct laser interference patterning (DLIP) processing and the applied tribological load.

The results obtained in this study demonstrate the importance of optimizing the surface design to maximize the lubrication performance of CNT/CO-coated and laser-patterned stainless-steel surfaces.

Acknowledgements

T. MacLucas and S. Suarez wish to kindly acknowledge financial support by the Deutsche Forschungsgemeinschaft (DFG, German Research Foundation) within the project MU 959/47-1. Furthermore, the authors gratefully acknowledge funding in the ZuMat project, supported by the State of Saarland from the European Regional Development Fund (Europäischer Fonds für Regionale Entwicklung, EFRE). P. Grützmacher and C. Gachot would like to thank the Government of Lower Austria (WST3) for financially supporting the endowed professorship tribology at the TU Wien. V. Presser thanks Eduard Arzt (INM) for his continuing support.

Open Access This article is licensed under a Creative Commons Attribution 4.0 International License, which permits use, sharing, adaptation, distribution and reproduction in any medium or format, as long as you give appropriate credit to the original author(s) and the source, provide a link to the Creative Commons licence, and indicate if changes were made.

The images or other third party material in this article are included in the article's Creative Commons licence, unless indicated otherwise in a credit line to the material. If material is not included in the article's Creative Commons licence and your intended use is not permitted by statutory regulation or exceeds the permitted use, you will need to obtain permission directly from the copyright holder.

To view a copy of this licence, visit http://creativecommons.org/licenses/by/4.0/.

References

[1] Rosenkranz A, Reinert L, Gachot C, Mücklich F. Alignment and wear debris effects between laser-patterned steel surfaces under dry sliding conditions. *Wear* **318**(1–2): 49–61 (2014)

[2] Gachot C, Rosenkranz A, Reinert L, Ramos-Moore E, Souza N, Müser M H, Mücklich F. Dry friction between laser-patterned surfaces: Role of alignment, structural wavelength and surface chemistry. *Tribol Lett* **49**: 193–202 (2013)

[3] Rosenkranz A, Heib T, Gachot C, Mücklich F. Oil film lifetime and wear particle analysis of laser-patterned stainless steel surfaces. *Wear* **334–335**: 1–12 (2015)

[4] Etsion I. State of the art in laser surface texturing. *J Tribol* **127**: 248–253 (2005)

[5] Chilamakuri S K, Bhushan B. Optimization of asperities for laser-textured magnetic disk surfaces. *Tribol Trans* **40**(2): 303–311 (1997)

[6] Song Y, Premachandran Nair R, Zou M, Wang Y A. Adhesion and friction properties of micro/nano-engineered superhydrophobic/hydrophobic surfaces. *Thin Solid Films* **518**(14): 3801–3807 (2010)

[7] Mücklich F, Lasagni A, Daniel C. Laser interference metallurgy—Periodic surface patterning and formation of intermetallics. *Intermetallics* **13**(3–4): 437–442 (2005)

[8] Mücklich F, Lasagni A, Daniel C. Laser interference metallurgy—Using interference as a tool for micro/nano structuring. *Int J Mater Res* **97**(10): 1337–1344 (2006)

[9] Scharf TW, Prasad S V. Solid lubricants: A review. *J Mater Sci* **48**: 511–531 (2013)

[10] Rosenkranz A, Grützmacher P G, Espinoza R, Fuenzalida V M, Blanco E, Escalona N, Gracia F J, Villarroel R, Guo L C, Kang R Y, Mucklich F, Suarez S, Zhang Z Y. Multi-layer $Ti_3C_2T_x$-nanoparticles (MXenes) as solid lubricants—Role of surface terminations and intercalated water. *Appl Surf Sci* **494**: 13–21 (2019)

[11] Reinert L, Suárez S, Rosenkranz A. Tribo-mechanisms of carbon nanotubes: Friction and wear behavior of CNT-reinforced nickel matrix composites and CNT-coated bulk nickel. *Lubricants* **4**(2): 11 (2016)

[12] Reinert L, Green I, Gimmler S, Lechthaler B, Mücklich F, Suàrez S. Tribological behavior of self-lubricating carbon nanoparticle reinforced metal matrix composites. *Wear* **408–409**: 72–85 (2018)

[13] Scharf T W, Neira A, Hwang J Y, Tiley J, Banerjee R. Self-lubricating carbon nanotube reinforced nickel matrix composites. *J Appl Phys* **106**: 013508 (2009)

[14] Kim K T, Cha S, Hong S H. Hardness and wear resistance of carbon nanotube reinforced Cu matrix nanocomposites. *Mater Sci Eng A* **449–451**: 46–50 (2007)

[15] Suárez S, Rosenkranz A, Gachot C, Mücklich F. Enhanced tribological properties of MWCNT/Ni bulk composites—Influence of processing on friction and wear behaviour. *Carbon* **66**: 164–171 (2014)

[16] Tan J, Yu T, Xu B, Yao Q. Microstructure and wear resistance of nickel-carbon nanotube composite coating from brush plating technique. *Tribol Lett* **21**: 107–111 (2006)

[17] Guiderdoni C, Estournès C, Peigney A, Weibel A, Turq V, Laurent C. The preparation of double-walled carbon nanotube/Cu composites by spark plasma sintering, and their hardness and friction properties. *Carbon* **49**: 4535–4543 (2011)

[18] Reinert L, Varenberg M, Mücklich F, Suárez S. Dry friction and wear of self-lubricating carbon-nanotube-containing surfaces. *Wear* **406–407**: 33–42 (2018)

[19] Thomas B J C, Boccaccini A R, Shaffer M S P. Multi-walled carbon nanotube coatings using electrophoretic deposition (EPD). *J Am Ceram Soc* **88**(4): 980–982 (2005)

[20] MacLucas T, Suarez S. On the solid lubricity of electrophoretically deposited carbon nanohorn coatings. *Lubricants* **7**(8): 62 (2019)

[21] Xu J, Chen X, Grützmacher P, Rosenkranz A, Li J, Jin J, Zhang C H, Luo J B. Tribochemical behaviors of onion-like carbon films as high-performance solid lubricants with variable interfacial nanostructures. *ACS Appl Mater Interfaces* **11**: 25535–25546 (2019)

[22] Schäfer C, Reinert L, MacLucas T, Grützmacher P, Merz R, Mücklich F, Suarez S. Influence of surface design on the solid lubricity of carbon nanotubes-coated steel surfaces. *Tribol Lett* **66**: 89 (2018)

[23] Reinert L, Lasserre F, Gachot C, Grützmacher P, MacLucas T, Souza N, Mucklich F, Suarez S. Long-lasting solid lubrication by CNT-coated patterned surfaces. *Sci Rep* **7**: 42873 (2017)

[24] MacLucas T, Schütz S, Suarez S, Mücklich F. Surface protection of austenitic steels by carbon nanotube coatings. *Surf Topogr Metrol Prop* **6**: 014005 (2018)

[25] Reinert L, Schütz S, Suárez S, Mücklich F. Influence of surface roughness on the lubrication effect of carbon nanoparticle-coated steel surfaces. *Tribol Lett* **66**: 45 (2018)

[26] Hirata A, Igarashi M, Kaito T. Study on solid lubricant properties of carbon onions produced by heat treatment of diamond clusters or particles. *Tribol Int* **37**(11–12): 899–905 (2004)

[27] Hirata A, Yoshioka N. Sliding friction properties of carbon nanotube coatings deposited by microwave plasma chemical vapor deposition. *Tribol Int* **37**(11–12): 893–898 (2004)

[28] Dickrell P L, Pal S K, Bourne G R, Muratore C, Voevodin A A, Ajayan P M, Schadler L S, Sawyer W G. Tunable friction behavior of oriented carbon nanotube films. *Tribol Lett* **24**: 85–90 (2006)

[29] Miyoshi K, Street K W, Vander Wal R L, Andrews R, Sayir A. Solid lubrication by multi-walled carbon nanotubes in air and in vacuum. *Tribol Lett* **19**: 191–201 (2005)

[30] Zhang R, Ning Z, Zhang Y, Zheng Q, Chen Q, Xie H, Zhang Q, Qian W Z, Wei F. Superlubricity in centimetres-long double-walled carbon nanotubes under ambient conditions. *Nat Nanotechnol* **8**: 912–916 (2013)

[31] Berman D, Narayanan B, Cherukara M J, Sankaranarayanan S K R S, Erdemir A, Zinovev A, Sumant A V. Operando tribochemical formation of onion-like-carbon leads to macroscale superlubricity. *Nat Commun* **9**: 1164 (2018)

[32] Berman D, Deshmukh S A, Sankaranarayanan S K R S, Erdemir A, Sumant A V. Macroscale superlubricity enabled by graphene nanoscroll formation. *Science* **348**(6239): 1118–1122 (2015)

[33] Gong Z, Bai C, Qiang L, Gao K, Zhang J, Zhang B. Onion-like carbon films endow macro-scale superlubricity. *Diam Relat Mater* **87**: 172–176 (2018)

[34] Yu M F, Lourie O, Dyer M J, Moloni K, Kelly T F, Ruoff R S. Strength and breaking mechanism of multi-walled carbon nanotubes under tensile load. *Science* **287**(5453): 637–640 (2000)

[35] Wong E W, Sheehan P E, Lieber C M. Nanobeam mechanics: Elasticity, strength, and toughness of nanorods and nanotubes. *Science* **277**(5334): 1971–1975 (1997)

[36] Salvetat J P, Bonard J M, Thomson N B, Kulik A J, Forró L, Benoit W, Zuppiroli L. Mechanical properties of carbon nanotubes. *Appl Phys A* **69**: 255–260 (1999)

[37] Meyers M A, Mishra A, Benson D J. Mechanical properties of nanocrystalline materials. *Prog Mater Sci* **51**(4): 427–556 (2006)

[38] Rosenkranz A, Costa H L, Baykara M Z, Martini A. Synergetic effects of surface texturing and solid lubricants to tailor friction and wear—A review. *Tribol Int* **155**: 106792 (2021)

[39] Thomas B J C, Shaffer M S P, Freeman S, Koopman M, Chawla K K, Boccaccini A R. Electrophoretic deposition of carbon nanotubes on metallic surfaces. *Key Eng Mater* **314**: 141–146 (2006)

[40] Boccaccini A R, Cho J, Roether J A, Thomas B J C, Jane Minay E, Shaffer M S P. Electrophoretic deposition of carbon nanotubes. *Carbon* **44**(15): 3149–3160 (2006)

[41] Wu Z S, Pei S, Ren W, Tang D, Gao L, Liu B, Li F, Liu C, Chen H M. Field emission of single-layer graphene films prepared by electrophoretic deposition. *Adv Mater* **21**(17): 1756–1760 (2009)

[42] Zeiger M, Jäckel N, Aslan M, Weingarth D, Presser V. Understanding structure and porosity of nanodiamond-derived carbon onions. *Carbon* **84**: 584–598 (2015)

[43] Ayache J, Beaunier L, Boumendil J, Ehret G, Laub D. *Sample preparation handbook for transmission electron microscopy: Techniques*. Springer Science & Business Media, 2010.

[44] Blau P J. On the nature of running-in. *Tribol Int* **38**(11–12): 1007–1012 (2005)

[45] Aouadi S M, Gao H, Martini A, Scharf T W, Muratore C. Lubricious oxide coatings for extreme temperature applications: A review. *Surf Coat Technol* **257**: 266–277 (2014)

[46] Bieda M, Siebold M, Lasagni A F. Fabrication of sub-micron surface structures on copper, stainless steel and titanium using picosecond laser interference patterning. *Appl Surf Sci* **387**: 175–182 (2016)

[47] Artyukov I A, Zayarniy D A, Ionin A A, Kudryashov S I, Makarov S V, Saltuganov P N. Relaxation phenomena in electronic and lattice subsystems on iron surface during its ablation by ultrashort laser pulses. *JETP Lett* **99**: 51–55 (2014)

Timothy MACLUCAS. He received his bachelor's degree in materials and process engineering in 2014 from Zurich University of Applied Sciences. In 2016, he obtained a joint master's degree in advanced materials science and engineering from Saarland University and Luleå University of Technology. Currently, he is working as a doctoral researcher at the Chair of Functional Materials at Saarland University. His research fields include electrophoretic deposition of carbon nanoparticles and tribological properties of carbon nanoparticle coatings on surface-structured metals.

Carsten GACHOT. He received his Ph.D. from the Saarland University in Germany in 2012 where he studied the effects of laser interference patterning on the microstructure and topography of metallic surfaces with a focus on tribological applications under Prof. Frank Mücklich and Prof. Martin H. Müser. For this work, he was awarded by the European Honda initiation grant in 2011. Prof. Gachot was academic visitor at the tribology group at Imperial College London and is currently the head of the tribology research group at Vienna University of Technology. Additionally, he is a visiting professor at Pontifical Catholic University in Santiago de Chile and chief editor of the peer reviewed journal *Industrial Lubrication and Tribology* of the Emerald Publishing Group Leeds UK.

III. Degradation analysis of tribologically loaded carbon nanotubes and carbon onions

T. MacLucas[1], P. Grützmacher[2], S. Husmann[3,4], J. Schmauch[5], S. Keskin[3], S. Suarez[1], V. Presser[3,4,6], C. Gachot[2,*] and F. Mücklich[1]

[1] *Chair of Functional Materials, Saarland University, Campus D3.3, Saarbrücken 66123, Germany*

[2] *Institute for Engineering Design and Product Development, TU Wien, Lehárgasse 6, 1060 Vienna, Austria*

[3] *INM – Leibniz Institute for New Materials, 66123 Saarbrücken, Germany*

[4] *Department of Materials Science & Engineering, Saarland University, Campus D2.2, 66123 Saarbrücken, Germany*

[5] *Department of Experimental Physics, Campus D2.2, Saarland University, 66123 Saarbrücken, Germany*

[6] *Saarene – Saarland Center for Energy Materials and Sustainability, Campus C4.2, 66123 Saarbrücken, Germany*

Published in **"npj Materials Degradation"** (2023) (IF: 5.1 [2022])

Accessible online at: https://doi.org/10.1038/s41529-023-00346-5

Own contribution: Conceptualization, sample preparation, tribometry, characterization, data analysis, figures, tables, writing – original draft

ARTICLE OPEN

Check for updates

Degradation analysis of tribologically loaded carbon nanotubes and carbon onions

T. MacLucas[1]✉, P. Grützmacher[2], S. Husmann[3,4], J. Schmauch[5], S. Keskin[3], S. Suarez[1], V. Presser[3,4,6], C. Gachot[2]✉ and F. Mücklich[1]

Coating laser-patterned stainless-steel surfaces with carbon nanotubes (CNT) or carbon onions (CO) forms a tribological system that provides effective solid lubrication. Lubricant retention represents the fundamental mechanism of this system, as storing the particles inside the pattern prevents lubricant depletion in the contact area. In previous works, we used direct laser interference patterning to create line patterns with three different structural depths on AISI 304 stainless-steel platelets. Electrophoretic deposition subsequently coated the patterned surfaces with either CNTs or COs. Ball-on-disc friction tests were conducted to study the effect of structural depth on the solid lubricity of as-described surfaces. The results demonstrated that the shallower the textures, the lower the coefficient of friction, regardless of the applied particle type. This follow-up study examines the carbon nanoparticles' structural degradation after friction testing on substrates patterned with different structural depths (0.24, 0.36, and 0.77 µm). Raman characterization shows severe degradation of both particle types and is used to classify their degradation state within Ferrari's three-stage amorphization model. It was further shown that improving CNT lubricity translates into increasing particle defectivity. This is confirmed by electron microscopy, which shows decreasing crystalline domains. Compared to CNTs, CO-derived tribofilms show even more substantial structural degradation.

npj Materials Degradation (2023)7:31 ; https://doi.org/10.1038/s41529-023-00346-5

INTRODUCTION

Global efforts to move away from fossil resources kindle the need for oil-free forms of lubrication. Solid lubricants represent an exciting alternative as they offer higher thermal stability, functionality under vacuum, applicability under higher loads, and avoid issues related to containment. A material group that is particularly interesting in this regard and has attracted significant interest from the tribology community are carbon nanoparticles, more specifically, multiwalled carbon nanotubes (CNT) and carbon onions (CO). Due to their respectively cylindrical and spherical shape, it is assumed that these particles can roll when subjected to shear, thus acting like a microscale roller bearing, but in effect, the lubrication mechanism remains speculative. The lubricity of these particles, however, is well documented in the literature regardless of their use as a coating[1–9], additive[10–13], or composite phase[14–21]. To better understand their respective lubrication mechanisms, the CNTs' and COs' structural degradation during tribological loading requires more in-depth research.

The standard technique for assessing the structural condition of crystalline and amorphous carbon is Raman spectroscopy. The interpretation of experimental Raman spectra of CNTs and COs is derived primarily from studies on graphite, graphene, and single-walled carbon nanotubes[22–30]. Morphological differences between these particles (curvature, multilayered structure) affect the polarizability of the carbon bonds and can alter the resulting spectra[28]. Reinert et al. examined the structural deterioration of CNTs in CNT/nickel composites[21]. Conformal contact friction tests were conducted on a ring-on-block tribometer against an SAE 1045 steel ring at a load of 20 N. As contact pressure increased, more particle defects were observed, and presented a four-stage model describing the degradation from highly crystalline to nanocrystalline carbon.

In a previous study, we performed friction tests with CNT and CO coatings on laser-patterned stainless-steel surfaces[9]. Direct laser interference patterning (DLIP) was used to create superficial line patterns with a periodicity of 3.5 µm. During DLIP, two or more high-power laser pulses are brought to interfere directly on the substrate surface to create well-defined patterns[31]. The resulting substrate surfaces were then coated by electrophoretic deposition (EPD), a coating technique during which a voltage is applied to conductive substrates immersed in a suspension, causing the dispersed carbon nanoparticles to migrate to the electrode of opposite charge. In the following, the findings of that work are briefly summarized for better understanding. As illustrated in Fig. 1, linear reciprocal ball-on-disc testing was conducted on line-patterned (periodicity = 3.5 µm) stainless-steel substrates with three different structural depths (high-, intermediate-, and low depth, HD, ID, and LD, respectively). The lubricity of the CNT-coated and CO-coated samples was compared to uncoated equivalents at a load of 100 mN. A correlation was identified between lubricity and structural depth, which varied between 0.78 µm (HD), 0.37 µm (ID), and 0.22 µm (LD). The results show that CNT and CO coatings lubricate more efficiently as the structural depth decreases. Patterned but uncoated samples (HD, ID, and LD) exhibit slightly lower COFs than the nonpatterned and uncoated reference[9]. Coating the pattern reduced the COF values considerably over the entire testing period, regardless of particle type. The key finding, however, was the emergence of a trend displayed by the COF development of both CNT- and CO-coated substrates: the lower the structural depth of the pattern, the lower its COF. Although deeper structures retain lubricant particles

[1]Chair of Functional Materials, Saarland University, Campus D3.3, Saarbrücken 66123, Germany. [2]Institute for Engineering Design and Product Development, TU Wien, Lehárgasse 6, 1060 Vienna, Austria. [3]INM – Leibniz Institute for New Materials, 66123 Saarbrücken, Germany. [4]Department of Materials Science & Engineering, Saarland University, Campus D2.2, 66123 Saarbrücken, Germany. [5]Department of Experimental Physics, Campus D2.2, Saarland University, 66123 Saarbrücken, Germany. [6]saarene – Saarland Center for Energy Materials and Sustainability, Campus C4.2, 66123 Saarbrücken, Germany. ✉email: timothy.maclucas@uni-saarland.de; Carsten.gachot@tuwien.at

better, their lubricity is less effective since the direct particle supply to the contact is hampered by higher slope angles.

This study represents a follow-up to our previous work, and we investigate the degradation process of the CNTs and COs as an integral part of the resulting tribofilms during friction testing. For that purpose, Raman spectroscopy and electron microscopy were used to analyze the nanocarbons' structural condition.

RESULTS AND DISCUSSION

Raman analysis

In the pristine material, the characteristic Raman features of CNTs include the D-, G-, D′-, and G′-band (Fig. 2)[22,23]. At a laser wavelength of 532 nm, the D-band is located at 1350 cm^{-1} and corresponds to the breathing mode of A_{1g} symmetry. In perfect (highly oriented pyrolytic) graphite (HOPG), this mode is forbidden[32] and becomes active in the presence of defects such as grain boundaries or vacancies, among others[23,29,33]. The (G+D′)-band is a convolution of the G- and D′-bands and is among the most pronounced bands in the Raman spectra of CNTs and/or COs. The G-band appears at 1582 cm^{-1} and is associated with the E_{2g} phonon. In pristine CNTs, the (G+D′)-band exhibits a distinct shoulder toward higher wavenumbers. This can be attributed to defect-induced double resonance, which gives rise to the D′-band between 1617 cm^{-1} and 1625 cm^{-1}. Like the D-band, the D′-band is activated by crystalline defects[24]. The dispersive G′-band (or 2D-band) is located around 2700 cm^{-1} at an excitation wavelength of 532 nm and originates from electron-hole intervalley scattering[34]. It represents an overtone of the D-band and indicates long-range order; hence, it disappears with increasing degradation and/or amorphization[30,35].

Quantifying intensity, position, and full width at half maximum (FWHM) of the Raman bands require suitable fittings. The G-band originates from first-order scattering and is, thus, related to one oscillator only (one phonon process)[34]. Therefore, the G-band is best approximated by a Lorentzian, which is used to describe phonon behavior within the Lorentz oscillator model and thus provides a precise physical meaning. In the case of the D-, D′- and G′-band, which descend from double-resonance Raman scattering corresponding to a convolution of a large number of oscillators (Lorentzian), a single Voigtian is used for approximation. Voigtian peaks are not the preferred choice as they lack the physical background; however, they are suitable for describing a convolution of Lorentzian peaks and providing a proper fitting.

Figure 3a–d depicts the Raman spectra of pristine CNTs and CNTs after tribological testing on the laser-patterned surfaces. Based on the spectral features described previously, a set of indicators can be derived, described in more detail in the following section. In conjunction with the three-stage amorphization model of graphite by Ferrari and Robertson[23], these indicators allow for evaluating the particles' degradation state. We use this framework to assess the defectivity of the CNTs in their respective wear track. The data used for this analysis are listed in Table 1.

The D/G-band ratio (also referred to as the defect index) indicates a measure of crystalline disorder[29]. Previous studies considered the normalized intensity ratio (I_D/I_G) or the integrated area ratio (A_D/A_G). As certain defects do not affect intensity but lead to a broadening of the band and vice versa[23], we consider both. Figure 3e shows their development as a function of structural depth. Our pristine CNTs exhibit low defectivity with values of 0.57 (I_D/I_G) and 0.70 (A_D/A_G). After friction testing on the coated HD surface, the D-band has grown significantly in intensity; hence the defect index has increased to 1.35 (I_D/I_G) and 1.68 (A_D/A_G). This can be attributed to different degradation processes, such as decreasing crystallite size, breaking covalent bonds, and deformation resulting from the mechanical stress occurring in the contact[23,27,29]. The defect indices continue to

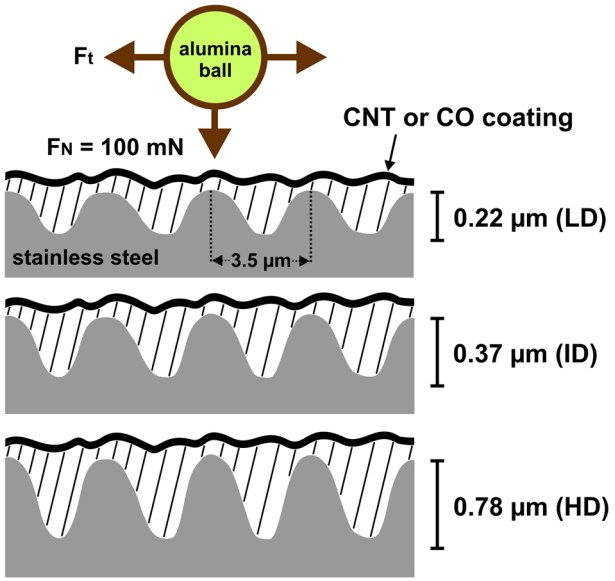

Fig. 1 Cross-section scheme of line-patterned steel substrates with varying structural depths. It illustrates the friction testing conducted on these surfaces coated with either CNTs or COs as conducted by MacLucas et al.[9].

increase for the worn CNTs on ID with an I_D/I_G of 1.39 and an A_D/A_G of 1.83 before reaching a maximum on LD with 1.41 (I_D/I_G) and 2.01 (A_D/A_G). These values agree with those obtained by Cançado et al. for defective graphene[24].

A similar development can be observed for the single fit position of the G-band (X_G), which shifts upward as a function of increasing graphitic disorder (Fig. 3e). However, this is less of a shift but more accurately a modification of the band shape owing to the growing D′-band[21,23]. As a result of the frictional stress the particles are exposed to, X_G shifts from 1582.2 cm^{-1} (pristine) to 1587.1 cm^{-1} (HD), 1589.6 cm^{-1} (ID), and 1589.0 cm^{-1} (LD).

Simultaneously, the development of the purity ratio $I_{G'}/I_D$ (also normalized as proposed by DiLeo et al. [36]), and its areal equivalent $A_{G'}/A_D$, show an equally clear (decreasing) trend (Fig. 2f), indicating a strong correlation. This can be explained by incorporating non-carbon impurities, for example, oxygen, into the particles' crystalline structure as they become increasingly defective. While pristine CNTs maintain high purity (1.30 $I_{G'}/I_D$ and 1.73 $A_{G'}/A_D$), it drops steeply following exposure to tribological load. On HD, the particles show a purity of 0.27 ($I_{G'}/I_D$) and 0.33 ($A_{G'}/A_D$), which reduces continuously as structural depth decreases, reaching a minimum of 0.16 ($I_{G'}/I_D$), respectively, 0.18 ($A_{G'}/A_D$) on LD. Moreover, Ferreira et al. have shown $A_{G'}/A_G$ to be a reliable indicator in graphene and HOPG as it decreases considerably with increasing defectivity[30]. Pristine CNT exhibits an $A_{G'}/A_G$ of 1.20 compared to 0.56 on HD after being subjected to tribological load. This is followed by a gradual decrease to a value of 0.42 on ID and, finally, the minimum value of 0.36 on LD (Fig. 3f).

Generally, the FWHM of the G-band (W_G) is used to measure crystallinity or structural disorder. However, Ferreira and coworkers have shown that band broadening due to increasing defectivity is not limited to the G-band. Accordingly, W_D and $W_{G'}$ are included in this analysis[30]. The FWHM of W_D and $W_{G'}$ show an identical development: the respective FWHM values continuously increase from pristine to HD and ID and then show a jump to a maximum on LD (Fig. 3g). In contrast, W_G remains at roughly the same level except for LD, where a substantial increase occurs. A previously observed pattern repeats itself: exposure to friction

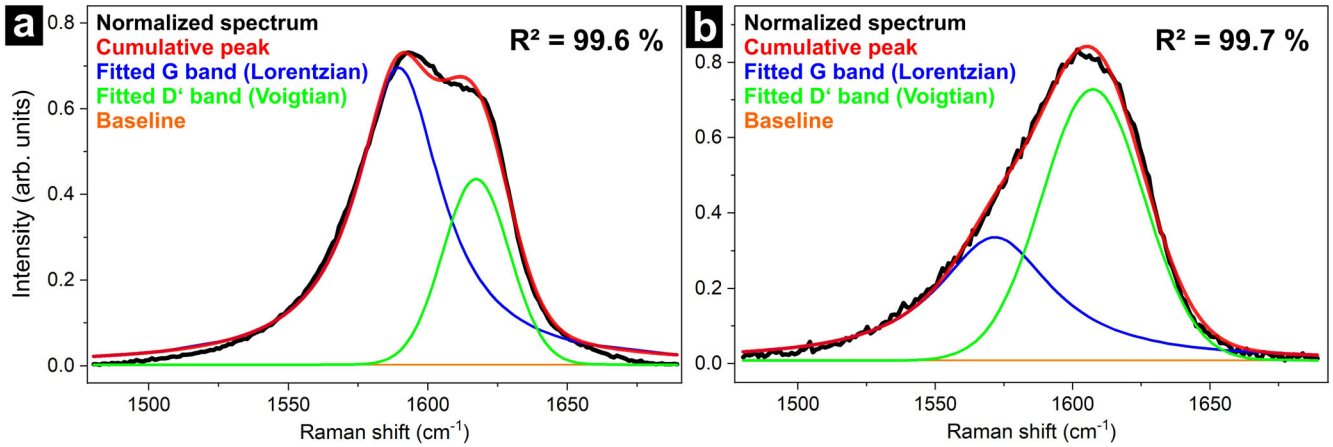

Fig. 2 Two-peak fit of the (G+D')-Raman band. Exemplary two-peak fits of the (G+D')-band in the Raman spectrum of **a** CNTs and **b** COs. A Lorentzian peak shape is used to fit the G-band, and a Voigtian peak profile is used to fit the D'-band.

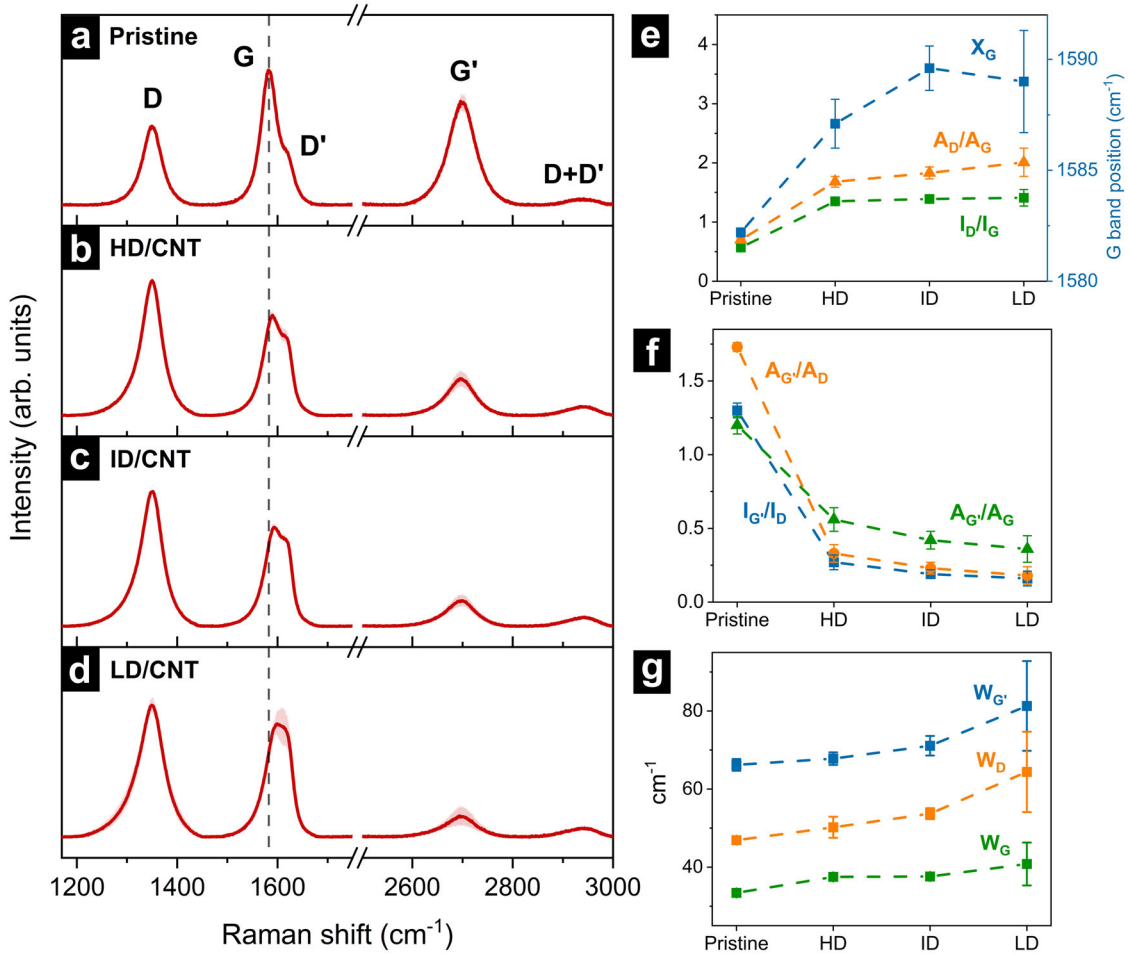

Fig. 3 Raman spectra and indicator developments of CNTs in pristine condition and after tribological testing. Raman spectra of **a** pristine CNTs and CNTs after tribological testing on **b** HD, **c** ID, and **d** LD surfaces, including standard deviation of spectral intensities (red area). Development of **e** I_D/I_G, A_D/A_G, X_G **f** $I_{G'}/I_D$, $A_{G'}/A_D$, $A_{G'}/A_G$ and **g** W_D, W_G, $W_{G'}$ with increasing structural depth (error bars represent standard deviation from three independent measurements).

causes the FWHM values and the CNT's defectivity to rise. This disorder further increases as a function of surface pattern depth.

Within Ferrari and Robertson's three-stage amorphization model, CNTs are classified as stage 1 due to the upshift of the G-band position X_G from 1582.2 cm^{-1} (pristine) to 1589.0 cm^{-1} (LD), indicating a transformation from graphitic to nanocrystalline graphitic carbon (Fig. 4). This is corroborated by the I_D/I_G development with values rising continuously from 0.57 (pristine)

Table 1. Overview of the Raman indicators derived from the spectral features of the respective particles.

	I_D/I_G (-)	A_D/A_G	$I_{G'}/I_D$	$A_{G'}/A_D$	$A_{G'}/A_G$	W_D (cm^{-1})	W_G	$W_{G'}$	X_G
CNT									
Pristine	0.57 ± 0.01	0.70 ± 0.02	1.30 ± 0.05	1.73 ± 0.03	1.20 ± 0.06	46.9 ± 0.4	33.4 ± 0.2	66.2 ± 1.5	1582.2 ± 0.2
HD	1.35 ± 0.05	1.68 ± 0.09	0.27 ± 0.05	0.33 ± 0.06	0.56 ± 0.08	50.2 ± 2.7	37.5 ± 0.8	67.8 ± 1.6	1587.1 ± 1.1
ID	1.39 ± 0.03	1.83 ± 0.10	0.19 ± 0.03	0.23 ± 0.04	0.42 ± 0.06	53.7 ± 1.4	37.6 ± 1.0	71.1 ± 2.5	1589.6 ± 1.0
LD	1.41 ± 0.14	2.01 ± 0.24	0.16 ± 0.05	0.18 ± 0.06	0.36 ± 0.09	64.4 ± 10.3	40.8 ± 5.5	81.3 ± 11.5	1589.0 ± 2.3
CO									
Pristine	1.50 ± 0.27	1.87 ± 0.26	0.57 ± 0.03	0.65 ± 0.04	1.21 ± 0.16	57.0 ± 1.3	41.7 ± 2.5	69.7 ± 1.4	1576.7 ± 0.8
HD	3.83 ± 1.22	4.80 ± 1.38	0.11 ± 0.03	0.17 ± 0.05	0.76 ± 0.23	78.0 ± 5.1	56.2 ± 4.7	124.6 ± 44.1	1569.0 ± 8.9
ID	2.06 ± 0.62	2.91 ± 0.76	0.15 ± 0.12	0.22 ± 0.14	0.58 ± 0.22	87.1 ± 12.4	54.2 ± 5.4	228.3 ± 176.2	1577.0 ± 7.6
LD	2.69 ± 1.30	3.56 ± 1.50	0.09 ± 0.04	0.15 ± 0.10	0.47 ± 0.20	83.2 ± 10.2	55.2 ± 11.4	172.4 ± 134.7	1577.8 ± 11.9

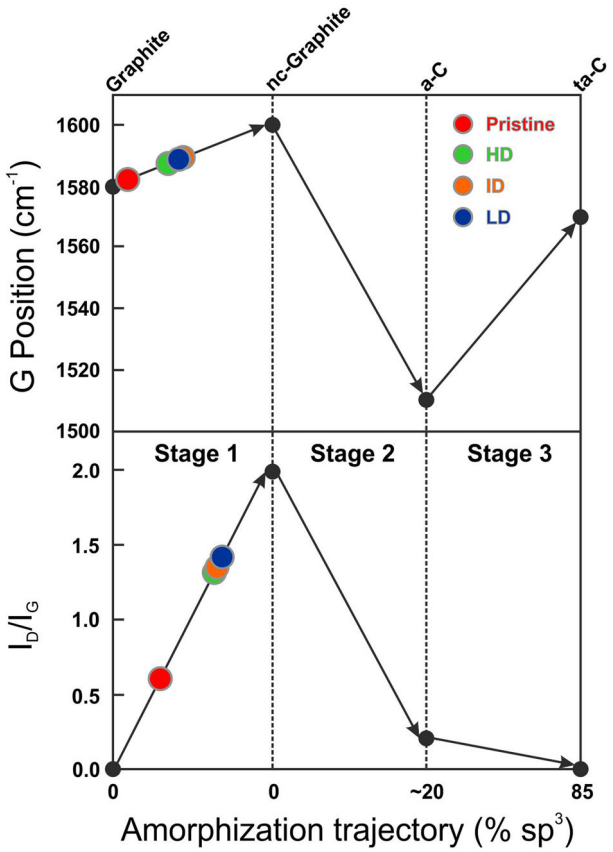

Fig. 4 Carbon amorphization trajectory according to Ferrari and Robertson, including data of the characterized CNTs (adapted from ref. [23]). It shows a schematic variation of the G-band position and I_D/I_G (obtained with 514 nm) depending on crystallinity as well as sp^2/sp^3 content of the particles.

to 1.41 (LD). However, the condition of the particles on the different surfaces shows finer nuances:

- For HD, although the G- and D′-bands overlap to a large degree, the D′-band shoulder is visible (Fig. 3b) and significantly higher compared to that of the pristine material. As the (D+D′)-band is present, the CNTs on this surface are classified as stage 1 (d), which describes an advanced stage of the transformation from mono- to polycrystalline graphite.
- The Raman spectrum of ID closely resembles HD, except that the D′-band shoulder has moved up slightly. Despite all indicators showing higher defectivity, lower purity, and a stronger upshift of X_G, the CNTs on ID are still classified as stage 1 (d). However, particles on this surface have progressed further on their trajectory toward nanocrystalline graphite compared to those on HD.
- For LD, the distinct shoulder has entirely vanished due to the strong growth of the D′-band. Regarding its shape, the convoluted (G+D′)-band can now be considered uniform, which classifies the degradation state of the CNT on LD as stage 1 (e)[28]. In addition, eight out of nine indicators show the CNTs on LD to be the most defective, with X_G very close to that of the CNTs on ID.

The Raman spectrum of the carbon onions shows the same characteristic bands as the CNTs (Fig. 5a–d). However, the bands' positions may vary slightly due to the more substantial curvature impacting bond polarizability and, thus, the Raman scattering process. The G-band, for example, is shifted slightly downward (1580 cm^{-1}) compared to CNT/graphite (1582 cm^{-1}). In contrast to the CNTs, tribo-induced oxidation does occur during friction testing on CO-coated surfaces, giving rise to an additional broad band around 670 cm^{-1}, a convolution of vibrational modes associated with FeO, Fe_2O_3, and Fe_3O_4[37]. This can be explained by the fact that, unlike COs, CNTs can form coherent patches on top of the patterns, which effectively separate the sliding surfaces and, thus, prevent oxidation[38].

Except for X_G, all indicators show pristine COs to be of superior structural quality and purity than any of the loaded particles (Fig. 5e–g). Further, six out of nine indicators show HD to be more defective than ID. More specifically, the defect and the purity ratios, $A_{G'}/A_G$ and W_G, attribute a higher defectivity to the particles on HD, whereas X_G, W_D, and $W_{G'}$ are higher for those on ID. However, due to their often large standard deviations and associated overlapping, it is difficult to consider the particles of one surface more defective than the other. Four out of nine indicators attribute the highest defectivity to the COs on LD. Concerning the remaining indicators of I_D/I_G, A_D/A_G, W_D, W_G, and $W_{G'}$, the COs on LD exhibit the second-highest defectivity. Therefore, the entirety of indicators suggests the COs on LD be the most defective overall.

In contrast to the CNTs, the COs indicator values for I_D/I_G and X_G do not fit the three-stage amorphization model after Ferrari and Robertson, which could be attributed to more substantial curvature. However, according to the model, the single peak shape of the G+D′-band observable on all surfaces suggests the particles have surpassed stage 1 (e) and reached stage 2. Thus, the transformation to nanocrystalline graphite is completed. The COs on LD seem to have progressed furthest toward stage 2 (a), representing the initial amorphization phase. Compared to the (G+D′)-band of the CNTs on LD, the CO-bands are notably sharper,

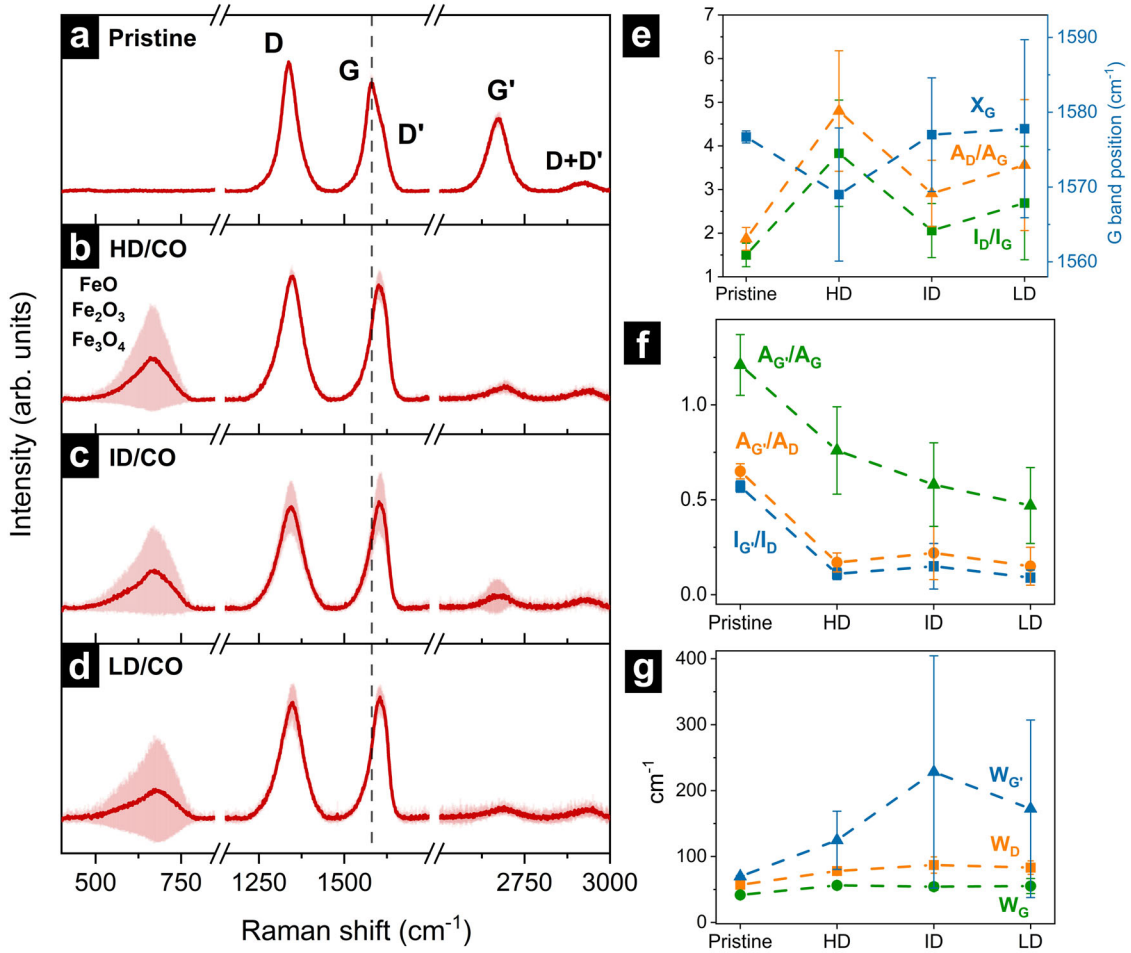

Fig. 5 Raman spectra and indicator developments of COs in pristine condition and after tribological testing. Raman spectra of **a** pristine COs and COs after tribological testing on **b** HD, **c** ID, and **d** LD surfaces, including standard deviation of spectral intensities (red area). Development of **e** I_D/I_G, A_D/A_G, X_G **f** $I_{G'}/I_D$, $A_{G'}/A_D$, $A_{G'}/A_G$ and **g** W_D, W_G, $W_{G'}$ with increasing structural depth (error bars represent standard deviation from three independent measurements).

likely to result from a more developed D′-band. Based on absolute indicator values, COs exhibit a stronger overall defectivity than CNTs. However, this type of comparison should be treated with caution as the curvature influences the Raman interaction of sp^2-hybridized carbon (curvature-induced defect scattering)[39]. COs are smaller than CNTs and three-dimensionally curved (0D carbon allotrope), implying a significantly stronger overall curvature. The results of this Raman analysis indicate that coated patterns with low structural depth lead to stronger degradation (along with superior lubricity, as shown in our previous work). This could be explained by the fact that low structural depths are generally associated with relatively flat slopes, which facilitate particle transfer from the depths of the grooves directly into the contact, where the particles are exposed to shear forces and, thus, deteriorate.

Electron microscopy characterization

Complementary to Raman analysis, cross-sectional transmission electron micrographs from the center of the wear tracks were prepared to study the nanocarbons' condition after friction testing.

On HD, the CNT-based tribofilm can be divided into three distinct areas representing different states of degradation (Fig. 6a). At the bottom of the groove, the CNTs remain in pristine condition with visible voids between the individual agglomerates (state 1). The area directly above can be identified as a transition zone where the CNTs' porosity begins to fade due to increasing tribological loading and interaction with the tribological interface (state 2). The top layer was in direct contact with the counter body and, thus, directly exposed to shear stress, causing a full compression of the tribofilm (state 3). In addition, this layer incorporates and stores the resulting wear particles. Both films on ID and LD largely correspond to state 3, which is plausible considering the shallowness of the reservoirs (Fig. 6b, c). However, at the substrate/film interface on ID and LD, the shape of individual CNT agglomerates can be identified, indicating state 2.

A gradual decrease in overall crystallinity from HD to LD can be observed when comparing higher magnification TEM images of the tribofilms' near-surface zones (Pt-coating/film interface). On HD (Fig. 6d), large CNT fragments (contoured in teal) are present, whereas, on ID (Fig. 6e), the fragments are fewer and substantially smaller and contain noncrystalline domains (marked in red), which is not the case on HD. The tribofilm on LD (Fig. 6f) contains few, if any, and small crystalline domains. With a value of 3.48 Å, the interlayer spacing of the CNT fragments on HD lies above the literature range of 3.38–3.41 Å; (depending on chirality). It gradually increases further with decreasing depth, reaching 3.84 Å on LD. Generally, there is a tendency for the interlayer spacing to increase as deformation and/or degradation progresses[40].

The TEM images show that the CO-derived tribofilms (Fig. 7a–f) contain considerably more wear particles than their CNT-derived

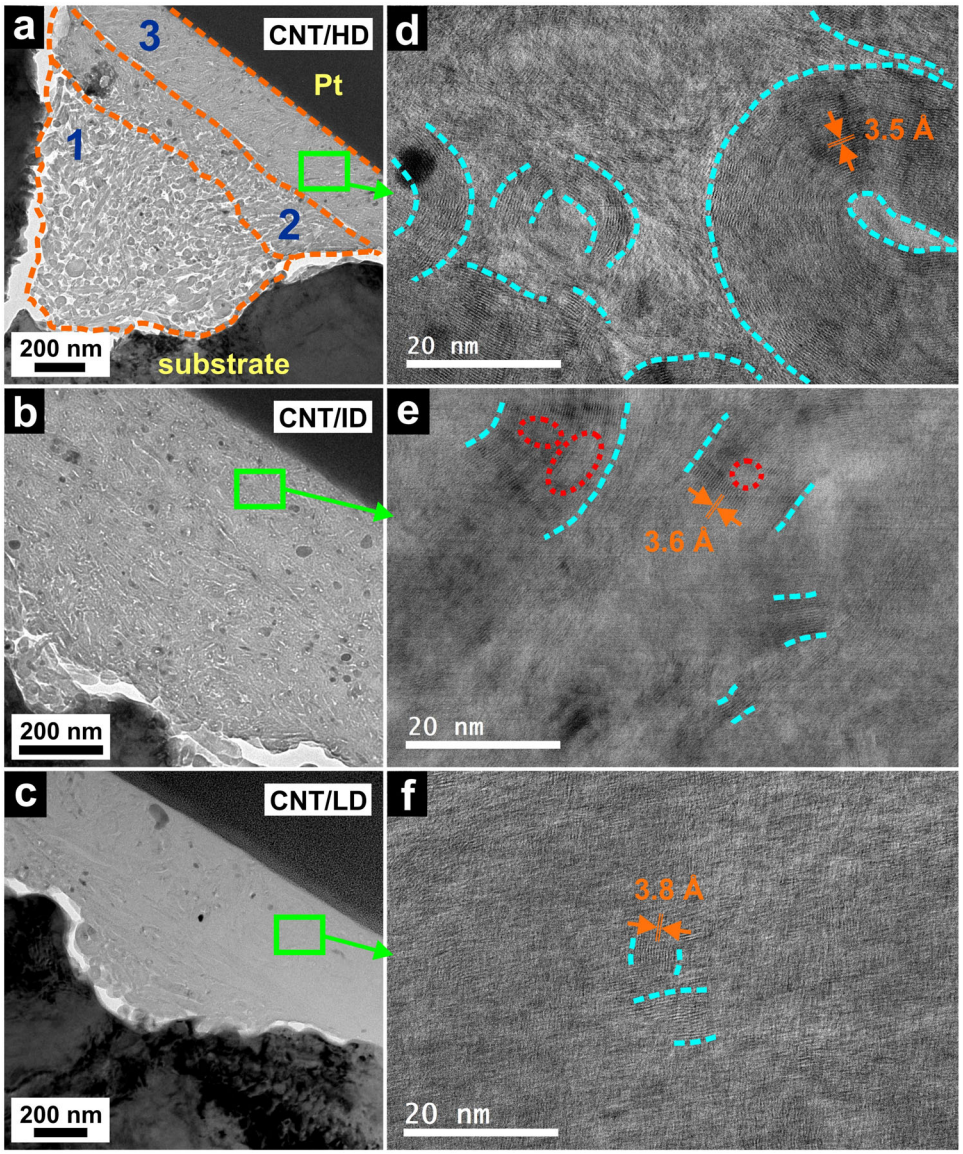

Fig. 6 Post friction test, cross-sectional TEM images of the CNT coatings. Representative images of the tribofilm at lower magnification on **a** HD, **b** ID, and **c** LD. Representative images of the tribofilm close to the interface at higher magnification on **d** HD, **e** ID, and **f** LD. Identifiable CNT fragments are contoured in teal. The red circles in (**e**) represent noncrystalline areas within the CNT fragments.

equivalents (Fig. 6a–f). Moreover, regardless of structural depth, none of the CO films show any signs of structural alteration at low magnification. However, transmission electron micrographs at higher magnification (Fig. 7d–f) show the tribofilms on HD (Fig. 7d) and LD (Fig. 7f) to contain few and small crystalline domains, similar to those on CNT/LD (Fig. 6f). The tribofilm on LD indicates stronger defectivity as the fragments are barely recognizable as such, whereas those on HD are larger. The spherical morphology of pristine COs[5,41] appears to have vanished entirely at the tribofilms' topmost surface, likely due to heavy degradation causing the original particles to break down into smaller fragments that continue to degrade further until crystallinity disappears entirely. Exactly that seems to have occurred on ID (Fig. 7e), where no crystalline structures are detected. Simultaneously, the tribofilm on ID exhibits the highest wear particle concentration, which might have been a possible accelerator for particle degradation during tribological testing compared to LD and HD.

Raman and electron microscopy characterization of the CO- and CNT-derived tribofilms concurrently indicate strong overall deterioration due to tribological testing, with COs being considerably more degraded. Several factors need to be considered to explain this outcome. In pristine conditions, COs are already more defective than the CNTs, as shown by Raman analysis. COs are also smaller and spherical (as opposed to cylindrical), which results in decreased mechanical (and chemical) stability as greater curvature is associated with stronger inherent strain[42]. In addition, contact pressures at the particle/counter body interface and between individual COs and/or agglomerates are increased during sliding as contact areas are smaller. It is also possible that some of the COs have remaining nanodiamond cores despite high-temperature annealing, which would cause additional inherent strain due to density differences between the graphitized shell and the sp^3 core[43]. In conclusion, COs have an increased tendency to degrade under tribological stress compared to CNTs.

According to the Raman indicators, the COs on LD are the most defective, followed by HD and ID. In contrast, TEM analysis suggests ID is the most defective, followed by LD and HD. TEM images and Raman data, thus, do not match relative particle defectivity for COs, and a trend, as observed with the CNTs, is not

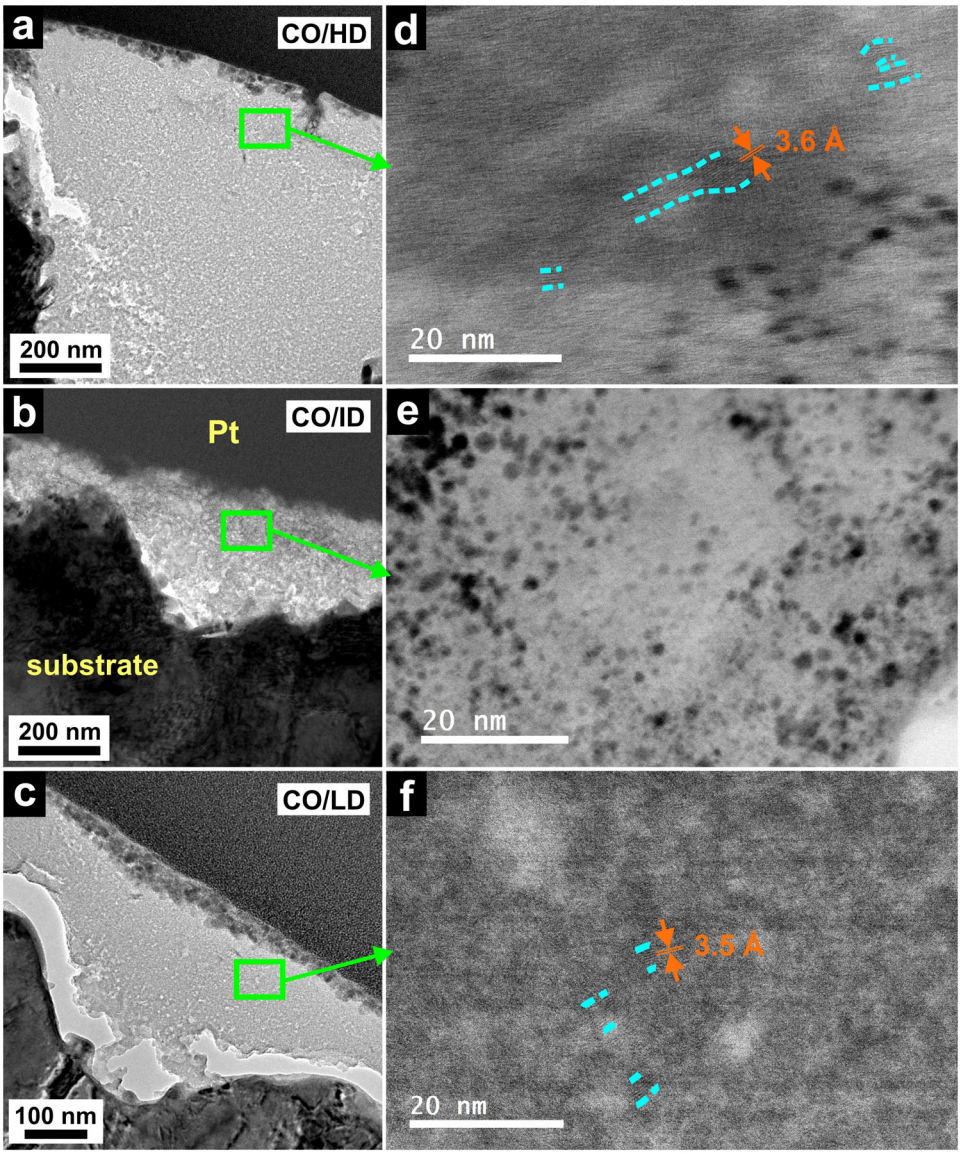

Fig. 7 Post friction test, cross-sectional TEM images of the CO coatings. Representative images of the tribofilm at lower magnification on **a** HD, **b** ID, and **c** LD. The gap between the substrate surface and tribofilm in (**c**) is a consequence of sample preparation. Representative images of the tribofilm close to the interface at higher magnification on **d** HD, **e** ID, and **f** LD. Identifiable crystalline fragments are contoured in teal.

discernible. However, directly comparing the results of both techniques is unsuitable due to the Raman signal's limited probing depth of the tribofilms; hence, both techniques should be viewed as complementary.

It was further shown that the COF of the CNTs (on all surfaces) and the COs on LD remain constant after running-in, although the particles become increasingly degraded. It has long been assumed that CNTs and COs behave similarly to a bearing in that they at least partially roll. Considering these results, rolling can be eliminated as the primary lubrication mechanism of CNTs and COs.

Summary of the results

This work provides an in-depth degradation analysis of CNT and CO coatings exposed to friction testing on laser-patterned AISI 304 stainless-steel surfaces with varying structural depths. The results demonstrate the occurrence of oxidation on all CO-coated wear tracks, regardless of structural depth, whereas none is detected in any of the CNT-coated wear tracks. This finding agrees well with the EDS results of our previous work. Furthermore, obtained Raman indicator values of the CNTs are in good agreement with Reinert et al. despite differing testing parameters such as contact situation, load, and relative humidity[21]. Regarding particle classification within Ferrari's three-stage amorphization model, the CNTs are classified between pristine and nanocrystalline graphite, whereas the COs have entered the transition stage from nanocrystalline graphite to hydrogenated amorphous carbon, although no amorphous carbon was detected. These findings are consistent with TEM. Raman analysis further reveals a direct correlation between pattern depth, lubricity, and CNT degradation. More specifically, as CNT lubricity improves with shallowing patterns, the particles become more defective. TEM also confirms this as it shows gradually shrinking crystalline domains with decreasing structural depth. Characterization of the CO-derived tribofilm shows even more substantial structural degradation than observed with CNTs. This can be explained by the COs' spherical geometry combined with their smaller size, as both factors

contribute to stronger curvature and, thus, higher σ-bond tension. As a result, COs are less resistant to mechanical degradation. Finally, by demonstrating sustained and constant lubricity despite continuous particle degradation, rolling can be rejected as a lubrication mechanism of CNTs and COs.

METHODS

Material

Commercially available multiwall CNTs with an outer diameter of 30–85 µm, a length of 10–15 µm, and >98% purity were purchased at Graphene Supermarket. The COs used were synthesized by annealing detonation nanodiamonds (NaBond Technologies Co.) in a vacuum furnace (1100-3580-W1, Thermal Technology Inc.) at a temperature of 1700 °C for 1 h at a rate of 10 °C min^{-1}[43,44]. The resulting particle diameter is 4–8 nm, with a purity of >98%. After thoroughly cleaning with isopropanol and acetone, mirror-polished AISI 304 austenitic stainless-steel platelets (20 × 20 mm^2, Brio Kontrollspiegel GmbH) were used as substrate material.

Pulsed direct laser interference patterning

A neodymium-doped yttrium aluminum garnet (Nd:YAG) pulsed laser (Edgewave PX-series InnoSlab) integrated into a laser system RDX 500 nano (Pulsar Photonics) was used to create three different line patterns with structural depths of 0.22, 0.37, and 0.78 µm on the substrate surface with a periodicity of 3.5 µm at a pulse duration of 12 ps. The patterning process is described in greater detail elsewhere[9].

Solution preparation and electrophoretic deposition

The deposition solution consisted of 80 ml of isopropanol, 10 ml of triethylamine (ACROS Organics, >99% purity), and 8 mg of carbon nanoparticle content. During the first step of dispersion, the solution was exposed to shear mixing using an Ultra-Turrax (T25 by IKA) for 10 min at 7000 rpm. The second step consisted of ultrasonication (Bandelin Sonorex RK514BH) for 10 min (CNT) and 45 min (CO). During the subsequent deposition, the patterned platelet and a nonpatterned but otherwise identical platelet used as a counter electrode were arranged in parallel and immersed in the solution. A DC voltage of 150 V was applied for the CNT-containing solution and 300 V for the CO-containing solution for 15 min.

Tribological testing

A ball-on-disc tribometer (CSM Instruments) was used in linear-reciprocating mode to investigate how the coefficient of friction (COF) evolves. Measurements were conducted at a normal load of 100 mN transversal to the line pattern at a stroke length of 0.6 mm and a velocity of 1 mm s^{-1}. Alumina balls (6 mm diameter, grade 28, Kugel Pompel HSI-Solutions GmbH) were chosen as a counter body. Further tribometrical specifications are described elsewhere[9].

Electron microscopy

Scanning electron microscopy (SEM) images of the wear tracks were prepared using a Helios NanoLab 600 dual beam workstation equipped with a focused ion beam (FIB; FEI) at an acceleration voltage of 5 kV and a current of 1.4 nA. Transmission electron microscopy (TEM) at low magnification was conducted with a JEOL JEM 2010F at an acceleration voltage of 200 kV, whereas for high magnification TEM, a JEOL JEM-ARM200F was used at 200 kV. TEM foils were taken from the center of the wear track and prepared using the abovementioned Helios workstation.

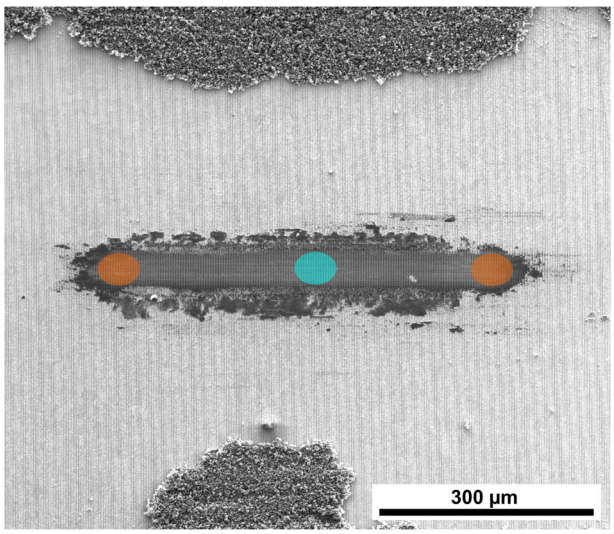

Fig. 8 Exemplary top view scanning electron micrograph of a CO-coated wear track (low depth laser pattern) post friction testing. This image marks the areas where the Raman measurements were conducted.

Raman spectroscopy

An inVia confocal Raman microscope (Renishaw) with a spectral resolution of 1.2 cm^{-1} was used to analyze the structural integrity of the remaining carbon nanoparticles in the resulting wear tracks after the tribological tests conducted in our previous work[9]. The spectra were acquired with an excitation wavelength of 532 nm, a laser power of 0.5% (corresponding to approximately 500 µW), a 50x-objective (numerical aperture: 0.9), and a grating of 2400 lines mm^{-1}. The spectrometer was calibrated using a single-crystal silicon sample. Measurements were conducted at three different spots in each wear track and outside (pristine). Inside the wear track, two measurements were taken in the center (Fig. 8, area marked in teal) and one at one of the edges (Fig. 8, area marked in orange). As for the pristine particles, measurements were taken on coating sections outside of the wear tracks. Automated processing of the gathered data included cosmic ray, background removal, and intensity normalization ([0,1]).

DATA AVAILABILITY

The data that support the findings of this study are available from the corresponding author upon reasonable request.

Received: 17 November 2022; Accepted: 20 March 2023;
Published online: 19 April 2023

REFERENCES

1. Schäfer, C. et al. Influence of surface design on the solid lubricity of carbon nanotubes-coated steel surfaces. *Tribol. Lett.* **66**, 89 (2018).
2. Reinert, L. et al. Long-lasting solid lubrication by CNT-coated patterned surfaces. *Sci. Rep.* **7**, 42873 (2017).
3. Maclucas, T., Schütz, S., Suarez, S. & Mücklich, F. Surface protection of austenitic steels by carbon nanotube coatings. *Surf. Topogr. Metrol. Prop.* **6**, 14005 (2018).
4. Reinert, L., Schütz, S., Suárez, S. & Mücklich, F. Influence of surface roughness on the lubrication effect of carbon nanoparticle-coated steel surfaces. *Tribol. Lett.* **66**, 45 (2018).
5. Hirata, A., Igarashi, M. & Kaito, T. Study on solid lubricant properties of carbon onions produced by heat treatment of diamond clusters or particles. *Tribol. Int.* **37**, 899–905 (2004).
6. Hirata, A. & Yoshioka, N. Sliding friction properties of carbon nanotube coatings deposited by microwave plasma chemical vapor deposition. *Tribol. Int.* **37**, 893–898 (2004).

7. Dickrell, P. L. et al. Tunable friction behavior of oriented carbon nanotube films. *Tribol. Lett.* **24**, 85–90 (2006).
8. Miyoshi, K., Street, K. W., Vander Wal, R. L., Andrews, R. & Sayir, A. Solid lubrication by multiwalled carbon nanotubes in air and in vacuum. *Tribol. Lett.* **19**, 191–201 (2005).
9. MacLucas, T. et al. Influence of structural depth of laser-patterned steel surfaces on the solid lubricity of carbon nanoparticle coatings. *Friction* **11**, 1276–1291 (2022).
10. Chen, C. S., Chen, X. H., Xu, L. S., Yang, Z. & Li, W. H. Modification of multiwalled carbon nanotubes with fatty acid and their tribological properties as lubricant additive. *Carbon* **43**, 1660–1666 (2005).
11. Peng, Y., Hu, Y. & Wang, H. Tribological behaviors of surfactant-functionalized carbon nanotubes as lubricant additive in water. *Tribol. Lett.* **25**, 247–253 (2007).
12. Lu, H. F. et al. Synthesis and lubricating performance of a carbon nanotube seeded miniemulsion. *Carbon* **45**, 936–942 (2007).
13. Kristiansen, K., Zeng, H., Wang, P. & Israelachvili, J. N. Microtribology of aqueous carbon nanotube dispersions. *Adv. Funct. Mater.* **21**, 4555–4564 (2011).
14. Reinert, L., Suárez, S. & Rosenkranz, A. Tribo-mechanisms of carbon nanotubes: friction and wear behavior of CNT-reinforced nickel matrix composites and CNT-coated bulk nickel. *Lubricants* **4**, 11 (2016).
15. Reinert, L. et al. Tribological behavior of self-lubricating carbon nanoparticle reinforced metal matrix composites. *Wear* **408–409**, 72–85 (2018).
16. Scharf, T. W., Neira, A., Hwang, J. Y., Tiley, J. & Banerjee, R. Self-lubricating carbon nanotube reinforced nickel matrix composites. *J. Appl. Phys.* **106**, 013508 (2009).
17. Kim, K. T., Cha, S. I. L. & Hong, S. H. Hardness and wear resistance of carbon nanotube reinforced Cu matrix nanocomposites. *Mater. Sci. Eng. A* **448–451**, 46–50 (2007).
18. Suárez, S., Rosenkranz, A., Gachot, C. & Mücklich, F. Enhanced tribological properties of MWCNT/Ni bulk composites: influence of processing on friction and wear behaviour. *Carbon* **66**, 164–171 (2014).
19. Tan, J., Yu, T., Xu, B. & Yao, Q. Microstructure and wear resistance of nickel-carbon nanotube composite coating from brush plating technique. *Tribol. Lett.* **21**, 107–111 (2006).
20. Guiderdoni, C. et al. The preparation of double-walled carbon nanotube/Cu composites by spark plasma sintering, and their hardness and friction properties. *Carbon* **49**, 4535–4543 (2011).
21. Reinert, L., Varenberg, M., Mücklich, F. & Suárez, S. Dry friction and wear of self-lubricating carbon-nanotube-containing surfaces. *Wear* **406–407**, 33–42 (2018).
22. Dresselhaus, M. S., Dresselhaus, G., Saito, R. & Jorio, A. Raman spectroscopy of carbon nanotubes. *Phys. Rep.* **409**, 47–99 (2005).
23. Ferrari, A. & Robertson, J. Interpretation of Raman spectra of disordered and amorphous carbon. *Phys. Rev. B Condens. Matter Mater. Phys.* **61**, 14095–14107 (2000).
24. Cançado, L. G. et al. Quantifying defects in graphene via Raman spectroscopy at different excitation energies. *Nano Lett.* **11**, 3190–3196 (2011).
25. Ferrari, A. C. & Robertson, J. Resonant Raman spectroscopy of disordered, amorphous, and diamondlike carbon. *Phys. Rev. B Condens. Matter Mater. Phys.* **64**, 075414 (2001).
26. Brown, S. D. M., Dresselhaus, M. S., Jorio, A. & Dresselhaus, G. Observations of the D-band feature in the Raman spectra of carbon nanotubes. *Phys. Rev. B Condens. Matter Mater. Phys.* **64**, 073403 (2001).
27. Pimenta, M. A. et al. Studying disorder in graphite-based systems by Raman spectroscopy. *Phys. Chem. Chem. Phys.* **9**, 1276–1291 (2007).
28. Ferrari, A. C. & Basko, D. M. Raman spectroscopy as a versatile tool for studying the properties of graphene. *Nat. Nanotechnol.* **8**, 235–246 (2013).
29. Tuinstra, F. & Koenig, J. L. Raman spectrum of graphite. *J. Chem. Phys.* **53**, 1126–1130 (1970).
30. Martins Ferreira, E. H. et al. Evolution of the Raman spectra from single-, few-, and many-layer graphene with increasing disorder. *Phys. Rev. B Condens. Matter Mater. Phys.* **82**, 125429 (2010).
31. Lasagni, A. F. et al. Direct laser interference patterning, 20 years of development: from the basics to industrial applications. *SPIE Proc.* **10092**, 1009211 (2017).
32. Hiura, H., Ebbesen, T. W., Tanigaki, K. & Takahashi, H. Raman studies of carbon nanotubes. *Chem. Phys. Lett.* **202**, 509–512 (1993).
33. Thomsen, C. & Reich, S. Double resonant Raman scattering in graphite. *Phys. Rev. Lett.* **85**, 5214–5217 (2000).
34. Gontijo, R. N., Resende, G. C., Fantini, C. & Carvalho, B. R. Double resonance Raman scattering process in 2D materials. *J. Mater. Res.* **34**, 1976–1992 (2019).
35. Lehman, J. H., Terrones, M., Mansfield, E., Hurst, K. E. & Meunier, V. Evaluating the characteristics of multiwall carbon nanotubes. *Carbon* **49**, 2581–2602 (2011).
36. DiLeo, R. A., Landi, B. J. & Raffaelle, R. P. Purity assessment of multiwalled carbon nanotubes by Raman spectroscopy. *J. Appl. Phys.* **101**, 064307 (2007).
37. Oh, S. J., Cook, D. C. & Townsend, H. E. Characterization of iron oxides commonly formed as corrosion products on steel. *Hyperfine Interact.* **112**, 59–66 (1998).
38. MacLucas, T., Leonhard-Trautmann, P., Suarez, S. & Mücklich, F. Long-term lubricity of carbon nanoparticle coatings on periodically laser-patterned metallic surfaces. *Tribol. Lett.* **70**, 123 (2022).
39. Podila, R., Rao, R., Tsuchikawa, R., Ishigami, M. & Rao, A. M. Raman spectroscopy of folded and scrolled graphene. *ACS Nano* **6**, 5784–5790 (2012).
40. Liu, M. & Cowley, J. M. Structures of carbon nanotubes studied by HRTEM and nanodiffraction. *Ultramicroscopy* **53**, 333–342 (1994).
41. He, C. N., Shi, C. S., Du, X. W., Li, J. J. & Zhao, N. Q. TEM investigation on the initial stage growth of carbon onions synthesized by CVD. *J. Alloy. Compd.* **452**, 258–262 (2008).
42. Haddon, R. C. Chemistry of the fullerenes: the manifestation of strain in a class of continuous aromatic molecules. *Science* **261**, 1545–1550 (1993).
43. Zeiger, M., Jäckel, N., Mochalin, V. & Presser, V. Review: carbon onions for electrochemical energy storage. *J. Mater. Chem. A* **4**, 3172–3196 (2015).
44. Zeiger, M., Jäckel, N., Aslan, M., Weingarth, D. & Presser, V. Understanding structure and porosity of nanodiamond-derived carbon onions. *Carbon* **84**, 584–598 (2015).

ACKNOWLEDGEMENTS

T.M. and S.S. wish to gratefully acknowledge financial support from the Deutsche Forschungsgemeinschaft (DFG, German Research Foundation) and Saarland University within the 'Open Access Publication Funding' program and project MU 959/47-1. Further funding by the ZuMat project, supported by the State of Saarland from the European Regional Development Fund (Europäischen Fonds für Regionale Entwicklung, EFRE), is kindly acknowledged. P.G. and C.G. would like to thank the Government of Lower Austria (WST3) for financially supporting the endowed professorship tribology at the TU Wien. The INM authors thank Eduard Arzt (INM) for his continuing support. Finally, the authors would like to express their gratitude to Prof. Marcos A. Pimenta (Federal University of Minas Gerais, BR) for his support with the Raman analysis.

AUTHOR CONTRIBUTIONS

T.M.: conceptualization, investigation, formal analysis, visualization, writing—original draft. P.G.: formal analysis, writing—review and editing. S.H.: formal analysis, writing—review and editing. J.S.: investigation. S.K.: methodology, S.S.: conceptualization, investigation, writing—review and editing. V.P.: resources, writing—review and editing. C.G.: supervision, formal analysis, writing—review and editing, funding acquisition. F.M.: supervision, resources, funding acquisition.

FUNDING

Open Access funding enabled and organized by Projekt DEAL.

COMPETING INTERESTS

The authors declare no competing interests.

ADDITIONAL INFORMATION

Correspondence and requests for materials should be addressed to T. MacLucas or C. Gachot.

Reprints and permission information is available at http://www.nature.com/reprints

Publisher's note Springer Nature remains neutral with regard to jurisdictional claims in published maps and institutional affiliations.

Open Access This article is licensed under a Creative Commons Attribution 4.0 International License, which permits use, sharing, adaptation, distribution and reproduction in any medium or format, as long as you give appropriate credit to the original author(s) and the source, provide a link to the Creative Commons license, and indicate if changes were made. The images or other third party material in this article are included in the article's Creative Commons license, unless indicated otherwise in a credit line to the material. If material is not included in the article's Creative Commons license and your intended use is not permitted by statutory regulation or exceeds the permitted use, you will need to obtain permission directly from the copyright holder. To view a copy of this license, visit http://creativecommons.org/licenses/by/4.0/.

© The Author(s) 2023

IV. Multiwall carbon nanotubes for solid lubrication of highly loaded contacts

Timothy MacLucas[1], Andreas Klemenz[2], Patrick Grünewald[3], Volker Presser[3,4,5], Leonhard Mayrhofer[2], Gianpietro Moras[2], Sebastian Suarez[1,4], Martin Dienwiebel[2,7], Frank Mücklich[1], and Michael Moseler[2,6,8,9,*]

[1] *Chair of Functional Materials, Saarland University, Campus D3.3, Saarbrücken 66123, Germany*

[2] *Fraunhofer Institute for Mechanics of Materials IWM, MicroTribology Center µTC, Woehlerstr. 11, 79108 Freiburg, Germany*

[3] *INM – Leibniz Institute for New Materials, 66123 Saarbrücken, Germany*

[4] *Department of Materials Science & Engineering, Saarland University, Campus D2.2, 66123 Saarbrücken, Germany*

[5] *Saarene – Saarland Center for Energy Materials and Sustainability, Saarbrücken, Germany*

[6] *Modelling of Functional Nanomaterials Group, Institute of Physics, University of Freiburg, Hermann-Herder-Str. 3, 79104 Freiburg, Germany*

[7] *Karlsruhe Institute of Technology (KIT), IAM - Institute for Applied Materials, MicroTribology Center µTC, Straße am Forum 7, 76131 Karlsruhe, Germany*

[8] *Freiburg Materials Research Center, University of Freiburg, Stefan-Meier-Str. 21, 79104 Freiburg, Germany*

[9] *Cluster of Excellence livMatS, Freiburg Center for Interactive Materials and Bioinspired Technologies, University of Freiburg, Georges-Köhler-Allee 105, 79110 Freiburg, Germany*

Published in **"ACS Applied Nano Materials"** (2023) (IF: 5.9 [2022])

Accessible online at: https://doi.org/10.1021/acsanm.2c04729

Own contribution: sample preparation, tribometry, characterization, writing – original draft, figures, tables, discussion

ACS APPLIED NANO MATERIALS

www.acsanm.org Article

Multiwall Carbon Nanotubes for Solid Lubrication of Highly Loaded Contacts

Timothy MacLucas,*,¶ Andreas Klemenz,¶ Patrick Grünewald, Volker Presser, Leonhard Mayrhofer, Gianpietro Moras, Sebastian Suarez, Martin Dienwiebel, Frank Mücklich, and Michael Moseler*

Cite This: *ACS Appl. Nano Mater.* 2023, 6, 1755−1769 Read Online

ACCESS | Metrics & More | Article Recommendations | Supporting Information

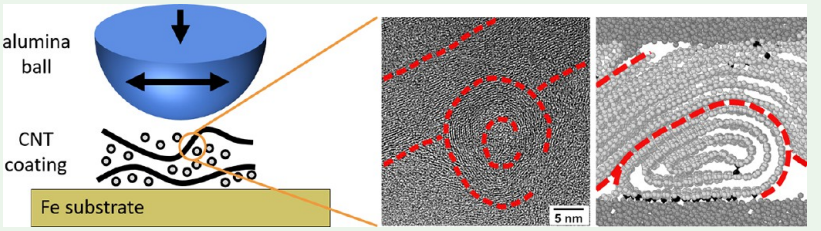

ABSTRACT: When lubrication of rolling bearings with oil or grease is not possible, for example because the lubricant evaporates in vacuum, solid lubrication by multiwall carbon nanotubes (MWCNT) is a viable alternative. To understand the mechanisms underlying MWCNT lubrication of highly loaded contacts, we combine an experimental approach with large-scale molecular dynamics (MD) simulations. Tribometry is performed on ground iron plates coated with two different types of MWCNTs by electrophoretic deposition. Although structural differences in the MWCNT materials result in slightly different running-in behavior, most of the tests converge to a steady-state coefficient of friction of 0.18. The resulting wear tracks and tribolayers are subjected to structural and chemical characterization and suggest a tribo-induced phase transformation resulting in tribolayers that consist of MWCNT fragments, iron oxide, and iron carbide nanoparticles embedded in an amorphous carbon matrix. Covalent bonding of the tribolayer to the iron surface and low carbon transfer to the alumina counter body indicate sliding at the tribolayer/ball interface as the dominant mechanism underlying MWCNT solid lubrication. MD simulations of nascent a-C tribofilms lubricated by MWCNT bundles and stacks of crossed MWCNTs reveal two different sliding regimes: a low-load regime that leaves the MWCNTs intact and a high-load regime with partial collapse of the tube structure and formation of a-C regions. The critical load for this transition increases with the filling ratio of the MWCNT and the packing density of the stacks. The former determines the stability of the MWCNT, while the latter controls the local stresses at the MWCNT crossings. For both MWCNT materials, the high-load regime is predicted for the experimental loads. This is confirmed by a remarkable agreement between transmission electron microscopy (TEM) and atomistic simulation images. Based on the findings of this work, a multistep lubrication mechanism is formulated for MWCNT coatings rubbing against alumina on an iron substrate.

KEYWORDS: *multiwall carbon nanotubes, solid lubrication, sliding tests, molecular dynamics, tribo-induced phase transition*

Downloaded via UNIV SAARLAND on February 7, 2024 at 14:03:02 (UTC).
See https://pubs.acs.org/sharingguidelines for options on how to legitimately share published articles.

INTRODUCTION

Highly loaded tribological contacts occur in many machine elements, such as roller bearings or gears. To ensure low friction and wear values, lubricants are needed to separate the interacting surfaces of the tribological contact from each other. In most cases, fluid-based media such as oils or greases are employed as lubricants. Solid lubricants as alternative lubrication media are used as soon as oils or greases fail (e.g., in a vacuum) or when they are undesirable (e.g., food industry).

Solid lubrication by carbon nanomaterials could result in reduced friction losses compared to traditional solid lubricants such as graphite, MoS_2, and poly(tetrafluoroethylene) (PTFE). The use of multiwall carbon nanotubes as an effective solid lubricant, especially when applied as a coating on metallic substrates, has been demonstrated in various studies.[1−6] To lubricate for extended periods, multiwall carbon nanotubes (MWCNT) coatings must be combined with a textured surface to avoid particle depletion in the contact.[1−3,7] Direct laser interference patterning (DLIP) and grinding have been used to produce suitable surface patterns with distinct topographical minima that serve as reservoirs for a continuous supply of MWCNTs to lubricate contacting asperities.[1,3,7] At the same time, these surface patterns are expected to capture

Received: October 29, 2022
Accepted: January 13, 2023
Published: January 26, 2023

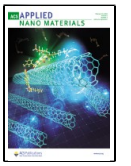

© 2023 The Authors. Published by American Chemical Society

and store newly formed wear particles, preventing the acceleration of the wear process.[8−10]

Despite experimental evidence of their lubricity, our knowledge about the basic lubrication mechanisms of MWCNT coatings has remained limited.[1−6] In some studies, rolling MWCNTs on graphite surfaces have been observed when the MWCNT axes are parallel to the graphite surfaces.[11,12] Based on these observations, it can be speculated whether MWCNTs may seemingly form a nanoscale roller bearing between two surfaces. In contrast, little or no rolling has been observed in atomistic simulations with diamond surfaces and amorphous carbon.[13,14] To date, no consensus has been reached on this issue, and the dominant mechanisms of lubrication by MWCNTs are not yet understood.

This study aims at understanding how the initial structure and structural evolution of MWCNTs determine the tribological behavior of MWCNT solid lubrication on a textured surface. To gain microscopic insight into the underlying lubrication processes, we use a combined approach of experimental friction testing, post-experimental characterization, and classical molecular dynamics (MD) simulations. On the experimental side, MWCNT coatings are prepared on P180-ground iron platelets using electrophoretic deposition (EPD). EPD is a solution-based coating technique established in recent years as a simple and cost-effective means to deposit homogeneous and uniform sp^2 carbon nanoparticle coatings on conductive substrates.[1−3,15−17] After tribological tests on the coated substrates, energy-dispersive X-ray spectroscopy (EDS), transmission electron microscopy (TEM), and Raman spectroscopy were conducted on the resulting wear tracks to investigate chemical changes on the surface, the interface between the tribolayer and the substrate, and the degradation of the MWCNTs.

The influence of contact pressure on the structural integrity and friction mechanism of MWCNTs in a sliding contact is further studied by molecular dynamics (MD) simulations using a reactive empirical bond-order potential.[18,19] We consider MWCNT bundles and stacks of crossed MWCNTs between two amorphous carbon surfaces under sliding conditions and maximum pressures of tens of GPa. Amorphous carbon is used as a model for an amorphous tribomaterial that often forms on metallic surfaces after a short running-in process. These atomistic simulations are performed to understand why severe structural degradation occurs under tribological load despite the high mechanical stability of MWCNTs. The structural characteristics of the resulting simulated carbon tribolayer are compared to corresponding experimental TEM images.

RESULTS AND DISCUSSION

Coating Characterization. Two types of commercially available MWCNTs (cheap tubes: CT; graphene supermarket tubes: GS) were purchased and deposited by EPD on P180-ground iron platelets. The structures of the resulting coatings are shown in Figure 1. Scanning electron micrographs of the CT coatings indicate the presence of a large number of agglomerates uniformly distributed on the ground iron surface (Figure 1a). Instead of a homogeneous deposition, a pronounced island formation is observed. The agglomerates scatter considerably in size, with the largest specimens reaching a maximum Feret diameter of about 15 μm. Due to the absence of a continuous coating, the topography of the underlying surface is visible. Conversely, the GS coatings form a thin layer (Figure 1b) with fewer and smaller agglomerates

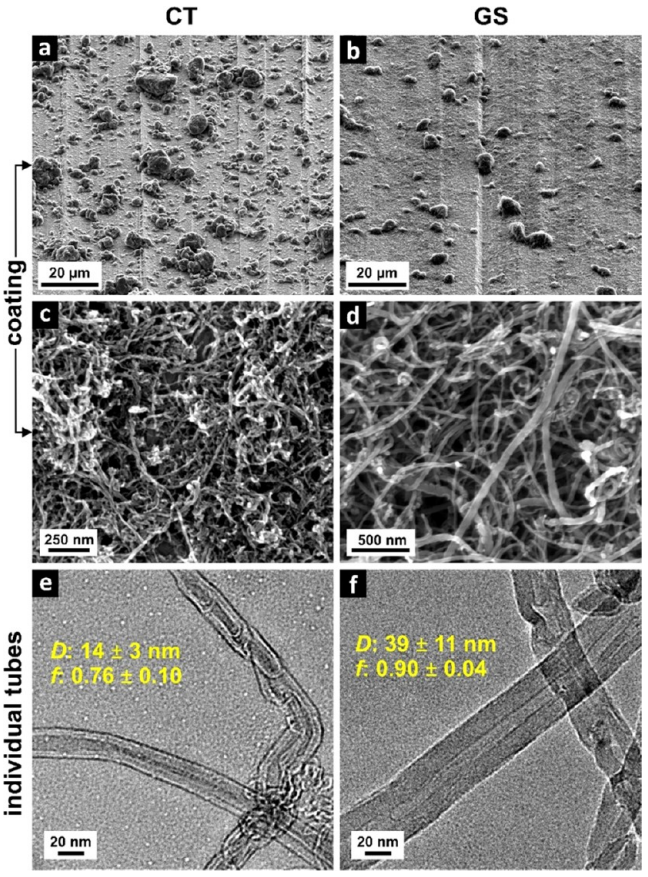

Figure 1. Structure of MWCNT coatings on ground iron surfaces. Tilted (52°) scanning electron micrographs of CT coating (a) and GS coating (b) and the corresponding top view images at higher magnification (c, d), respectively. Transmission electron micrographs of individual CT (e) and GS (f) MWCNTs, including their outer diameter D and filling ratios f.

(max. Feret diameter ranging between 5 and 10 μm) that uniformly covers the sharp edges of the ground substrate.

As shown by the top view micrographs in Figure 1c,d, GS have a significantly larger void volume and, thus larger intertube spacing. Transmission electron micrographs of both MWCNT species show distinct bamboo-like structures (Figure 1e,f). This is a feature often observed in CVD-synthesized MWCNTs.[20,21] With an outer diameter D of 39 ± 11 nm (inner diameter: 11 ± 2 nm), the GS are approximately 3 times thicker than the CTs (14 ± 3 nm; inner diameter: 7 ± 2), and both exhibit a polydisperse diameter distribution, as indicated by the manufacturers. The degree of filling of MWCNTs with inner walls is characterized by the filling ratio f. The thickness of each CNT wall is assumed to be 3.4 Å, which is the interlayer distance between two graphene layers in graphite. The filling ratio is then defined as the ratio between the cross-sectional area of all walls and the total cross-sectional area of the MWCNT $f = \frac{A_{walls}}{A_{total}} = \frac{(r_o + 1.7\ \text{Å})^2 - (r_i - 1.7\ \text{Å})^2}{(r_o + 1.7\ \text{Å})^2}$ with r_i and r_o the radii of the inner and outermost CNT walls, respectively. The CTs have a filling ratio of 0.76 ± 0.10. The CTs are thus not completely filled, while the GS tubes exhibit f = 0.90 ± 0.04, indicating an increased filling.

In summary, GS and CT are two morphologically different CNT types, specifically regarding filling ratio and outer diameter. The former affects the mechanical stability while

https://doi.org/10.1021/acsanm.2c04729
ACS Appl. Nano Mater. 2023, 6, 1755−1769

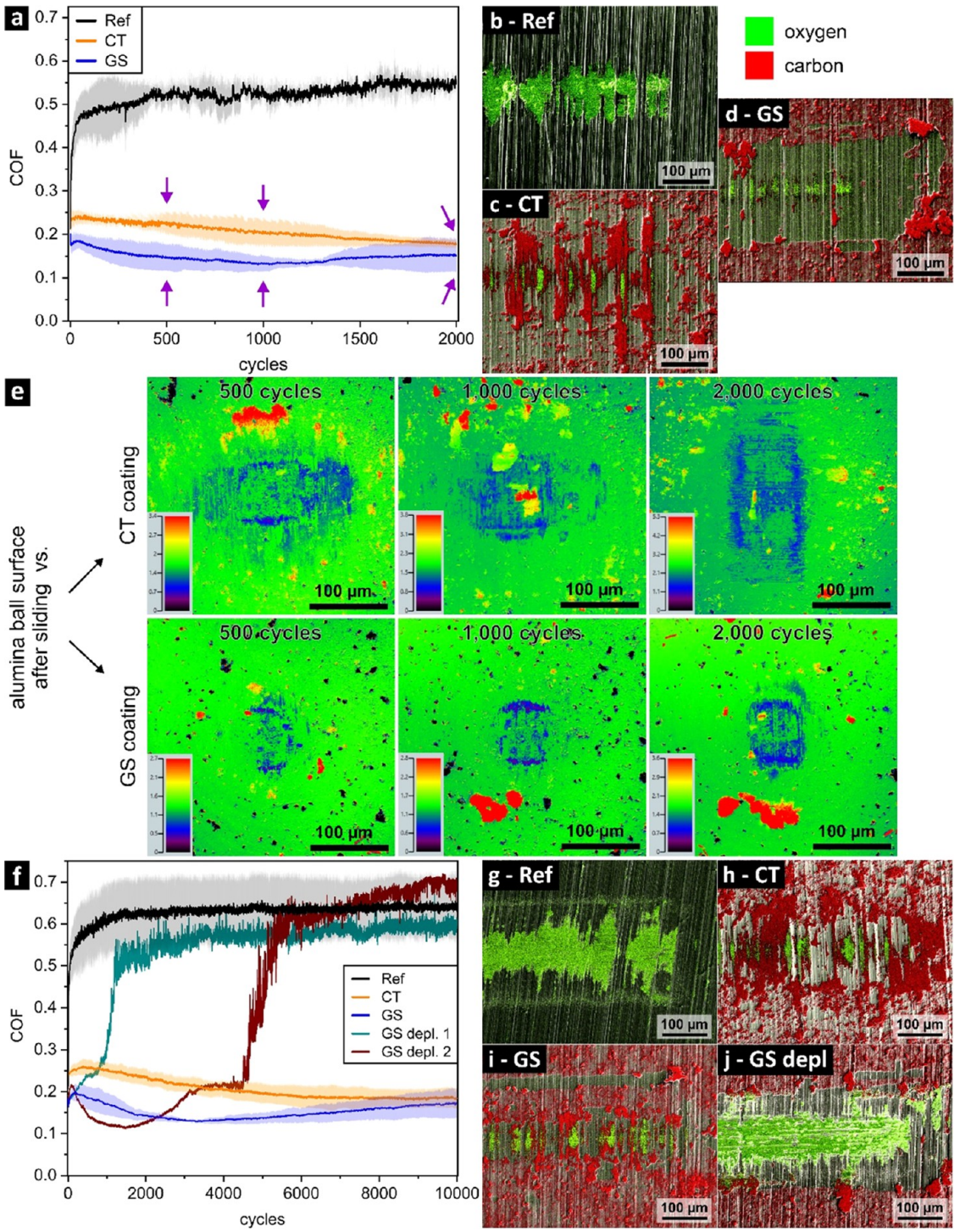

Figure 2. Short-term friction test (ball-on-disc) of an MWCNT lubricated iron surface. (a) COF evolution of CT- and GS-coated directionally ground substrates (P180) compared to the COF of an uncoated reference over 2000 reciprocating test cycles. (b–d) EDS/SEM overlay of the wear tracks after friction testing: (b) unlubricated reference, (c) CT-coated, and (d) GS-coated iron surfaces (see also S11 in the Supporting Information for images of other wear tracks). (e) Height profiles of confocal laser scanning micrographs showing the wear tracks on the alumina counter body after short-term tribological testing against CT- and GS-coated iron surfaces. The contact area is marked by blue wear scars, while the red areas mark transferred CNT patches (height scale in μm). Long-term friction test on an MWCNT lubricated iron surface. (f) COF evolution of CT- and GS-coated directionally ground substrate (P180) compared to an uncoated reference over 10,000 reciprocating test cycles. (g–j) EDS/SEM overlay of the surface after long-term friction testing: (g) reference, (h) CT- and (i) GS-coated wear tracks with low friction final state. (j) GS-coated wear track with high-friction final state due to lubricant depletion. Carbon is marked in red, and oxygen in green.

the latter defines the surface-area-to-volume ratio. The smaller CTs therefore have a larger surface area, which results in a stronger van der Waals interaction between the nanotubes, increasing the likelihood of agglomeration. It is of high scientific and technological interest to understand whether the

https://doi.org/10.1021/acsanm.2c04729
ACS Appl. Nano Mater. 2023, 6, 1755–1769

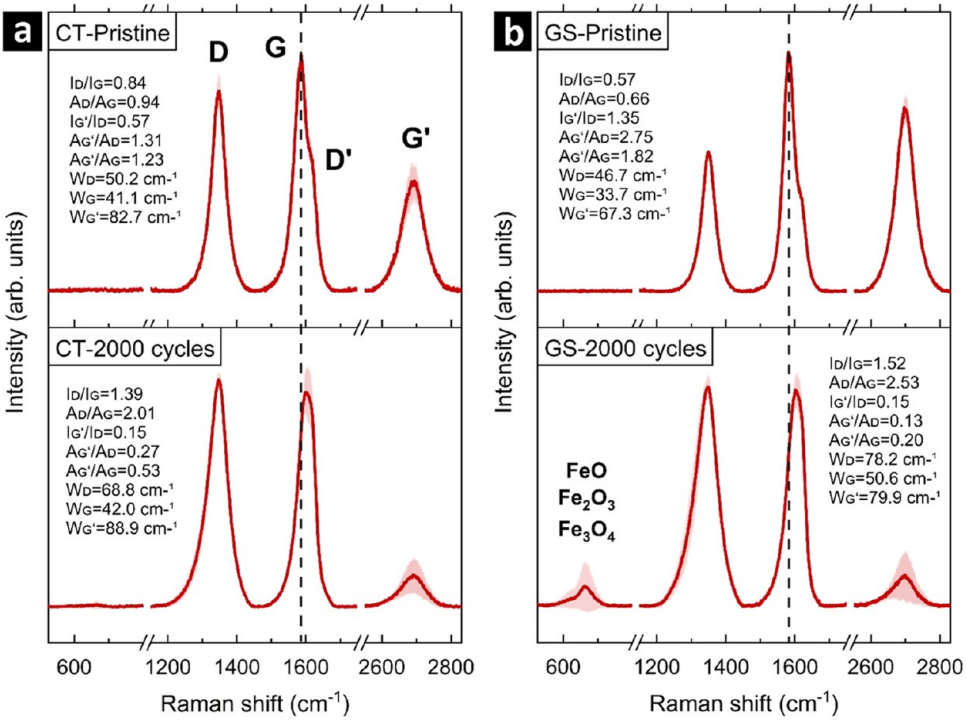

Figure 3. Raman spectra of (a) CT and (b) GS-MWCNT coatings before and after friction testing.

different nanostructures affect the solid lubricity of MWCNT coatings.

Tribological Experiments and Material Transfer Analysis. To examine the lubricating properties of GS and CT coatings, linear reciprocal friction tests are carried out on P180-ground iron surfaces (Figure 2a). The sliding direction is perpendicular to the grooves on the surface to allow a lubricant reservoir effect in the contact zone (as shown for laser-structured metallic surfaces by Reinert et al.).[1] An uncoated surface is used as an unlubricated reference system. Starting from a value of about 0.2, the coefficient of friction (COF) increases abruptly to just above 0.50 within the first 400 cycles and remains relatively constant thereafter at values between 0.50 and 0.55. This running-in behavior was previously observed for other tribological systems and is not untypical.[22] Accordingly, the scanning electron micrograph of the resulting wear track overlaid with an EDS oxygen map (Figure 2b) shows oxygen-rich patches along the center of the track where the counter body was in direct contact with the substrate, indicating severe tribo-induced oxidation.

In the case of the CT coatings, the COF starts at 0.24 and continuously decreases from there to just below 0.18 over 2000 cycles. Thus, the presence of the CT coating on the substrate leads to a reduction of the COF by a factor of 2 to 3 compared to the steady-state COF of the unlubricated system. The carbon overlay in Figure 2c (red) shows large patches of carbonaceous material that remained in the center of the wear track throughout the test. However, there are also areas where the coating was largely removed, resulting in mild local oxidation (green patches in Figure 2c).

GS coatings exhibit a different type of running-in behavior (Figure 2a). The COF starts at 0.20 and drops immediately until reaching a minimum of 0.13 after about 1200 cycles. This marks a turning point where the COF increases again, reaching 0.15 over the remaining 800 cycles. The scanning electron microscopy (SEM)/EDS overlay of the wear track (Figure 2d) shows that most of the GS-derived carbon has been removed and that sliding has caused mild oxidation of the central wear track. However, the small remaining amount of GS-derived carbon still provides effective solid lubrication. A likely increase in carbon starvation upon further sliding could trigger a transition to a high-friction state.

To investigate the long-term performance of the MWCNT coatings, a second set of friction tests over 10,000 cycles (Figure 2f) was conducted. For the unlubricated iron surface, the COF evolution is consistent with the corresponding short-term measurements (compare Figure 2f with Figure 2a). However, the long-term friction signal saturates at a slightly higher COF. As expected, tribo-induced surface oxidation of the long-term Ref (Figure 2g) is more pronounced than in the unlubricated short-term test (Figure 2b). The frictional behavior in the long-term tests of the CT-coated samples is also consistent with the corresponding short-term tests, except for a slightly prolonged running-in time of the former (compare orange curves in Figure 2f and Figure 2a). The EDS map of the CT-coated wear track after 10,000 cycles (Figure 2h) is similar to that after 2000 cycles (Figure 2c). Also, most individual long-term tests exhibit a similar friction response to the short-term tribotests for the GS-coated surfaces.

Material transfer from the tribofilm to the alumina counter body during friction testing is assessed using confocal laser scanning microscopy (CLSM; Figure 2e). The resulting images are presented as height profiles. The contact area is marked by blue wear scars, whereas transferred carbon patches that protrude from the surface are marked as red. A relatively large carbon patch is located at the center of the wear track that slid against CTs for 1000 friction cycles. Moreover, minute carbon patches can be observed in the wear scar of the alumina after sliding against GS- and CT-coated surfaces for 2000 cycles. The carbon has most likely been pressed into superficial pores or fatigue-related pits. No material transfer was observed in any

https://doi.org/10.1021/acsanm.2c04729
ACS Appl. Nano Mater. 2023, 6, 1755−1769

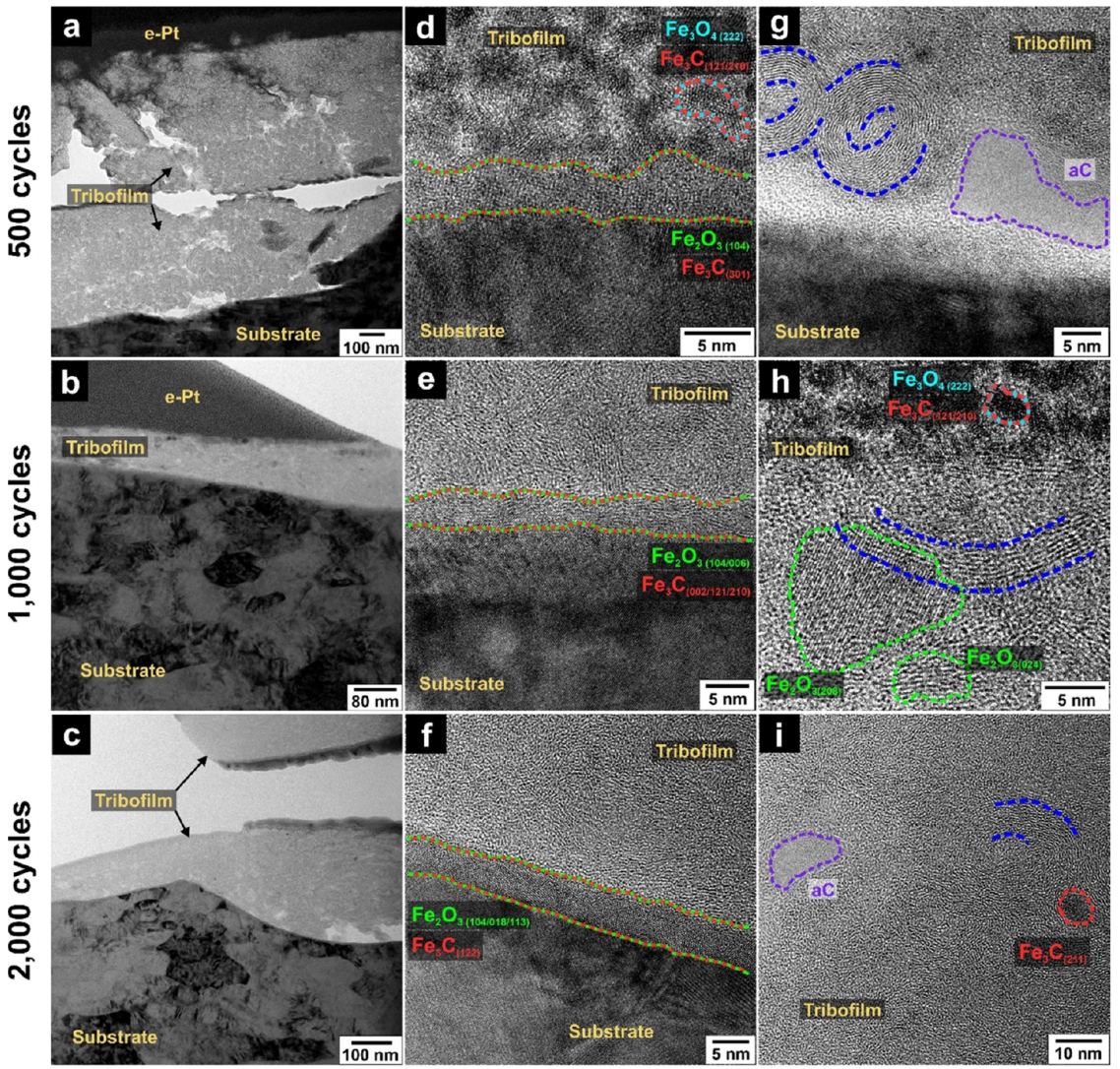

Figure 4. Near-surface cross-sectional transmission electron micrographs of the CT-derived tribofilm/substrate interfaces after (a, d, g) 500, (b, e, h) 1000, and (c, f, i) 2000 testing cycles. The CT fragments are contoured in blue.

of the other wear tracks. In conclusion, the material transfer is marginal, if it occurs at all. This demonstrates no significant covalent bonding between the alumina ball and the MWCNT coating.

During long-term tests, the GS coatings show different tribological behaviors. After a low friction period of roughly 1000 (GS depl 1 in Figure 2f) to 4500 (GS depl 2 in Figure 2f) cycles, the COF increases abruptly and approaches the steady-state friction level of the unlubricated iron. This bifurcation in the frictional behavior of the GS-coated systems can also be observed in the EDS maps. In the case of continuous lubrication (which occurred in 6 out of 8 tests), considerable amounts of carbon remain in the wear track (Figure 2i), often more than after 2000 cycles. In contrast, the two samples that end in a high-friction state show complete carbon starvation after the test (Figure 2j). In this case, the EDS map shows severe oxidation in the center of the wear track. However, its characteristic oxygen coverage differs from the unlubricated case (Figure 2g) as island formation has occurred, indicating adhesion as the dominant wear mechanism. This type of oxidation has been observed by Reinert et al.[1] and MacLucas et al.[2] after performing similar friction tests on MWCNT-coated austenitic stainless steel surfaces. The similar oxidation patterns on iron substrates are a strong indication of tribo-induced surface hardening.

Provided that the particles are retained in the contact, GS coatings show superior lubrication (smaller COF) until the standard deviations of both MWCNT types begin to overlap (after approx. 1500 cycles and 6000 cycles, respectively). It appears that the ground iron surface retains CT-derived carbon more easily than GS, presumably due to the smaller size of the CTs as they fit better into the underlying grooves. Obtained COF values are in good agreement with similar friction experiments of CNT-based lubrication systems on stainless steel substrates[1,23,24] and graphite on steel in humid air.[25]

Raman Characterization. Next, structural changes in the MWCNTs are characterized by Raman spectroscopy. At an excitation wavelength of 532 nm, the Raman spectra of multiwall carbon nanotubes typically show three distinct features in the 500−2800 cm^{-1} range: the D-band (1350 cm^{-1}), the G + D′-band (1580−1600 cm^{-1}), and the G′-band (2700 cm^{-1}) (Figure 3a, top). The G + D′-band is a superimposition of the G-band (1582 cm^{-1}) and the D′-bands

https://doi.org/10.1021/acsanm.2c04729
ACS Appl. Nano Mater. 2023, 6, 1755−1769

(1617−1625 cm^{-1}), the latter being responsible for the characteristic shoulder (shown in Figure 3a,b, top).

To carefully assess the structural degradation of the MWCNTs during the short-term test, a set of indicators derived from the spectra are considered. For peak analysis, the D-band, D′-band, and G′-band were fitted with Voigtian peak profiles, whereas the G-band was fitted using a Lorentzian peak profile, all with floating peak positions. The D/G ratio reflects the defectivity of the particles. It is applied either as the normalized intensity ratio (I_D/I_G) or the integrated area ratio (A_D/A_G) both of which have been used for the structural analysis of carbon materials.[26] Furthermore, our analysis includes the full width at half-maximum of the D-band (W_D), G-band (W_G), and G′-band ($W_{G'}$), which are sensitive to defect density, particularly at defect distances (L_D) of 10−15 nm and below.[26,27] An increase in these indicators is attributed to an increase in defectiveness.[26,28−30] By contrast, an increase in the G′/D ratio ($I_{G'}/I_D$, $A_{G'}/A_D$, denoted as the purity index) and $A_{G'}/A_G$ implies a decrease in defectivity.[26,31] The D band occurs only in imperfect graphitic structures owing to the A_{1G} breathing mode, and its intensity grows with increasing defectivity.[28] Comparing both MWCNT coatings, the D band intensities in pristine condition (Figure 3a,b) show that GS tubes are significantly less defective than CT. This is not only reflected by I_D/I_G, but the entirety of indicators can be attributed to a stronger strain exerted on the carbon atoms in CNT walls with smaller diameter, thus facilitating the incorporation of defects into the walls.[32] After completing friction testing, the indicators suggest considerable degradation of MWCNTs in both coating types. This is illustrated in particular by the formation of a uniform G + D′-band and its upshift (dashed lines in Figure 3a,b as reference), which is a change in shape due to the increasing intensity of the D′-band and simultaneously decreasing the intensity of the G-band. Additionally, oxide formation is detected (Figure 3b, bottom), confirming the previously observed GS depletion in the wear track. Based on Raman characterization, both MWCNT types show strong signs of structural degradation after tribological testing, although the applied load and corresponding maximum Hertzian pressure are low (0.36 GPa).

Transmission Electron Microscopy. For a detailed analysis of the MWCNT-derived tribofilms and interfaces to the iron substrates, TEM was performed on focused ion beam cross sections from the wear tracks. Due to the surface texture induced by P180-grinding, tribolayer thickness varies greatly. However, it generally ranges between 15 and 600 nm in the deepest grooves. Comparison of the CT-derived tribofilm at 500 (Figure 4a), 1000 (Figure 4b), and 2000 (Figure 4c) cycles shows a reduction in void sizes and hence a strong compression of the tribofilm with increasing test duration. Independent of the cycles number, an interfacial layer between substrate and tribofilm can be identified (Figure 4d−f) in which lattice spacings of 1.60, 2.20, and 2.30 Å and several values in the range of 2.65−2.75 Å occur, corresponding to lattice planes of Fe_2O_3 (hematite), namely, (018), (113), (006), and (104), respectively. Additionally, Fe_3C (cementite) is found after 500 cycles with a measured spacing of 1.58 Å (301) and after 2000 cycles with 1.75/1.78 Å (122); see Figure 4d−f. Layer spacings of 2.24 and 2.33 Å in the interfacial layer after 1000 cycles (Figure 4e) indicate (002) and (210/121) orientations of Fe_3C. However, these spacings could also be assigned to Fe_2O_3 (113) and (006), respectively. Moreover, there is strong evidence of Fe_3O_4 (220) (magnetite) in the interfacial layer after 1000 cycles and Fe_3O_4 (800) after 2000 cycles. Particularly, the former is the only plausible phase in the lattice space regime around 3.18 Å. Similar oxide formation in the tribolayer was observed by Grützmacher et al. with $Ti_3C_2T_X$ multilayer coatings.[33]

The transmission electron micrographs depicted in Figure 4g−i show the composition of the CT coatings at different stages of the friction test. After 1000 and 2000 test cycles, crystalline nanoparticles embedded in the MWCNT-derived carbon matrix can be identified. Within the particles, lattice spacings corresponding to Fe_3C (211) and Fe_2O_3 (024/208) planes are clearly visible. Some particles cannot be assigned definitively (Figure 4d,h, circled red/teal). The lattice spacing could originate from either Fe_3C (121/210) or Fe_3O_4 (222) planes.

The carbon matrix in Figure 4g comprises different structures, including ordered sp^2-hybridized carbon from crystalline CT fragments to less ordered turbostratic carbon (t-C) and completely amorphous carbon (a-C). In the zones with CT fragments, we measure lattice spacings between 3.50 and 4.05 Å, which is larger than the literature value of 3.43 Å for ideal MWCNTs. Most likely, friction-induced deformations of the tube cross section (from circular to polygonal) lead to strong local bending or even defects at sufficiently high strains. In this case, the lattice spacing is increased, as described by Liu et al.,[34] whose calculated values agree with ours.

The size of the crystalline domains of the CT fragments decreases with an increasing number of test cycles. Figure 4g−i shows the micrographs taken from a specific film; see Figures S5−S9 in the Supporting Information for more micrographs. This indicates a gradual tribo-induced phase transformation of the CT coating, leading to the growth of t-C and a-C zones.

The GS-derived tribofilms show a similar densification behavior during friction testing as the CT-derived tribofilms (Figure S4a−c). The resulting carbon matrices (Figure S4g−i) are structurally very similar to their CT equivalents (Figure 4g−i) and contain the same particles (Figure 4d,f−i, Fe_3O_4 was also found in the CT-derived tribofilm). However, the GS tube fragments are larger and show a higher degree of structural integrity regardless of the test duration. Overall, the images confirm the results of the Raman analysis that the majority of the carbonaceous material in the films is nanocrystalline and contains areas of completely amorphous carbon.

Discussion of the Experimental Results. Tribological testing has shown that applying MWCNT coatings onto an iron substrate leads to a significant friction reduction and that the MWCNT diameter influences the friction behavior. For most tests, the large-diameter GS initially exhibited a lower COF than the small-diameter CT. Furthermore, the COF of GS decreases faster and reaches a turning point, followed by a slight but steady increase. In contrast, for the CTs, the COF decreases continuously during the first test and reaches a plateau during the long-term test after about 9000 cycles, possibly reaching a steady state. As a result, the COFs converge in both experiments, indicating an approaching crossing and superior CT lubrication in the longer term. The packing density could be an influencing factor for the different COF evolutions. Assuming a cylindrical shape, larger MWCNTs have a lower packing density than smaller tubes. During the first cycles, when the particle agglomerates are compressed, the COF decreases. Once fully compressed, the particles exert more counter pressure leading to a COF increase, and because

https://doi.org/10.1021/acsanm.2c04729
ACS Appl. Nano Mater. 2023, 6, 1755−1769

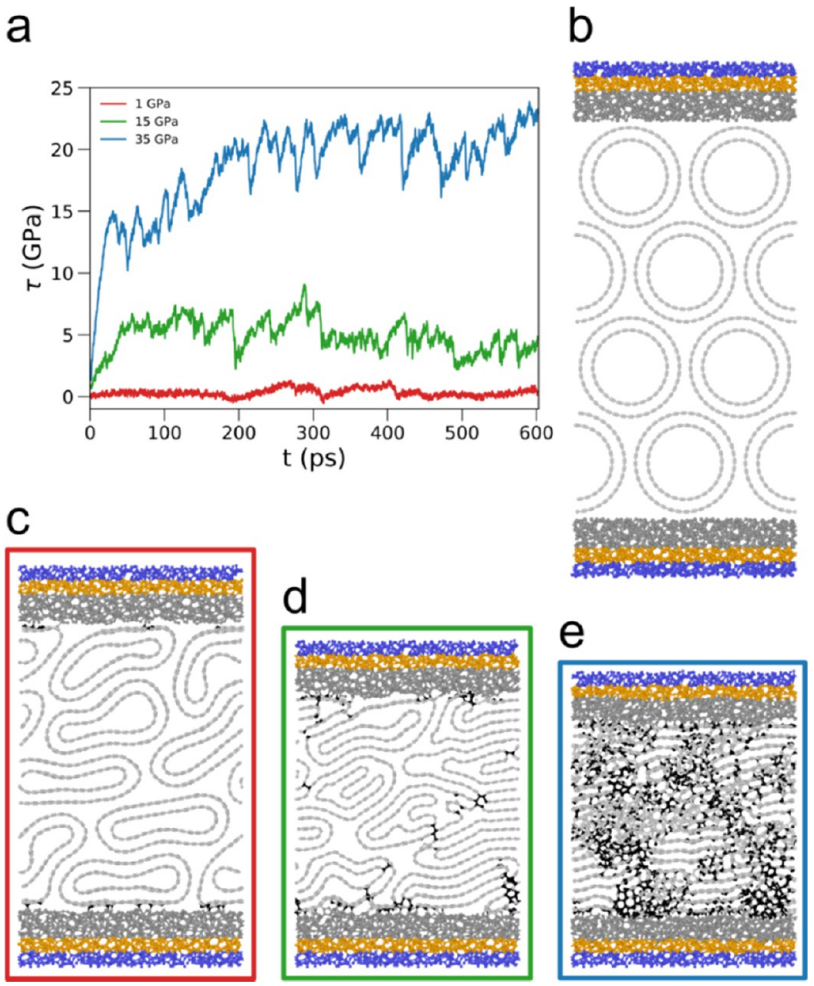

Figure 5. Atomistic simulations of a two-walled (20,20)-MWCNT bundle pressurized and sheared between a-C surfaces. (a) Evolution of shear stress for different normal pressures. (b–e) Snapshots of the systems: (b) initial system prior to pressurization; (c–e) during steady-state sliding under 1 GPa (c), 15 GPa (d), and 35 GPa (e) normal pressures. Gray spheres represent free carbon atoms, while blue atoms represent rigid layers and orange atoms thermalization layers. Higher normal pressures lead to the formation of bonds between sp^3-hybridized carbon atoms (marked in black in (c–e)), resulting in damage of the MWCNTs.

of their size, GS reaches this point first. Hence, their COF starts to increase sooner. Simultaneously, the real contact area increases throughout the test due to the continued flattening of the topographical maxima. As more interfacial area becomes available for the MWCNTs, the load is distributed over more tubes, which reduces the overall friction more effectively over time. In the case of GS, the amount of tribofilm held in the wear track can vary significantly, unlike the CT-coated wear tracks, which consistently hold considerable amounts during the friction tests. This absence of starvation could explain the persistent COF decrease for the CT and why this effect is less pronounced for the GS. The oxidation in the undepleted wear tracks is comparable and can be described as minor. Once carbon depletion in GS-coated wear tracks sets in (2/8 in the long-term tests), the COF starts to increase sharply and approaches that of the reference along with severe wear track oxidation. Based on the uniform shape of the G + D′-band and its "upshift", both MWCNT species would be classified either as stage 1(f) within the three-stage amorphization model of Ferrari and Robertson, corresponding to fully nanocrystalline graphite, or possibly early stage 2, describing the transition from nanocrystalline graphite to hydrogenated amorphous carbon.[28] Corresponding transmission electron micrographs confirm the loss of crystallinity of most of the carbon material without reaching complete amorphization (particularly Figures 4f,i and S4d,f) and are thus in good agreement with the Raman analysis. Localized aC formation results from continuous mechanical degradation in areas of particularly high mechanical stresses exerted by counter-body pressure during friction testing. GS fragments (Figure 4e,g–i) show a higher degree of structural integrity regardless of completed cycles and are, therefore, larger than their CT equivalents. This can be explained by the more significant curvature of small-diameter tubes, leading to increased strain on the carbon bonds in the MWCNT walls. Hence, large-diameter tubes are more resistant to mechanical degradation, which will likely also impact the COF evolution.

Atomistic Simulations. Since carbon nanotubes are considered among the strongest structural building blocks for synthesizing nanomaterials,[35] the observed morphological transition to amorphous carbon at a relatively small load of 100 mN is rather surprising. Therefore, atomistic simulations are performed to elucidate the pressure- and sliding-induced degradation of MWCNTs and to explore the loading conditions that may lead to the observed a-C formation. First, we study solid lubrication by MWCNT bundles. Figure 5

https://doi.org/10.1021/acsanm.2c04729
ACS Appl. Nano Mater. 2023, 6, 1755–1769

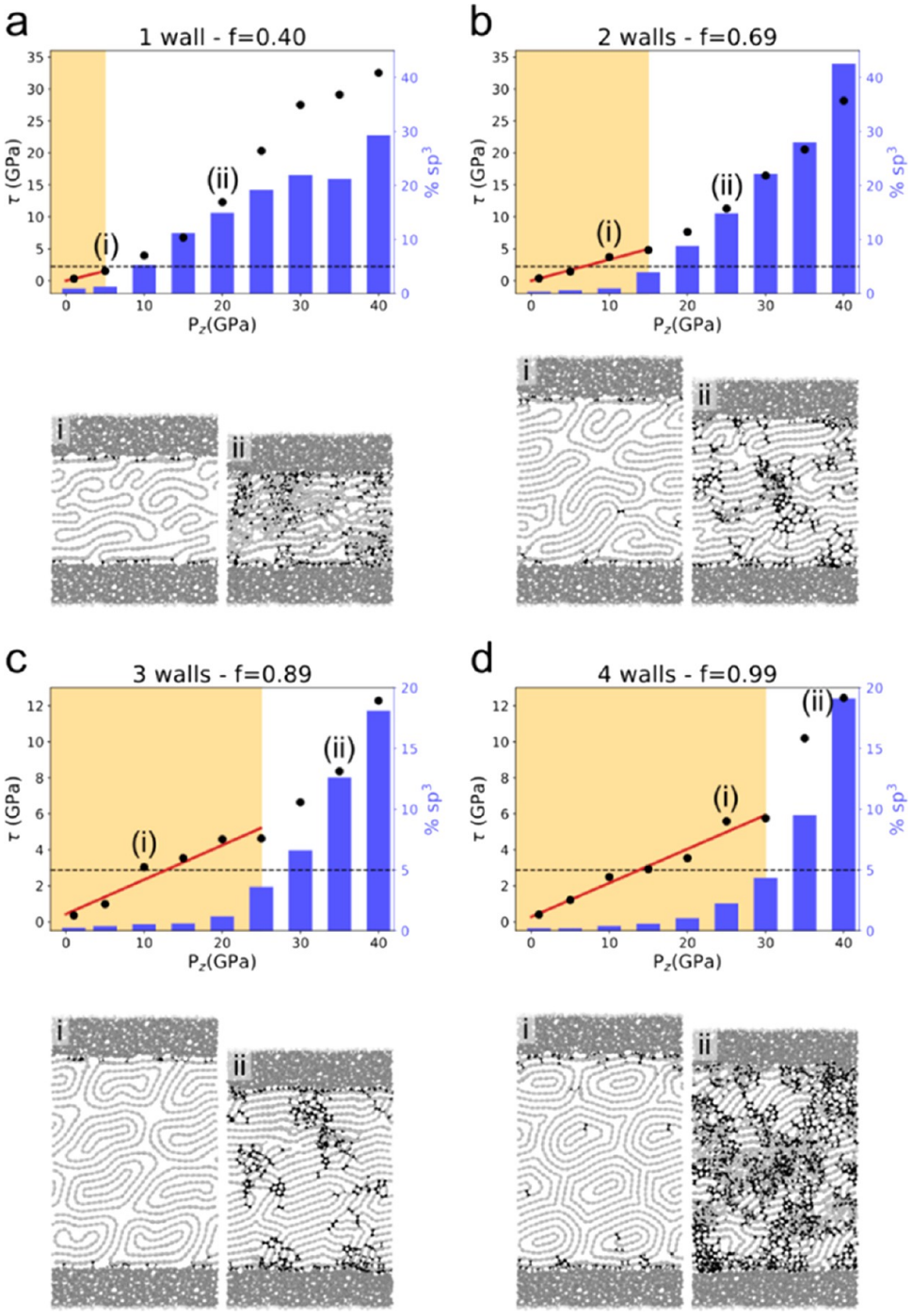

Figure 6. Atomistic simulations of the average steady-state shear stress $\langle\tau\rangle$ of (20,20) MWCNTs for various normal pressures P_z and filling ratios f. A distinction can be made between a low- and a high-pressure regime. At low normal pressures, the MWCNTs are hardly damaged (subpanels i) as indicated by an sp^3 fraction below 5% (blue bars in the orange shaded areas), $\langle\tau\rangle$ is low and follows Amonton's law (red straight lines). At higher P_z, severe damage to the MWCNTs (see subpanels ii) is related to an sp^3 fraction greater than 5%, leading to a nonlinear increase of $\langle\tau\rangle$. It should be noted that the pressure P_z^{trans} required to initiate the transition depends on f.

illustrates the typical response of an array of MWCNTs subject to various normal loads. The simulation model consists of identical two-wall (20,20)-MWCNTs in dense packing between two a-C surfaces (Figure 5b). This model mimics an experimental situation in which an MWCNT bundle is tribologically loaded between an already existing tribolayer and a carbon transfer film. A normal pressure P_z is applied to two rigid layers at the top and bottom of the respective a-C slabs[36] (blue atoms in Figure 5b), and the system is sheared by displacing the top rigid layer with a speed of 30 m/s. The system temperature of 300 K is controlled by coupling the two orange regions in Figure 5 to a Langevin thermostat.

The evolution of the shear stress τ is shown in Figure 5a for three different P_z (1, 15, and 35 GPa). After a short running-in period, a steady state in the frictional response is reached for all simulations. For P_z = 1 GPa, the rather low steady-state τ of 0.4 GPa (red curve in Figure 5a) can be explained by sliding within an irregular array of strongly deformed MWCNTs

https://doi.org/10.1021/acsanm.2c04729
ACS Appl. Nano Mater. 2023, 6, 1755−1769

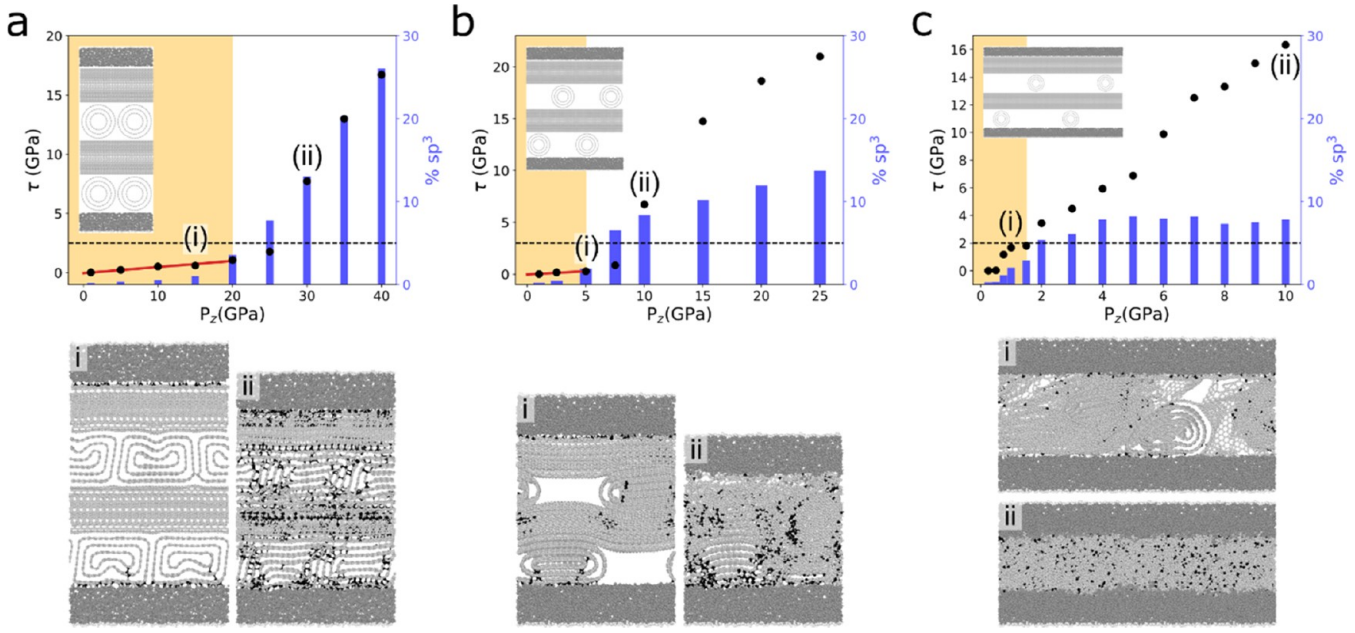

Figure 7. Layers of crossed (20,20) MWCNTs as a model for a real CNT layer. While densely packed CNTs behave almost like ideal bundles (a), incomplete filling of the region between the aC layers increases the contact pressure at the crossings, resulting in kinking of the MWCNTs and a significant reduction in the normal pressures required to induce the transition from the low- to high-friction regime and to degrade the MWCNTs (b, c). If the distance between the CNTs is large enough, the CNTs degrade by rupturing their walls (c(i)) instead of continuous amorphization (b(ii)), and the required normal pressure for severe damage decreases to 1 GPa (c).

(Figure 5c and Movie_12c in the Supporting Information). At higher pressures, the MWCNTs get connected by intertube covalent C−C bonds (black bonds in Figure 5d,e). Consequently, sliding requires bond breaking (Movie_12d and Movie_12e in the Supporting Information). This induces damage to the MWCNTs, which becomes more pronounced with increasing normal pressure. As a result, the sliding-induced shear stress increases with P_z (green and blue curves in Figure 5a) leading for instance to $\langle\tau\rangle$ = 5 GPa for P_z = 15 GPa and $\langle\tau\rangle$ = 21 GPa for P_z = 35 GPa.

To further investigate the influence of the MWCNT structure, we vary the number of nanotube walls from a single wall to a complete filling of the outer (20,20) wall with concentric inner tubes (corresponding to a filling ratio f between 0.40 and 0.99). Sliding simulations at various P_z are performed to investigate the stability range of the MWCNTs under load (Figure 6). When sliding at low normal pressures, the MWCNTs are hardly damaged for all f; see snapshots (i) in Figure 6. Under these circumstances, a linear relationship can be observed between the average shear stresses $\langle\tau\rangle$ and the normal pressures P_z, and thus an Amonton friction law $\langle\tau\rangle = \mu P_z$ can be fitted (red straight lines in Figure 6). This regime ends in all cases at an sp^3-hybridized carbon fraction of approximately 5% above which a nonlinear increase in shear stress with pressure occurs. Panels (ii) show characteristic snapshots in this high-pressure regime. The normal pressure P_z^{trans}, required for the transition between the low- and high-pressure regimes, shows a clear dependence on the MWCNT structure. While for single-walled (20,20) nanotubes a P_z^{trans} of 10 GPa is already sufficient to cause severe damage (Figure 6a), P_z^{trans} increases significantly with increasing f. For completely filled four-wall (20,20) MWCNTs, more than 30 GPa is required to trigger intertube bonding (Figure 6d).

Additional simulations are performed for (10,10) and (40,40)-MWCNTs (Figures S1 and S2) and P_z^{trans} is determined for all cases. Interestingly, P_z^{trans} increases roughly linearly with f and is approximately independent of the nanotube diameter (Figure S3). Therefore, it is possible to fit a function $P_z^{\text{trans}}(f) = \alpha + \beta f$ with $\alpha = -1.63$ and $\beta = 32.6$. Based on our TEM characterization (Figure 1), we estimated f_{CT} = 0.76 and f_{GS} = 0.90 for the CT- and GS-type MWCNTs, respectively. Our simple expression predicts $P_z^{\text{trans}}(f_{\text{CT}})$ = 23 GPa and $P_z^{\text{trans}}(f_{\text{GS}})$ = 28 GPa. The hardness of our iron substrate is of the order of 1 GPa, so it is unlikely that asperity-level local contact pressures can reach such high values in our MWCNT coatings. The question, therefore, arises to what extent the systems simulated so far reflect the actual experimental conditions in the tribological contacts.

While all MWCNTs in ideal bundles are identical, a broad distribution of MWCNT diameters is to be expected in technological systems (as shown in Figure 1c−f), which makes the formation of densely packed structures difficult. Similarly, it cannot be expected that all axes of the MWCNTs will adopt the same orientation. Usually, the EPD growth of MWCNT coatings produces a film of randomly packed nanotubes reminiscent of a felt (Figure 1). A characteristic feature of such a random fabric is the contact between two differently oriented MWCNTs. Locally, this resembles a point contact between two crossed cylinders (Figure 1c,d), leading to a sizable stress intensification compared to the line contact between two parallel cylinders.

Therefore, we consider alternating monolayers of orthogonal MWCNTs as simple model systems for CT and GS coatings (Figure 7). Here, three-walled (20,20)-CNTs are used, which have a filling ratio similar to the GS in our experiments. We simulate different densities of the resulting nanotube fabric by systematically varying the distance d between two neighboring parallel MWCNTs in a monolayer (Figure 7). For a distance d = 2.95 nm between the CNT axes, the parallel MWCNTs are in close contact, and a complete filling of the monolayers is

https://doi.org/10.1021/acsanm.2c04729
ACS Appl. Nano Mater. 2023, 6, 1755−1769

established. In this case, the transition pressure P_z^{trans} = 25 GPa (Figure 7a) is in the same range as for an ideal bundle of three-walled (20,20) MWCNTs. An increase in d leads to a local stress intensification resulting in a significant reduction of P_z^{trans}. At a distance d = 4.43 nm between the MWCNT axes, the transition pressure is reduced to P_z^{trans} = 7.5 GPa (Figure 7b). At a distance d = 11.81 nm, severe damage to the MWCNTs already occurs at P_z = 1 GPa (Figure 7c). Instead of a continuous amorphization process, damage proceeds via localized rupture of the MWCNT walls (snapshot (i) in Figure 7c). Accordingly, no significant increase in the content of sp^3-hybridized carbon is observed here despite the strong degeneration of the MWCNTs at P_z = 1 GPa.

Now, we elaborate a simple argument for the scaling of P_z^{trans} with MWCNT distance d. The transition pressure is given by the force on the top rigid a-C layer F_z^{trans} divided by the area A of the a-C layer: $P_z^{trans} = \frac{F_z^{trans}}{A}$. Due to stress intensification, the local pressure at the crossing points $P_z^{trans,\times}$ is larger and can be estimated by $P_z^{trans,\times} = \frac{F_z^{trans}}{n_\times a_\times}$, where $n_\times$ denotes the number of crossing points between two orthogonal layers and $a_\times$ a characteristic contact area of a crossing. Consequently, we obtain $P_z^{trans} = \frac{P_z^{trans,\times} n_\times a_\times}{A} = P_z^{trans,\times} a_\times \rho_\times$, where $\rho_\times$ is the areal density of point contacts between crossed MWCNTs. Since $\rho_\times = \frac{1}{d^2}$ holds for our model structures, this simple back-of-the-envelope derivation predicts a $P_z^{trans} \sim \frac{1}{d^2}$ scaling. Indeed, a plot of P_z^{trans} from our crossed (20,20) MWCNT MD simulations vs tube distance d follows closely the predicted scaling (Figure 8) and, as expected, an f of 0.96 for (10,10)

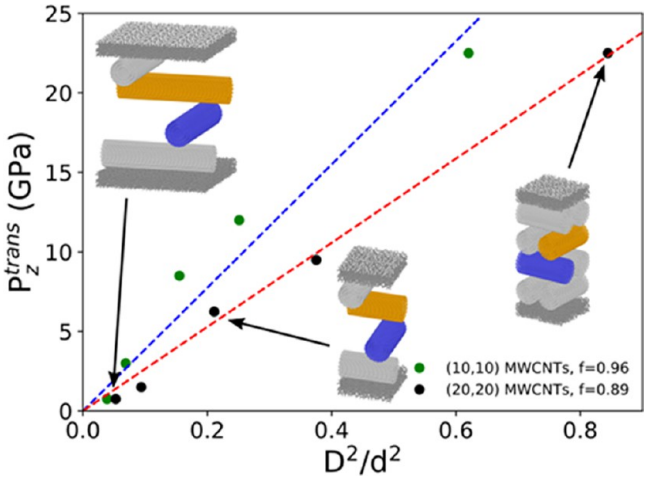

Figure 8. Transition pressure P_z^{trans} as a function of the ratio between the square of the outer tube diameter D and the distance between parallel MWCNTs d (see text for details). A linear relation can fit the MD data $P_z^{trans} = P_z^{trans,\times} \frac{D^2}{d^2}$ resulting in $P_z^{trans,\times} \approx 26.4$ GPa for three-walled (20,20) MWCNTs (red line) and $P_z^{trans} \approx 38.7$ GPa for two-walled (10,10) MWCNTs (blue line).

MWCNTs results in a higher P_z^{trans} (blue line in Figure 8) and a lower one of 0.89 for (20,20) MWCNTs (red line in Figure 8). For assumed crossing densities $\rho_\times < 0.005\ nm^{-2}$, the estimated transition pressures would be well below 1 GPa, which would correspond to realistic local contact pressures in our experiments. However, this value is derived for (20,20) MWCNTs with D = 2.71 nm, while, for instance, $D \approx 14$ nm for the CT. Since the contact area of two crossing MWCNT scales as $a_\times \sim D^2$ and since our MD simulations of MWCNT bundles suggest that $P_z^{trans,\times}$ is roughly independent of D and depends only on the filling ratio (Figure S3) $P_z^{trans,\times}(f)$, we obtain

$$P_z^{trans}(f, D) = P_z^{trans,\times}(f) D^2 \rho_\times$$

From Figure 8, we obtain an estimate for the transition pressure at the crossings $P_z^{trans,\times}$ = 26.4 GPa for a filling ratio of f = 0.89. Based on our high-resolution TEM (HR-TEM) images, we obtain a rough estimate of $\rho_\times$ in our CT and GS coatings: $\rho_\times \approx 0.00025 \frac{1}{nm^2}$ and $\rho_\times \approx 0.00014 \frac{1}{nm^2}$, which results in $P_z^{trans} \approx 1.2$ GPa and $P_z^{trans} \approx 5.5$ GPa, respectively. These values are upper estimates of the experimentally active transition pressures since defects in the tubes, longer time scales for the transitions in the experiments, or even catalytic effects due to the interaction with the metallic or oxide substrates are not considered. Furthermore, the CNTs in the simulations are all of the same size, whereas on a real surface, a size distribution is expected. This could lead to large CNTs being more likely to contact each other, further increasing the effective distance between CNT crossings and, thus, the local pressures.

Comparison of Atomic-Scale Structures from MD Simulations and TEM Images. Now that we have established the plausibility of MWCNT degradation under the experimental conditions and, thus, the formation of an MWCNT-fragment/a-C composite, we return to the transmission electron micrographs to search for characteristic features found in the MD trajectories. Indeed, a more detailed examination of the GS-derived tribofilm after 500 cycles reveals arrangements of GS tubes, or at least fragments thereof, that resemble the MD results. In some cases, the exact contact situation of two individual tubes crossing each other can be observed (compare Figures 7−9a with 9b,c). Hence, our MD results are likely to be transferable to experiments and may provide novel insights into the degradation behavior of MWCNTs on the atomic length scale. More complex tube arrangements with further crossed contacts are presented in Figure 9d. Ideal bundles, on the other hand, are not observed. No less significant is the onset of amorphization observed in the kink of an otherwise relatively crystalline GS fragment (Figure 9e). Amorphization is more pronounced at the inner kink than outside, where small, at least partially crystalline domains are still visible. This phenomenon has been observed at various locations in both CT- and GS-derived tribofilms and can be attributed to a higher degree of mechanical strain on the inside.

The TEM observations shown in Figure 9b,c support the MWCNT arrangement on which our atomistic simulations are based and are consistent with the degradation patterns observed in the MD. Thus, our simulations provide novel insights into the friction mechanism at the atomic level. As shown by the Raman data and TEM imaging, both MWCNTs degrade substantially over 2000 friction cycles. However, lubricity is maintained. Hence, our investigations suggest that the rolling and sliding of MWCNTs in steady-state plays little, if any, role. Instead, we propose the following multistage process to describe the MWCNT solid lubrication mechanism between two sliding surfaces (alumina on iron):

https://doi.org/10.1021/acsanm.2c04729
ACS Appl. Nano Mater. 2023, 6, 1755−1769

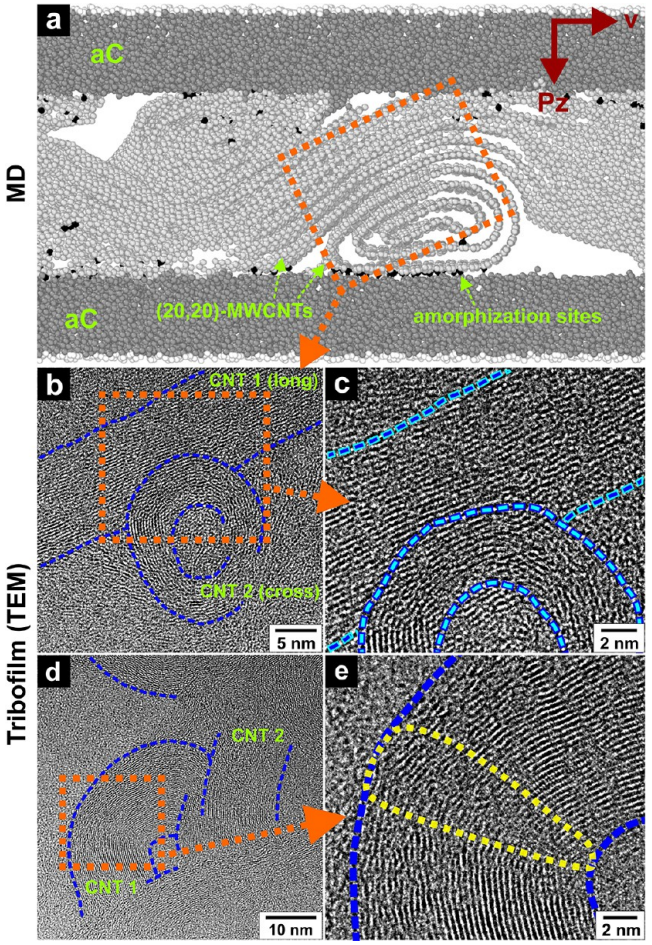

Figure 9. (a) Atomistic snapshot of crossed three-walled (20,20)-MWCNTs during a simulation at 30 m/s and P_z = 1.5 GPa. The black spots represent amorphization sites. Transmission electron micrographs of the GS-derived tribofilm after 500 cycles show (b) two crossed tube sections and (c) their contact point at higher magnification. Transmission electron micrographs of (d) more complex arrangements of multiple tubes or tube fragments and (e) a kink in a GS tube at higher magnification.

- Stage 1 (compaction): During the initial cycles of tribological load, the MWCNT coating on the iron substrate is compacted, as shown by the HR-TEM images in Figures 4a–c and S4a–c. Rolling and/or sliding of individual MWCNT or agglomerates, including mixed forms, may occur during this period.
- Stage 2 (deformation): Once the coating is fully compacted, the range of motion of the MWCNTs becomes severely restricted (preventing rolling), and the film begins to carry most of the occurring shear forces (as indicated by the blue shear zone in Figure 10). For a given pressure, the degree of lateral deformation depends strongly on the tube filling ratio. As shown by our simulations (Figure 6), the lower the filling ratio, the lower the mechanical resistance to deformation, and curvature-induced strain caused by severe deformation will substantially increase the local reactivity of the carbon structure.
- Stage 3 (tribo-chemical reaction): Tribo-induced shear stress applied to the film causes covalent tube-substrate bonding and carbon enrichment and oxidation of the superficial iron substrate. This results in the formation of an interfacial layer on the substrate surface consisting of iron oxide and carbide (as shown by lattice spacing analysis). Continued shearing of the hardened and brittle interfacial layer leads to the formation of Fe_2O_3, Fe_3O_4, and Fe_3C wear particles embedded in the film, shown in Figure 4. Moreover, the strain at the contact points between crossed tube sections becomes sufficiently high to induce local sp^3 transformation, resulting in cross-linking and MWCNT fragmentation at the crossing points (Figures 7and 9). Further sliding of the cross-linked material induces further damage to the nanotubes, as shown by the results of the Raman characterization. Accumulating disordered zones results in the formation of an a-C matrix that hosts MWCNT fragments and iron oxide/iron carbide nanoparticles, as suggested by our Raman analysis.
- Stage 4 (interfacial sliding): The resulting MWCNT/a-C composite tribofilm has a significantly higher mechanical strength and stronger covalent adhesion to the iron substrate than the initial MWCNT coating. Therefore, the shear interface (velocity accommodation zone) shifts to the tribofilm/counter-body interface. Consequently, MWCNTs in the contact are exposed to heavy mechanical stress, leading to various degradation mechanisms, such as exfoliation.
- Stage 5 (passivation): Shear forces, for example, cause superficial carbon bonds to break. The resulting dangling bonds are immediately terminated by ambient molecules (such as water or O_2), inhibiting bonding to the counter body.[37] This is supported by CLSM imaging of the counter-body wear tracks, showing minor, if any, tribofilm transfer (Figure 2e).

For better visualization, Figure 10 shows a schematic representation of the state of the contact before and after each process described by the proposed lubrication mechanism. In addition to the aforementioned steps, occasionally (in 2 out of 8 cases), the lubricity of GS on the directionally ground iron substrate can fail. This leads to a final stage 6 (starvation), during which the sliding ball pushes the tribomaterial to the edges of the wear track and thus out of the contact, resulting in carbon depletion. The absence of the protective and lubricating GS layer results in the oxidation of the metallic substrate (Figure 2j) and a sharp increase in friction and wear (Figure 2f).

SUMMARY AND CONCLUSIONS

Instead of traditional solid lubricants, MWCNT could be used in high-load applications. Often is speculated that a nanoscale roller-bearing mechanism underlies the lubricity of MWCNTs. In a combined approach using experimental friction tests with subsequent characterization and MD simulations, we have investigated the lubrication properties of MWCNT coatings on iron substrates and the underlying mechanisms. Experimentally, friction tests on ground and MWCNT-coated iron substrates have shown that the coatings can significantly reduce surface friction over extended periods. Characterization of the wear tracks clearly showed the gradual degradation of the MWCNTs during sliding. Atomistic modeling of the coatings provided an explanation for why the MWCNTs degrade at comparatively low pressures despite their high mechanical stability. Stress intensification at the crossing points between two MWCNTs leads to low macroscopic pressures

https://doi.org/10.1021/acsanm.2c04729
ACS Appl. Nano Mater. 2023, 6, 1755−1769

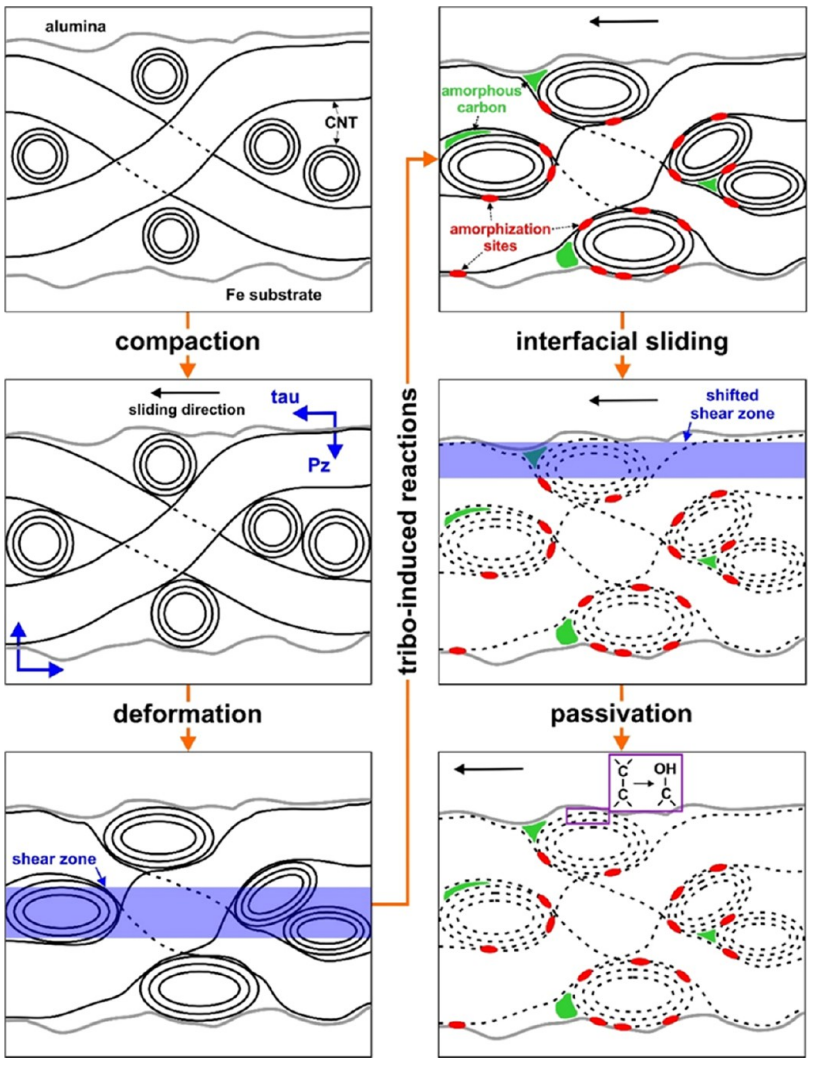

Figure 10. Schematic representation of the proposed multistage process describing the solid lubrication mechanism of an MWCNT coating between alumina and a ground iron substrate under tribological load.

being sufficient to locally reach the high pressures required for the degradation of a single tube. A simple estimation showed that this shifts the onset of film degradation to a range consistent with typical experimental parameters. We then discovered that the MWCNT arrangement on which the atomistic simulations were based was consistent with TEM images of the tribofilm. Based on the combination of experimental results and insights from atomistic simulation, we propose a multistage friction mechanism for MWCNT coatings between sliding surfaces. Finally, the results of this study disprove the theory that MWCNTs act as nanoscale roller bearings.

METHODS

Materials and Substrate Preparation. Two types of CVD-grown multiwall CNTs were used for this study. Large-diameter CNTs were purchased at Graphene Supermarket and exhibit an outer diameter of 30−85 nm with a length of 10−15 μm. Small-diameter CNTs were purchased at Cheap Tubes, Inc. and have an outer diameter of 8−15 nm with a length of 10−50 μm. Iron platelets (99.5% purity, Goodfellow GmbH) measuring 20 × 20 mm^2 with a thickness of 1 mm were used as substrate material. To create a directed surface roughness perpendicular to the sliding direction of the counter body, the platelets were ground using a TegraPol grinding and polishing machine (Struers) with P180 grit sandpaper resulting in a root mean square roughness S_Q = 155 ± 15 nm (50× objective, λ_C = 8 μm). In this study, sliding is carried out perpendicular to the grooves on the surfaces to allow a lubricant reservoir effect at the contact zone (as shown for laser-structured metallic surfaces in ref 1). We have also tested the parallel case (for line structures generated by laser interference patterning), and the effect is also observable but to a lesser extent.

Suspension Preparation and Electrophoretic Deposition. EPD suspensions were prepared with 70 mL of isopropanol, 10 mL of triethylamine (Acros Organics, 99% purity) as an additive to support particle deposition, and a 0.1 mg/mL particle concentration of solvent. As shown in Scheme 1, the suspensions were subjected to 10 min of shear mixing (Ultra-Turrax T25, IKA) at 7000 rpm followed by 10 min ultrasonication (Bandelin Sonorex RK514BH) during particle dispersion. Subsequently, two parallel aligned iron platelets connected to a DC voltage source were immersed in the suspension, separated by a distance of 1.3 cm. As their electrophoretic mobility differs, the particles were deposited with different parameters to achieve homogeneous coatings which a thickness of <0.5 μm due to simulative restrictions. GS was deposited for 1 min at 100 V and reached a thickness of 0.42 ± 0.04 μm, whereas CT was deposited at 200 V for 3 min resulting in a thickness of 0.33 ± 0.03 μm. Coating thickness was measured by laser scanning microscopy using an Olympus LEXT OLS4100 with a 50x objective (NA: 0.95) at a laser wavelength of 405 nm. The difference between the CT- and the GS

https://doi.org/10.1021/acsanm.2c04729
ACS Appl. Nano Mater. 2023, 6, 1755−1769

Scheme 1. Suspension Preparation and Subsequent Deposition Prior to Fiction Testing

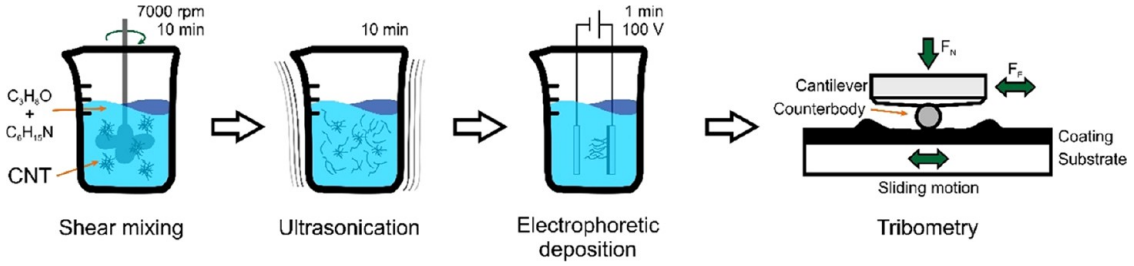

coating thickness should not play a significant role with respect to their lubricity (see S10 in the Supporting Information for an in-depth discussion).

Tribological Testing. The time evolution of the friction coefficient was measured using a ball-on-disc tribometer (CSM Instruments) in linear-reciprocating mode. At the start, a cantilever is loaded onto the substrate with a precise force using piezoactuation to accurately set up the normal load. During the experiment, the deflection of the elastic arms in the horizontal and vertical directions is measured using optical fiber displacement sensors with high precision and accuracy. The stiffness in both directions is known as normal stiffness = 0.1536 (mN/μm) and lateral stiffness = 0.2094 (mN/μm). Alumina balls with a diameter of 6 mm (grade 28, Anton Paar GmbH) were used as counter bodies. A normal load of 100 mN was applied at a velocity of 1 mm/s and a stroke length of 0.6 mm. With a Poisson ratio of 0.22 (alumina) and 0.30 (Fe) as well as Young's moduli of 375 GPa (alumina), and 210 GPa (Fe), this corresponds to a maximum Hertzian contact pressure of 0.36 GPa. Testing was conducted at room temperature and a constant relative humidity of 4 ± 1%. Each sample was measured at least three times to ensure statistical representation.

Materials Characterization. Scanning electron micrographs of the coatings and wear tracks were made using a Helios NanoLab 600 dual-beam workstation (SEM/FIB) by FEI at an acceleration voltage of 5 kV and a current of 1.4 nA. Subsequent EDS characterization of the wear tracks was performed with an integrated EDS detector at an acceleration voltage of 15 kV and a current of 11 nA. Site-specific TEM lamellae were extracted with an Omniprobe 100 micromanipulator and fixed to a standard Cu TEM holder.

To evaluate the structural integrity of the CNTs, Raman characterization was conducted on an inVia Raman microscope (Renishaw) with a laser power of about 2 mW at 532 nm. A 50× objective (numeric aperture: 0.9) was used with a grating of 2,400 lines/mm, resulting in a spectral resolution of 1.2 cm^{-1}. The system was calibrated by the use of a piece of single-crystalline silicon. Measuring points were located in the center of the wear tracks, and each spot was characterized three times (2 accumulations) for statistical representation. Atomic Force Microscopy was used to measure the topography in a Dimension Icon (Bruker) in the PeakForce Tapping mode with a Scanasyst Air Cantilever operated at a drive frequency of 2 kHz and a scan rate of 0.447 Hz. The region of interest with an aspect ratio of 1:1 has a width of 20 μm and 1024 pixels. Subtraction of a planar background was used in the analysis software Gwyddion for post-processing.

For the TEM measurements, first, electron transparent lamellae were prepared from the wear tracks by focused ion beam (FIB) milling using an FEI Strata 400 dual-beam system. Before FIB preparation of each TEM lamella, a protective platinum layer was deposited on the surfaces. The TEM investigations of CNT structures were performed with an FEI Titan3 80−300 (Thermo Fisher Scientific) equipped with a Gatan imaging filter of Tridiem 865 ER (Gatan, Inc.).

ImageJ was used to determine lattice spacing. The resulting spacings were then compared to ICDD data.

Computational Methods. Classical molecular dynamics was used for atomistic simulations.[18] The interatomic forces were modeled with a Tersoff−Brenner bond-order potential, which uses a modified cutoff scheme to ensure correct modeling of covalent bond formation and breakage.[19,38] A time step of 0.1 fs was used in all simulations. Layers of single-wall and multiwall nanotubes between layers of amorphous carbon (aC) were used to model MWCNT degradation. The aC layers were prepared by positioning carbon atoms at random positions in a periodic cubic supercell. A density of 2.2 g/cm^3 was achieved by adjusting the number of carbon atoms. To achieve a realistic atomic configuration, these systems were first heated to 2000 K, freely propagated for 10 ps, and then quenched by coupling them to a Langevin thermostat at 300 K for 100 ps.

To model ideal CNT bundles, eight MWCNTs were used in a quasi-two-dimensional configuration between two aC blocks. These were arranged in four layers with parallel axes in a close-packed structure (Figure 5b), and shear took place perpendicular to them. Due to the computational cost of these simulations, we were restricted to MWCNTs with significantly smaller diameters than those used in our experiments. (10,10)-, (20,20)-, and (40,40)-MWCNTs were used, the number of inner walls varied from a single wall to a complete filling with inner walls with different concentric walls, each 3.4 Å separated from each other. For example, the double-walled (20,20)-MWCNT in Figure 5 consists of a (20,20)- and a (15,15)-wall. The dimensions of the systems were such that six unit cells along the CNT axes were included in the supercells, and the outer walls of each MWCNT were separated by 3 Å initially. (10,10)-CNTs have a diameter of 13.6 Å; thus, in the direction of sliding, they have a length of 33.1 Å, (20,20)- and (40,40)-CNTs have diameters of 27.1 and 54.2 Å, respectively, and the supercells have lengths of 60.3 and 114.6 Å, respectively. In armchair MWCNTs, the unit cells have a length of 2.46 Å along the CNT axes; accordingly, all systems have a length of 14.76 Å along the axes.

The pressure in the systems was controlled by a barostat coupled to stiff layers at the bottom and top of the aC layers blue atoms in Figure 5,[36] and the temperature was controlled by coupling two layers to a Langevin thermostat orange atoms in Figure 5.[39] All simulations were performed at a temperature of 300 K. For shearing, the upper stiff layer was displaced horizontally at a constant velocity of 30 m/s. The shear stresses τ were determined by the forces acting on the rigid layers. Three passes of the upper aC layer over the lower one were simulated during the sliding simulations. The shear stresses were evaluated during the second and third passes to allow the system to reach a steady state. At the same time, the damage of the CNTs was characterized by determining the number of nearest neighbors of each atom within a 2 Å radius. Atoms that had 4 or more nearest neighbors were considered sp^3-hybridized, and all other atoms as sp^2-hybridized. The ratio of the numbers was used as a measure for the deviation from the typical structure of CNT walls (100% 3-fold coordinated).

To simulate crossed (20,20) MWCNTs, aC layers with a quadratic base were used. Five different distances of the CNT axes from each other were employed: 29.5, 44.3, 59.1, 88.6, and 118.1 Å, which correspond to direct contact and to distances of roughly 1.5, 2, 3, and 4 MWCNT diameters between the axes. Since the CNT axes are rotated by 90° with respect to each other in successive layers, the result is a quadratic area of the aC layers with edge lengths of 12, 18, 24, 36, and 48 unit cells of (20,20) MWCNTs.

https://doi.org/10.1021/acsanm.2c04729
ACS Appl. Nano Mater. 2023, 6, 1755−1769

■ ASSOCIATED CONTENT

Supporting Information

The Supporting Information is available free of charge at https://pubs.acs.org/doi/10.1021/acsanm.2c04729.

Additional MD simulation results for (10,10) and (40,40) MWCNT (Figures S1 and S2); relationship between transition pressure and filling ratio for (10,10), (20,20), and (40,40) MWCNTs (Figure S3); near-surface cross-sectional transmission electron micrographs of the GS-derived tribofilm/substrate (Figure S4); additional transmission electron micrographs of the samples shown in Figure 4 (Figures S5−S9); role of coating thickness for tribological evaluation (S10); and lubricant retention (S11) (PDF)

Video of MD simulation shown in Figure 5c (Movie_12c) (MP4)

Video of MD simulation shown in Figure 5d (Movie_12d) (MP4)

Video of MD simulation shown in Figure 5e (Movie_12e) (MP4)

■ AUTHOR INFORMATION

Corresponding Authors

Timothy MacLucas − *Chair of Functional Materials, Saarland University, Saarbrücken 66123, Germany*; Email: timothy.maclucas@uni-saarland.de

Michael Moseler − *Fraunhofer Institute for Mechanics of Materials IWM, MicroTribology Center μTC, 79108 Freiburg, Germany; Modelling of Functional Nanomaterials Group, Institute of Physics, University of Freiburg, 79104 Freiburg, Germany; Freiburg Materials Research Center, University of Freiburg, 79104 Freiburg, Germany; Cluster of Excellence livMatS, Freiburg Center for Interactive Materials and Bioinspired Technologies, University of Freiburg, 79110 Freiburg, Germany*; orcid.org/0000-0002-7064-1351; Email: michael.moseler@iwm.fraunhofer.de

Authors

Andreas Klemenz − *Fraunhofer Institute for Mechanics of Materials IWM, MicroTribology Center μTC, 79108 Freiburg, Germany*; orcid.org/0000-0001-5677-5639

Patrick Grünewald − *INM—Leibniz Institute for New Materials, 66123 Saarbrücken, Germany*

Volker Presser − *INM—Leibniz Institute for New Materials, 66123 Saarbrücken, Germany; Department of Materials Science & Engineering, Saarland University, 66123 Saarbrücken, Germany; Saarene—Saarland Center for Energy Materials and Sustainability, 66123 Saarbrücken, Germany*; orcid.org/0000-0003-2181-0590

Leonhard Mayrhofer − *Fraunhofer Institute for Mechanics of Materials IWM, MicroTribology Center μTC, 79108 Freiburg, Germany*

Gianpietro Moras − *Fraunhofer Institute for Mechanics of Materials IWM, MicroTribology Center μTC, 79108 Freiburg, Germany*; orcid.org/0000-0002-4623-2881

Sebastian Suarez − *Chair of Functional Materials, Saarland University, Saarbrücken 66123, Germany; Department of Materials Science & Engineering, Saarland University, 66123 Saarbrücken, Germany*

Martin Dienwiebel − *Fraunhofer Institute for Mechanics of Materials IWM, MicroTribology Center μTC, 79108 Freiburg, Germany; Karlsruhe Institute of Technology (KIT), IAM—Institute for Applied Materials, MicroTribology Center μTC, 76131 Karlsruhe, Germany*; orcid.org/0000-0001-7682-0441

Frank Mücklich − *Chair of Functional Materials, Saarland University, Saarbrücken 66123, Germany*

Complete contact information is available at: https://pubs.acs.org/10.1021/acsanm.2c04729

Author Contributions

[¶]T.M. and A.K. contributed equally to this work. T.M.: sample preparation, tribometry, characterization, writing, figures, tables, discussion. A.K.: simulation, writing, figures, tables, discussion. P.G.: characterization. V.P.: discussion, review. L.M.: discussion, review. G.M.: discussion, review. S.S.: sample preparation, characterization, writing, discussion. M.D.: characterization, discussion, review. F.M.: discussion, review. M.M.: simulation, writing, discussion. All authors approved the final version of the manuscript.

Notes

The authors declare no competing financial interest.

■ ACKNOWLEDGMENTS

All authors gratefully acknowledge funding by Deutsche Forschungsgemeinschaft (DFG, German Research Foundation) via the priority program SPP2074 within the projects MU 959/44-1, MO 879/21-1, and DI 1494/7-1. Furthermore, T.M., S.S., and F.M. gratefully acknowledge funding for the ZuMat project, supported by the State of Saarland from the European Regional Development Fund (Europäischen Fonds für Regionale Entwicklung, EFRE). Funding for the PFIB/SEM instrument by the German Research Foundation is greatly acknowledged (INS 256/510-1 FUGG). Atomistic simulations have been carried out at the Jülich Supercomputing Centre (Grant No. hfr19). The authors thank Reinhard Schneider from the Laboratory for Electron microscopy at the Karlsruhe Institute of Technology for performing the TEM measurements and Samantha Husmann from the Energy Materials group at the Leibniz Institute for New Materials (INM) in Saarbrücken for her contribution to the Raman analysis. V.P. thanks Eduard Arzt (INM) for his continued support.

■ REFERENCES

(1) Reinert, L.; Lasserre, F.; Gachot, C.; Grützmacher, P.; MacLucas, T.; Souza, N.; Mücklich, F.; Suarez, S. Long-Lasting Solid Lubrication by CNT-Coated Patterned Surfaces. *Sci. Rep.* **2017**, *7*, No. 42873.

(2) Maclucas, T.; Schütz, S.; Suarez, S.; Mücklich, F. Surface Protection of Austenitic Steels by Carbon Nanotube Coatings. *Surf. Topogr.: Metrol. Prop.* **2018**, *6*, No. 014005.

(3) Schäfer, C.; Reinert, L.; MacLucas, T.; Grützmacher, P.; Merz, R.; Mücklich, F.; Suarez, S. Influence of Surface Design on the Solid Lubricity of Carbon Nanotubes-Coated Steel Surfaces. *Tribol. Lett.* **2018**, *66*, No. 89.

(4) Dickrell, P. L.; Sinnott, S. B.; Hahn, D. W.; Raravikar, N. R.; Schadler, L. S.; Ajayan, P. M.; Sawyer, W. G. Frictional Anisotropy of Oriented Carbon Nanotube Surfaces. *Tribol. Lett.* **2005**, *18*, 59−62.

(5) Dickrell, P. L.; Pal, S. K.; Bourne, G. R.; Muratore, C.; Voevodin, A. A.; Ajayan, P. M.; Schadler, L. S.; Sawyer, W. G. Tunable Friction Behavior of Oriented Carbon Nanotube Films. *Tribol. Lett.* **2006**, *24*, 85−90.

(6) Miyoshi, K.; Street, K. W.; Vander Wal, R. L.; Andrews, R.; Sayir, A. Solid Lubrication by Multiwalled Carbon Nanotubes in Air and in Vacuum. *Tribol. Lett.* **2005**, *19*, 191−201.

(7) Reinert, L.; Schütz, S.; Suárez, S.; Mücklich, F. Influence of Surface Roughness on the Lubrication Effect of Carbon Nanoparticle-Coated Steel Surfaces. *Tribol. Lett.* **2018**, *66*, No. 45.
(8) Rosenkranz, A.; Heib, T.; Gachot, C.; Mücklich, F. Oil Film Lifetime and Wear Particle Analysis of Laser-Patterned Stainless Steel Surfaces. *Wear* **2015**, *334*−*335*, 1−12.
(9) Rosenkranz, A.; Reinert, L.; Gachot, C.; Mücklich, F. Alignment and Wear Debris Effects between Laser-Patterned Steel Surfaces under Dry Sliding Conditions. *Wear* **2014**, *318*, 49−61.
(10) Rosenkranz, A.; Costa, H. L.; Baykara, M. Z.; Martini, A. Synergetic Effects of Surface Texturing and Solid Lubricants to Tailor Friction and Wear − A Review. *Tribol. Int.* **2021**, *155*, No. 106792.
(11) Falvo, M. R.; Taylor, R. M.; Helser, A.; Chi, V.; Brooks, F. P.; Washburn, S.; Superfine, R. Nanometre-Scale Rolling and Sliding of Carbon Nanotubes. *Nature* **1999**, *397*, 236−238.
(12) Buldum, A.; Lu, J. P. Atomic Scale Sliding and Rolling of Carbon Nanotubes. *Phys. Rev. Lett.* **1999**, *83*, 5050−5053.
(13) Heo, S.; Sinnott, S. B. Effect of Molecular Interactions on Carbon Nanotube Friction. *J. Appl. Phys.* **2007**, *102*, No. 064307.
(14) Ni, B.; Sinnott, S. B. Tribological Properties of Carbon Nanotube Bundles Predicted from Atomistic Simulations. *Surf. Sci.* **2001**, *487*, 87−96.
(15) Boccaccini, A. R.; Cho, J.; Roether, J. A.; Thomas, B. J. C.; Minay, E. J.; Shaffer, M. S. P. Electrophoretic Deposition of Carbon Nanotubes. *Carbon* **2006**, *44*, 3149−3160.
(16) MacLucas, T.; Suarez, S. On the Solid Lubricity of Electrophoretically Deposited Carbon Nanohorn Coatings. *Lubricants* **2019**, *7*, No. 62.
(17) Alderete, B.; MacLucas, T.; Espin, D.; Brühl, S. P.; Mücklich, F.; Suarez, S. Near Superhydrophobic Carbon Nanotube Coatings Obtained via Electrophoretic Deposition on Low-Alloy Steels. *Adv. Eng. Mater.* **2021**, *23*, No. 2001448.
(18) Thompson, A. P.; Aktulga, H. M.; Berger, R.; Bolintineanu, D. S.; Brown, W. M.; Crozier, P. S.; in 't Veld, P. J.; Kohlmeyer, A.; Moore, S. G.; Nguyen, T. D.; Shan, R.; Stevens, M. J.; Tranchida, J.; Trott, C.; Plimpton, S. J. LAMMPS - a Flexible Simulation Tool for Particle-Based Materials Modeling at the Atomic, Meso, and Continuum Scales. *Comput. Phys. Commun.* **2022**, *271*, No. 108171.
(19) Brenner, D. W.; Shenderova, O. A.; Harrison, J. A.; Stuart, S. J.; Ni, B.; Sinnott, S. B. A Second-Generation Reactive Empirical Bond Order (REBO) Potential Energy Expression for Hydrocarbons. *J. Phys.: Condens. Matter* **2002**, *14*, 783−802.
(20) Lin, M.; Tan, J. P. Y.; Boothroyd, C.; Loh, K. P.; Tok, E. S.; Foo, Y.-L. Dynamical Observation of Bamboo-like Carbon Nanotube Growth. *Nano Lett.* **2007**, *7*, 2234−2238.
(21) Lee, C. J.; Park, J. Growth Model of Bamboo-Shaped Carbon Nanotubes by Thermal Chemical Vapor Deposition. *Appl. Phys. Lett.* **2000**, *77*, 3397−3399.
(22) Blau, P. J. On the Nature of Running-In. *Tribol. Int.* **2005**, *38*, 1007−1012.
(23) MacLucas, T.; Daut, L.; Grützmacher, P.; Guitar, M. A.; Presser, V.; Gachot, C.; Suarez, S.; Mücklich, F. Influence of Structural Depth of Laser-Patterned Steel Surfaces on the Solid Lubricity of Carbon Nanoparticle Coatings. *Friction* **2022**, 1−16.
(24) MacLucas, T.; Leonhard-Trautmann, P.; Suarez, S.; Mücklich, F. Long-Term Lubricity of Carbon Nanoparticle Coatings on Periodically Laser-Patterned Metallic Surfaces. *Tribol. Lett.* **2022**, *70*, No. 123.
(25) Berman, D.; Erdemir, A.; Sumant, A. V. Graphene: A New Emerging Lubricant. *Mater. Today* **2014**, *17*, 31−42.
(26) Ferreira, E. H. M.; Moutinho, M. V. O.; Stavale, F.; Lucchese, M. M.; Capaz, R. B.; Achete, C. A.; Jorio, A. Evolution of the Raman Spectra from Single-, Few-, and Many-Layer Graphene with Increasing Disorder. *Phys. Rev. B* **2010**, *82*, No. 125429.
(27) Cançado, L. G.; Jorio, A.; Ferreira, E. H. M.; Stavale, F.; Achete, C. A.; Capaz, R. B.; Moutinho, M. V. O.; Lombardo, A.; Kulmala, T. S.; Ferrari, A. C. Quantifying Defects in Graphene via Raman Spectroscopy at Different Excitation Energies. *Nano Lett.* **2011**, *11*, 3190−3196.
(28) Ferrari, A. C.; Robertson, J. Interpretation of Raman Spectra of Disordered and Amorphous Carbon. *Phys. Rev. B* **2000**, *61*, 14095−14107.
(29) Cançado, L. G.; Jorio, A.; Pimenta, M. A. Measuring the Absolute Raman Cross Section of Nanographites as a Function of Laser Energy and Crystallite Size. *Phys. Rev. B* **2007**, *76*, No. 64304.
(30) Reinert, L.; Varenberg, M.; Mücklich, F.; Suárez, S. Dry Friction and Wear of Self-Lubricating Carbon-Nanotube-Containing Surfaces. *Wear* **2018**, *406*−*407*, 33−42.
(31) DiLeo, R. A.; Landi, B. J.; Raffaelle, R. P. Purity Assessment of Multiwalled Carbon Nanotubes by Raman Spectroscopy. *J. Appl. Phys.* **2007**, *101*, No. 064307.
(32) Niyogi, S.; Hamon, M. A.; Hu, H.; Zhao, B.; Bhowmik, P.; Sen, R.; Itkis, M. E.; Haddon, R. C. Chemistry of Single-Walled Carbon Nanotubes. *Acc. Chem. Res.* **2002**, *35*, 1105−1113.
(33) Grützmacher, P. G.; Suarez, S.; Tolosa, A.; Gachot, C.; Song, G.; Wang, B.; Presser, V.; Mücklich, F.; Anasori, B.; Rosenkranz, A. Superior Wear-Resistance of Ti3C2Tx Multilayer Coatings. *ACS Nano* **2021**, *15*, 8216−8224.
(34) Liu, M.; Cowley, J. M. Structures of Carbon Nanotubes Studied by HRTEM and Nanodiffraction. *Ultramicroscopy* **1994**, *53*, 333−342.
(35) Yu, M. F.; Lourie, O.; Dyer, M. J.; Moloni, K.; Kelly, T. F.; Ruoff, R. S. Strength and Breaking Mechanism of Multiwalled Carbon Nanotubes under Tensile Load. *Science* **2000**, *287*, 637−640.
(36) Pastewka, L.; Moser, S.; Moseler, M. Atomistic Insights into the Running-in, Lubrication, and Failure of Hydrogenated Diamond-like Carbon Coatings. *Tribol. Lett.* **2010**, *39*, 49−61.
(37) Konicek, A. R.; Grierson, D. S.; Sumant, A. V.; Friedmann, T. A.; Sullivan, J. P.; Gilbert, P. U. P. A.; Sawyer, W. G.; Carpick, R. W. Influence of Surface Passivation on the Friction and Wear Behavior of Ultrananocrystalline Diamond and Tetrahedral Amorphous Carbon Thin Films. *Phys. Rev. B* **2012**, *85*, No. 155448.
(38) Pastewka, L.; Pou, P.; Pérez, R.; Gumbsch, P.; Moseler, M. Describing Bond-Breaking Processes by Reactive Potentials: Importance of an Environment-Dependent Interaction Range. *Phys. Rev. B* **2008**, *78*, No. 161402.
(39) Frenkel, D.; Smit, B.; Ratner, M. A.*Understanding Molecular Simulation: From Algorithms to Applications*; Academic Press: San Diego, 1996; Vol. *2*.

https://doi.org/10.1021/acsanm.2c04729
ACS Appl. Nano Mater. 2023, 6, 1755−1769

V. Long-term lubricity of carbon nanoparticle coatings on periodically laser-patterned metallic surfaces

Timothy MacLucas, Philipp Leonhard-Trautmann, Sebastian Suarez, Frank Mücklich

Chair of Functional Materials, Dept. of Materials Science and Engineering, Saarland University, Campus D3.3, Saarbrücken 66123, Germany

Published in **"Tribology Letters"** (2022) (IF: 3.2 [2022])
Accessible online at: https://doi.org/10.1007/s11249-022-01667-3

Own contribution: sample preparation, tribometry, characterization, writing – original draft, figures, tables, discussion

Tribology Letters (2022) 70:123
https://doi.org/10.1007/s11249-022-01667-3

ORIGINAL PAPER

Long-Term Lubricity of Carbon Nanoparticle Coatings on Periodically Laser-Patterned Metallic Surfaces

Timothy MacLucas[1] · Philipp Leonhard-Trautmann[1] · Sebastian Suarez[1] · Frank Mücklich[1]

Received: 22 August 2022 / Accepted: 14 October 2022 / Published online: 31 October 2022
© The Author(s) 2022

Abstract
The lubricity of coatings made from different types of carbon nanoparticles such as carbon onions, carbon nanohorns and carbon nanotubes is investigated on line-patterned AISI 304 stainless-steel substrates using ball-on-disc tribometry over 200,000 sliding cycles. Picosecond direct laser interference patterning is used to create line-patterns on the substrate surfaces which are subsequently coated by electrophoretic deposition. Friction testing is conducted on as-processed surfaces in linear reciprocal mode at a normal load of 100 mN with alumina and 100Cr6 as counter body materials. The resulting wear tracks on the substrates as well as wear scars on the counter bodies are characterized by scanning electron microscopy as well as energy-dispersive X-ray spectroscopy. Tribometry shows that CNTs have the ability to maintain lubricity against both counter body materials. CO and CNH coatings sustain their lubricity against 100Cr6 over the full test duration but fail against alumina. In contrast to alumina, substantial carbon transfer from the substrate surface to 100Cr6 counter body is observed.

Keywords Solid lubricant coatings · Carbon nanotubes · Carbon onions · Carbon nanohorns · Long-term lubricity · Tribometry

1 Introduction

Graphitic nanocarbons represent a material family that includes particles with a variety of different geometries and sizes. Carbon nanotubes (CNT) are among its most prominent members with a proven record of providing effective solid lubrication as a coating [1–4], reinforcing phase in composites [5–8] or lubricant additive [9–11]. Despite different particle morphologies, carbon onions (CO) and carbon nanohorns (CNH) have also demonstrated their ability to significantly reduce friction [12–14], although their tribological properties have not been as intensively researched.

Due to weak adhesion between carbon nanoparticles and metallic substrates, surface texturing is required to prevent their removal from the contact during tribological load, as demonstrated for CNT coatings on stainless steel by Reinert et al. [3]. When combining textured surfaces with carbon nanoparticle coatings, the grooves can act as lubricant reservoirs, providing a steady lubricant supply directly into the contact. Simultaneously, filled reservoirs absorb generated wear particles, thus, preventing them from entering the contact.

Such surface textures can be manufactured in the form of precisely tailored patterns using picosecond direct laser interference patterning (ps-DLIP) [15, 16]. During ps-DLIP, the interference of two or more pulsed sub beams directly on the substrates' surface induces photothermal processes at the interference maxima, resulting in the formation of grooves, grids or dimples with periodicities and aspect ratios that are adjustable to a certain extent. The texture offered by ps-DLIP line-patterns is well suited to carbon nanoparticle coatings, as their aspect ratio is well matched to accommodate and store considerable amounts of particles.

As-processed surfaces are subsequently coated using electrophoretic deposition (EPD), a method for depositing dispersed carbon nanoparticles from a solution onto a conductive substrate by applying a sufficiently high voltage. EPD is well-established for producing homogeneous coatings made from various sp^2-hybridized carbon nanoparticles as it combines simplicity, short processing times, applicability to complex substrate geometries, upscaling potential and cost-effectiveness, while allowing for reproducible deposition results [3, 12, 17–19].

✉ Timothy MacLucas
timothy.maclucas@uni-saarland.de

[1] Department of Materials Science and Engineering, Saarland University, Campus D3.3, 66123 Saarbrücken, Germany

A major criterium for any lubrication system is its ability to maintain lubricity over significant periods of time against different counter body materials without the need for re-supply. In this context, Schäfer et al. conducted tribometry on CNT-coated and cross-patterned austenitic steel substrates over 110,000 cycles at a load of 1 N [1]. The cross-patterns had a structural depth of 1 µm and were manufactured using femto-second direct laser writing. Experiments were conducted on a ball-on-disc tribometer in rotational mode using an alumina counter body (6 mm diameter) at 25 °C and 45% relative humidity. A coefficient of friction (COF) < 0.2 was maintained for about 45,000 cycles before starting to increase considerably.

In this work, coatings made of three different types of carbon nanoparticle on line-patterned stainless-steel platelets are subjected to ball-on-disc friction testing over 200,000 cycles (240 m). The objective is to investigate and compare their respective long-term COF developments against two technically relevant counter body materials: on the one hand, alumina due to its inertness and 100Cr6 as a common bearing steel. Based on the results of MacLucas et al., a low structural depth of 0.23 µm was chosen for the pattern in order to optimize the lubricity of the particle coatings [4].

2 Experimental Section

2.1 Materials

CVD-grown multiwall CNTs with a diameter of 30–85 nm and a length of 10–15 µm purchased at Graphene Supermarket (USA) were utilized. The COs were synthesized by annealing nanodiamonds (NaBond Technologies Co., purity > 98%, particle diameter: 4–8 nm) in a vacuum furnace (model 1100–3580-W1, Thermal Technology Inc.) at 1750 °C for 3 h at a rate of 10 °C/min [20]. Commercially available dahlia-type CNH with a 60–120 nm cluster diameter and a single horn diameter of 2–5 nm (Carbonium SRL, Italy) were used. Mirror-polished AISI 304 austenitic stainless-steel platelets (20 × 20 mm^2, 1 mm thick) purchased at Brio Kontrollspiegel GmbH (Germany) were used as substrate material. The platelets were thoroughly cleaned with acetone and isopropanol prior to ps-DLIP processing and EPD.

2.2 Picosecond DLIP

A Nd:YAG pulsed laser (Edgewave PX-series InnoSlab) integrated into a RDX 500 nano laser system (Pulsar Photonics GmbH, Germany) was used to fabricate line-patterns on the AISI 304 platelets. The system operates at a wavelength of 532 nm and the samples were processed at 0.5 W. Aforesaid patterns were created with a periodicity (line spacing) of 3.5 µm using two interfering sub beams with a pulse duration of 12 ps. Finally, the patterned surfaces were cleaned by ultrasonication in citric acid, acetone and isopropanol for 15 min each to remove superficial oxide produced during the laser-processing.

2.3 Confocal Laser Scanning Microscopy (CLSM)

An Olympus LEXT OLS4100 confocal laser scanning microscope was utilized to measure the structural depth of the patterns, coating thicknesses. The microscope was operated with a 50 × objective (N.A.: 0.95) at a laser wavelength of 405 nm and a vertical and lateral resolution of 10 nm and 120 nm, respectively. The mean height R_C was used as a measure for the structural depth of the line-patterns over a sampling length of 259 µm. To ensure statistical representation, R_C was determined for 10 different profile lines on images taken at three different spots on the patterned sample surfaces. As the coating thickness cannot be determined directly on the sample surface due to its patterning, separate depositions were made on non-patterned platelets on which deposition parameters were optimized to achieve the target thickness of 4.0–4.5 µm. Subsequently, the optimized parameters were applied to the coating of the patterned surfaces to ensure comparable film thickness.

2.4 Dispersion Preparation and Electrophoretic Deposition

Each dispersion used for electrophoretic deposition contained 70 ml of isopropanol, 10 ml of trimethylamine (ACROS Organics, purity: 99%) and 7 mg of carbon nanoparticle content (0.1 mg/ml solvent). For dispersion, the colloids were subjected to shear mixing (Ultra-Turrax IKA T25), followed by ultrasonication in a Bandelin Sonorex RK514BH (for 10 min each). Subsequently, both the substrate and a comparable platelet representing the counter electrode were immersed in the dispersion and arranged in parallel. After being connected to a DC voltage supply, deposition was conducted at 300 V for 3 min (CNT, CNH) and 4.5 min (CO) to ensure comparable coating thickness.

2.5 Tribometry

A ball-on-disc tribometer (CSM instruments) was used for friction testing in linear reciprocal mode with a stroke length of 0.6 mm at a load of 100 mN. Sliding direction was transversal to that of the line-pattern and performed at a velocity of 1 mm/s. Balls with a diameter of 6 mm from either alumina (Kugel Pompel, GD24) or 100Cr6 steel (Kugel Pompel, Kl.3) were deployed as counter bodies which corresponds to a Hertzian pressure of 0.31 GPa (100Cr6 vs AISI304) and 0.36 GPa (alumina vs AISI304), respectively. Testing was

carried out at room temperature and 4% relative humidity. To attenuate excessive COF oscillation in the graphs, the raw data were slightly smoothed using a Savitzky-Golay filter (50 p). Each sample was measured thrice to ensure statistical representation.

2.6 Wear Track Characterization

A Helios G4 PFIB CXe dual beam work station (Thermo Fisher Scientific, USA) with an integrated EDAX detector for energy-dispersive x-ray spectroscopy (EDS) was employed to characterize the resulting wear tracks at an acceleration voltage of 5 kV and a beam current of 1.6 nA. Chemical mapping was conducted with 8 cumulative frames.

3 Results and Discussion

3.1 Surface Characterization

Figure 1 depicts top view CLSM images of the line-patterned AISI 304 stainless steel substrates after ps-DLIP processing including representative line profiles. As-processed surfaces were subsequently coated with COs (Fig. 1a), CNH (Fig. 1b) and CNTs (Fig. 1c). R_C was determined based on line profiles at different locations to get a representative value for the overall structural depth of the respective pattern. As shown by the images, all surfaces are homogeneously patterned and have close to identical line profiles as well as structural depths.

Figure 2 depicts CO-, CNH- and CNT-coating sections on non-patterned steel surfaces as coating thickness cannot be reliably measured directly on as-processed surfaces. In this case, the profile height of the left (blue rectangle) and right (red rectangle) coating sections are compared to that of an uncoated section in the middle (blue square) on non-patterned and mirror-polished substrates to determine coating thickness. The exact same EPD parameters used for the deposition on non-patterned surfaces were subsequently used to coat the patterned surfaces. The mean thicknesses of all coatings range between 4.2 and 4.4 µm and are, thus, comparable, so that coating thickness can be eliminated as an influencing factor.

3.2 Long-Term Tribological Testing

Figure 3a shows the coefficient of friction (COF) development of the carbon nanoparticle coatings against an alumina

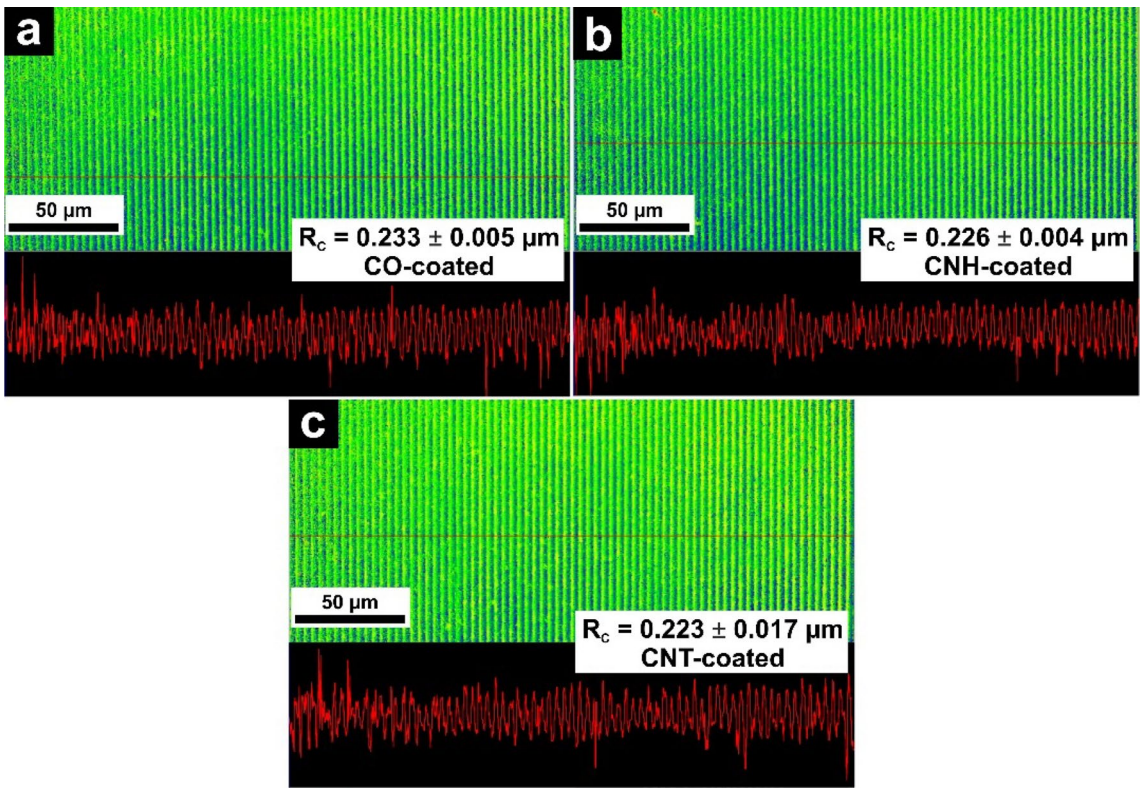

Fig. 1 Top view confocal laser scanning micrographs of the line-patterned AISI 304 substrate which were subsequently coated with **a** COs, **b** CNH and **c** CNTs. In addition to that, the images show representative line profiles and the overall structural depth (R_C) of the respective pattern (Color figure online)

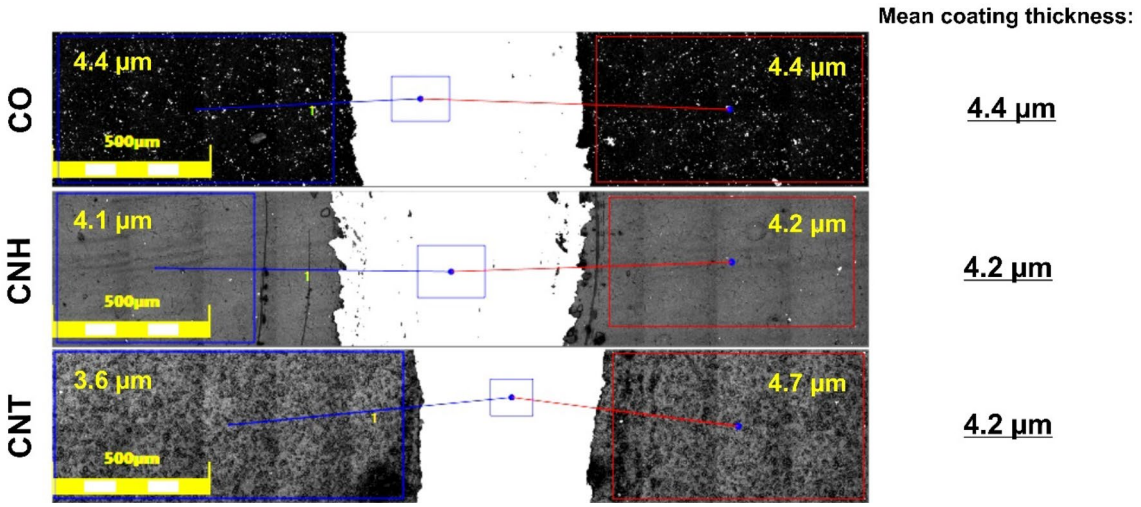

Fig. 2 Confocal laser scanning micrographs of the coatings on non-patterned AISI 304 substrate where the profile height of the marked coating sections (blue rectangles on the left and red rectangles on the right) is compared to that of the uncoated section (blue square in the middle) in order to determine the mean thickness of the CO-, CNH- and CNT-coatings (Color figure online)

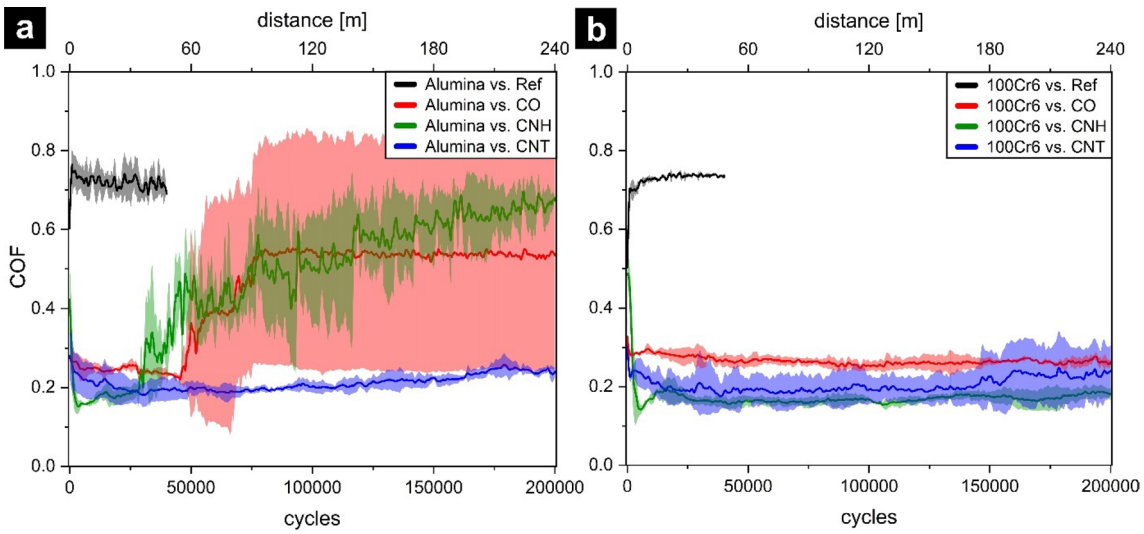

Fig. 3 COF development of CO-, CNT- and CNH-coatings on laser-patterned stainless-steel surfaces against both **a** alumina and **b** 100Cr6 counter bodies (Color figure online)

counter body over 200,000 cycles. A plain uncoated steel surface serves as reference (Ref). Within the initial cycles, its COF rises sharply to 0.76, followed by a slight decrease. According to Blau, this running-in behaviour can be assigned to type b, which is typically observed with non-lubricated metals [21]. After 40,000 cycles, Ref can be considered run-in whilst ranging around 0.70, corresponding well with comparable literature [3]. The COs show a type f behaviour with a subsequent decrease to a COF of 0.22. This is followed by an abrupt and sharp increase until entering steady-state after 78,000 cycles, maintaining a COF of 0.54 throughout the remaining cycles. The COs' extreme standard deviation is due to inconsistent lubricity as during one measurement, lubrication is maintained over the full distance whereas the other two failed prematurely. The running-in of CNH is characterized by a steep initial decline, reaching a COF of 0.17, followed by a steady increase (type h). After 30,000 cycles, the rise increases considerably and the COF continues to climb throughout the test, not reaching a steady-state at all with a final value of 0.66. The likely cause of the observed COF increase is a gradual lubricant depletion, setting in after roughly 30,000 cycles, despite the

surface patterning. Similar to the COs, the CNTs display a distinct type f running-in behaviour with a minimum COF of 0.18 after 30,000 cycles. Subsequently, the COF increases slightly but steadily over the remaining testing period, reaching a final COF of 0.24. CNTs are the only particle type able to maintain lubricity against alumina over the full duration of the friction test.

The COF development of the carbon nanoparticle coatings against a 100Cr6 counter body is presented in Fig. 3b. Unlike alumina, Ref shows a type a running-in and enters steady-stage after approximately 20,000 cycles at 0.73. Resembling a type h, the CO coatings' running-in differs from the measurements against alumina also. Consequently, the COF shows a slight decline and enters steady-state after about 50,000 cycles from which on, it remains around 0.26. The CNHs' running-in strongly resembles that against alumina and can be classified accordingly as type h. In contrast, however, after running-in during which a minimum COF of 0.14 was reached, steady-state is established around 45,000 completed cycles with the COF ranging between 0.16 and 0.18 for the residual test duration. The CNTs running-in remains unchanged by switching the counter body (type f), reaching steady-state lubrication at approximately 45,000 cycles. After 140,000 cycles, the COF starts to increase again, along with the standard deviation, resulting in a final value of 0.24.

In summary, CNTs are able to maintain a lower COF than the COs for almost 150,000 cycles, after which the standard deviations begin to overlap. The CNHs' COF, on the other hand, can be considered significantly lower than that of the COs over the full testing period. Moreover, CNH represent the only particle type able to maintain a COF below 0.20, deemed the threshold for effective solid lubrication by Aouadi et al. [22]. In contrast to tribological testing against the alumina counter body, all carbon nanoparticle coatings were able to sustain lubricity against 100Cr6. It should be noted, that sp^2 carbon nanoparticles are expected to degrade heavily during this type of friction testing as reported specifically for CNTs [1, 3, 5]. It is, therefore, not entirely correct to refer to these particles as such after friction testing, but rather as a tribofilm derived from the respective particle.

3.3 Morphological & Chemical Wear Track Analysis

The SEM image in Fig. 4a shows a heavily worn wear track on the uncoated AISI 304 substrate after rubbing against an alumina counter body (reference) over 40,000 cycles. Adhesion with subsequent delamination represent the main wear mechanisms, however, adhesion is more dominant as indicated by clearly recognizable and characteristic island formation throughout the wear track. Bright green areas throughout the wear track in the corresponding EDS map (Fig. 4b) indicate severe oxidation.

Friction testing against 100Cr6 also leads to heavy wear caused by adhesion (Fig. 4c), however, the resulting wear track is notably wider than its alumina equivalent depicted in Fig. 4a. Since 100Cr6 is softer, permanent deformation is dominant, resulting in a larger contact area. The oxygen map in Fig. 4d reveals severe and uniform oxidation. Furthermore, the particle pile-up at the bottom right of the track in Figs. 4c and d reveals the formation and subsequent removal of oxidic wear particles from the contact.

As previously indicated, the COs inconsistent tribological behaviour suggests fundamentally different lubrication conditions which is confirmed by Fig. 5a–d. The SE micrograph in Fig. 5a shows a fully depleted wear track with pronounced island formation, which is characteristic of adhesion as the dominant wear mechanism. The corresponding EDS map depicted in Fig. 5b verifies complete carbon removal along with severe substrate oxidization, extensive wear particle formation and their subsequent deposition directly next to the wear track. In contrast, Fig. 5c depicts a much narrower and less worn track in which the original surface pattern is well preserved (inset for higher magnification). Considering its chemical map (Fig. 5d), remaining tribofilm can be identified along the edges of the wear track, where minor oxidation has occurred. Of the three CO-coated wear tracks, depletion occurred in two cases while lubrication was maintained in one case. Figure 5e shows island formation once again, therefore, the CNH-coated wear tracks were worn in the same way as the reference or depleted CO tracks: complete carbon removal resulted in severe oxidation, often causing a significant oxide pile-up at the end of the wear track (Fig. 5f). Figure 5g shows the CNT-coated wear track in the centre of which the remnants of the laser-pattern can still be identified and appear to be largely intact (inset for higher magnification). In this case, considerable amounts of CNT-derived carbon remained in the grooves of the pattern and formed large patches, sustaining effective lubrication with no apparent oxidation (Fig. 5h). Bulging at the right end of the wear track demonstrates good coating cohesion.

Unlike alumina, the CO and CNH coatings are not fully removed during friction testing against 100Cr6 (Fig. 6a and c). In the case of COs, the filled grooves are distinct and the line-pattern is well preserved, whereas on the CNH-coated surface, the pattern has been partially worn away (insets for higher magnification). Elemental mapping shows relatively small amounts of CO-derived tribofilm along the edges of the contact area as well as minimum local oxidation at both ends of the wear track (Fig. 6b). In CNH-coated wear tracks, oxidation is more pronounced and can be classified as minor (Fig. 6d). Secondly, the CNH-derived tribofilm is more abundant and spread over a larger area outside of the contact. The remaining carbon is sufficiently abundant for patches to be formed. After rubbing against 100Cr6, the CNT-coated wear track looks similar to its alumina equivalent with the

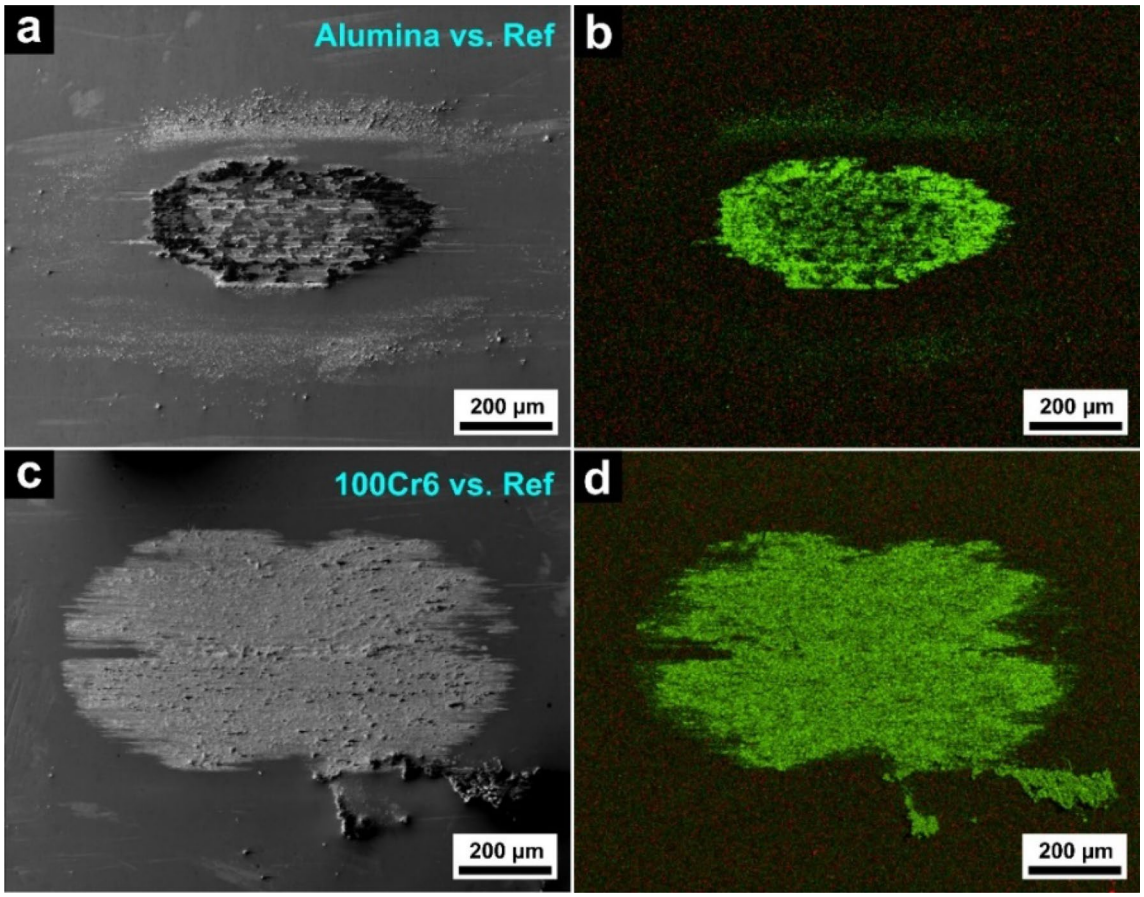

Fig. 4 Scanning electron micrographs of representative uncoated substrates (reference) after rubbing against an **a** alumina and **c** 100Cr6 ball for 40,000 friction cycles. Corresponding EDS maps against **b** alumina and **d** 100Cr6. Green stands for oxygen, red for carbon (Color figure online)

substrate pattern still clearly recognizable (Fig. 6e, inset for higher magnification). The corresponding EDS map reveals significant amounts of carbon, often in the form coherent patches on top of the pattern, with no discernible substrate oxidation (Fig. 6f).

3.4 Material Transfer

Figure 7a shows a typical wear scar on the alumina counter body after friction testing with failed lubrication. The SEM/EDS overlay depicted in Fig. 7b, shows adhesion-induced iron transfer from the substrate wear track to the alumina ball. The thin red film observable in Fig. 7c represents negligible amounts of carbon likely stemming from atmospheric contamination.

After friction testing with successful lubrication, material transfer is either minor (Fig. 8a) or non-detectable (Fig. 8c) as confirmed by the corresponding carbon maps (Fig. 8b and d). Similar to Fig. 7c, the red bands visible in Fig. 8b originate from atmospheric pollution. In case of effective lubrication, the resulting wear scars on the alumina are typically smaller compared to those created by unlubricated friction.

Figure 9a shows EDS mapping of a representative wear scar on a 100Cr6 counter body after tribometry against a reference surface, leading to severe oxidation, as indicated by the bright green areas surrounding the contact. More specifically, oxidic wear particles were generated and subsequently removed from the contact. After testing against CO-, CNH- and CNT-coated surfaces (Fig. 9b–d), the resulting wear scars are smaller compared to that of the reference and oxidation is considerably reduced. The images further demonstrate substantial carbon transfer from the coated substrate to the counter body during tribological load. This phenomenon is particle-independent and can be explained by the formation of covalent bonds between carbon and substrate iron as indicated by MacLucas et al. [4] whereas alumina is far less reactive.

The results have shown that solely CNTs are able to maintain solid lubricity over the full duration of the friction test with no detectable oxidation on any of the substrates against both counter body materials. We believe patch formation to be the principal reason for this behaviour as the presence of patches on top of the pattern effectively separates the sliding surfaces. Due to the

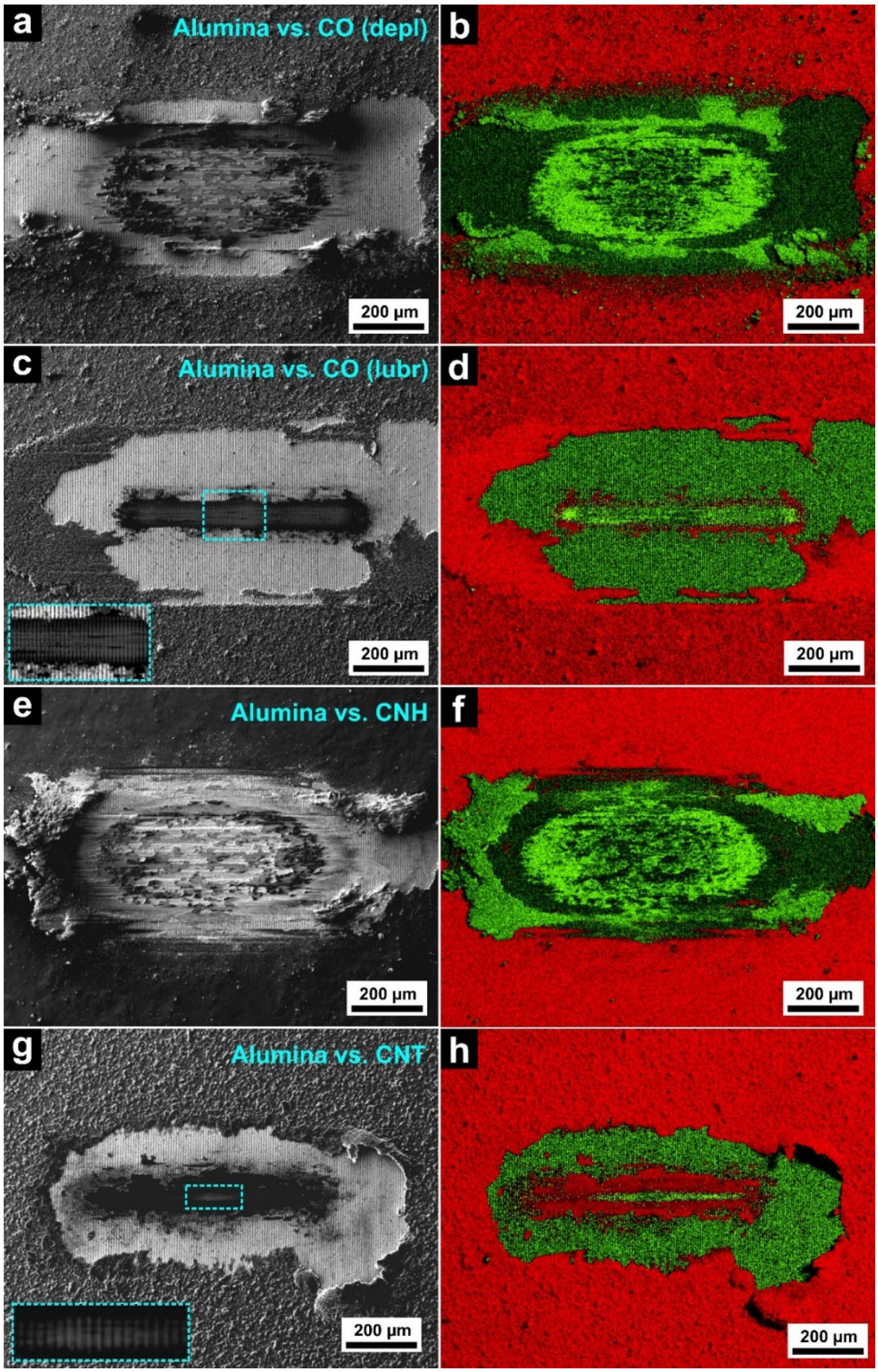

Fig. 5 Scanning electron micrographs of representative wear tracks coated with **a** CO (depl), **c** CO (lubr), **e** CNH and **g** CNT after exposure to 200,000 friction cycles against an alumina ball. Corresponding EDS maps of **b** CO (depl), **d** CO (lubr), **f** CNH and **h** CNT. Green stands for oxygen, red for carbon (Color figure online)

combination of cylindrical morphology and van der Waals interactions, CNTs are able to form strong entanglements. Consequently, their agglomerates are interconnected while embedded in a continuous matrix of CNT coating, thus, facilitating the formation of patches with a strong cohesion. Once formed, those patches are difficult to remove from the contact as they are likely connected with the underlying CNTs in the grooves and thus anchored in the pattern as illustrated by Fig. 10. Against 100Cr6, CNH are the only coating type able to sustain a mean COF < 0.2 and, thus, effective solid lubrication according to Aouadi et al. throughout the test [22]. In this case, CNH also

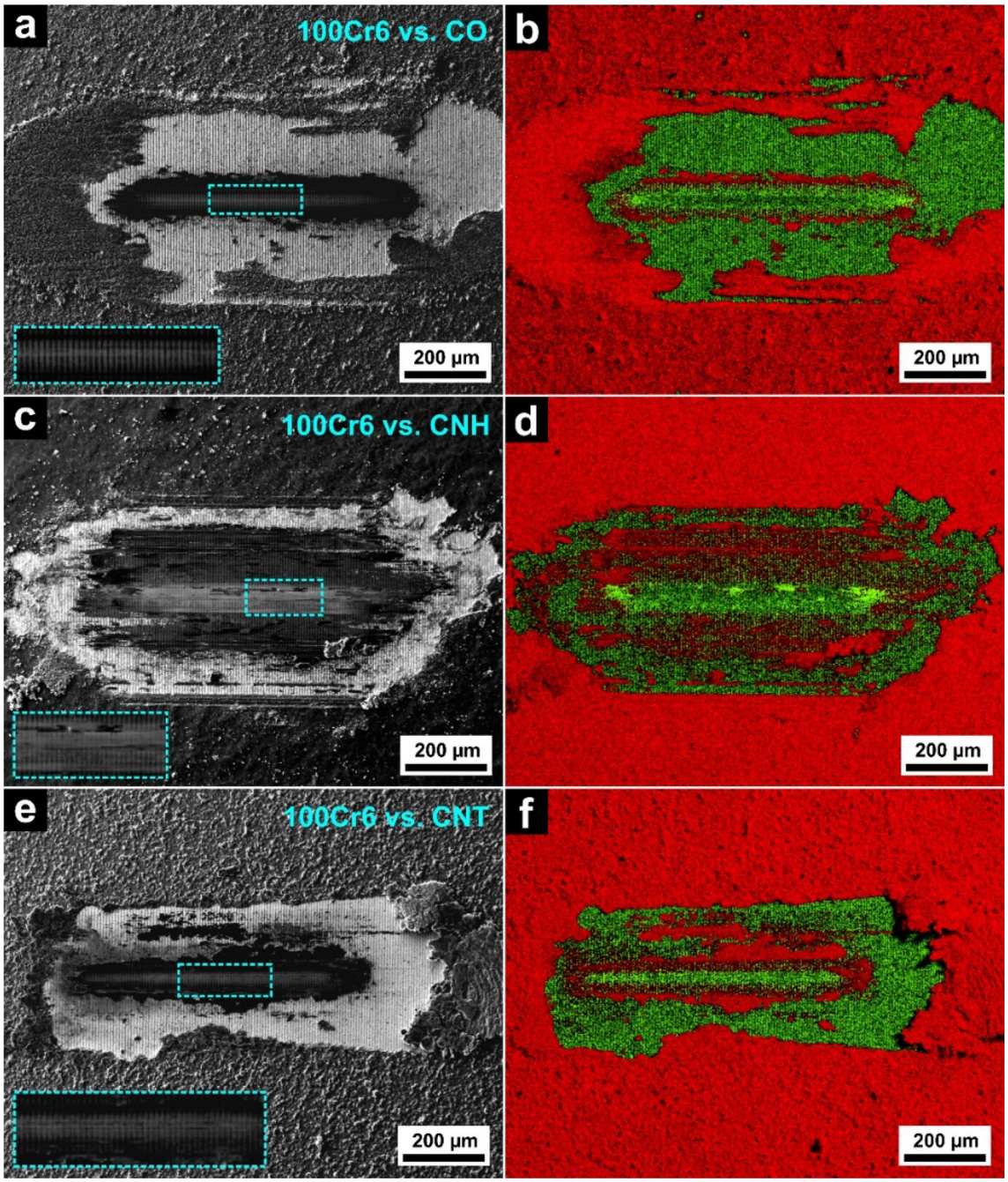

Fig. 6 Scanning electron micrographs of representative wear tracks coated with **a** CO, **c** CNH and **e** CNT after exposure to 200,000 friction cycles against a 100Cr6 ball. Corresponding EDS maps of **b** CO, **d** CNH and **f** CNT. Green stands for oxygen, red for carbon (Color figure online)

form patches, however, compared to CNT patches, they are spread over a larger region which could explain lower COF values as the contact area is increased and thus the contact pressure is reduced. As the morphology of the nanocarbons varies, the character and certain properties of their agglomerates change and so do those of the resulting coatings. Most importantly, individual CNH and CO agglomerates are not interconnected, hence they are more easily removed than CNTs. The CNH patches are therefore further away from the wear track centre and thus unable to achieve complete separation of the sliding surfaces against a spherical counter body which explains the occurrence of oxidation. EDS analysis of the contact area on the 100Cr6 balls has shown that whenever lubrication is maintained

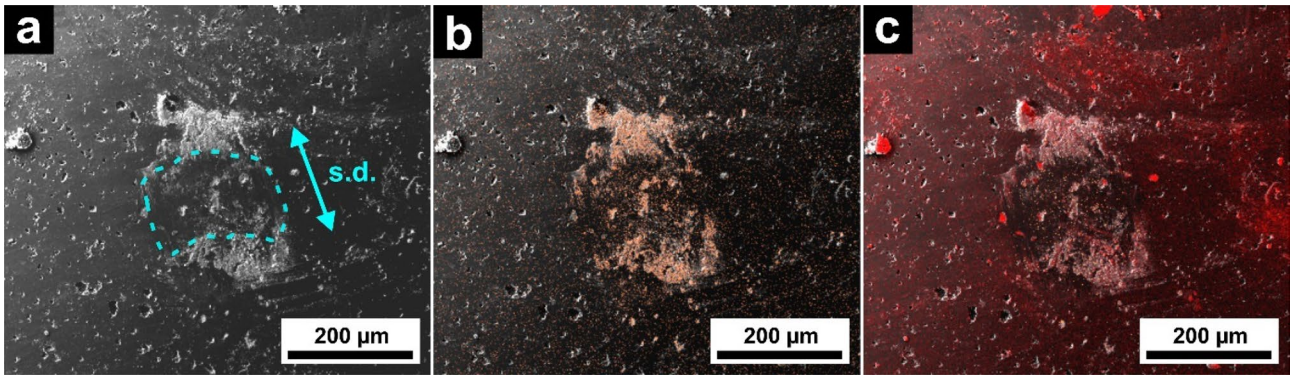

Fig. 7 **a** SE micrograph of a representative wear scar on an alumina ball after 200,000 friction test cycles with failed lubrication. The outline of the wear scar (dotted line) and sliding direction (s.d.) are marked in teal. EDS/SEM overlays for **b** iron (orange) and **c** carbon (red) (Color figure online)

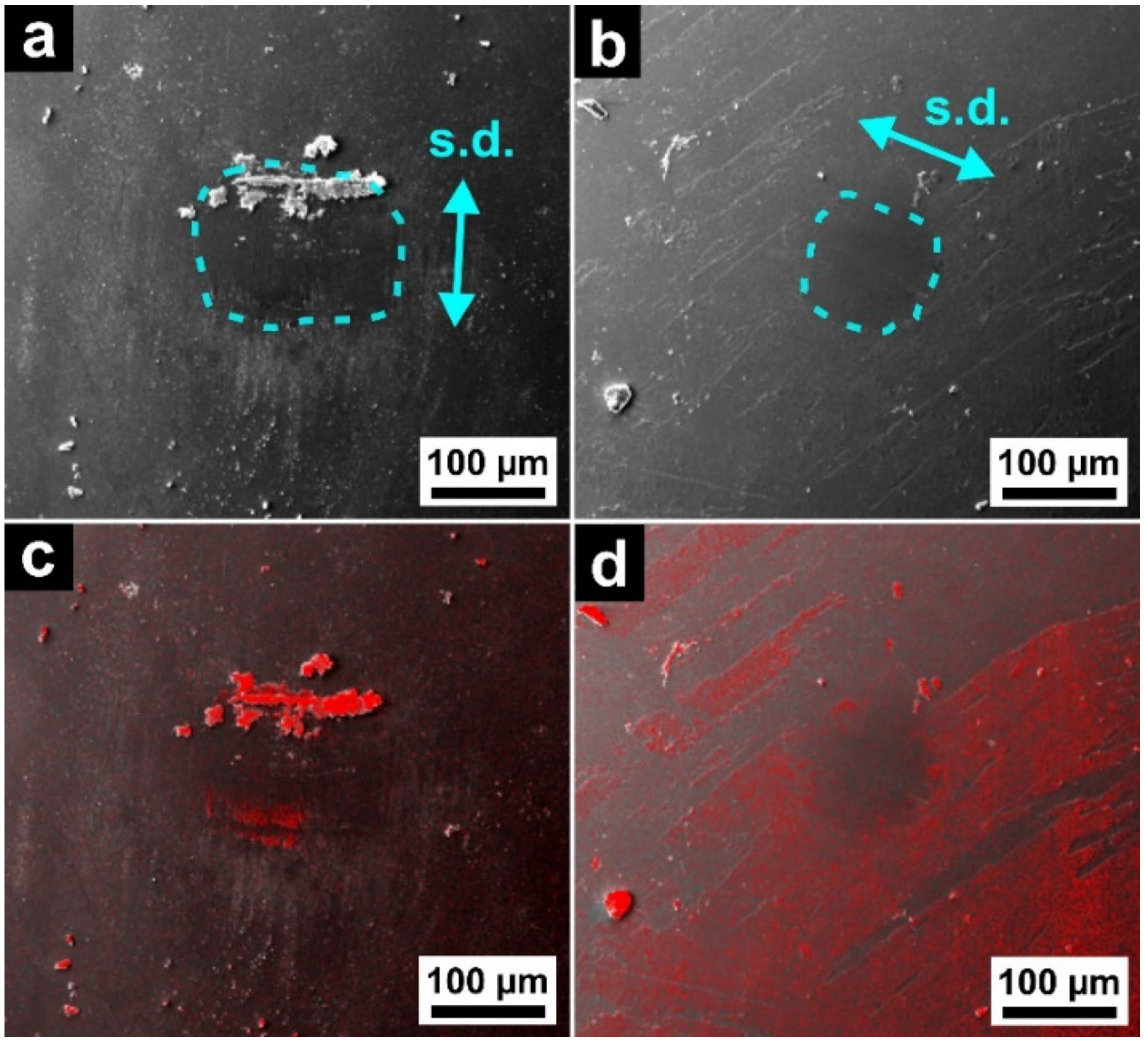

Fig. 8 SE micrographs of representative wear scars on an alumina counter body after 200,000 friction test cycles with functioning lubrication resulting either in **a** minor and **b** no material transfer. The outline of the wear scar (dotted line) and sliding direction (s.d.) are marked in teal. **c** and **d** show corresponding SEM/EDS overlays with red representing carbon (Color figure online)

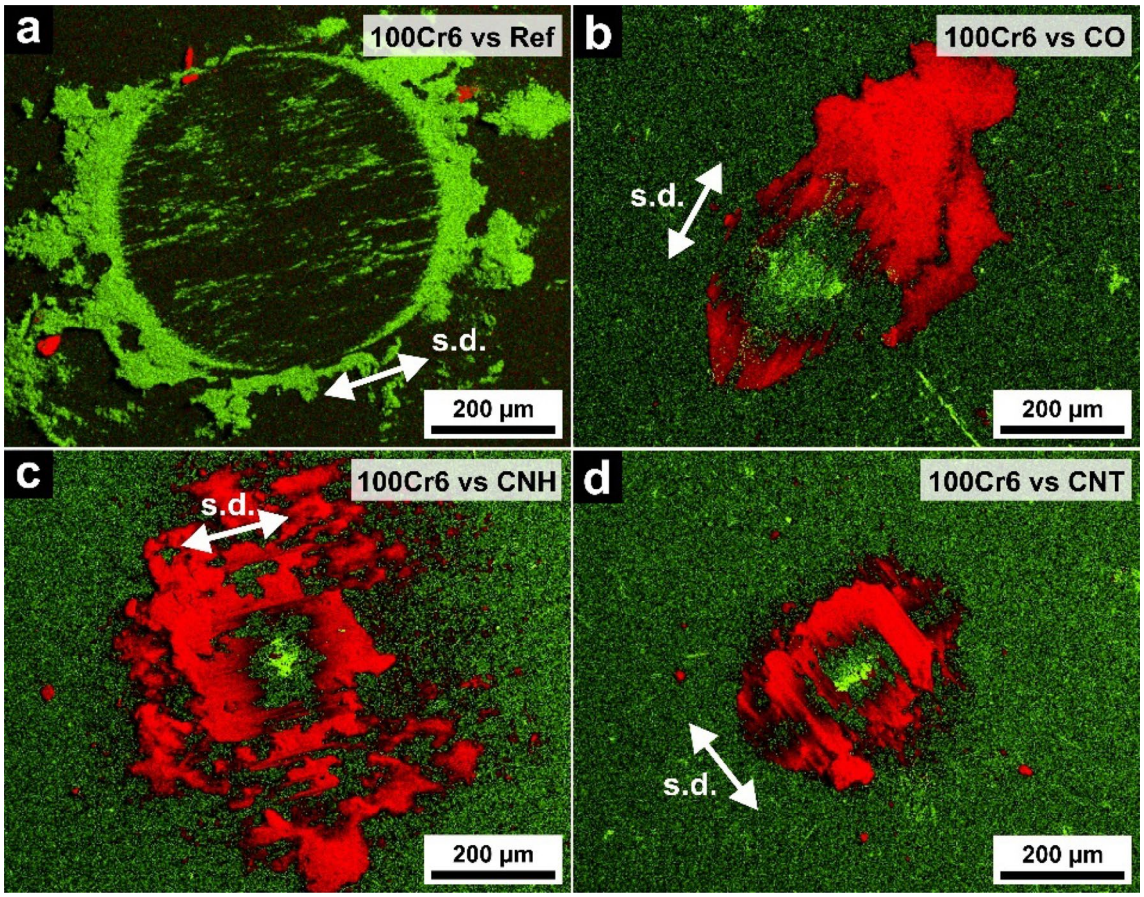

Fig. 9 EDS elemental maps showing representative wear scars on the 100Cr6 balls after rubbing against **a** Ref, **b** CO, **c** CNH and **d** CNT. Green stands for oxygen, red for carbon. The sliding direction (s.d.) is marked by a white arrow (Color figure online)

over the full testing period, significant amounts of carbon are transferred from the coated surface onto the counter body. In contrast, very little carbon, if any, is transferred when sliding against alumina.

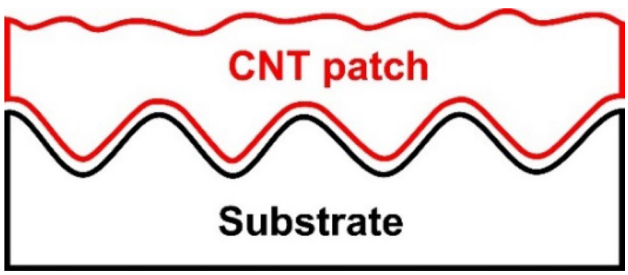

Fig. 10 Schematic cross-section showing CNTs on top of the line-patterned substrate forming cohesive patches with the CNTs stored in the grooves due to counter body pressure during friction testing. As a result, surface adhesion is greatly improved as the patch is interlocked in the grooves (Color figure online)

4 Conclusions

During this study, long-term solid lubrication properties of CO-, CNH- and CNT-coatings on patterned steel substrates were investigated against two technically relevant counter body materials. For that purpose, ball-on-disc tribometry was used in linear reciprocal mode and the resulting substrate wear tracks as well as counter body wear scars were analysed by SEM and EDS. The following three key conclusions can be drawn:

(1) CNT coatings are able to provide long-term lubricity against alumina and 100Cr6 without detectable substrate oxidation. This can be explained by the formation of coherent patches that prevent direct contact of the sliding surfaces.
(2) All particle types were able to lubricate against 100Cr6 over 200,000 friction cycles due to considerable carbon transfer from the patterned/coated surface to the counter body.
(3) CNH achieved the lowest absolute friction against 100Cr6 with a steady-state COF around 0.17

The results presented in this work highlight the impact of particle morphology on the tribological properties of nanocarbon coatings on patterned steel surfaces, despite their physical and chemical similarities.

Funding Open Access funding enabled and organized by Projekt DEAL. T. MacLucas gratefully acknowledges financial support by the Deutsche Forschungsgemeinschaft (DFG, German Research Foundation) within the project MU 959/47-1. S. Suarez and F. Mücklich acknowledge funding by the ZuMat project, supported by the State of Saarland from the European Regional Development Fund (Europäischen Fonds für Regionale Entwicklung, EFRE).

Declarations

Conflict of interest The authors declare that they have no conflicts of interest.

Open Access This article is licensed under a Creative Commons Attribution 4.0 International License, which permits use, sharing, adaptation, distribution and reproduction in any medium or format, as long as you give appropriate credit to the original author(s) and the source, provide a link to the Creative Commons licence, and indicate if changes were made. The images or other third party material in this article are included in the article's Creative Commons licence, unless indicated otherwise in a credit line to the material. If material is not included in the article's Creative Commons licence and your intended use is not permitted by statutory regulation or exceeds the permitted use, you will need to obtain permission directly from the copyright holder. To view a copy of this licence, visit http://creativecommons.org/licenses/by/4.0/.

References

1. Schäfer, C., Reinert, L., MacLucas, T., Grützmacher, P., Merz, R., Mücklich, F., Suarez, S.: Influence of surface design on the solid lubricity of carbon nanotubes-coated steel surfaces. Tribol. Lett. **66**, 1–5 (2018)
2. MacLucas, T., Schütz, S., Suarez, S., Mücklich, F.: Surface protection of austenitic steels by carbon nanotube coatings. Surf. Topogr. Metrol. Prop. **6**, 14005 (2018)
3. Reinert, L., Lasserre, F., Gachot, C., Grützmacher, P., MacLucas, T., Souza, N., Mücklich, F., Suarez, S.: Long-lasting solid lubrication by CNT-coated patterned surfaces. Sci. Rep. **7**, 42873 (2017)
4. MacLucas, T., Daut, L., Grützmacher, P., Guitar, M.A., Presser, V., Gachot, C., Suarez, S., Mücklich, F.: Influence of structural depth of laser-patterned steel surfaces on the solid lubricity of carbon nanoparticle coatings. Friction (2022)
5. Reinert, L., Suárez, S., Rosenkranz, A.: Tribo-mechanisms of carbon nanotubes: friction and wear behavior of CNT-reinforced nickel matrix composites and CNT-coated bulk nickel. Lubricants **4**, 11 (2016)
6. Kim, K.T., Cha, S.I., Hong, S.H.: Hardness and wear resistance of carbon nanotube reinforced Cu matrix nanocomposites. Mater. Sci. Eng. A **449**, 46 (2007)
7. Scharf, T.W., Neira, A., Hwang, J.Y., Tiley, J., Banerjee, R.: Self-lubricating carbon nanotube reinforced nickel matrix composites. J. Appl. Phys. **106**, 013508 (2009)
8. Suárez, S., Rosenkranz, A., Gachot, C., Mücklich, F.: Enhanced tribological properties of MWCNT/Ni bulk composites—influence of processing on friction and wear behaviour. Carbon N. Y. **66**, 164–171 (2014)
9. Kristiansen, K., Zeng, H., Wang, P., Israelachvili, J.N.: Microtribology of aqueous carbon nanotube dispersions. Adv. Funct. Mater. **21**, 4555–4564 (2011)
10. Lu, H.F., Fei, B., Xin, J.H., Wang, R.H., Li, L., Guan, W.C.: Synthesis and lubricating performance of a carbon nanotube seeded miniemulsion. Carbon N. Y. **45**, 936–942 (2007)
11. Peng, Y., Hu, Y., Wang, H.: Tribological behaviors of surfactant-functionalized carbon nanotubes as lubricant additive in water. Tribol. Lett. **25**, 247–253 (2007)
12. MacLucas, T., Suarez, S.: On the solid lubricity of electrophoretically deposited carbon nanohorn coatings. Lubricants **7**, 62 (2019)
13. Hirata, A., Igarashi, M., Kaito, T.: Study on solid lubricant properties of carbon onions produced by heat treatment of diamond clusters or particles. Tribol. Int. **37**, 899–905 (2004)
14. Joly-Pottuz, L., Bucholz, E.W., Matsumoto, N., Phillpot, S.R., Sinnott, S.B., Ohmae, N., Martin, J.M.: Friction properties of carbon nano-onions from experiment and computer simulations. Tribol. Lett. **37**, 75–81 (2010)
15. Bieda, M., Siebold, M., Lasagni, A.F.: Fabrication of sub-micron surface structures on copper, stainless steel and titanium using picosecond laser interference patterning. Appl. Surf. Sci. **387**, 175–182 (2016)
16. Aguilar-Morales, A.I., Alamri, S., Lasagni, A.F.: Micro-fabrication of high aspect ratio periodic structures on stainless steel by picosecond direct laser interference patterning. J. Mater. Process. Technol. **252**, 313–321 (2018)
17. Alderete, B., MacLucas, T., Espin, D., Brühl, S.P., Mücklich, F., Suarez, S.: Near superhydrophobic carbon nanotube coatings obtained via electrophoretic deposition on low-alloy steels. Adv. Eng. Mater. **23**, 2001448 (2021)
18. Boccaccini, A.R., Cho, J., Roether, J.A., Thomas, B.J.C., Jane-Minay, E., Shaffer, M.S.P.: Electrophoretic deposition of carbon nanotubes. Carbon N. Y. **44**, 3149–3160 (2006)
19. Thomas, B.J.C., Shaffer, M.S.P., Freeman, S., Koopman, M., Chawla, K.K., Boccaccini, A.R.: Electrophoretic deposition of carbon nanotubes on metallic surfaces. Key Eng. Mater. **314**, 141–146 (2006)
20. Zeiger, M., Jäckel, N., Aslan, M., Weingarth, D., Presser, V.: Understanding structure and porosity of nanodiamond-derived carbon onions. Carbon N. Y. **84**, 584–598 (2015)
21. Blau, P.J.: On the nature of running-in. Tribol. Int. **38**, 1007–1012 (2005)
22. Aouadi, S.M., Gao, H., Martini, A., Scharf, T.W., Muratore, C.: Lubricious oxide coatings for extreme temperature applications: a review. Surf. Coat. Technol. **257**, 266–277 (2014)

Publisher's Note Springer Nature remains neutral with regard to jurisdictional claims in published maps and institutional affiliations.

VI. Combining carbon nanoparticle coatings and laser surface texturing for enhanced lubricity under high loads

T. MacLucas[1], P. Grützmacher[2], P. Leonhard-Trautmann[1], S. Suarez[1], C. Gachot[2,*] and F. Mücklich[1]

[1] *Chair of Functional Materials, Saarland University, Campus D3.3, Saarbrücken 66123, Germany*

[2] *Institute for Engineering Design and Product Development, TU Wien, Lehárgasse 6, 1060 Vienna, Austria*

Published in **"Tribology Letters"** (2024) (IF: 3.2 [2022])

Accessible online at: https://doi.org/10.1007/s11249-024-01837-5

Own contribution: Sample preparation, tribometry, data analysis, characterization, writing – original draft, project administration

Tribology Letters (2024) 72:38
https://doi.org/10.1007/s11249-024-01837-5

ORIGINAL PAPER

Combining Carbon Nanoparticle Coatings and Laser Surface Texturing for Enhanced Lubricity Under High Loads

T. MacLucas[1] · P. G. Grützmacher[2] · P. Leonhard-Trautmann[1] · S. Suarez[1] · C. Gachot[2] · F. Mücklich[1]

Received: 5 September 2023 / Accepted: 30 January 2024
© The Author(s) 2024

Abstract
Developing new lubrication concepts greatly contributes to improving the energy efficiency of mechanical systems. Nanoparticles such as those based on carbon allotropes or 2D materials have received widespread attention due to their outstanding mechanical and tribological performance. However, these systems are limited by a short wear life. Combining nanoparticle coatings with laser surface texturing has been demonstrated to substantially improve their durability due to the reservoir effect which prevents immediate particle removal from the contact. In this study, we investigate the high-load (20 N) tribological performance of AISI 304 austenitic stainless-steel substrates, which are line-patterned by laser interference patterning and subsequently coated with different carbon nanoparticle coatings (carbon nanotubes, carbon onions, carbon nanohorns) against alumina and 100Cr6 counter bodies. In addition to that, benchmark testing is performed with conventional solid lubricant coatings (graphite, MoS_2, WS_2). Electrophoretic deposition is used as the main coating technique along with air spraying (for WS_2). All coatings substantially improve friction compared to the purely laser-patterned reference. Among all coating materials, carbon nanotubes demonstrate superior lubricity and the longest wear life against 100Cr6 and alumina counter bodies. Detailed characterization of the resulting wear tracks by energy-dispersive X-ray spectroscopy, scanning electron microscopy, and confocal laser scanning microscopy provides insights into the friction mechanisms of the various solid lubricant particles. Further, material transfer is identified as an important aspect for effective and long-lasting lubrication.

Keywords Solid lubricant coatings · Carbon nanotubes · Carbon onions · Carbon nanohorns · Conventional solid lubricants · High load tribometry

1 Introduction

The development of advanced lubrication systems has been an important aspect of modern engineering, as it plays a crucial role in improving the efficiency and durability of mechanical systems, which directly affects overall energy consumption and CO_2 emissions [1]. For many applications, the typically used liquid lubricants are not suitable due to their limited temperature stability or problems related to their evaporation or to contamination [2, 3]. Therefore, solid lubricants in particular have attracted significant attention due to their excellent lubrication properties, high thermal stability and resistance to oxidation, evaporation, and corrosion. Typical solid lubricants are based on polymers (e.g., PTFE [4]), soft metals (e.g., gold [5]) or 2D materials (e.g., graphite [6], transition metal dichalcogenides (TMD) [7, 8] and MXenes [9]).

In recent years, carbon nanoparticles have emerged as promising candidates for solid lubrication, particularly in the form of coatings [10–12]. Carbon nanoparticles combine unique physical and chemical properties, such as high strength, low density, and high conductivity [13]. The mechanical stability stemming from the combination of mechanical strength with cylindrical (CNT), respectively, spherical (CO, CNH) shapes and a layered morphology (CNT and CO) makes these particles highly interesting for bearing high loads.

✉ T. MacLucas
timothy.maclucas@uni-saarland.de

✉ C. Gachot
Carsten.gachot@tuwien.at

[1] Chair of Functional Materials, Saarland University, Campus D3.3, 66123 Saarbrücken, Germany

[2] Institute for Engineering Design and Product Development, Research Unit Tribology, TU Wien, Lehárgasse 6, 1060 Vienna, Austria

Published online: 11 March 2024

However, a major issue for many solid lubricant coatings is a lack of substrate adhesion, which results in a lubricant-depleted contact. This is particularly true for carbon nanoparticles as they don't form covalent bonds with metallic substrates during the coating process [12]. This shortcoming can be tackled by the introduction of surface textures, as those fabricated by laser surface texturing. Laser surface texturing has also gained considerable attention as a technique for improving the tribological properties of metallic surfaces and solid lubricant coatings [2, 3, 12]. During sliding, micro and nano-scale surface features on the substrate material act as lubricant reservoirs and trap wear particles, thus reducing friction and wear [14–16]. A particularly effective technique to create laser textures in the lower µm-scale is direct laser interference patterning (DLIP), which is based on the interference of two or more high-power laser beams [17]. Upon overlapping the laser beams on the surface of the target, material is directly ablated at the so-called interference maxima positions, resulting in the generation of periodic patterns (e.g., lines, cross, or dimples) inside the area of the spot (with diameters of several hundreds of micrometers to several millimeters), even using only a single laser pulse [18]. Additionally, the interaction between laser and material can be tuned by using different laser pulse durations and for ultrashort laser pulses (i.e., pulse duration < 10 ps) the thermal effect on the material is minimal resulting in negligible modification of the material near the created surface textures [19]. When it comes to the combination of laser patterns and solid lubricants, the textures have been shown to store solid lubricant particles in their topographical minima and thus, effectively form reservoirs from where the particles are continuously released into the contact during tribological loading [2, 3, 12, 16]. By creating lubricant-filled reservoirs, the lifetime of the lubrication is significantly extended as the particles are protected from immediate removal from the contact [11, 12, 20].

There are numerous methods to fabricate solid lubricant coatings, such as sputtering [21], burnishing [22], drop casting [23], spray coating [8], and electrophoretic deposition (EPD) [12]. The combination of textured surfaces and coatings applied by EPD is particularly suitable as this process is fast, scalable, offers excellent process control and replicates the laser-induced textures extremely well.

This study investigates the lubricity of carbon nanoparticle coatings (i.e., carbon nanotubes (CNT), carbon onions (CO), and carbon nanohorns (CNH)) on laser patterned AISI304 steel surfaces under high load against 100Cr6 and alumina counter bodies in atmospheric conditions. Additionally, the tribological performance is directly compared to surfaces coated with the widely used solid lubricants graphite, WS_2, and MoS_2.

2 Experimental Section

2.1 Materials

As substrate material, mirror-polished austenitic stainless-steel platelets (AISI 304, 20 mm × 20 mm, 1 mm thick) purchased at Brio Kontrollspiegel GmbH (Germany) was used. Prior to surface patterning and EPD, the platelets were thoroughly rinsed using ultrasonication and cleaned with acetone and isopropanol. Multiwall CNTs were synthesized by chemical vapor deposition (CVD) and purchased at Graphene Supermarket (USA). The particles measure 10–15 µm in length and 30–85 nm diameter. Dahlia-type CNH were purchased from Carbonium SRL (Italy). The clusters measure 60–120 nm in diameter with a single horn diameter of 2–5 nm. COs were fabricated by annealing nanodiamonds (purity > 98%, particle diameter: 4–8 nm, NaBond Technologies Co.) in a vacuum furnace (model 1100-3580-W1, Thermal Technology Inc.) at 1750 °C for 3 h at a rate of 10 °C/min [24]. The graphite powder is a synthetic conducting grade (99.99%, 325 mesh) and was purchased at Alfa Aesar (USA). Both MoS_2 (98%, 325 mesh, which corresponds to 44 µm) and WS_2 (99.8%) powders were purchased from Thermo Scientific (USA).

2.2 Dispersion and Coating Preparation

To prepare for EPD, each dispersion consisted of 70 ml of isopropanol, 10 ml of triethylamine (ACROS Organics, purity: 99%). For the carbon nanoparticles, a concentration of 0.1 mg/ml (solvent) was used, for MoS_2 0.4 mg/ml and for graphite 0.2 mg/ml. Subsequently, the dispersions were subjected to shear mixing (using an Ultra-Turrax IKA T25) and ultrasonication (using a Bandelin Sonorex RK514BH) for 10 min each. During the next step, the substrate and an uncoated AISI 304 platelet (counter electrode) were both immersed in the dispersion and placed parallel to each other. To achieve comparable coating thickness in the 4–5 µm range, the CNTs were deposited for 5 min 45 s, the CNH for 2 min 45 s, the COs for 6 min 15 s, graphite for 4 min 20 s and MoS_2 for 6 min 30 s, all at 300 V. As it is difficult to obtain homogeneous WS_2 coatings via EPD in the 4–5 µm range, air spraying was used as an alternative and 8 ml of WS_2 solution (concentration 28.6 mg/ml) were sprayed onto the substrate.

2.3 Picosecond Direct Laser Interference Patterning

To create line-patterns on the AISI304 substrate platelets (mirror-polished), a Nd:YAG pulsed laser (Edgewave PX-series InnoSlab) integrated into a RDX 500 nano laser

system (Pulsar Photonics GmbH, Germany) was used. The laser operates at a wavelength of 532 nm and the samples were processed at 0.5 W with a pulse duration of 12 ps. The line-patterns were fabricated using two interfering sub-beams and have a periodicity (line spacing) of 3.5 µm. To remove superficial contamination such has oxides, the patterned substrates were sonicated in citric acid, acetone and isopropanol for 15 min each.

2.4 Confocal Laser Scanning Microscopy

To assess the depth of the patterns and the coating thicknesses, an Olympus LEXT OLS4100 confocal laser scanning (CLS) microscope was utilized. The microscope is equipped with a 50 × objective (N.A.: 0.95) and operates at a laser wavelength of 405 nm, providing a vertical resolution of 10 nm and a lateral resolution of 120 nm. R_C (mean height) was used as a measure for the structural depth of the line-patterns over a sampling length of 259 µm. To obtain statistically significant results, R_C was measured for 10 different profile lines on images taken from three distinct spots on the patterned sample surfaces. The coating thickness cannot be measured directly on the patterned surfaces due to their irregularity. For that reason, separate depositions were made on unpatterned surfaces to optimize the deposition parameters so that the coating thickness is 4–5 µm. The optimized parameters were then applied to coat the patterned surfaces, ensuring comparable film thickness.

2.5 Tribometry

Friction testing was conducted on a MFT-2000 tribometer (Rtec, USA) in ball-on-disc setting at a load of 20 N. Measurements were performed in linear reciprocal mode at a stroke length of 1 mm, a velocity of 1 mm/s, and a data acquisition rate of 30 Hz. The sliding direction was perpendicular to the course of the line-pattern. 6 mm balls made from either 100Cr6 steel (Kugel Pompel, Kl.3) or alumina (Kugel Pompel, GD24 which roughly corresponds to an $R_a < 0.045$ µm) were used as counter bodies which corresponds to a Hertzian pressure of 1.78 GPa (100Cr6 vs. AISI 304, with a Young's modulus of 210 GPa for both materials and a Poisson ratio of 0.29 for 100Cr6 and 0.28 for AISI 304) and 2.08 GPa (alumina vs. AISI 304, alumina with a Young's modulus of 375 GPa and a Poisson ratio of 0.25), respectively. Testing was carried out at room temperature and a relative humidity of 25–30%. To ensure statistical representation, each sample was measured three times. The mean COF and the corresponding standard deviations were determined for every single (temporal) measurement point. The raw data was filtered using a Savitzky-Golay filter (25 p) to smooth excessive COF oscillation.

2.6 Wear Track Characterization

To examine the resulting wear tracks, a Helios G4 PFIB CXe dual beam workstation (Thermo Fisher Scientific, USA) with an integrated EDAX detector for energy dispersive x-ray spectroscopy (EDS) was used. Characterization was conducted at a beam current of 1.6 nA and an acceleration voltage of 5 kV. Chemical mapping was performed with 8 cumulative frames.

3 Results and Discussion

3.1 Surface Characterization

The CLS micrographs in Fig. 1 show the top view of the line-patterned AISI 304 steel substrates that were processed by ps-DLIP. Additionally, the images include representative line profiles. To determine R_C, line profiles at various locations were analyzed to obtain a value that is representative of the overall pattern depth. It can be observed that all surfaces have been uniformly patterned, and their line profiles and structural depths are close to identical. These as-processed surfaces were subsequently coated with different solid lubricants.

To ensure comparable coating thickness, the EPD deposition parameters of the CNTs, COs, CNH, graphite, and MoS_2 as well as the solution volume used for air spraying WS_2 were determined such that the resulting thickness of all solid lubricant coatings falls in the 4–5 µm range. Figure 2 shows two sections of each lubricant coating on unpatterned and mirror-polished substrate surfaces. The coating sections are separated by a strip, where the coatings were removed using a soft piece of paper to avoid scratching. Coating thickness is determined by comparing the mean profile height of the left (red rectangle) and right (teal rectangle) coating sections to that of the uncoated strip in the middle (smaller rectangles) as coating thickness cannot be reliably measured directly on line-patterned surfaces. To assess coating uniformity, the profiles belonging to the green lines are shown below the respective micrograph. The identical EPD parameters used for the deposition on unpatterned surfaces were then used to coat the patterned surfaces. As the mean thicknesses of all lubricant coatings is between 4.25 and 5.00 µm, they can be regarded as comparable. Consequently, coating thickness can be neglected as a factor of influence.

3.2 Tribometry and Wear Track Characterization

3.2.1 Counter Body Material: 100Cr6

Figure 3a shows the COF development of the different coatings including an unpatterned and uncoated reference (Ref)

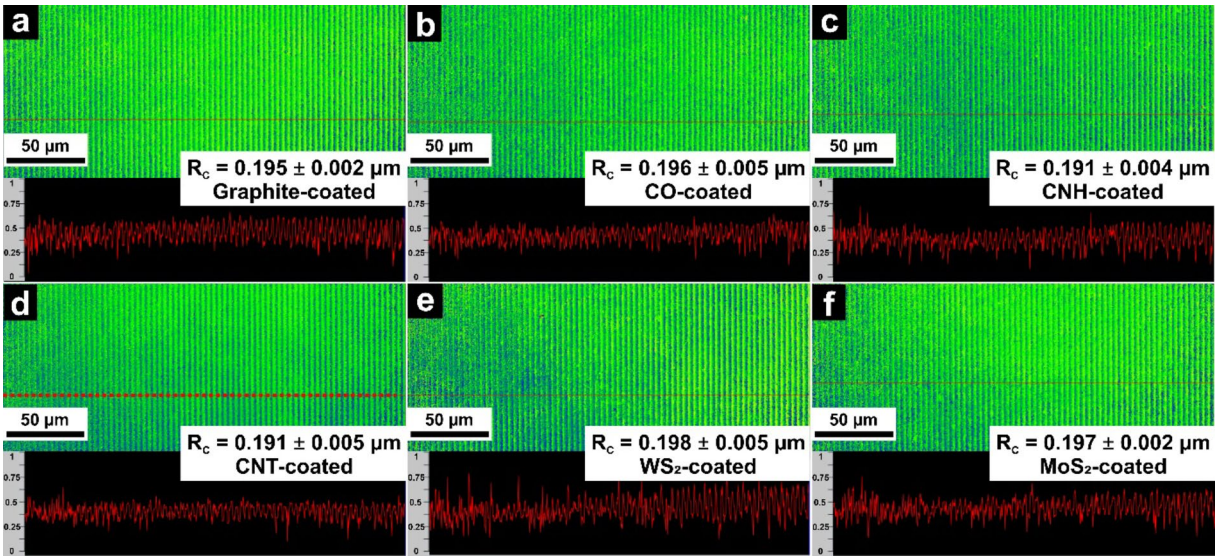

Fig. 1 Top view confocal laser scanning micrographs of the line-patterned AISI 304 substrates which were subsequently coated with **a** graphite, **b** COs, **c** CNH, **d** CNTs, **e** WS_2, and **f** MoS_2. In addition to that, the images show representative line profiles and the overall structural depth (R_C) of the respective pattern

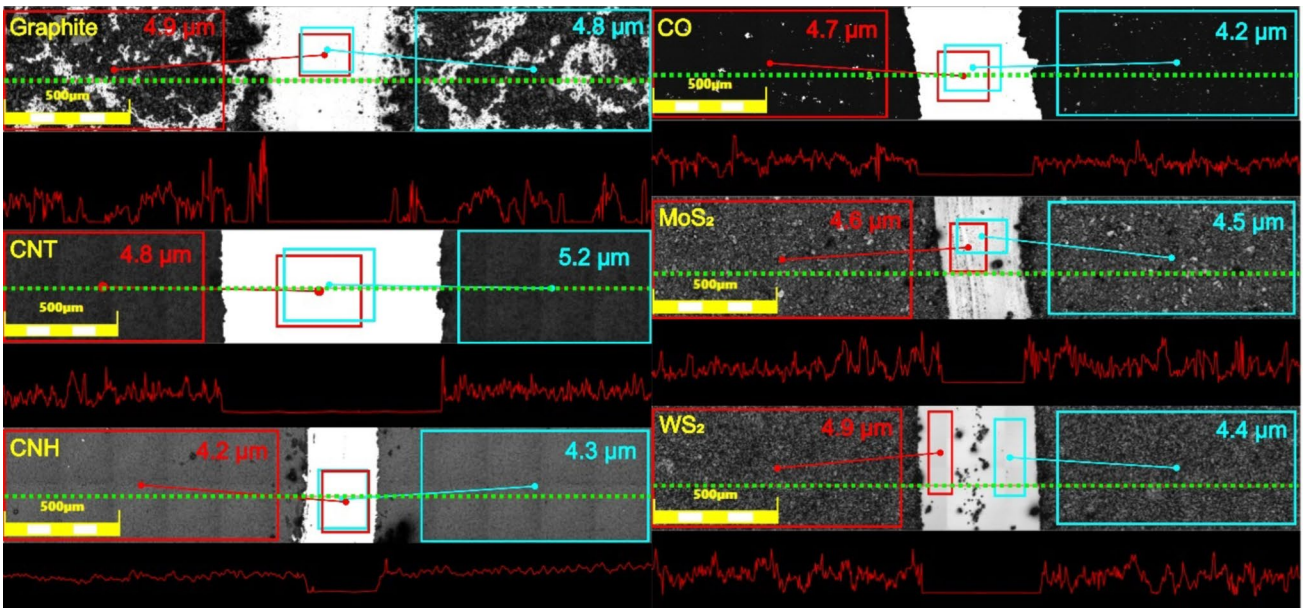

Fig. 2 Top view confocal laser scanning micrographs of the different solid lubricant coatings on unpatterned AISI304 substrate. The profile height of the marked coating sections (red and teal rectangles on the left and right, respectively) is compared to that of the uncoated section (accordingly colored rectangles in the middle) to determine the thickness of the lubricant coatings. The profiles related to the green lines are depicted directly below the respective micrograph. The height values on the y-axis are in µm

during friction testing against a 100Cr6 counter body over 1 h. According to Blau, the reference exhibits a type (c) run-in behavior, which is fittingly associated with unlubricated metals [25, 26]. Continuous asperity truncation leads to an increasingly conformal surface and causes an increase of the initial friction as well as the formation of wear particles, some of which are deposited in the surface grooves. After extensive asperity removal, the counter body comes into contact with the low-lying, low-shear debris layer which could explain the drop after the first COF peak. Once most of the wear particles are removed from the contact, the second peak is possibly caused by abrasion from the remaining debris [26, 27]. Steady-state friction is reached after 300 cycles at a COF of 0.60. Concerning the coated samples,

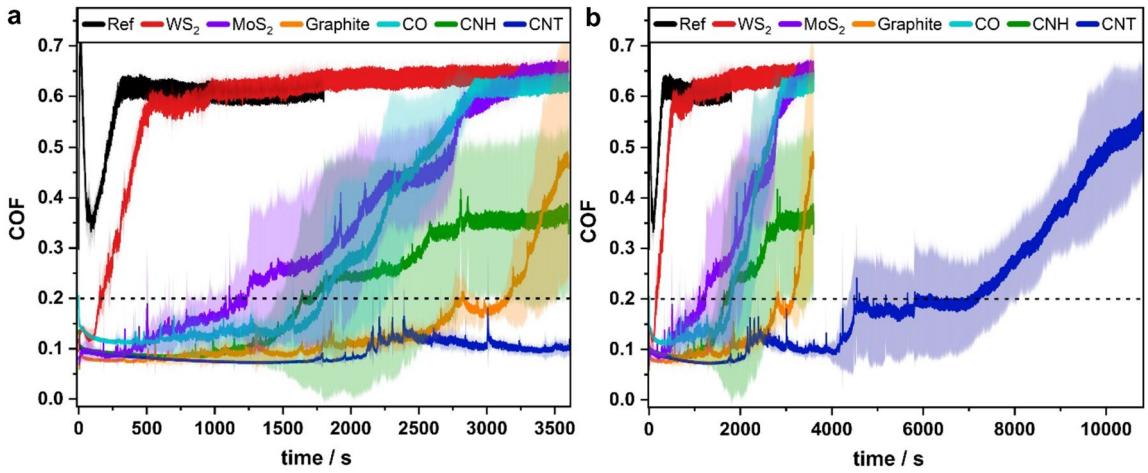

Fig. 3 **a** COF development of lubricant-coated and line-patterned substrates against a 100Cr6 ball at a load of 20 N over 3600 s (1 h) and **b** over 10,800 s (3 h). Friction testing was conducted at room temperature and a relative humidity of 25–30%. The shaded areas correspond to the standard deviation of the respective sample. The dashed line represents the upper limit of effective solid lubrication

initially all show a significant improvement compared to the reference sample with COFs between 0.05 and 0.15. However, over the course of the experiments, the lubricity of the laser-patterned and coated samples degrades, and the lifetime depends strongly on the coating material. The lubricity of the two TMDs fades first. This is particularly true for WS_2, whose COF increases immediately and sharply after only 100 s of sliding, reaching the reference COF after roughly 900 s. MoS_2 performs significantly better as it maintains a COF below 0.10 for roughly 350 s from where the COF slowly increases to the reference level after 3200 s. The discrepancy in the TMDs' friction behavior could be explained by a difference in shear strength. The poor performance of the TMD coatings in ambient conditions was to be expected due to the formation of MoO_3 and WO_3, respectively.

Graphite shows highly effective lubricity, which declines slowly but steadily. After 3000 s, its COF surges sharply and a final value of 0.48 is reached after 3600 s. As defined by Aouadi et al., a COF below 0.2 is considered effective solid lubrication (marked by dashed line) since irreversible deformation of the contact surfaces is likely to occur for COF values above 0.2 [28]. On that basis, the CO and CNH coatings provide effective solid lubrication for roughly 1750s and graphite for about 3150 s. The fact that graphite lubricates at high load and a relative humidity of 25–30% is consistent with recent findings by Morstein et al. [6]. The best performing carbon nanoparticle coating is the CNT coating. From the beginning, the CNT coating maintains a lubricating steady-state with COF values between 0.07 and 0.10. After 2000s, the COF rises moderately to 0.16 including multiple localized peaks. After that, the COF decreases again and reaches a final value of just below 0.1 after 3600 s, which corresponds to a friction reduction by a factor of 6 compared to the reference. The described peaks also appear in the curves of most other coatings, exclusively during the lubricating phase, and suggest adhesion, probably even material transfer according to Blau [26]. This phenomenon could also relate to temporary lubricant starvation in the contact that is followed by a replenishment of the contact with fresh lubricious particles from lower regions of the patterns (i.e., the particle reservoirs). A combination of both is also conceivable. To investigate how long the CNTs can maintain their lubricity under extreme load, the test duration was extended to 10,800 s (3 h) (Fig. 3b). After 4100 s, the CNTs' COF start to increase to just under 0.20 and somewhat stabilizes between 0.15 and 0.20. About another 3000 s later, the COF rises again, this time continuously and evenly until the end of the test. With 0.54, the final COF is still below the reference value of 0.60. CNT coatings provide effective solid lubrication against 100Cr6 at a load of 20 N over a period of 7100 s (almost 2 h), representing a lubrication extension by a factor of 2.3 compared to the graphite coating.

As shown by EDS mapping in Fig. 4 (bright green represents oxidation), applying a load of 20 N in the chosen experimental setup leads to severe oxidation of the reference wear track, which measures roughly 600 µm in width. The wear tracks of WS_2 and MoS_2 are even wider (750 µm and 650 µm, respectively) and exhibit oxidation of comparable magnitude. Compared to that, oxidation inside the wear tracks of CO, CNH is similarly severe, but they are narrower (both roughly 540 µm wide), while the graphite track is with 660 µm again wider. Considering the final COF values of graphite and CNH are lower than that of CO, this not reflected in the scale and oxidation state of the wear

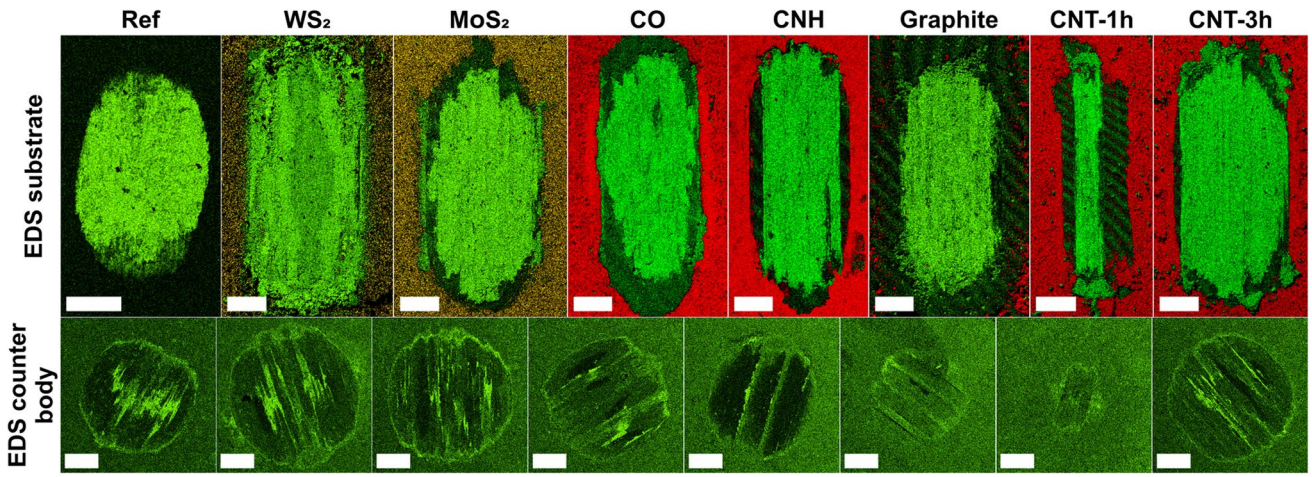

Fig. 4 EDS maps of the substrate wear tracks of the reference and the surfaces coated with WS_2, MoS_2, CO, CNH, graphite, CNT-1 h after friction testing against a 100Cr6 counter body for 3600 s at 20 N. Additionally, the EDS map of CNT-3 h after 10,800 s of testing is shown. Below, EDS maps of the wear tracks on the 100Cr6 counter body surface after rubbing against the reference and the surfaces coated with WS_2, MoS_2, CO, CNH, graphite, CNT-1 h, CNT-3 h are depicted. In the EDS maps, green stands for oxygen, yellow for sulfur, and red for carbon. The scale bars are 250 µm in the EDS maps of the substrate wear tracks and otherwise 200 µm

tracks since they are comparable. Severe oxidation also occurs on the CNT-1 h wear track, however, at 150 µm, the oxidized strip is a quarter of the width of the reference. Due to effective lubrication, wear is milder and consequently, the enlargement of the real contact area is delayed, resulting in narrower oxidation regions. The low COF values of the CNTs after 1 h are remarkable considering the degree of substrate oxidation and the fact that no significant amounts of carbon are detected in the wear track. MacLucas et al. made similar findings after ball-on-disc friction testing on directionally ground and CNT-coated iron surfaces [29]. This further demonstrates, how little carbon is required to maintain an effective solid lubrication. After 3 h, the CNT-coated wear track is also heavily oxidized although its final COF is slightly below that of the other failed lubricant coatings. The wave-like patterns surrounding the wear tracks of graphite and CNT-1 h are generated by the Moiré effect, which is caused by a superimposition of the periodic surface pattern and the scanning electrons. In both cases, the occurrence of the Moiré effect indicates that the line patterns next to the oxidized stripes are at least partially intact.

Oxygen mapping is also used for the wear tracks on the counter bodies, primarily to assess the extent of their oxidation and their dimensions. Severely oxidized areas can be observed in the wear tracks of the reference, WS_2, MoS_2, CO, and CNT-3 h with center widths ranging from 600 (Ref) to 675 µm (MoS_2). Although the size of the CNH track is similar to the previously mentioned samples, there is only minor oxidation which is restricted to two thin stripes in the middle of the wear track. At roughly 450 µm, the graphite track is notably smaller and less oxidized. After friction testing using a similar tribological setup, Morstein et al. observed the transfer of graphite-derived carbon from a graphite-coated iron substrate to a 100Cr6 counter body, which would explain the reduced wear and oxidation of our counter bodies [30]. Measuring 330 µm in width, the CNT-1 h track is roughly half as wide as the reference wear track and, thus, the smallest out of all counter body wear tracks. At the same time, the CNT-1 h wear track shows the least amount of oxidation (minor, if any), which agrees well with the superior tribological performance of the CNTs. This substantial improvement is probably due to remnants of CNT-derived carbon, transferred from the substrate surface to the counter body, therefore, forming a tribo-system that incorporates the acting shear stresses and protects the surface. However, this material transfer to the 100Cr6 counter body cannot be detected by EDS as the counter body contains about 1 wt.% of carbon and, therefore, it cannot be distinguished whether the detected carbon stems from transferred CNTs or from the counter body material. This becomes evident by comparing the carbon maps of the references' counter body track (Fig. 5a), which was never in contact with a carbon coating, and the corresponding CNT track (Fig. 5b) where carbon transfer is likely to have occurred.

3.2.2 Counter Body Material: Alumina

Figure 6a shows the COF development of the same solid lubricant coatings against an alumina counter body over 1 h. The run-in of the reference curve cannot be definitively assigned to a curve type, instead it shows characteristics of types (b) and (d). The curve most closely resembles type (d) with a COF drop after the second peak, as is characteristic for type (b). This agrees well with Blau,

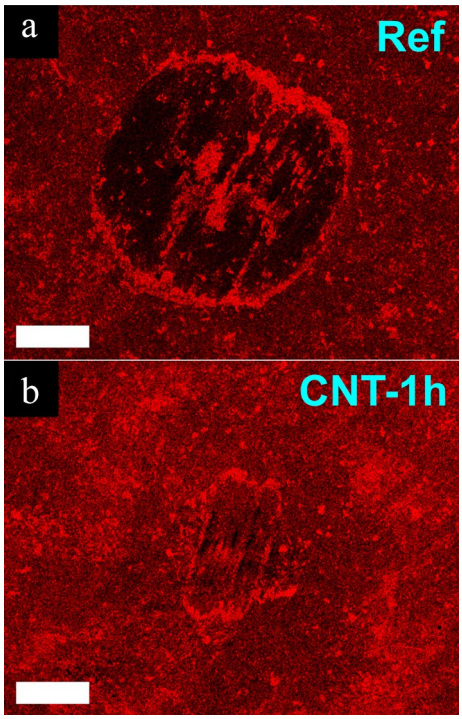

Fig. 5 EDS maps of the 100Cr6 counter body wear tracks after sliding against **a** the reference and **b** CNT-coated substrate for 3600 s at 20 N. In the EDS maps, red represents carbon. The scale bars are 200 µm

according to whom this behavior is often observed in ferrous or ferrous-nonferrous pairings, among others [26]. After running-in, the COF reaches a steady-state just below 0.70 after 800 s [25]. Similar to testing against 100Cr6, the lubricity of the TMDs fails first and MoS_2 significantly outperforms WS_2.

The COF development of the CNH and CO coatings is similar. After an initial COF drop, both enter a lubricating steady-state. During this stage, the COF of the CNH coating (< 0.10) is lower, yet starts to rise after 300 s, while the CO coating maintains lubricity longer at a slightly higher COF, however, it starts to increase more steeply after about 2500 s. After 3600 s, their COF values are around 0.60 and continue rising, but are still well below the reference value. Starting below 0.10, the COF of graphite starts to increase early, stabilizes after 2750 s and remains constant at 0.40 until the end of the test. It should be noted that, in contrast to sliding against 100Cr6, CO and CNH exhibit better lubricity than graphite for a majority of the first roughly 3000 s. The CNTs maintain a lubricating steady-state for more than 2000s, after which the COF starts to rise, reaching a final value of 0.24. After sliding against alumina for 3600 s, CNTs and graphite exhibit the lowest COF values of all coating materials. However, the CNT coating provides effective solid lubrication for over 3000 s compared to the 800 s of graphite which corresponds to lubrication extension by a factor of 3.8. At the same time, their lubricities are the least reproducible as expressed by substantial standard deviations and since they overlap, friction testing was prolonged to 10,800 s (3 h) (Fig. 6b). During the extension, the COF of both coatings increases gradually, however, that of graphite rises more steeply and matches the reference value after 6000 s, whereas the final COF of the CNT coating remains slightly below.

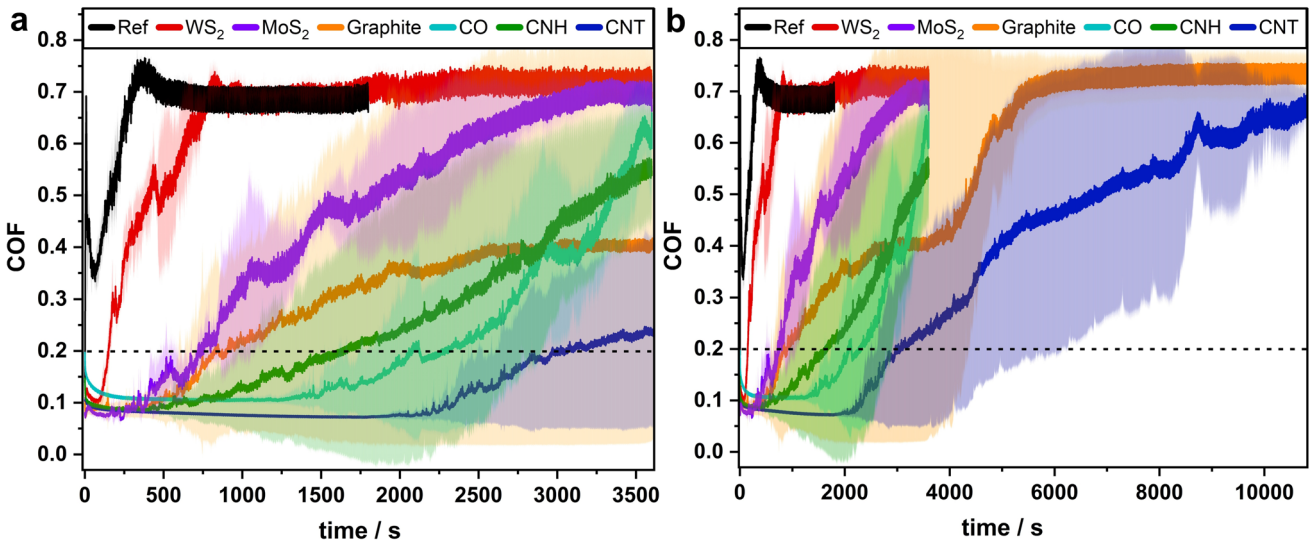

Fig. 6 **a** COF development of lubricant-coated and line-patterned substrates against an alumina ball at a load of 20 N over 3600 s (1 h) and **b** over 10,800 s (3 h). Friction testing was conducted at room temperature and a relative humidity of 25–30%. The shaded areas correspond to the standard deviation of the respective sample. The dashed line represents the upper limit of effective solid lubrication

Regarding the alumina curves, the localized peaks occur significantly less frequently and are less pronounced compared to the 100Cr6 curves. This is in good agreement with Blau's adhesion hypothesis as 100Cr6 steel is considerably more reactive than alumina and thus both substrate and coating materials adhere more readily.

It is also worth noting that all carbon nanoparticle coatings, irrespective of counter body material, exhibit a type (f) run-in behavior. As shown in our previous work [29], CNT coatings are compacted during the initial phase of tribological loading, so that the COF decreases continuously during the early stage of running-in. This is followed by a lubricating steady-state which explains the development of a type (f) curve. Similar curve development suggests that particle compaction also occurs in CO and CNH coatings.

Figure 7 shows an overview of EDS maps, characterizing the resulting wear tracks on the substrates and the alumina counter bodies after friction testing. The extent of substrate oxidation and the oxidation width of the reference, WS_2, and MoS_2 tracks are almost identical to those wear tracks that were rubbed against 100Cr6. The CO- and CNH-coated wear tracks are also severely oxidized but narrower than those of the Ref and the TMD-coated surfaces at 365 µm and 330 µm for CO and CNH, respectively. That fact that the two wear tracks are similar in width aligns well with their COF development. They are also narrower than their corresponding wear tracks against 100Cr6. Although their COFs are below the Ref, no significant amounts of carbon are detected in the wear track center, merely traces on the edges of the oxidized areas. Regarding the CNT- and graphite-coated wear tracks (after 1 h), the Moiré effect occurs again, this time, however, inside the tracks and slightly distorted, particularly in the case of graphite. This is a strong indication that the laser patterns have been largely preserved, which is confirmed by the respective CLS micrographs which are shown in Fig. S1 of the Supplementary Information. For both coatings, these images show lines of the original pattern remaining in much of the wear track, and they are usually at least partially filled with particles. Fittingly, EDS characterization also corroborates the presence of carbon in both wear tracks as well as on the edges, and no oxidation. These findings are in good agreement with those of MacLucas et al. who reported on the formation of CNT patches after conducting friction tests using a similar tribological setup with CNT-coated and line-patterned stainless-steel surfaces [11]. Subsequent EDS characterization also revealed no substrate oxidation, implying a complete separation of the sliding surfaces. The wire-like morphology of the CNTs fosters particle entanglement resulting in strong coherence of large particle sections. Furthermore, strong compression exerted by the counter body during sliding appears to bond the superficial patches with the particles in the reservoirs. As a result, the patches become mechanically anchored within the topographical minima of the surface pattern, leading to longer particle retention. Although graphite-derived carbon also remains in the wear track after 1 h, and CNT patch formation was observed at significantly lower loads, this phenomenon could be a contributing factor for the CNTs' superior high

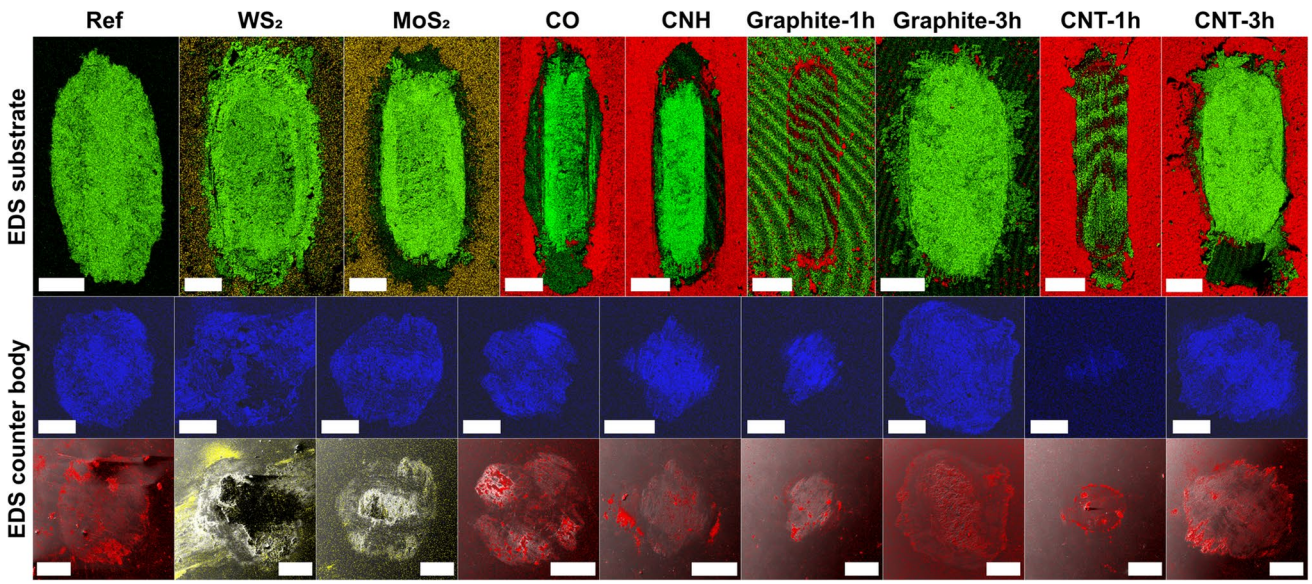

Fig. 7 EDS maps of the substrate wear tracks of the reference and the surfaces coated with WS_2, MoS_2, CO, CNH, graphite-1 h, graphite-3 h, CNT-1 h, CNT-3 h after friction testing against an alumina counter body for 3600 s or 10,800 s at 20 N. EDS maps and SEM/EDS overlays of the wear tracks on the alumina counter body surface after rubbing against the reference and the surfaces coated with WS_2, MoS_2, CO, CNH, graphite-1 h, graphite-3 h, CNT-1 h, and CNT-3 h. In the EDS maps, blue stands for iron, yellow for sulfur, and red for carbon. The scale bar is 250 µm in the EDS maps of the substrate wear tracks and otherwise 200 µm

load lubricity compared to the other nanocarbons during high load friction. In contrast, COs aggregate strongly and form large clusters owing to their size and curvature, which are easily removed from the reservoirs and thus from the contact during sliding, leading to relatively fast lubricant depletion [3]. After 3 h, the CNT lubrication is about to fade completely, whereas the graphite lubrication has already failed after 2 h. Despite comparable degrees of oxidation, the wear tracks of graphite and CNT are also slightly narrower (570 µm and 540 µm, respectively) than that of the reference which is expected due to the initial lubrication.

As can be derived from the standard deviation of the COF development of graphite-1 h and CNT-1 h, the wear tracks differ to a degree, however, we consider the presented wear tracks to be the most representative (the CLS micrographs of all graphite-1 h wear tracks are provided in the Supplementary Information, Fig. S2).

EDS maps of iron (blue), sulfur (yellow), and carbon (red) are used to assess material transfer from the substrate surface to the alumina counter body. With respect to iron, the material transfer from the AISI304 substrate to the counter body material is considerable in the case of Ref, WS_2, MoS_2, CO, graphite-3 h, and CNT-3 h. In the case of CNH, the iron transfer is still substantial, but less pronounced compared to the previously mentioned samples. Even less iron is transferred to the counter body for graphite-1 h and hardly any iron transfer to the counter body is observable for CNT-1 h. In addition to that, sulfur mapping was carried out in the case of the TMDs, and notable amounts are found at the edges of the counter body wear tracks after rubbing against the WS_2 coating, whereas none is detected for MoS_2.

Carbon is measured in varying quantities on the alumina surface due to different degrees of atmospheric contamination. This is made particularly evident by the carbon map of the Ref sample which indicates the presence of carbon although it was never in contact with a carbon-coated surface. This is corroborated by the shading caused by large dirt particles which are non-compressed unlike the transferred carbon. Therefore, solely increased carbon concentrations (bright red) either within the wear tracks or at the edges compared to the surrounding area were considered as transferred material. Concerning graphite-3 h, the carbon quantity inside of its wear tracks is not increased compared to the surrounding areas except for minute remnants at the edges. On the CNT-3 h counter body, carbon concentrations at the edges are clearly elevated, suggesting carbon transfer, albeit minor.

It would explain why the final COF of CNT-3 h is marginally lower compared to that of graphite-3 h. The carbon concentrations are minimally elevated inside the counter body tracks of CO and CNH. In addition, the CNH track also shows considerable amounts of transferred carbon just outside of the wear track edges. The carbon traces are likely responsible for their slightly lower COF compared to the reference. Overall, the carbon transfer, especially inside the wear tracks, is comparable and this is reflected by a similar COF development. After rubbing against the graphite coating for 1 h, EDS mapping clearly shows small carbon patches inside the wear track that outlasted the frictional stress and continue to lubricate. The largest amount of carbon, however, is found on the counter body wear track of CNT-1 h, both inside and at the edges, along with a large dirt particle in the middle of the track. During previous works involving CNT coatings sliding against alumina in similar conditions, we observed that material transfer from substrate to alumina was either minor or non-existent [11, 29]. According to the mechanism formulated by MacLucas and co-workers, the dangling bonds are quickly saturated by atmospheric compounds [29]. It is conceivable, however, that CNT degradation is greatly enhanced under high loads (20 N) and therefore, more reactive dangling bonds are formed. This could explain an increased transfer of CNT-derived carbon in contrast to earlier studies conducted at lower loads (100 mN). Overall, a strong correlation between COF development and material transfer from the substrate to the alumina counter body can be observed: The higher the carbon transfer, particularly inside the wear track, the lower the COF and the iron transfer.

4 Conclusion

In this study, comparative friction testing of three types of carbon nanoparticle coatings and conventional solid lubricant coatings is conducted on line-patterned AISI 304 substrates against two technically relevant counter body materials (100Cr6 and alumina) at a load of 20 N. Regardless of counter body material, the results show the lubricity of the CNT coating to be superior compared the other solid lubricants in terms of COF and lubrication duration.

Against 100Cr6, the CNT-coated substrate exhibits severe oxidation, whereas on the counter body surface, oxidation is minor. Given the severity of the substrate oxidation, it is remarkable that the COF is still around 0.1, demonstrating how little carbon is required in the contact to provide effective solid lubrication. In addition, long-term testing reveals that the CNTs' COF is still below that of the reference. The numerous localized peaks in the COF curves as well the low extent of counter body wear track oxidation are strong indicators of carbon transfer. Furthermore, CNH and graphite are also able to maintain lubrication against 100Cr6, however, their COF values are higher and substrate oxidation is significantly enhanced.

After sliding against alumina for 3600 s, no oxidation is detected on the CNT-coated substrate, which is in accordance with a previous study by MacLucas et al. where the

formation of surface-separating CNT patches was observed. This phenomenon might contribute to the outperformance of CNT coatings against the other solid lubricant coatings. This also corresponds to the fact that, if at all, only small amounts of iron are transferred along with significant amounts of carbon. At the same time, graphite also sustains lubricity but at a higher COF level. In both cases, the original line-patterns are at least partially retained. During long-term testing against alumina, the COF of graphite rises steeply and quickly reaches the reference value, whereas in the case of CNT, the COF increases more slowly and gradually, and the final COF remains below the reference level.

The results of this work demonstrate the potential of CNT-based solid lubrication systems for high load applications. Our findings further illustrate the efficacy of the reservoir effect achieved by combining lubricant coatings with well-defined surface patterns for extending the lubricity of conventional solid lubricant coatings in various industrial applications.

Supplementary Information The online version contains supplementary material available at https://doi.org/10.1007/s11249-024-01837-5.

Author Contributions Conceptualization: T.M., S.S., C.G.; Formal analysis: T.M.; Investigation: T.M., P.L., S.S.; Writing—original draft: T.M., P.G.G.; Project administration: T.M., P.G.G., S.S.; Funding acquisition, supervision: C.G., F.M.; Writing—review and editing: S.S., P.G.G., C.G. and F.M. All authors reviewed and approved the final version of the manuscript.

Funding Open Access funding enabled and organized by Projekt DEAL. This work was financially supported by the German Research Foundation (Deutsche Forschungsgemeinschaft, DFG) within the projects MU 959/47-1 and the State of Saarland from the European Regional Development Fund (Europäischen Fonds für Regionale Entwicklung, EFRE) within the ZuMat project. Funding for the PFIB/SEM instrument by DFG is greatly acknowledged (INST 256/510-1 FUGG).

Data Availability The research data supporting the findings presented in this paper will be made available by the corresponding authors upon reasonable request.

Declarations

Conflict of interest The authors declare that they have no conflicts of interest.

Open Access This article is licensed under a Creative Commons Attribution 4.0 International License, which permits use, sharing, adaptation, distribution and reproduction in any medium or format, as long as you give appropriate credit to the original author(s) and the source, provide a link to the Creative Commons licence, and indicate if changes were made. The images or other third party material in this article are included in the article's Creative Commons licence, unless indicated otherwise in a credit line to the material. If material is not included in the article's Creative Commons licence and your intended use is not permitted by statutory regulation or exceeds the permitted use, you will need to obtain permission directly from the copyright holder. To view a copy of this licence, visit http://creativecommons.org/licenses/by/4.0/.

References

1. Holmberg, K., Erdemir, A.: Influence of tribology on global energy consumption, costs and emissions. Friction **5**, 263–284 (2017). https://doi.org/10.1007/s40544-017-0183-5
2. Rosenkranz, A., Costa, H.L., Baykara, M.Z., Martini, A.: Synergetic effects of surface texturing and solid lubricants to tailor friction and wear – a review. Tribol. Int.. Int. **155**, 106792 (2021). https://doi.org/10.1016/j.triboint.2020.106792
3. MacLucas, T., Daut, L., Grützmacher, P., Guitar, M.A., Presser, V., Gachot, C., Suarez, S., Mücklich, F.: Influence of structural depth of laser-patterned steel surfaces on the solid lubricity of carbon nanoparticle coatings. Friction **11**, 1276–1291(2023). https://doi.org/10.1007/s40544-022-0664-z
4. Burris, D.L., Sawyer, W.G.: A low friction and ultra low wear rate PEEK/PTFE composite. Wear **261**, 410–418 (2006). https://doi.org/10.1016/j.wear.2005.12.016
5. Scharf, T.W., Prasad, S.V.: Solid lubricants: a review. J. Mater. Sci. **48**, 511–531 (2013). https://doi.org/10.1007/s10853-012-7038-2
6. Morstein, C.E., Klemenz, A., Dienwiebel, M., Moseler, M.: Humidity-dependent lubrication of highly loaded contacts by graphite and a structural transition to turbostratic carbon. Nat. Commun. **13**, 5958 (2022). https://doi.org/10.1038/s41467-022-33481-9
7. Vazirisereshk, M.R., Martini, A., Strubbe, D.A., Baykara, M.Z.: Solid lubrication with MoS2: a review. Lubricants (2019). https://doi.org/10.3390/LUBRICANTS7070057
8. Grützmacher, P.G., Schranz, M., Hsu, C.J., Bernardi, J., Steiger-Thirsfeld, A., Hensgen, L., Rodríguez Ripoll, M., Gachot, C.: Solid lubricity of WS2 and Bi2S3 coatings deposited by plasma spraying and air spraying. Surf. Coat. Technol. (2022). https://doi.org/10.1016/j.surfcoat.2022.128772
9. Grützmacher, P.G., Suarez, S., Tolosa, A., Gachot, C., Song, G., Wang, B., Presser, V., Mücklich, F., Anasori, B., Rosenkranz, A.: Superior wear-resistance of Ti3C2Tx multilayer coatings. ACS Nano **15**, 8216–8224 (2021). https://doi.org/10.1021/acsnano.1c01555
10. Reinert, L., Varenberg, M., Mücklich, F., Suárez, S.: Dry friction and wear of self-lubricating carbon-nanotube-containing surfaces. Wear (2018). https://doi.org/10.1016/j.wear.2018.03.021
11. MacLucas, T., Leonhard-Trautmann, P., Suarez, S., Mücklich, F.: Long-term lubricity of carbon nanoparticle coatings on periodically laser-patterned metallic surfaces. Tribol. Lett.. Lett. **70**, 123 (2022). https://doi.org/10.1007/s11249-022-01667-3
12. Reinert, L., Lasserre, F., Gachot, C., Grützmacher, P., MacLucas, T., Souza, N., Mücklich, F., Suarez, S.: Long-lasting solid lubrication by CNT-coated patterned surfaces. Sci. Rep. **7**, 42873 (2017). https://doi.org/10.1038/srep42873
13. Choudhary, N., Hwang, S., Choi, W.: Carbon Nanomaterials: A Review. In: Bhushan, B., Luo, D., Schricker, S.R., Sigmund, W., Zauscher, S. (eds.) Handbook of Nanomaterials Properties, pp. 709–769. Springer, Berlin, Heidelberg (2014)
14. Rosenkranz, A., Grützmacher, P.G., Gachot, C., Costa, H.L.: Surface texturing in machine elements—a critical discussion for rolling and sliding contacts. Adv. Eng. Mater. **21**, 1900194 (2019). https://doi.org/10.1002/adem.201900194
15. Rosenkranz, A., Grützmacher, P.G., Murzyn, K., Mathieu, C., Mücklich, F.: Multi-scale surface patterning to tune friction under mixed lubricated conditions. Appl. Nanosci. (2019). https://doi.org/10.1007/s13204-019-01055-9
16. Schäfer, C., Reinert, L., MacLucas, T., Grützmacher, P., Merz, R., Mücklich, F., Suarez, S.: Influence of surface design on the solid lubricity of carbon nanotubes-coated steel surfaces. Tribol. Lett. **66**, 1–15 (2018)

17. Lasagni, A.F., Gachot, C., Trinh, K.E., Hans, M., Rosenkranz, A., Roch, T., Eckhardt, S., Kunze, T., Bieda, M., Günther, D., Lang, V., Mücklich, F.: Direct laser interference patterning, 20 years of development: from the basics to industrial applications. In: Proc. SPIE 10092, Laser-based Micro- and Nanoprocessing XI. p. 1009211 (2017). https://doi.org/10.1117/12.2252595
18. Braun, P., Grützmacher, P., Frohnapfel, L., Mücklich, F., Durst, K.: Nanoscale patterning of metallic surfaces with laser patterned tools using a nanoimprinting approach. Appl. Surf. Sci. (2023). https://doi.org/10.1016/j.apsusc.2022.155786
19. Müller, D.W., Fox, T., Grützmacher, P.G., Suarez, S., Mücklich, F.: Applying ultrashort pulsed direct laser interference patterning for functional surfaces. Sci. Rep. **10**, 3647 (2020). https://doi.org/10.1038/s41598-020-60592-4
20. MacLucas, T., Schütz, S., Suarez, S., Mücklich, F.: Surface protection of austenitic steels by carbon nanotube coatings. Surf. Topogr. **6**, 14005 (2018)
21. Voevodin, A.A., Bultman, J., Zabinski, J.S.: Investigation into three-dimensional laser processing of tribological coatings. Surf. Coat. Technol. **107**, 12–19 (1998). https://doi.org/10.1016/S0257-8972(98)00543-X
22. Voevodin, A.A., Zabinski, J.S.: Laser surface texturing for adaptive solid lubrication. Wear **261**, 1285–1292 (2006). https://doi.org/10.1016/j.wear.2006.03.013
23. Rosenkranz, A., Grützmacher, P.G., Espinoza, R., Fuenzalida, V.M., Blanco, E., Escalona, N., Gracia, F.J., Villarroel, R., Guo, L., Kang, R., Mücklich, F., Suarez, S., Zhang, Z.: Multi-layer Ti3C2Tx-nanoparticles (MXenes) as solid lubricants—role of surface terminations and intercalated water. Appl. Surf. Sci. **494**, 13–21 (2019). https://doi.org/10.1016/j.apsusc.2019.07.171
24. Zeiger, M., Jäckel, N., Aslan, M., Weingarth, D., Presser, V.: Understanding structure and porosity of nanodiamond-derived carbon onions. Carbon NY **84**, 584–598 (2015). https://doi.org/10.1016/j.carbon.2014.12.050
25. Blau, P.J.: On the nature of running-in. Tribol. Int.. Int. **38**, 1007–1012 (2005). https://doi.org/10.1016/j.triboint.2005.07.020
26. Blau, P.J.: Friction Science and Technology. CRC Press, Boca Raton (2008)
27. Blau, P.J.: Interpretations of the friction and wear break-in behavior of metals in sliding contact. Wear **71**, 29–43 (1981)
28. Aouadi, S.M., Gao, H., Martini, A., Scharf, T.W., Muratore, C.: Lubricious oxide coatings for extreme temperature applications: a review. Surf. Coat. Technol. **257**, 266–277 (2014)
29. MacLucas, T., Klemenz, A., Grünewald, P., Presser, V., Mayrhofer, L., Moras, G., Suarez, S., Dienwiebel, M., Mücklich, F., Moseler, M.: Multiwall carbon nanotubes for solid lubrication of highly loaded contacts. ACS Appl. Nano Mater. **6**, 1755–1769 (2023). https://doi.org/10.1021/acsanm.2c04729
30. Morstein, C.E., Dienwiebel, M.: Graphite lubrication mechanisms under high mechanical load. Wear **477**, 203794 (2021). https://doi.org/10.1016/j.wear.2021.203794

Publisher's Note Springer Nature remains neutral with regard to jurisdictional claims in published maps and institutional affiliations.

5.2. Unpublished results

5.2.1. Lubricity in vacuum

Within the broader objective of researching the lubricity of carbon nanoparticle coatings under extreme operating conditions and benchmarking them against conventional solid lubricant coatings, friction tests were performed under vacuum using a specialized tribometer. Due to its complexity, each sample was measured once. Furthermore, the raw data was slightly filtered using a Savitzky-Golay filter (25p) to smoothen excessive COF variation. The experimental parameters are listed in **Tab. 3**.

Table 3. Overview of the experimental parameters used for the tribological tests under vacuum.

Type:	Pin-on-disc (oscillating)
Pin material:	440C
Pin curvature:	12 mm
Load:	2 N
Temperature:	Room temperature
Vacuum:	$< 10^{-5}$ mbar
Track length:	60 mm
Speed:	6 mm/s
Cycles:	5000 (~ 30 m)

The COF development of the different lubricant coatings during running-in is displayed in **Fig. 18a** (running-in) and **Fig. 18b** (full test duration). The COF development of the TMDs is remarkably similar as they lubricate effectively at a COF around 0.1 over the full duration of the test. Since their COF remains remarkably constant, they cannot be assigned to any running-in type as defined by Blau [49]. The COF of the carbon coatings immediately increases to the range between 0.6 and 0.8 with occasional spikes beyond that and thus do not lubricate. Some of the sharper spikes are characteristic of material transfer [44]. The running-in of carbons is also comparable and may be assigned as type (b).

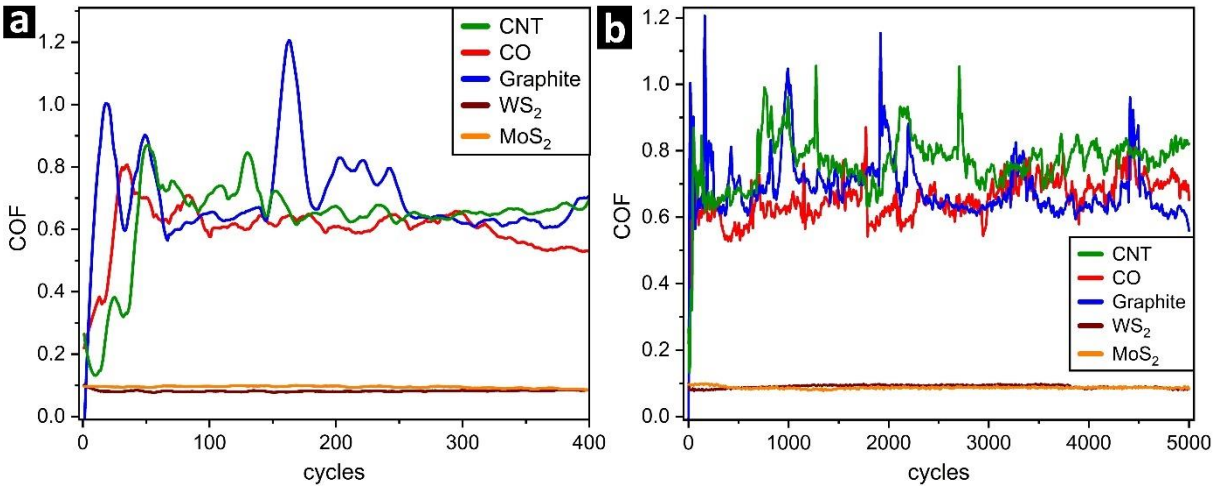

Figure 18. COF development of CNT, CO, graphite, WS_2 and MoS_2 coatings on line patterned AISI 304 stainless steel substrates in vacuum (<10^{-5} mbar) (a) during running-in and (b) over the full length of the test.

After conducting tribological testing on the CNT-coated sample in a vacuum, no carbon was detected in the wear track of either sliding surface (**Fig. 19a-b**). This indicates that the carbon was completely removed, which explains the high COF values. Although complete lubricant removal is also observed for the CO coating (**Fig. 19c-d**), carbon is detected outside of the counter body wear track, suggesting the occurrence of material transfer before the carbon was removed. The observed vacuum lubricity of CNT and CO contradicts the rolling hypothesis and supports the developed lubrication mechanism (**publication IV**) that relies on passivation to impede material transfer from the coating surface to the counter body. The mechanical forces exerted by the counter body during sliding cause the superficial bonds of the compacted carbon coating to break. Under atmospheric conditions, the resulting dangling bonds become saturated whereas under vacuum, this process cannot occur. This results in the coating material bonding to the mating steel surface, followed by material transfer and removal of the coating material from the contact. The wear tracks associated with the graphite-coated substrate are comparable to the CNT-coated surfaces and shown elsewhere (Appendix A). The wear tracks related to the TMD-coated substrates show substantial material transfer from the substrate to the counter body in both cases (illustrated in **Fig. 20a-d**) which explains the low COF values.

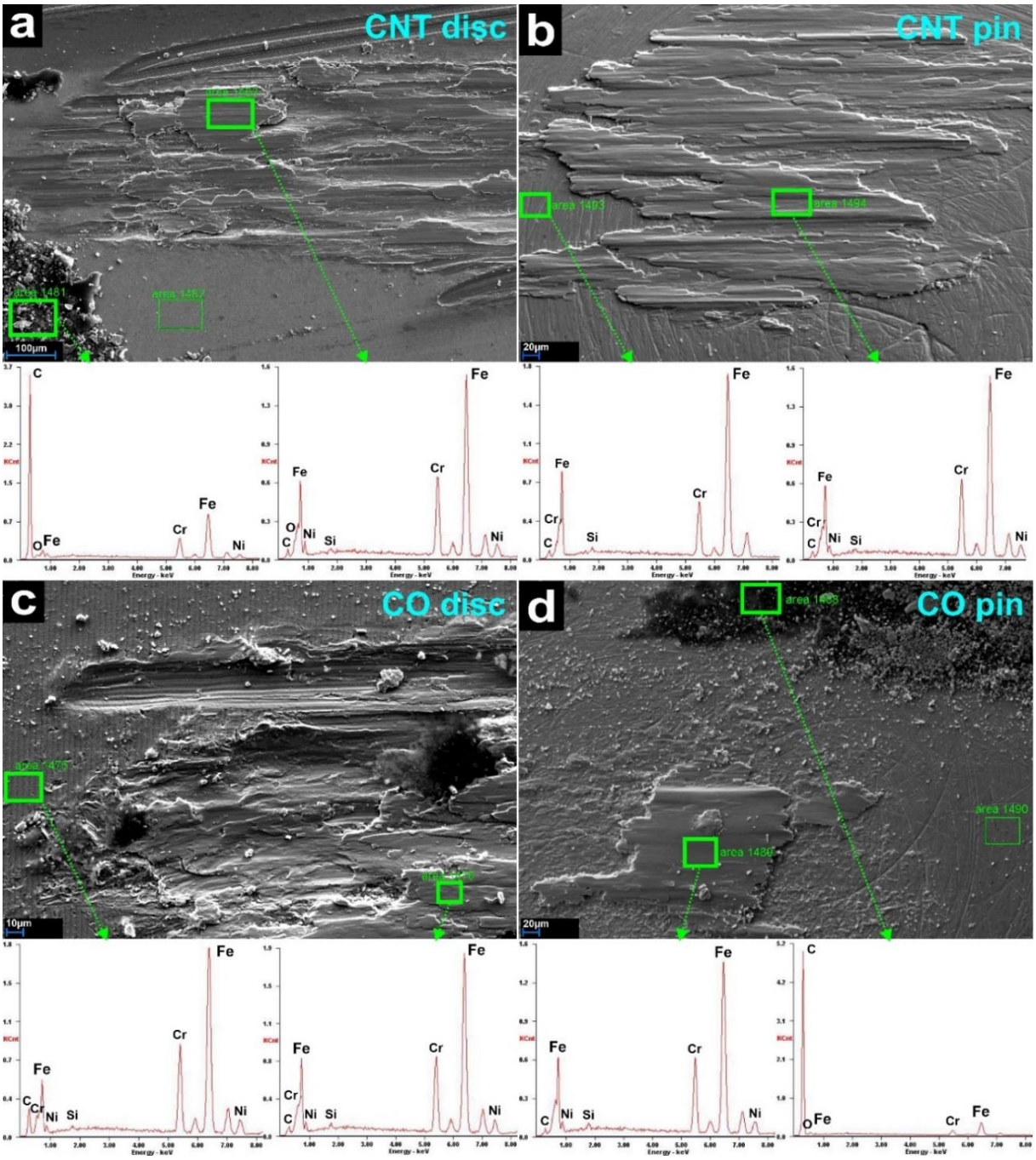

Figure 19. Scanning electron micrographs showing the wear tracks on the substrate (disc) and the counter body (pin) after tribological testing of CNT- (a,b) and CO-coated (c,d) substrates in vacuum (< 10^{-5} mbar). Below the micrographs, EDS spectra of selected areas are depicted.

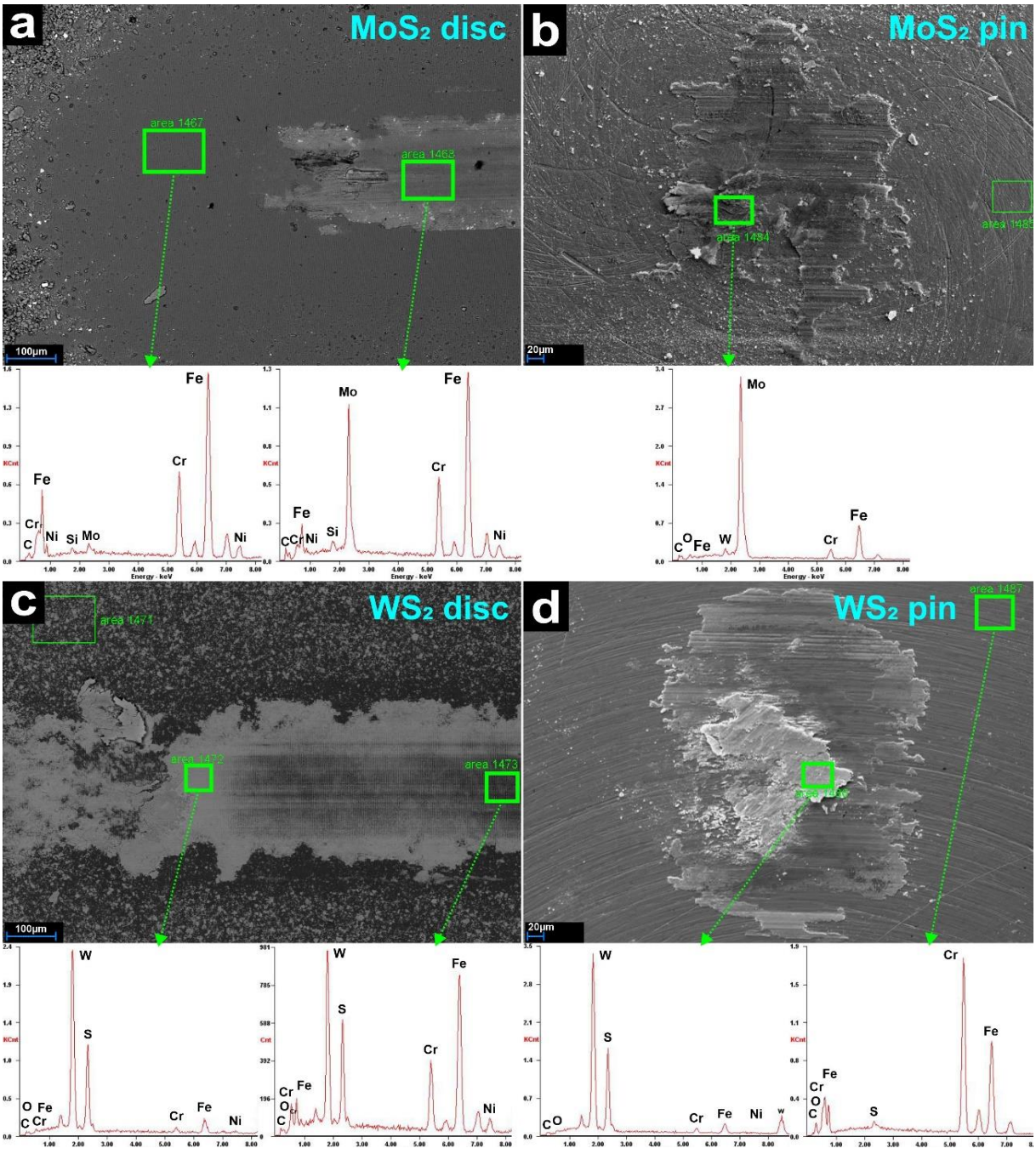

Figure 20. Scanning electron micrographs showing the wear tracks on the substrate (disc) and the counter body (pin) after tribological testing of MoS_2- (a,b) and WS_2-coated (c,d) substrates in vacuum ($<10^{-5}$ mbar). Below the micrographs, EDS spectra of selected areas are depicted.

5.2.2. Lubricity at elevated temperatures

As part of a comprehensive investigation into the lubricating properties of carbon nanoparticle coatings in highly demanding environments, and their comparison with conventional solid lubricant coatings, friction experiments were conducted at a temperature of 300 °C. Each coating was tested twice and the experimental parameters are listed in **Tab. 4**.

Table 4. Overview of the experimental parameters used during tribological testing at 300 °C.

Type:	Ball-on-disc (oscillating)
Ball material:	100Cr6
Ball curvature:	10 mm
Load:	5 N
Temperature:	300 °C
Rel. humidity:	20-30 %
Track length:	4 mm
Speed:	8 mm/s (1 Hz)
Time:	2000 s

Fig. 21a shows the initial phase of the COF development and the running-in behaviors of the different coatings. Based on the different break-in curve shapes described by Blau, the COs can be assigned a type (b), whereas the other carbon coatings most closely resemble a type (d) [49]. By contrast, the lubricating TMDs are type (b) with a low drop after the initial peak. It should be noted that type (b) can occur both in dry and lubricated contacts.

As depicted in **Fig. 21b**, the COF of the CNT, CNH and graphite coatings increases instantly and sharply and enters steady-state between 0.8 and 1.0. Furthermore, their COF developments exhibit numerous sharp and pronounced COF spikes within the initial 200 s. These localized spikes are indicative of adhesion caused by localized welding (COF increases) and subsequent shearing of the formed joints (COF drops) between the mating surfaces. The lubricity of the COs also fades rapidly, however, the steady-state COF ranges slightly lower between 0.7 and 0.8. In a study conducted by Hirata et al., friction testing of CO particles on a silicon disc against a stainless-steel ball in air at 300 °C revealed effective lubricity, with a steady-state COF of around 0.20 [102]. Furthermore, in vacuum at 300 °C, the COF was even lower (0.025). The published results strongly contradict our data, however, several experimental parameters such as the applied load (0.44 N), the substrate material (Si disc), counter body diameter (4.8 mm)

and sliding speed (11 mm/s) deviate significantly from the parameters used in this test. Based on a COF of 0.025, it can be confidently inferred that the COs have rolled, indicating the presence of a monolayer of non-contiguous particles due to their high agglomeration tendency. It can be confidently assumed that the Si discs used by Hirata et al. were of semiconductor grade and had a significantly lower roughness than technical surfaces, making rolling more likely to occur on their smooth surface. Also, no information was disclosed regarding the coating method employed.

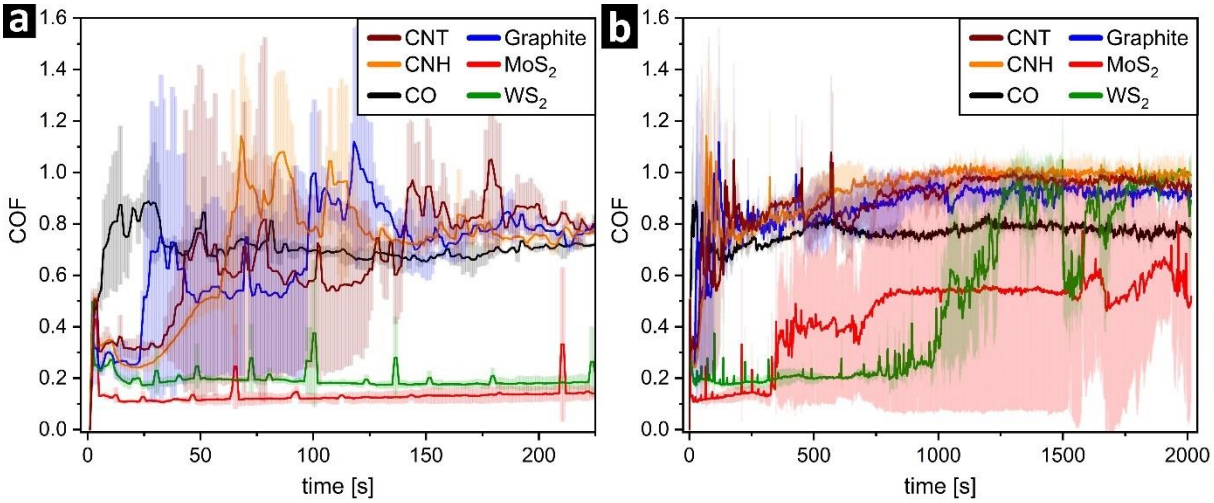

Figure 21. COF development of CNT, CO, CNH, graphite, WS_2 and MoS_2 coatings on line-patterned AISI 304 stainless steel substrates at 300 °C (a) during running-in and (b) over 2000 s.

WS_2 maintains a COF of around 0.20 for approximately 800 s. After that, the COF gradually increases to 0.90 and then suddenly drops to 0.50 after 1500 s. This drop is then followed by a progressive increase, resulting in a final COF of 0.90. During the first 300 s, the COF of MoS_2 increases slightly from 0.11 to 0.13, resulting in the lowest initial friction coefficients of all coatings. Next, the COF increases to 0.50-0.55 after around 700 s and remains constant for 800 s before the COF starts to oscillate, reaching a final COF of roughly 0.5. The obtained results show that WS_2 lubricates more effectively over a longer period of time, however, the lubricity of WS_2 decreases suddenly and completely compared to MoS_2. It should be noted that the standard deviations overlap (especially in the case of MoS_2, the standard deviation is considerable) hence further measurements are required to render a conclusive assessment on the comparative lubricity. At 300 °C, the measured lubricity of WS_2 and MoS_2 is superior to that of all the tested carbon coatings and in accordance with the existing literature [139,140]. This can be attributed to various factors. Prolonged exposure to high temperatures during the heating

process in the tribometer chamber (which represents an uncontrolled environment) allows the chromium oxide layer on the sample surfaces to grow thicker. As a consequence, less substrate iron is available during friction testing which influences substrate adhesion of the carbon-based lubricants negatively and could contribute to early lubricant depletion. Moreover, reactivity is greatly enhanced at 300 °C, therefore, it is conceivable that other substances (e.g., atmospheric nitrogen) are incorporated into the sp^2 lattice at defect sites and other reactive sites such as strongly bent sections in CNTs or the tip of a CNH cone (pyramidalization) or the dangling bonds at the edges. In addition, defect mobility is increased at the elevated temperature. In sum, this can lead to a zipper-like mechanism that destabilizes and even cuts through sp^2 carbon layers as demonstrated by Terrones et al. which would greatly accelerate the mechanical degradation as well as oxidation of all the examined particle types [141]. Compared to the other carbons, the COs show a slightly lower COF, possibly because they often have a residual sp^3 core that is significantly less reactive hence these nanodiamond cores could remain in the contact and provide some degree of lubricity.

The measured COF values of the failed lubrications at 300 °C are higher than what is typically measured at room temperatures. This could be explained by a softening, respectively, an increased ductility of the mating surfaces which results in an increased real contact area and thus higher friction coefficients.

6. Summary and conclusions

The findings presented in this work provide novel insights into a solid lubrication system that is based on a reservoir effect enabled by the synergy between carbon nanoparticle coatings and textured metallic surfaces. The objective of this dissertation was to optimize the manufacturing of homogeneous carbon nanoparticle coatings, investigate and optimize their lubrication properties on DLIP-patterned austenitic steel surfaces, and compare their lubricity to conventional solid lubricant coatings in extreme conditions.

First, it was demonstrated that uniform CNT coatings can be deposited reproducibly in the desired thickness up to approximately 20 µm (**publication I**). Analysis of the deposition thicknesses further revealed that coating growth is linear during the initial phase of the deposition and eventually plateaus. This behavior was independent of oxidation state of the CNT or which additive is used. Two additives were used to support the deposition process and the results showed that Mg-Nit yields higher deposition rates than TEA. The coating thickness could be approximated quite accurately during the initial linear growth period using the Hamaker law. As a result, cumbersome, and expensive characterization could be omitted and hence this work makes a decisive contribution to improving the applicability of CNT coatings on AISI 304 steel.

Moreover, the texture beneath the coating, in that case the DLIP-induced line patterns, was optimized to decrease friction (**publication II**). Tribological experiments revealed that the shallower the coated pattern, the lower the resulting COF. The flanks of shallow patterns were less steep than those of deeper patterns, which possibly facilitated lubricant supply to the contact and thus resulted in lower friction.

A more in-depth degradation analysis of the coating particles remaining in the wear tracks presented in **publication II** showed oxidation on the CO-coated surfaces and no oxidation on their CNT-coated equivalents (**publication III**), confirming the results from EDS characterization presented in **publication II**. The analysis further revealed that COs degrade more rapidly than CNTs. Additionally, in the case of CNTs, a direct correlation between structural depth of the pattern, lubricity, and degradation was observed. More precisely, as CNT lubricity improves with shallowing patterns, particle degradation increased. Despite ongoing

particle degradation, the sustained and consistent lubricity exhibited, rejected the plausibility of rolling as the primary lubrication mechanism for both CNTs and COs.

By combining tribological experiments with CNT coatings on textured iron surfaces with the simulation of appropriately constructed atomistic models, a plausible explanation was found for the strong degradation of mechanically highly stable CNT particles at low loads (**publication IV**). These findings further lead to the development of a 5-step lubrication mechanism that confirmed the dismissal of rolling as the principal lubrication mechanism for CNTs. Due to the chemical similarity of the different carbon nanoparticles, the lubrication and degradation mechanisms formulated for CNTs are likely to be at least partially transferable to COs and potentially to CNH.

In a separate set of friction tests, the ability of CNT, CO, and CNH coatings to provide solid lubrication against different counter body materials over extensive periods of time was investigated (**publication V**). Since all particle types were sp^2 hybridized, this study further evaluated the influence of particle morphology on the lubricity as solely CNTs demonstrated the ability to form patches. This was attributed to the CNTs' "spaghetti-like" morphology which enables strong particle entanglement of and thus the formation of agglomerates and patches. The discovery of coherent CNT patches on the line patterns of the substrate represents one of the most significant findings of this dissertation as they separate the sliding surfaces and effectively prevent substrate oxidation in long-term friction testing. The patches formed by CNT coatings hold enormous potential for wear reduction in technical applications and require further research and optimization.

With respect to extreme operating environments, tribometry was conducted on line-patterned stainless steel, coated with different types of carbon nanoparticles and conventional solid lubricants in vacuum, elevated temperatures, and high loads. In contrast to the TMDs, none of the carbon-based solid lubricants were able to lubricate in vacuum conditions. This is consistent with the lubrication mechanism presented in **publication IV**, which suggests that a lack of passivation in vacuum results in covalent bonding between the dangling carbon bonds and the steel surface, leading to heavy material transfer. The wear track characterization supports this claim, as it indicated the complete removal of all carbon coatings. It is evident that the carbon nanoparticles did not function as a lubricant at elevated temperatures either. This outcome was not surprising, given that rolling is not the primary lubrication mechanism. Despite refuting the rolling hypothesis, the CNT coatings exhibited the strongest lubrication performance during high-load benchmark testing and were thus the most effective among all solid lubricant coatings when tested against 100Cr6 and alumina (**publication VI**). The CNTs' superior lubricity may

be attributed to the patch formation mentioned above, which was unique to CNTs when compared to the other tested coating materials. Furthermore, the resulting wear tracks after sliding against 100Cr6 for 1h were a remarkable display of how little CNT is required for effective solid lubrication.

When comparing the lubricity of all three types of carbon nanoparticles (CNT, CO, and CNH) in any operational setting where the particles lubricated and regardless of the counter body material, CNTs demonstrated the lowest friction coefficients over the longest periods of time. This was reflected accordingly in the oxidation of the wear track. When evaluated against alumina, CNH and CO showed similar COF development and wear track oxidation. Sliding against 100Cr6, CNH achieved a significantly lower COF than CO in the long-term friction test and maintained markedly lower COF values after 2800 s at high loads.

Throughout the different tribological experiments, the COF values of CNT coatings on AISI 304 steel surfaces were extremely reproducible and consistent with the existing literature [16,105,142]. Furthermore, Hirata et al. slid a steel ball against individual CO particles spread on a Si wafer and measured COF values well below 0.1 both in air and vacuum [97]. The low COF values indicated partial, if not complete, rolling in that specific configuration. Within this dissertation, lubricating CO coatings deposited by EPD consistently yielded COF values between 0.2 and 0.3, indicating that the occurring lubrication mechanism is different. The results presented in this dissertation stand in strong opposition to the long-standing hypothesis of rolling as the principal lubrication mechanism of carbon nanoparticle coatings in sliding contacts.

7. Outlook

At various stages of the presented dissertation, further aspects of considerable scientific interest emerged, which shall be discussed in this chapter.

With respect to the deposition process, the literature suggests the use of additives during EPD to set the wetting behavior of carbon nanoparticle coatings, to increase the deposition rate or to improve particle dispersion and, thus, coating homogeneity. Since our group has used triethylamine successfully in combination with isopropanol (solvent) [104,138,143], ascertaining to what extent TEA supports the dispersion of carbon nanotubes as well as other carbon nanoparticles and to examine the underlying chemical mechanisms could be of scientific interest. Since TEA is a harmful compound, understanding the mechanism could help to minimize the amount of TEA in the EPD solution without deteriorating the deposition result. Based on literature research and remarks by Prof. Dr. Hansjörg Grützmacher (Deputy head of Laboratory of Inorganic Chemistry, Eidgenössische Technische Hochschule Zurich), a hypothetical reaction mechanism for the dispersion of carbon nanoparticles in the EPD solution was formulated:

(1) In the presence of isopropanol and TEA, a substantial fraction of the primary oxygen-containing functional groups of the particles, COOH, deprotonate to COO^- and H^+.

(2) The proton (hydrogen ion) attaches to the free electron pair of the nitrogen atom in the TEA molecule and forms an ammonium.

(3) In the case of the strongly solvating isopropanol, hydrogen bonds are formed between COO^- and the hydroxy groups of isopropanol or between N^+ and the hydroxy groups. Since the concentration of the isopropanol molecules is much higher than TEA, these hydrogen bonds are formed preferentially and there is no strong interaction between COO^- and the ammonium.

(4) Formation of a complex between COO^- and ammonium based on weak (non-covalent) forces.

As a result, steric repulsion between the side chains of different ammonia molecules or ammonia and CNT would counteract agglomeration. To verify the presence of ammonia in the EPD solution and thus the dispersion effect, the following procedure could be employed:

(1) Acid-oxidation of the carbon nanoparticles to increase the COOH density (without destroying particle integrity)
(2) Acid-base titration to determine the concentration of COOH groups and thus at the same time the minimum TEA concentration for optimal dispersion according to the reaction mechanism [144,145]
(3) FTIR spectroscopy to detect the COOH groups [146]
(4) ^{13}C NMR spectroscopy to detect the ammonium [147,148]

The workload necessary for this research endeavour is within the suitable scope for a bachelor's or master's thesis. Over the course of this dissertation, it was further discovered that specifically CNTs, do not require an additive to form homogeneous coatings via EPD which has positive implications for the practical application of CNTs as the hazardous TEA can be eliminated.

A major advantage of the EPD coating technique is scalability. The process is widely used in the industry, e.g., in the form of cathodic dip painting that is used in the automotive industry to paint car bodies. Upscaling EPD for CNT deposition requires optimization, however, it is technically feasible and thus also enable the large-scale implementation of lubrication systems based on CNT coatings. Regarding particle dispersion, ultrasonication could be replaced by techniques that are more suitable for continuous coating processes like microfluidics or techniques that consume less energy such as spontaneous exfoliation [149].

As shown in **publication II**, the lubricity of CNT and CO coatings on line-patterned stainless-steel substrates is based on the reservoir effect and improves with decreasing structural depth. However, in that study both the structural depth and the slope angle of the laser structures are inherently connected. To investigate which of these factors plays the dominant role regarding the lubricity enhancement, further research is required. The two main hypotheses are:

- **Hypothesis A:** The steepness of the flanks has a decisive influence on the lubricant supply in the contact. Structures with steep flanks impede the lubricant supply.
- **Experimental design for testing hypothesis A:** Tribological testing on 3 different CNT-coated patterns with identical structural depths but varying slope angles (**Fig. 22**). In the case of a Nd:YAG pulsed laser (Edgewave PX-series InnoSlab) with two sub-beams and a pulse duration of 12 ps (as used frequently within this dissertation), patterns with a line periodicity of 3.5 µm combined with a structural depth 0.5 µm would be reasonable as it represents a good compromise between low processing times and high reproducibility.

Figure 22. Schematic illustration of experimental design to probe hypothesis A. Friction testing will be conducted on 3 laser structures (CNT-coated) with identical structural depths but different slope angles.

- **Hypothesis B:** The structural depth has a decisive influence on the lubricant supply in the contact and thus on the lubricity.
- **Experimental design for testing hypothesis B:** Tribological testing on 3 different CNT-coated patterns with identical slope angles but varying structural depths (**Fig. 23**). In the case of a Nd:YAG pulsed laser (Edgewave PX-series InnoSlab) with two sub-beams and a pulse duration of 12 ps, patterns with a line periodicity of 3.5 µm and three depth ranges (0.5-0.7 µm, 1.0-1.2 µm and 1.5-2.0 µm) can be implemented well in practice.

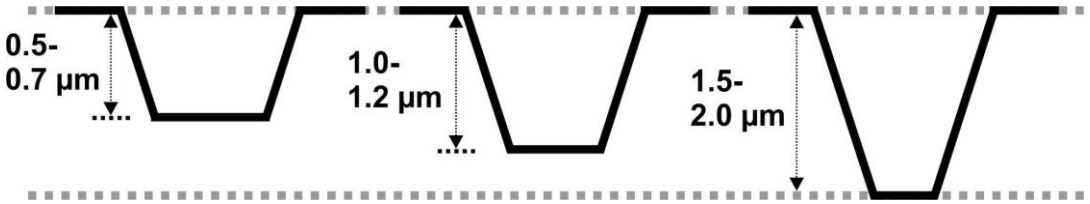

Figure 23. Schematic illustration of experimental design to probe hypothesis B. Friction testing will be conducted on 3 laser structures (CNT-coated) with identical slope angles but different structural depths.

Within this experimental series, two further, scientifically relevant aspects arise. Firstly, the lubricant supply may be influenced by particle morphology in which case the described experiments could be conducted with CO and/or CNH coatings in addition to the CNT coatings. The second aspect concerns the occurring mechanical stresses within the structures during frictional load and requires to be investigated by molecular dynamic simulation. How strong are these stresses? Where do they occur, and do they lead to the formation of covalent bonds at specific locations within the structures? These are highly relevant questions as localized bonding of the carbon-derived tribofilms to the substrate would enhance adhesion and thus the effectiveness of the entire lubrication system considerably.

Describing the formation of coherent CNT patches in a sliding contact for the first time, the findings from **publication V** lay the groundwork for a CNT-based solid lubrication system, that protects the underlying substrate from oxidation and thus potentially prevents the occurrence of substrate wear entirely. However, further research efforts are required to investigate the

formation, optimization and application range of the CNT patches. It is crucial to investigate how factors like the deposited coating thickness, the type and depth of the underlying substrate texture (preferably DLIP patterns) affect patch formation. Moreover, does increased CNT length facilitate patch formation and does that result in enhanced patch cohesion? It would be conceivable that an enhanced cohesion improves the resilience of the patches, making them more resistant towards sliding under high loads. The EDS images of the CNT-coated wear tracks (**Fig. 6, 8, 9** in **publication II**) indicate that CNT coatings form more extensive and resilient patches on deeper DLIP patterns. Based on SEM- and TEM cross-sections (**publications II** and **III**) as well as MD simulation findings (**publication VI**), it can be assumed, that the CNTs in the topographical minima of the structures are mechanically stabilized by compression and, therefore, anchor the entire patch and interlock it within the pattern. This would explain the above-described phenomenon since deeper anchors provide greater stability and resilience.

The most significant application field for solid lubricant coatings are extreme environments where oil-based lubrication is not suitable. Hence, the benchmark lubricity tests with the CNT coatings and conventional solid lubricant coatings (as conducted in **publication VI**) need to be extended to dry environments and extreme humidities.

The holy grail in tribology is to achieve superlubricity in ambient conditions which describes the condition of near frictionless sliding (COF < 0.01). A solid lubrication system involving a CNT coating recently demonstrated superlubricity in macroscale steel-steel contact in an ambient environment over 525’000 sliding cycles [150]. The lubrication is based on a synergistic effect between the CNT coating and PAO. More specifically, reciprocating disc-on-flat friction tests were conducted with a sacrificial coating made from vertically aligned CNTs on an AISI 316 stainless steel disc, and an uncoated M2 tool steel flat. In addition, a single drop of poly-alpha-olefin (PAO) was applied to the interface, to create a minimum quantity lubrication condition. The application of a CNT coating drastically reduced the amount of PAO required to maintain superlubricity. This further emphasizes the tribological potential of CNTs in technically relevant applications such as conventional bearing systems.

8. Not included publications

In the context of the present dissertation, additional research has been undertaken and subsequently published as open access articles in peer-reviewed and internationally recognized journals. Nevertheless, as these findings offer only a limited contribution towards addressing the aforementioned dissertation objectives, they were not included. Nevertheless, they shall be acknowledged:

1. **MacLucas, T.** & Suarez, S. On the Solid Lubricity of Electrophoretically Deposited Carbon Nanohorn Coatings. *Lubricants* **7**, (2019).
2. Schäfer, C. *et al*. Influence of surface design on the solid lubricity of carbon nanotubes-coated steel surfaces. *Tribol Lett* **66**, 1–15 (2018).
3. Reinert, L. *et al.* Long-lasting solid lubrication by CNT-coated patterned surfaces. *Sci Rep* **7**, 42873 (2017).

References

1. Liu, H., Yang, B., Wang, C., Han, Y. & Liu, D. The mechanisms and applications of friction energy dissipation. *Friction* vol. 11 839–864.
2. Holmberg, K. & Erdemir, A. Influence of tribology on global energy consumption, costs and emissions. *Friction 2017 5:3* **5**, 263–284 (2017).
3. Holmberg, K. & Erdemir, A. The impact of tribology on energy use and CO2 emission globally and in combustion engine and electric cars. *Tribol Int* **135**, 389–396 (2019).
4. Lasagni, A. F. *et al.* Direct laser interference patterning, 20 years of development: From the basics to industrial applications. in *Laser-based micro-and nanoprocessing XI* vol. 10092 186–196 (SPIE, 2017).
5. Bowden, F. P., Bowden, F. P. & Tabor, D. *The Friction and Lubrication of Solids*. vol. 1 (Oxford university press, 2001).
6. Sung, I. H., Lee, H. S. & Kim, D. E. Effect of surface topography on the frictional behavior at the micro/nano-scale. *Wear* **254**, 1019–1031 (2003).
7. Pu, X., Li, G. & Huang, H. Preparation, anti-biofouling and drag-reduction properties of a biomimetic shark skin surface. *Biol Open* **5**, 389–396 (2016).
8. Zhao, D. Y., Huang, Z. P., Wang, M. J., Wang, T. & Jin, Y. Vacuum casting replication of micro-riblets on shark skin for drag-reducing applications. *J Mater Process Technol* **212**, 198–202 (2012).
9. Bechert, D. W., Bruse, M., Hage, W., Van der Hoeven, J. G. T. & Hoppe, G. Experiments on drag-reducing surfaces and their optimization with an adjustable geometry. *J Fluid Mech* **338**, 59–87 (1997).
10. AeroSHARK - CleanTech Hub | Lufthansa Group. https://cleantechhub.lufthansagroup.com/de/schwerpunkte/flugzeugbezogene-hardware/aeroshark.html.
11. Aero Shark: Flugzeughersteller an Lufthansas Haihaut interessiert - aeroTELEGRAPH. https://www.aerotelegraph.com/flugzeughersteller-an-lufthansas-haihaut-interessiert.
12. Lang, A., Habegger, M. L. & Motta, P. Shark skin drag reduction. *Encyclopedia of nanotechnology* **19**, 2394–2400 (2012).
13. Die Natur als Vorbild: Lufthansa Group und BASF bringen Sharkskin-Technologie in Serie - Lufthansa Group. https://www.lufthansagroup.com/de/newsroom/meldungen/die-natur-als-vorbild-lufthansa-group-und-basf-bringen-sharkskin-technologie-in-serie.html.
14. Colclough, T. Role of additives and transition metals in lubricating oil oxidation. *Ind Eng Chem Res* **26**, 1888–1895 (1987).

15. Denison Jr, G. H. Oxidation of lubricating oils. *Ind Eng Chem* **36**, 477–482 (1944).

16. Reinert, L. *et al.* Long-lasting solid lubrication by CNT-coated patterned surfaces. *Sci Rep* **7**, 42873 (2017).

17. Bhushan, B. *Introduction to Tribology*. (John Wiley & Sons, 2013).

18. -logy | Meaning of suffix -logy by etymonline. https://www.etymonline.com/word/-logy.

19. Sorensen, A. C., Claud, E. & Soressi, M. Neandertal fire-making technology inferred from microwear analysis. *Sci Rep* **8**, 10065 (2018).

20. Davison, C. St. C. Transporting Sixty-Ton Statues in Early Assyria and Egypt. *Technol Cult* **2**, 11–16 (1961).

21. Shimotsuma, Y., Ogata, M., Nakatsuji, T. & Ozawa, Y. History of Tribology in Ancient Northeast Asia - The Japanese Sledge and the Chinese Chariot -. *Tribology Online* **6**, 174–179 (2011).

22. Guillaume Amontons. De la resistance causée dans les machines, tant par les frottemens des parties qui les composent, que par la roideur des cordes qu'on y employe, et la manière de calculer l'un et l'autre. *Mémoires de l'Académie* 206–227 (1699).

23. Amontons, G. 1699. De la résistance causée dans les machines. *Mémoires de l'Académie Royale A, A* 257–282.

24. Coulomb, C. A. *Théorie Des Machines Simples En Ayant Égard Au Frottement de Leurs Parties et à La Roideur Des Cordages*. (Bachelier, 1821).

25. Bowden, F. P. & Tabor, D. *The Friction and Lubrication of Solids, Volume 1*. (New York: Oxford Univ., 2001).

26. Bowden, D. F. P. & Tabor, D. *MECHANISM OF METALLIC FRICTION**. (1942).

27. Bowden, F. P., Tabor, D. & Taylor, G. I. The area of contact between stationary and moving surfaces. *Proc R Soc Lond A Math Phys Sci* **169**, 391–413 (1997).

28. Stachowiak, G. W. & Batchelor, A. W. *Engineering Tribology, Second Edition*. (Butterworth-Heinemann, 2000).

29. Hutchings, I. M. & Shipway, P. *Tribology: Friction and Wear of Engineering Materials*. (Butterworth-Heinemann, 2017).

30. Wang, H., Hu, Y.-Z. & Zhang, T. Simulations on atomic-scale friction between self-assembled monolayers: Phononic energy dissipation. *Tribol Int* **40**, 680–686 (2007).

31. Xu, L., Ma, T.-B., Hu, Y.-Z. & Wang, H. Vanishing stick–slip friction in few-layer graphenes: the thickness effect. *Nanotechnology* **22**, 285708 (2011).

32. Kawai, S. *et al*. Superlubricity of graphene nanoribbons on gold surfaces. *Science (1979)* **351**, 957–961 (2016).

33. Liu, X.-Z. *et al.* Dynamics of atomic stick-slip friction examined with atomic force microscopy and atomistic simulations at overlapping speeds. *Phys Rev Lett* **114**, 146102 (2015).

34. Tan, X., Guo, D. & Luo, J. Dynamic friction energy dissipation and enhanced contrast in high frequency bimodal atomic force microscopy. *Friction* 1–14 (2022).

35. Skuratovsky, S., Agmon, L. & Berkovich, R. Comparative study of dimensionality and symmetry breaking on nanoscale friction in the Prandtl–Tomlinson model with varying effective stiffness. *Tribol Lett* **68**, 1–11 (2020).

36. Box, C. L., Zhang, Y., Yin, R., Jiang, B. & Maurer, R. J. Determining the effect of hot electron dissipation on molecular scattering experiments at metal surfaces. *JACS Au* **1**, 164–173 (2020).

37. Hertl, N. *et al.* Random force in molecular dynamics with electronic friction. *The Journal of Physical Chemistry C* **125**, 14468–14473 (2021).

38. Kuehn, S., Loring, R. F. & Marohn, J. A. Dielectric fluctuations and the origins of noncontact friction. *Phys Rev Lett* **96**, 156103 (2006).

39. Kisiel, M. *et al.* Suppression of electronic friction on Nb films in the superconducting state. *Nat Mater* **10**, 119–122 (2011).

40. Yildiz, D., Kisiel, M., Gysin, U., Gürlü, O. & Meyer, E. Mechanical dissipation via image potential states on a topological insulator surface. *Nat Mater* **18**, 1201–1206 (2019).

41. Volokitin, A. I. & Persson, B. N. J. Electromagnetic Fluctuations at the Nanoscale. in *Theory and Applications* (Springer, 2017).

42. M. Samadashvili. Non-contact friction studied with pendulum AFM. (University of Basel, Basel (Switzerland), 2014).

43. Challen, J. M., McLean, L. J. & Oxley, P. L. B. Plastic deformation of a metal surface in sliding contact with a hard wedge: its relation to friction and wear. *Proceedings of the Royal Society of London. A. Mathematical and Physical Sciences* **394**, 161–181 (1984).

44. Blau, P. J. *Friction Science and Technology*. (CRC Press, Boca Raton, 2008).

45. Schroeder, T. A. & Wayman, C. M. Martensite-to-martensite transformations in Cu&.sbnd;Zn alloys. *Acta Metallurgica* **26**, 1745–1757 (1978).

46. Su, H. *et al.* Frictional heat-induced phase transformation on train wheel surface. *Journal of Iron and Steel Research International* **15**, 49–55 (2008).

47. Grützmacher, P. G. *et al.* Interplay between microstructural evolution and tribo-chemistry during dry sliding of metals. *Friction* **7**, 637–650 (2019).

48. Blau, P. J. Interpretations of the friction and wear break-in behavior of metals in sliding contact. *Wear* **71**, 29–43 (1981).

49. Blau, P. J. On the nature of running-in. *Tribol Int* **38**, 1007–1012 (2005).

50. Brinksmeier, E., Garbrecht, M., Meyer, D. & Dong, J. Surface hardening by strain induced martensitic transformation. *Production Engineering* **2**, 109–116 (2008).

51. Gwidon W. Stachowiak & Andrew W. Batchelor. Chapter 7 - Elastohydrodynamic Lubrication. in *Engineering Tribology (Fourth Edition)* (eds. Stachowiak, G. W. & Batchelor, A. W.) 293–370 (Butterworth-Heinemann, Boston, 2014).

52. Green, I. & Woodruff, G. W. *POISSON RATIO EFFECTS AND CRITICAL VALUS IN SPHERICAL AND CYLINDRICAL HERTZIAN CONTACTS*. *Int. J. of Applied Mechanics and Engineering* vol. 10 (2005).

53. Sung, I.-H., Lee, H.-S. & Kim, D.-E. Effect of surface topography on the frictional behavior at the micro/nano-scale. *Wear* **254**, 1019–1031 (2003).

54. Rapoport, L. *et al.* Friction and wear of MoS2 films on laser textured steel surfaces. *Surf Coat Technol* **202**, 3332–3340 (2008).

55. Etsion, I. State of the Art in Laser Surface Texturing. *J Tribol* **127**, 248–253 (2005).

56. Suh, N. P., Mosleh, M. & Howard, P. S. Control of friction. *Wear* **175**, 151–158 (1994).

57. Reinert, L. *et al.* Long-lasting solid lubrication by CNT-coated patterned surfaces. *Sci Rep* **7**, 42873 (2017).

58. Rosenkranz, A., Szurdak, A., Grützmacher, P. G., Hirt, G. & Mücklich, F. Friction reduction induced by elliptical surface patterns under lubricated conditions. *Adv Eng Mater* **20**, 1700731 (2018).

59. Schäfer, C. *et al.* Influence of surface design on the solid lubricity of carbon nanotubes-coated steel surfaces. *Tribol Lett* **66**, 1–15 (2018).

60. Meriche, F. *et al.* Micro structuring of LiNbO3 by using nanosecond pulsed laser ablation. *Appl Surf Sci* **254**, 1327–1331 (2007).

61. Bieda, M., Siebold, M. & Lasagni, A. F. Fabrication of sub-micron surface structures on copper, stainless steel and titanium using picosecond laser interference patterning. *Appl Surf Sci* **387**, 175–182 (2016).

62. Toma, F.-L., Alamri, S., Leupolt, B., Kunze, T. & Barbosa, M. Functionalization of Suspension Sprayed HVOF TiO 2 Coatings by Direct Laser Interference Patterning. *Journal of Thermal Spray Technology* **30**, 1159–1173 (2021).

63. Lasagni, A. F., Acevedo, D. F., Barbero, C. A. & Mücklich, F. One-Step Production of Organized Surface Architectures on Polymeric Materials by Direct Laser Interference Patterning. *Adv Eng Mater* **9**, 99–103 (2007).

64. Lang, V., Roch, T. & Lasagni, A. F. High-Speed Surface Structuring of Polycarbonate Using Direct Laser Interference Patterning: Toward 1 m2 min−1 Fabrication Speed Barrier . *Adv Eng Mater* **18**, 1342–1348 (2016).

65. Wang, W., Boneberg, J. & Schmidt-Mende, L. Performance enhancement in Sb2S3 solar cell processed with direct laser interference patterning. *Solar Energy Materials and Solar Cells* **230**, 111235 (2021).

66. Wang, Y.-R., Olaizola, S. M., Han, I. S., Jin, C.-Y. & Hopkinson, M. Direct patterning of periodic semiconductor nanostructures using single-pulse nanosecond laser interference. *Opt Express* **28**, 32529–32539 (2020).

67. Gamaly, E. G., Rode, A. V, Luther-Davies, B. & Tikhonchuk, V. T. Ablation of solids by femtosecond lasers: Ablation mechanism and ablation thresholds for metals and dielectrics. *Phys Plasmas* **9**, 949–957 (2002).

68. Dausinger, F., Hugel, H. & Konov, V. I. Micromachining with ultrashort laser pulses: from basic understanding to technical applications. in *Proc.SPIE* vol. 5147 106–115 (2003).

69. Sugioka, K., Meunier, M. & Piqué, A. *Laser Precision Microfabrication*. vol. 135 (Springer, 2010).

70. Günther, D. *et al*. 1 - High precision patterning of biomaterials using the direct laser interference patterning technology. in *Laser Surface Modification of Biomaterials* (ed. Vilar, R.) 3–33 (Woodhead Publishing, 2016).

71. Leitz, K.-H., Redlingshöfer, B., Reg, Y., Otto, A. & Schmidt, M. Metal Ablation with Short and Ultrashort Laser Pulses. *Phys Procedia* **12**, 230–238 (2011).

72. Zhigilei, L. V, Lin, Z. & Ivanov, D. S. Atomistic Modeling of Short Pulse Laser Ablation of Metals: Connections between Melting, Spallation, and Phase Explosion. *The Journal of Physical Chemistry C* **113**, 11892–11906 (2009).

73. Winter, J. *et al.* Ultrashort single-pulse laser ablation of stainless steel, aluminium, copper and its dependence on the pulse duration. *Opt Express* **29**, 14561 (2021).

74. Allen, P. B. Theory of thermal relaxation of electrons in metals. *Phys Rev Lett* **59**, 1460 (1987).

75. Leveugle, E., Ivanov, D. S. & Zhigilei, L. V. Photomechanical spallation of molecular and metal targets: molecular dynamics study. *Applied Physics A* **79**, 1643–1655 (2004).

76. Paltauf, G. & Dyer, P. E. Photomechanical processes and effects in ablation. *Chem Rev* **103**, 487–518 (2003).

77. Ivanov, D. S. *et al.* Molecular dynamics study of the short laser pulse ablation: quality and efficiency in production. *Applied Physics A* **117**, 2133–2141 (2014).

78. Torrisi, L., Borrielli, A. & Margarone, D. Study on the ablation threshold induced by pulsed lasers at different wavelengths. *Nucl Instrum Methods Phys Res B* **255**, 373–379 (2007).

79. Byskov-Nielsen, J., Savolainen, J.-M., Christensen, M. S. & Balling, P. Ultra-short pulse laser ablation of metals: threshold fluence, incubation coefficient and ablation rates. *Applied Physics A* **101**, 97–101 (2010).

80. Ivanov, D. S. & Zhigilei, L. V. Combined atomistic-continuum modeling of short-pulse laser melting and disintegration of metal films. *Phys Rev B* **68**, 064114 (2003).

81. Yao, Y. L., Chen, H. & Zhang, W. Time scale effects in laser material removal: a review. *The International Journal of Advanced Manufacturing Technology* **26**, 598–608 (2005).

82. Ionin, A. A. *et al.* Nanoscale surface boiling in sub-threshold damage and above-threshold spallation of bulk aluminum and gold by single femtosecond laser pulses. *Laser Phys Lett* **13**, 025603 (2015).

83. Artyukov, I. *et al*. Relaxation phenomena in electronic and lattice subsystems on iron surface during its ablation by ultrashort laser pulses. *JETP Lett* **99**, 51–55 (2014).

84. Müller, D. W., Fox, T., Grützmacher, P. G., Suarez, S. & Mücklich, F. Applying Ultrashort Pulsed Direct Laser Interference Patterning for Functional Surfaces. *Sci Rep* **10**, (2020).

85. Pou-Álvarez, P. *et al.* Nanosecond, picosecond and femtosecond laser surface treatment of magnesium alloy: role of pulse length. *Surf Coat Technol* **427**, 127802 (2021).

86. Fang, S. *et al.* Fabrication of Interference Textures on Cemented Carbides Using Nanosecond and Femtosecond Laser Pulses. *Procedia CIRP* **87**, 216–221 (2020).

87. Sebenik, R. F. *et al.* Molybdenum and Molybdenum Compounds. in *Ullmann's Encyclopedia of Industrial Chemistry* (2000).

88. Baker, R. M. Sliding contacts-electrical characteristics. *Transactions of the American Institute of Electrical Engineers* **55**, 94–100 (1936).

89. Savage, R. H. Graphite lubrication. *J Appl Phys* **19**, 1–10 (1948).

90. Morstein, C. E., Klemenz, A., Dienwiebel, M. & Moseler, M. Humidity-dependent lubrication of highly loaded contacts by graphite and a structural transition to turbostratic carbon. *Nat Commun* **13**, 5958 (2022).

91. Sliney, H. E. Solid lubricant materials for high temperatures—a review. *Tribol Int* **15**, 303–315 (1982).

92. Brainard, W. A. *The Thermal Stability and Friction of the Disulfides, Diselenides, and Ditellurides of Molybdenum and Tungsten in Vacuum (109 to 106 Torr)*. (National Aeronautics and Space Administration, 1968).

93. Scharf, T. W. & Prasad, S. V. Solid lubricants: a review. *J Mater Sci* **48**, 511–531 (2013).

94. Briscoe, B. J. & Tabor, D. The effect of pressure on the frictional properties of polymers. *Wear* **34**, 29–38 (1975).

95. Bahadur, S. & Tabor, D. The wear of filled polytetrafluoroethylene. *Wear* **98**, 1–13 (1984).

96. Dickrell, P. L. *et al.* Frictional anisotropy of oriented carbon nanotube surfaces. *Tribol Lett* **18**, 59–62 (2005).

97. Hirata, A., Igarashi, M. & Kaito, T. Study on solid lubricant properties of carbon onions produced by heat treatment of diamond clusters or particles. *Tribol Int* **37**, 899–905 (2004).

98. MacLucas, T. & Suarez, S. On the Solid Lubricity of Electrophoretically Deposited Carbon Nanohorn Coatings. *Lubricants* **7**, (2019).

99. Yu, M.-F. *et al.* Strength and breaking mechanism of multiwalled carbon nanotubes under tensile load. *Science (1979)* **287**, 637–640 (2000).

100. Treacy, M. M. J., Ebbesen, T. W. & Gibson, J. M. Exceptionally high Young's modulus observed for individual carbon nanotubes. *Nature* **381**, 678–680 (1996).

101. Vaisman, L., Wagner, H. D. & Marom, G. The role of surfactants in dispersion of carbon nanotubes. *Adv Colloid Interface Sci* **128**, 37–46 (2006).

102. Hirata, A. & Saito, S. Solid lubrication with carbon onions at high temperature in vacuum. *MRS Online Proceedings Library (OPL)* **1085**, 1085-T05 (2008).

103. Berman, D., Erdemir, A. & Sumant, A. V. Graphene: a new emerging lubricant. *Materials today* **17**, 31–42 (2014).

104. MacLucas, T., Schütz, S., Suarez, S. & Mücklich, F. Surface protection of austenitic steels by carbon nanotube coatings. *Surf Topogr* **6**, 014005 (2018).

105. Reinert, L., Schütz, S., Suárez, S. & Mücklich, F. Influence of Surface Roughness on the Lubrication Effect of Carbon Nanoparticle-Coated Steel Surfaces. *Tribol Lett* **66**, 45 (2018).

106. Link, J. M., Salinas, E. Y., Hu, J. C. & Athanasiou, K. A. The tribology of cartilage: Mechanisms, experimental techniques, and relevance to translational tissue engineering. *Clinical Biomechanics* **79**, 104880 (2020).

107. Besra, L. & Liu, M. A review on fundamentals and applications of electrophoretic deposition (EPD). *Prog Mater Sci* **52**, 1–61 (2007).

108. Eugene Harsanyii. Method of coating radiant bodies. 1–4 (1933).

109. Grillon, F., Fayeulle, D. & Jeandin, M. Quantitative image analysis of electrophoretic coatings. *J Mater Sci Lett* **11**, 272–275 (1992).

110. Sarkar, P. & Nicholson, P. S. Electrophoretic Deposition (EPD): Mechanisms, Kinetics, and Application to Ceramics. *Journal of the American Ceramic Society* **79**, 1987–2002 (1996).

111. Hamaker, H. C. & Verwey, E. J. W. Part II.—(C) Colloid stability. The role of the forces between the particles in electrodeposition and other phenomena. *Transactions of the Faraday Society* **35**, 180–185 (1940).

112. Koelmans, H. *Suspensions in Non Aqueous Media*. (publisher unknown, 1955).

113. Hamaker, H. C. Formation of a deposit by electrophoresis. *Transactions of the Faraday Society* **35**, 279–287 (1940).

114. Atiq Ur Rehman, M., Chen, Q., Braem, A., Shaffer, M. S. P. & Boccaccini, A. R. Electrophoretic deposition of carbon nanotubes: recent progress and remaining challenges. *International Materials Reviews* **66**, 533–562 (2021).

115. Michaud, X., Shi, K. & Zhitomirsky, I. Electrophoretic deposition of LiFePO4 for Li-ion batteries. *Mater Lett* **241**, 10–13 (2019).

116. Boccaccini, A. R., Keim, S., Ma, R., Li, Y. & Zhitomirsky, I. Electrophoretic deposition of biomaterials. *J R Soc Interface* **7**, S581–S613 (2010).

117. Liang, H., Bu, Y., Zhang, J., Cao, Z. & Liang, A. Graphene oxide film as solid lubricant. *ACS Appl Mater Interfaces* **5**, 6369–6375 (2013).

118. Liu, Y., Chen, X., Li, J. & Luo, J. Enhancement of friction performance enabled by a synergetic effect between graphene oxide and molybdenum disulfide. *Carbon N Y* **154**, 266–276 (2019).

119. Thomas, B. J. C., Boccaccini, A. R. & Shaffer, M. S. P. Multi-walled carbon nanotube coatings using electrophoretic deposition (EPD). *Journal of the American Ceramic Society* **88**, 980–982 (2005).

120. MacLucas, T., Leonhard-Trautmann, P., Suarez, S. & Mücklich, F. Long-Term Lubricity of Carbon Nanoparticle Coatings on Periodically Laser-Patterned Metallic Surfaces. *Tribol Lett* **70**, 123 (2022).

121. MacLucas, T. *et al.* Influence of structural depth of laser-patterned steel surfaces on the solid lubricity of carbon nanoparticle coatings. *Friction* (2022).

122. Su, Y. & Zhitomirsky, I. Electrophoretic deposition of graphene, carbon nanotubes and composite films using methyl violet dye as a dispersing agent. *Colloids Surf A Physicochem Eng Asp* **436**, 97–103 (2013).

123. Raza, M. A. *et al.* Electrochemical behavior of graphene coatings deposited on copper metal by electrophoretic deposition and chemical vapor deposition. *Surf Coat Technol* **332**, 112–119 (2017).

124. Kim, S. *et al.* Spin-and spray-deposited single-walled carbon-nanotube electrodes for organic solar cells. *Adv Funct Mater* **20**, 2310–2316 (2010).

125. Mirri, F. *et al*. High-performance carbon nanotube transparent conductive films by scalable dip coating. *ACS Nano* **6**, 9737–9744 (2012).

126. Jang, E. Y., Kang, T. J., Im, H. W., Kim, D. W. & Kim, Y. H. Single-walled carbon-nanotube networks on large-area glass substrate by the dip-coating method. *Small* **4**, 2255–2261 (2008).

127. Somani, P. R. *et al*. Field electron emission of double walled carbon nanotube film prepared by drop casting method. *Solid State Electron* **51**, 788–792 (2007).

128. Monea, B. F., Ionete, E. I., Spiridon, S. I., Ion-Ebrasu, D. & Petre, E. Carbon nanotubes and carbon nanotube structures used for temperature measurement. *Sensors* **19**, 2464 (2019).

129. Kim, S. *et al.* Spin-and spray-deposited single-walled carbon-nanotube electrodes for organic solar cells. *Adv Funct Mater* **20**, 2310–2316 (2010).

130. Jo, J. W., Jung, J. W., Lee, J. U. & Jo, W. H. Fabrication of highly conductive and transparent thin films from single-walled carbon nanotubes using a new non-ionic surfactant via spin coating. *ACS Nano* **4**, 5382–5388 (2010).

131. Datsyuk, V. *et al*. Chemical oxidation of multiwalled carbon nanotubes. *Carbon N Y* **46**, 833–840 (2008).

132. Kim, H., Choi, H., Hwang, S., Kim, Y. & Jeon, M. Fabrication and characterization of carbon-based counter electrodes prepared by electrophoretic deposition for dye-sensitized solar cells. *Nanoscale Res Lett* **7**, 1–4 (2012).

133. Zhu, G., Pan, L., Lu, T., Xu, T. & Sun, Z. Electrophoretic deposition of reduced graphene-carbon nanotubes composite films as counter electrodes of dye-sensitized solar cells. *J Mater Chem* **21**, 14869–14875 (2011).

134. Enoki, T. Diamond-to-graphite conversion in nanodiamond and electronic properties of nanodiamond-derived carbon system. *Физика твердого тела* **46**, 635–640 (2004).

135. Maghsoudi, Sh. & Noroozian, E. HP-SPME of Volatile Polycyclic Aromatic Hydrocarbons from Water Using Multiwalled Carbon Nanotubes Coated on a Steel Fiber through Electrophoretic Deposition. *Chromatographia* **75**, 913–921 (2012).

136. Ata, M. S., Sun, Y., Li, X. & Zhitomirsky, I. Electrophoretic deposition of graphene, carbon nanotubes and composites using aluminon as charging and film forming agent. *Colloids Surf A Physicochem Eng Asp* **398**, 9–16 (2012).

137. Besra, L., Uchikoshi, T., Suzuki, T. S. & Sakka, Y. Experimental verification of pH localization mechanism of particle consolidation at the electrode/solution interface and its application to pulsed DC electrophoretic deposition (EPD). *J Eur Ceram Soc* **30**, 1187–1193 (2010).

138. Alderete, B. *et al.* Near Superhydrophobic Carbon Nanotube Coatings Obtained via Electrophoretic Deposition on Low-Alloy Steels. *Adv Eng Mater* **23**, 2001448 (2021).

139. Ouyang, J.-H., Li, Y.-F., Zhang, Y.-Z., Wang, Y.-M. & Wang, Y.-J. High-temperature solid lubricants and self-lubricating composites: A critical review. *Lubricants* **10**, 177 (2022).

140. Kumar, R., Hussainova, I., Rahmani, R. & Antonov, M. Solid Lubrication at High-Temperatures—A Review. *Materials* **15**, (2022).

141. Terrones, M. *et al.* N-doping and coalescence of carbon nanotubes: synthesis and electronic properties. *Applied Physics A* **74**, 355–361 (2002).

142. Reinert, L., Varenberg, M., Mücklich, F. & Suárez, S. Dry friction and wear of self-lubricating carbon-nanotube-containing surfaces. *Wear* **406**, 33–42 (2018).

143. MacLucas, T., Schütz, S., Suarez, S., Müller, F. & Mücklich, F. Parametric analysis of the coating thickness development of electrophoretically deposited carbon nanotube coatings. *Carbon Trends* **11**, 100265 (2023).

144. Datsyuk, V. *et al*. Chemical oxidation of multiwalled carbon nanotubes. *Carbon N Y* **46**, 833–840 (2008).

145. Gong, H., Kim, S.-T., Lee, J. D. & Yim, S. Simple quantification of surface carboxylic acids on chemically oxidized multi-walled carbon nanotubes. *Appl Surf Sci* **266**, 219–224 (2013).

146. Osorio, A. G., Silveira, I. C. L., Bueno, V. L. & Bergmann, C. P. H2SO4/HNO3/HCl—Functionalization and its effect on dispersion of carbon nanotubes in aqueous media. *Appl Surf Sci* **255**, 2485–2489 (2008).

147. Bac, C. G. *et al.* 13C NMR investigation of carbon nanotubes and derivatives. *Current Applied Physics* **1**, 149–155 (2001).

148. Zurek, E., Pickard, C. J., Walczak, B. & Autschbach, J. Density functional study of the 13C NMR chemical shifts in small-to-medium-diameter infinite single-walled carbon nanotubes. *J Phys Chem A* **110**, 11995–12004 (2006).

149. Nicolosi, V. *et al.* Spontaneous Exfoliation of Single-Walled Carbon Nanotubes Dispersed Using a Designed Amphiphilic Peptide. *Biomacromolecules* **9**, 598–602 (2008).

150. Kumara, C., Lance, M. J. & Qu, J. Macroscale superlubricity by a sacrificial carbon nanotube coating. *Mater Today Nano* **21**, 100297 (2023).

List of figures

[2] Shutterstock

Appendix A

Characterization of graphite-coated wear tracks after friction testing in vacuum

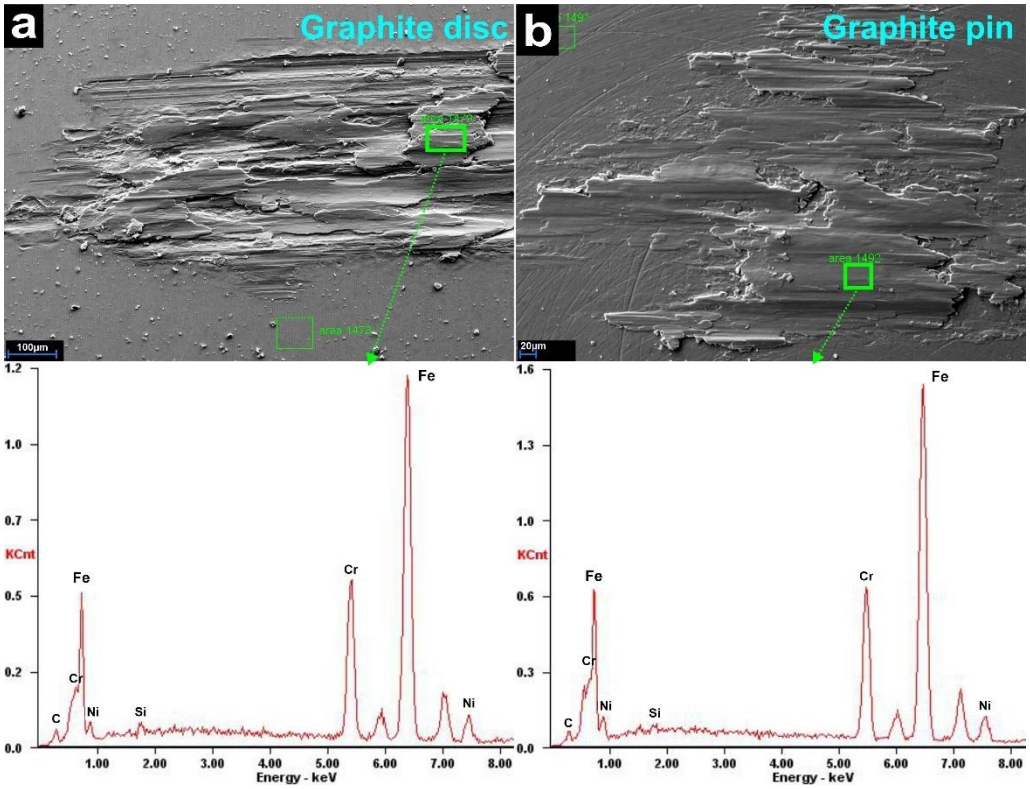

Figure 24. Scanning electron micrographs showing the wear tracks on the substrate (disc) and the counter body (pin) after tribological testing of graphite-coated (a,b) substrates in vacuum (<10^{-5} mbar). Below the micrographs, EDS spectra of selected areas are depicted.

The EDS spectra of the wear tracks on disc and pin are close to identical and neither show traces of carbon. Instead, Fe, Cr and Ni are detected which are alloying elements and stem from the substrate. The graphitic carbon appears to have been removed completely.